1-1-2013

Induced Damping And Its Relationship To Beneficial Energy Harvesting In Dielectric Elastomers With Application To Walking

Heather L. Lai
Wayne State University,

INDUCED DAMPING AND ITS RELATIONSHIP TO BENEFICIAL ENERGY HARVESTING IN DIELECTRIC ELASTOMERS WITH APPLICATION TO WALKING

by

HEATHER LAI

Submitted to the Graduate School

of Wayne State University,

Detroit, Michigan

in partial fulfillment of the requirements

for the degree of

DOCTOR OF PHILOSOPHY

2013

MAJOR: MECHANICAL ENGINEERING

Approved By:

_____

Advisor Date

_____

_____

_____

_____

ACKNOWLEDGEMENTS

I am incredibly thankful for the grace that God has poured into my life during this endeavor through the following people:

My husband, Wilkin Lai – without your encouragement, I never would have begun this project.

My father, Howard Havlicsek – without your expertise, not a single piece of hardware I developed for this project would have worked properly.

My advisor and mentor, Chin An Tan – without your oversight and insight, this project would not have been completed with excellence.

I would also like to gratefully acknowledge the Mechanical Engineering Department, the Division of Research and the Graduate School of Wayne State University for their support of this work.

TABLE OF CONTENTS

LIST OF TABLES

LIST OF FIGURES

NOMENCLATURE

Listed in order of first occurrence:

σ_i	principal stresses (Pa)
λ_i	stretch ratios in the principal directions
W	strain energy density function
p	hydrostatic pressure (Pa)
I_i	invariants of the deformation tensor
$\mathbf{F}$	Cauchy-Green deformation gradient tensor
x_{2avg}	theoretical average width due to the parabola shaped pull-in edges (m)
κ	boundary constraint coefficient
x_i	extension in principal directions; (x_1 - axial, x_2 -lateral, x_3 - transverse) (m)
σ_i^{MN}	principal stresses calculated using the modified Neo-Hookean model (Pa)
σ_i^{MM}	principal stresses calculated using the modified Moony-Rivlin model (Pa)
σ_i^{MY}	principal stresses calculated using the modified Yeoh model (Pa)
F_i	force in the principal directions (N)
$\mathbf{A}$	Helmholtz free energy of the system (J)
C	capacitance (farad)
Q	charge (coulomb)
V	voltage (volt)
ε_0	dielectric constant of a vacuum (8.85×10^{-12} F/m)
ε	permittivity of the dielectric material (Farads/meter)
ε_r	relative permittivity of the material
A	surface area of the compliant electrode (m^2); A_c at charge, A_d at discharge.
σ_M	Maxwell stress (Pa)
E	electric field (V/m)
$\tilde{\lambda}_i$	Maxwell stretch ratios
σ_{iM}	stresses in principle directions which result from Maxwell stress (Pa)

$\tilde{\lambda}$	equilibrium Maxwell stretch ratio; $\tilde{\lambda}_c$ at charge, $\tilde{\lambda}_d$ at discharge
$\sigma_{i(mech)}$	principle stress due to mechanical loading only (Pa)
V_c	charge voltage (V)
U_{elec}	electrical potential energy (J)
$U_{harvest}$	energy harvested (J)
$E_{\max}$	maximum electric field (V/m)
$\forall$	volume of DE film (m^3)
U_c	electric potential energy at charge (J)
U_d	electric potential energy at discharge (J)
d_v	viscoelastic damping force (N)
c	viscoelastic camping coefficient (N-s/m)
U_D	damping energy (J)
x_0	oscillation amplitude (m)
E^*	complex stiffness (Pa)
E'	energy storage modulus (Pa)
E''	energy loss modulus (Pa)
d_h	hysteretic damping force (N)
h	hysteretic damping coefficient (N/m); h_C constrained, h_D unconstrained condition
ζ_h	hysteretic equivalent damping ratio, ζ_r rotational equivalent damping ratio
δ	phase angle (or loss angle) (rad)
$\tan\delta$	tangent of loss angle, descriptor of mechanical damping
η	loss factor
η_d	dissipation factor
η_h	energy harvesting factor
ΔD	area enclosed by the extension / force curve (N-m)
k	stiffness; k_t translational stiffness (N/m), k_r rotational stiffness (N/rad)
c	viscous damping coefficient (N-s/m)

c_t	translational viscous damping coefficient (N-s/m)
c_r	rotational viscous damping coefficient (N-s/rad)
θ	angle of knee joint bend as measured from vertical (rad)
l_t	length of the tibia portion (m)
I	mass moment of inertia of knee joint test stand for tibia about knee joint (kg-m^2)
ω_d	damped natural frequency of the tibia during free oscillation (rad/s)
T_d	damped period of the tibia during free oscillation (s)
M_{k_r}	moment at knee joint due to stiffness of DE harvester (N-m)
$M_{k_{DEbaseline}}$	moment at knee joint due to stiffness of uncharged DE harvester (N-m)
$M_{k_{DEactive}}$	moment at knee joint due to stiffness of charged DE harvester (N-m)
M_{c_r}	moment at knee joint due to damping of DE harvester (N-m)
$M_{c_{DEbaseline}}$	moment at knee joint due to damping of uncharged DE harvester (N-m)
$M_{c_{DEactive}}$	moment at knee joint due to damping of charged DE harvester (N-m)
M_{DE}	moment at knee joint due to total DE behavior (N-m)
t_c	time at which DE charge occurs (s)
t_d	time at which DE discharge occurs (s)

1 Introduction

1.1 Motivation for this research

Current energy trends point to a dramatic need to change our energy production and consumption behaviors. On a large scale, both the reduction of energy consumption through the development of more energy efficient vehicles, buildings and manufacturing processes as well as the development of sustainable energy sources attached to the electrical grid such as solar, wind and wave energy are receiving much attention. However, there is also ongoing research into energy conservation on a much smaller scale. Energy scavengers have been considered for applications from rotating shafts and bridge vibration to chemical differentials and biomechanics in the human body. This type of energy harvesting provides a means for powering remote and imbedded wireless electronic devices while reducing the environmental hazards associated with our current dependence on batteries. This research, which focuses on low-level energy harvesting due to biomechanical motion using electroactive polymers is timely and critical for several important reasons:

- Existence of low power electronics
- Remote and mobile deployment of low power wearable medical electronics
- Development of soft polymer electromechanical devices
- Ability to control energy harvestings in a beneficial manner

Each of these motives will be discussed here to demonstrate the importance and relevance of the research presented here.

1.1.1 Low Power Electronics

As energy efficient electronics are being devised that are smaller and require much less power than conventional devices, a great need has arisen for the development of small scale efficient, inexpensive, and robust sustained energy sources. Small consumer electronics such as

cell phones or MP3 players have increasingly small power consumption requirements [1]. Table 1.1 provides examples of energy requirements for many regularly used portable devices. While laptops and other heavy computing devices require substantial power, devices such as MP3 players have much lower consumption. These low consumption devices are prime candidates for battery elimination using energy harvesting.

Table 1.1: Power requirement for consumer electronic applications [2].

Device	Average Usage (W)	Idle (W)
Laptop	15.6	14.0
Handheld	1.56	1.3
Cell phone	0.638	0.026
Pager	0.081	0.013
High-end MP3	2.98	1.9
Low-end MP3	0.327	0.14
Voice recorder	0.166	0.017

As medical technological advances continue to increase the variety of electronic devices which can be used to help control biological systems, the need to power these devices over long periods of time becomes critical. The following table provides an overview of power requirements for a few commonly used medical devices.

Table 1.2: Power requirement for current medical devices [3].

Device	Usage (W)
Insulin infusion pump	12
Pacemaker	5.6
Artificial Kidney [4]	5
Arterial pressure monitor	3
Blood coagulation monitor	0.5
Glucose level monitor	0.5

While some of these currently used monitoring systems are reasonable candidates for energy harvesting, there has been a recent movement to develop ultra-low power devices, creating a situation where low power medical monitoring devices could potentially make up a large portion of the wearable sensors used. Table 1.3 describes the power requirements for state of the art

components of wireless medical monitoring systems, demonstrating power requirements much lower than in the past.

Table 1.3: Power requirement for state of the art medical monitoring.

Device	Power Requirement
Streaming Biosensor [5]	2 mW
MedRadio receiver [6]	1.2 mW
Wireless body monitors [7]	20 µW
EEG seizure detection monitor [8]	0.99 µW

Currently most small scale electronic devices, such as those shown in Table 1.2 and Table 1.3 are powered by batteries which require either replacement or periodic access to the electrical grid for charging. For many applications these requirements severely reduce the effectiveness of the devices itself. The requirement that batteries be accessible prevents the development of devices which are inaccessible because of position (for example, embedded within a structure, or implanted within the human body), location (remote or inaccessible areas) or size (too small for manual replacement). Eliminating this need for continual replacement/recharging of batteries is a significant research issue of current interest. The development of ultra-low power devices such as those shown in Table 1.3 is a very important part of eliminating the need for a connection to the electrical grid, using energy scavenging to create truly wireless operation over the entire life of the device.

1.1.2 Wearable Medical applications

As described above, there are many developing low power medical applications which provide means to continually control or monitor biological systems on patients. Many of these devices are designed to be worn throughout the day while patients undergo activities of daily living. These types of devices include uses such as monitoring, rehabilitation, muscular assistance and prosthetics.

As described in the introduction, medical systems are one of the major candidates for biomechanical energy harvesting sources. These applications include wireless body sensor networks (WBSN), which monitor a wide range of biological vital signs including temperature, blood pressure, oxygen level, pulse and cardiac activity; telerehabilitation supervision which can monitor a patient undergoing rehabilitation for compliance with suggested activities; functional electrical stimulation (FES) which controls muscle behavior to alleviate gait dysfunction; and even powered prosthetics which can perform realistic human motions with low power requirements. The integration of smart damping using energy harvesting into each of these applications which currently rely on battery power could greatly improve their utility and longevity, improving the quality of life for those who use them.

As can be seen from the many potential applications of energy harvesting in the medical industry, research in this area is vitally important for the further development of sustainable, self-powered medical devices.

1.1.3 Electroactive Polymers

One class of materials which has been gaining increasing momentum over the last decade for use as both actuators and sensors is that of electroactive polymers (EAP). While individual devices represented by these materials can vary substantially, they all have in common that they convert strain energy stored within the structure into other forms of energy. The most widely utilized form of EAP are those with electromechanical coupling, meaning that mechanical strain energy within the material can be converted into electrical energy (and vice versa, for purpose of actuation). Unlike other types of electromechanical smart materials such as piezoelectric ceramics, which are often brittle, most EAPs have a low elastic modulus and can exhibit large strains without substantial stress generations [9]. This provides the means to produce a soft,

comfortable material which can be controlled to perform electromechanical coupling which can be used not only for sensing and actuation, but also for energy harvesting as well. In addition to this, recent techniques for producing flexible polymer printed circuit boards are beginning to emerge, providing a means to integrate the entire device, into a single, flexible, comfortable package. One type of EAP is the dielectric elastomer (DE) which utilizes the electrostatic forces built up across the dielectric polymer to convert between electrical and mechanical energy.

As research into DEs for use as energy harvesters increases, a unique opportunity presents itself through the development of these devices. However, as with most EAPs, dielectric elastomers are highly nonlinear and require novel models to describe their electromechanical coupling when undergoing mechanical strain. Not only is an understanding of the material itself critical, how this soft polymer energy harvester affects the host structure which it is attached is an equally important area of research.

1.1.4 Beneficial energy harvesting

One of the significant results of the development of low powered electronics is that increasingly sophisticated controls can be implemented using small scale electronics, providing a means to carefully control not only instruments being powered, but also the behavior of energy harvesting power supply itself. This ability to perform carefully controlled energy harvester has allowed for the development of beneficial (or "mutualistic") energy harvesting of biomechanical motions. The most promising example of beneficial energy harvesting is harvesting energy due to walking, either at the ankle or the knee joint [10].

Beneficial energy harvesting is based on the fact that energy harvesting devices modify their surroundings through the introduction of mechanical stiffness and damping induced by the conversion of mechanical energy in to electrical energy. Recent work by several different

research teams has begun to address the need to harness the dynamic effects that energy harvesting can potentially have on the host structures. These works include the PowerWalk, a commercially available knee joint harvester, can generate up to 14 W on level walking and greater than 25 W on steep terrain [11]. Also, a transfemoral prosthesis, developed by Andrysek et al. is able to generate up to 1.6 W using an adaptive, beneficial damping for a amputee walking at a fast pace [12]. Both of these devices are developed using a series of gears and clutches to engage and disengage the energy harvester as desired. The end result is an effective, yet bulky and noisy electromechanical energy harvester.

The need for development of carefully controlled wearable energy harvesting devices is clear, however, among the many research objectives which are necessary for a comprehensive development of this technology, a deeper understanding of the mechanical effect, which electromechanical energy harvesting has on the host structure is still lacking. Research is still needed to understand and model the effects of energy harvesting using soft polymers on the stiffness and damping of biomechanical systems.

By emphasizing both the growing need for remote, mobile electronics and increased development of the technology necessary for future commercial development, these four motivations provide clear justification for advancing research into understanding and modeling the effects on the wearer of electroactive polymer energy harvesting of biomechanical energy due to walking.

1.2 Dissertation Objectives and Organization

This research seeks to expand prior examination of energy harvesting by investigating the use of dielectric elastomers (DE), a class of electroactive polymer smart material, for harvesting energy due to human motion. The dissertation presented is composed of three distinct but related

objectives. The first objective is to characterize the behavior of DE energy harvesters by modeling the effects of key parameters such as dielectric and electrode material, bias voltage and device geometry on the energy harvesting of dielectric elastomer generators. The second objective is to develop a fundamental understanding of the alteration of the mechanical behavior, as described by stiffness and damping, which occurs as a result of DE energy harvesting. The final objective is to design, model and evaluate a DE generator for strategic, beneficial damping/energy harvesting during human locomotion. To accomplish these objectives, modeling and experimental goals have been established which provide the key components necessary for applying the behavior of dielectric elastomers to the development of controllable energy generating dampers.

This dissertation begins by describing the current technology of both energy harvesting and electroactive materials, providing a brief overview of recent advancements in the uses of energy harvesting, specifically describing methods for improving biomechanical energy harvesting as well as the current state of dielectric elastomers. The subsequent chapters of this dissertation explain the work performed in the completion of the research goals described above. Objective one is addressed in Chapter 3 through the development of a hyperelastic model for a DE energy harvester, including geometric, material and electrical concerns. The second objective is described in Chapter 4, where modifications to the stiffness and damping of the energy harvesting system are modeled and experimentally demonstrated for several applications of dielectric elastomer generators. The work involved in completing the final objective is explained in Chapter 5, through modeling and simulations demonstrating the mapping of the DE energy harvesting cycle to the human walking cycle for different energy harvesting conditions. The

account is then concluded with a discussion of the significance of this work and a description of the future work based on the results obtained through this research.

2 Background Literature Review

The following literature review provides background information pertaining to the three main areas of interest for this research: state-of-the-art energy harvesting techniques and applications, dielectric elastomer electroactive polymers, and beneficial energy harvesting control.

2.1 Energy Harvesting

As described previously, the need to find an efficient means of converting excess local energy (thermal, mechanical, chemical, etc.) to electrical energy for use powering electronic devices is a critical area of research. This section provides a survey of the current state of the art in energy harvesting, describing how these different techniques are used to meet the need for electricity, followed by a description of current applications of energy harvesting in several different disciplines.

2.1.1 Energy harvesting mechanisms

Harvesting energy from environmental sources is becoming a very important area of research and development. As miniature electronic devices become increasingly ubiquitous, small, unobtrusive energy sources are needed to power the devices. Some of the most commonly utilized sources of harvested energy are described in Table 2.1.

Table 2.1: Estimated Power Density for Traditional Energy Harvesting Sources [13, 14].

Source	Power Density (mW/cm^3)
Solar Cells	15
Piezoelectric	0.33
Thermoelectric	0.04

Each of these methods has promise in specific applications; however they each have shortcomings which prevent their use in many important situations. The use of solar cells for energy harvesting is well developed, and because of their high energy density, they are well suited for many applications, however in applications where there is no access to sunlight, or where the sunlight is intermittent, solar cells alone are not able to provide the needed energy. In such situations, piezoelectric energy harvesting devices have been proposed for capturing energy in the form of vibration, especially in structural applications such as health monitoring. These devices are often comprised of a cantilever beam with a tip mass tuned to the expected frequencies of the environmental excitation. Another important source of harvested energy is thermal gradients. Thermoelectric devices use the voltage generated at the joint of dissimilar materials which experience a temperature difference between them [1] This type of device can be used for situations where there are large temperature differences, for example the difference between the intake and exit air temperature in a combustion engine has been investigated for thermoelectric energy harvesting [15-17]. However, this technology is limited by the low conversion efficiency of thermoelectric devices using current materials.

The sources described above all play a very important role in the energy harvesting landscape, and there are many different potential applications for energy harvesting. Material development in all of these areas is increasing the conversion efficiencies and making them more suited to harvesting small amounts of energy, however, for scavenging low-level ambient energy on the milli- and nano-watt scale, there are also other important techniques which hold great promise.

Harvesting energy from biological sources

The focus of this research is wearable energy harvesting devices. A unique set of challenges presents itself in harvesting energy for devices which are to be used on the human body, either as implantable devices or as mobile devices which are worn or carried. Many different ideas have been investigated pertaining to harvesting energy from biological sources, allowing implanted/wearable devices to be completely free from external sources of power. The following description will describe many of the current developments focusing on harvesting energy from macro scale human motion.

Nanowires

There is a large amount of energy expended at the cellular level in biological systems, and with the advent of nanotechnology, it becomes possible to tap into some of these biological sources of ambient energy. Nanogenerators have been developed using flexible piezoelectric nanowires. When a series of nanowires are attached to the patient, they stretch and relax with the muscle motion [18, 19].

Bio Fuel Cells

Bio fuel cells (BFC) have been developed to convert biochemical energy, such as that stored in glucose/O_2 into electrical energy in compartmentless implantable devices. When this device is exposed to fluids such as blood which contain glucose, the glucose is electro-oxidized at the anode and the oxygen is electro-reduced to water at the cathode, creating fuel cell which has a power of 2.2 $\mu W/cm^2$ [20].

Thermal harvesting

Energy collected from human motion or thermal gradients could be used to provide energy to operate low power medical devices such insulin pumps, or medical monitoring sensors. Research has found between 1-5 K temperature difference within fatty layers in the body, which could provide a large enough thermal gradient to power certain medical devices using thermoelectric generators [21].

Biomechanical harvesting

Human motion is a source of readily available, low level mechanical energy which when collected properly can potentially reduce or eliminate the need for batteries. Table 2.2 provides a summary of the estimated energy available due to several of the currently discussed forms of human motion generation. The devices represented here range from bulky hand or leg cranks which have the largest energy harvesting capacity, but require bulky devices which must be utilized through the direct intension of the wearer, to devices which would generate very small power, but would also potentially require little or no effort on the part of the wearer.

Table 2.2: Estimated Energy Output from Human Motion [22, 23]

Source	Power Output (W)
Hand or Leg Cranked Generator	10–100
Heel Strike and Shoe Flexure	2–20
Backpack Suspension and Padding	0.5–5
Limb Swing	0.2–5
Torso Expansion From Breathing /Movement	0.1–1

Clearly, human motion provides a wide range of energy sources from which energy could potentially be extracted, and comparing the projected energy output from these different sources with Table 1.3, illustrates that the energy would be sufficient for ultra-low power applications. Numerous “wearable” energy harvesting mechanisms have been devised to harvest this energy.

The following section describes some of the most promising recent biomechanical energy harvesting devices.

a) Heel strike

Heel strike energy harvesting devices have been under development since the late 1990's. Investigations utilizing several different energy harvesting techniques were performed using both an electromagnetic generator and a piezoelectric generator. Walking tests resulted in an average net energy transfer of roughly 250 mJ/step for the electromagnetic generator and 3 mJ/step for the combined PVDF and PZT generator [24].

A more recent application of the heel strike concept is an electroactive heel strike device. This generator incorporates an electroactive material, dielectric elastomer, which will be discussed in greater detail throughout this research. These devices have been found to generate up to 800 mJ per heal strike without adding discomfort to the wearer [25].

One of the weaknesses found in devices such as heel strike energy harvesters which rely on very small strains due to the compression of the shoe sole is that they are not able to utilize the large strains experienced by limb articulation. Efforts are made through the design of the device to increase the strain by designing a bow in the PZT unimorph beam. However, as studies have indicated that a heel displacement greater than 1 cm will be noticed by the user [24], the material strain is limited by the comfort of the person wearing the device. Another concern for devices which rely on impacts is the amount of force the harvesting device experiences. Studies have shown normal heel strike forces upwards of 1000 N in average male subjects walking at a comfortable pace [26]. More strenuous activities will result in even larger forces, which could pose potential issues to the longevity of the device.

b) Center of mass motion

Several different center of mass energy harvesters have been developed, all of which utilize a backpack structure to house the harvesting device. Backpack energy harvesters utilize up and down motion of the center of mass which occurs during bipedal motion. The inertial forces which occur when a fully loaded backpack is worn during walking or running are converted into electrical energy using one of several different means. Several designs use an electromagnetic generator which is incorporated into the frame of the pack harvester [27, 28]. An entirely different design involves the use of a piezoelectric device on the strap of the backpack [60]. Unfortunately, the harvesting backpacks developed to date lead to increased fatigue for the wearer, reducing the device practical applications. For instance the electromagnetic generator backpack was found to increase the metabolic energy requirement by 3.2% (19.1 W) for the person wearing the device [10]

c) Ankle joint rotation

The ankle has also been targeted for energy regeneration. Work done on an ankle prosthesis is stored in a spring during the stance phase of the walking stride in order to release it back to the system when necessary. While there is no electromechanical energy harvesting in this design, the storage and release of energy results in a reduction in the usage of the batteries, extending the battery life [29].

d) Knee joint rotation

Electromechanical devices are a strong candidate for harvesting rotational energy. The PowerWalk, a commercially available knee joint harvester, can generate up to 14 W on level walking and greater than 25 W on steep terrain [11, 23]. This device, which is comprised of a gearbox and electromagnetic generator attached to a knee brace frame, has already been targeted

for use by infantry in both military and law enforcement applications. Additional modeling of the knee joint behavior has recently resulted in a refined version of this type of device which utilizes brushless motors and may allow for even greater control of knee joint motion energy harvesting [30].

In addition to electromagnetic generators, several other smart materials have been investigated for harvesting knee joint rotational energy. A piezoelectric device which uses a plucking technique to allow the piezoelectric cantilever beam to be actuated due to knee joint rotation and then oscillate at its resonance was developed. A preliminary prototype device produced an average power output of 2 mW [31]. There have also been preliminary developments by several groups into incorporating electroactive polymers into knee joint energy harvesting [32-34].

Clearly there are numerous techniques for harvesting energy from biological sources. This research will attempt to utilize the work that has already been performed in completing biomechanical energy harvesting to investigate a mechanism for converting mechanical energy due to walking into electrical energy which addresses some of the issues with previous methods described above.

2.1.2 Applications for energy harvesting

Many different applications benefit from energy harvesting technologies that convert ambient mechanical energy into electrical energy. Depending on the application considered, different types of energy harvesting will be most effective. The following describes several applications and their associated energy harvesting devices. Examples include structural health monitoring (SHM) for stationary structures such as bridges [35, 36], or mobile structures such as

aircrafts [37, 38], which demonstrate the potential for energy harvesting in various applications to effectively eliminate the need for batteries or wires.

Medical systems: As described in the introduction, medical systems are one of the major candidates for biomechanical energy harvesting sources. Each of the applications mentioned there are described here in greater detail.

a) Wireless Body Sensor Networks (WBSN): One of the fastest growing medical applications is that of wearable wireless sensor networks (WSN) used for monitoring patients both in hospitals and in remote locations. Many sensor systems have been developed which are designed to be worn by the patient throughout the day for extended periods of time. The development of comfortable, lightweight energy harvesting techniques will result in WSN devices which are able to operate more reliably for longer periods of time [39-42].

b) Telerehabilitation: Another important emerging area within the field of medicine is telerehabilitation. Studies have shown that continuing physical and occupational rehabilitation beyond the hospital stay is strongly tied with positive outcomes for patients suffering from a wide range of ailments, including stroke [43-45], musculoskeletal dysfunctions, and bone fractures [46]. These patients often require intensive, complex, repetitive motion tasks to promote new connections in the brain [47]. Telerehabilitation has been shown to provide the necessary accountability and guidance to make in-home physical therapy a success for patients required to perform intensive, repetitive motion tasks. However, there is little research in developing comfortable, lightweight, wearable rehabilitation devices that can be incorporated into the daily routines of people without bulky electronics and power supplies [48]. A major challenge in such development is the lack of sustainable power source that can be integrated into

the wearable devices. With the availability of low power electronics and continual reduction of the size of the electronics used for many of these applications, power requirements for wearable rehabilitation devices are significantly lower than they would have been in the past. Estimates on the power requirements can range from microwatts for basic sensing and wireless transmission to milliwatts for devices including more sophisticated tasks such as tactile feedback [49-51]. As the power requirements for wearable devices decreases, energy harvesting has greater potential to play a big role in the future of long term, in home rehabilitation.

c) Functional electrical stimulation: Another very promising area within medicine which will be positively impacted by development of biomechanical energy harvesting is functional electronic stimulation (FES). FES is used to actuate motor units through electrical impulses transmitted through surface electrodes, and it is already utilized extensively in the treatment of foot drop [52-54] and other pathological gaits found in patients with cerebral palsy [55], multiple sclerosis [56-58], stroke survivors [59], and other neurological diseases which result in gait dysfunction [60]. Because FES simply stimulates the patient's own muscles, operating the device requires relatively low power, and is ideally suited for small scale energy harvesting power supplies [61].

d) Prosthetics: Prosthetics used for increased limb mobility is another important medical application of energy harvesting. Both upper and lower limb powered prosthesis have seen great strides in development. Prosthetic motion is becoming more and more sophisticated and life-like, requiring reliable sources of electricity for longer periods of time, and techniques that can be used to reduce the size and weight of the required batteries will greatly increase the utility of these devices [12, 62].

Wireless communication systems: Wireless communication systems are currently commercially available by companies such as EnOcean, which produces an electromagnetic switch harvester which is used to power the wireless transmitters [63]. Microstrain, Inc. has developed commercially available energy harvesting circuitry which is designed to work with many different ambient energy sources including piezoelectric, electrodynamic, solar, and thermoelectric [64]. An independently tested application of their device is an energy harvesting sensor which is designed for use on the helicopter control rod or pitch link [65].

Structural health monitoring: Structural health monitoring has become a very important part of the maintenance and safety evaluations of many different types of structures. Time based maintenance schedules are replaced with wear based maintenance schedules, reducing waste while preventing undetected structural failures from occurring between regularly scheduled inspections. However, since it is difficult and expensive to power wireless devices for the life of the structure using batteries, energy harvesting has been extensively studied for this use [66]. Energy from the vibration of structures has successfully been used to power small wireless transmitters in sensor notes (mote sensor). One of the most common examples of energy harvesting for structural health monitoring involves a piezoelectric cantilever beam imbedded in a structure experiencing regular mechanical loads such as a bridge with heavy vehicle traffic or a building subject to large wind gust.

An example of this type of harvesting for SHM is a wireless impedance device (WID3). It operates at 2.8 V and is able to measure, reduce the data and wirelessly transmit it in approximately 20 seconds with an approximate current draw of 0.01 mA [35]. At this rate, it is estimated that it could perform one measurement a day for up to 5 years using current battery

technology, however if an alternate sustainable energy source were utilized, the operational life of the system would no longer be limited by energy availability. A similar, but more energy intensive example is the SHiMmer wireless ultrasonic structural health monitoring platform [36] which uses a combination of wind and solar power to collect the energy required to send and receive wireless signals, and perform more complex data computations on the measured ultrasonic data at each node. These and other similar examples [67] demonstrate that, when used in conjunction with wireless communication, energy harvesting can provide a means to develop intricate SHM systems on a wide range of structures.

Vibration reduction: Another important application of energy harvesting is for use with vibration reduction devices. One such example is piezoelectric energy harvesting involving piezoelectric sheets mounted to a flexible rotational shaft. Experiments indicated that 0.5 mW of energy could be extracted from a shaft rotating at 3400 rpm. It is suggested that the energy harvested from this application could potentially be used as part of resonance suppression or an active damping device [68]. Another example is the vibration suppression of a cantilever beam using piezoelectric actuators which are controlled by an array of precharged capacitors. Simulations of this self-powered, semi-passive control method demonstrate its ability to suppress vibration while powering an active control method requiring an external power supply [69].

Military applications: There is a great need in military applications to be able to provide soldiers with energy to power all of the electrical devices currently in combat. These devices include (but are not limited to): personal navigation system, medical status monitor, friendly ID beacon, communication link, magnetometer, chem/bio detector, and night vision scope. Many of these

devices require constant low level power for continual operation and the weight and size of battery packs required for operations could be greatly reduced when dismounted soldiers are constantly moving. For a three-day mission, a soldier may need as much as 13 kg of batteries [70]. The US Navy is also developing distributed wireless structural health monitoring systems for their aircrafts. Several different energy harvesting methods are currently being investigated to power such systems for use onboard Navy ships [71] and aircraft [37, 67, 72]. Other aircraft energy harvesting projects have also shown promise, with energy harvesting energy densities of up to 7 W/m^2 [38].

Consumer Electronics: Due to the decrease in size and power requirement for consumer electronics, the applications of energy harvesting to small electronics will only grow. As shown earlier, devices which require low computational energy such as cell phones, mp3 players and voice recorders hold promise for being able to be self-powered using simple and inexpensive energy harvesting techniques [73-75].

2.2 Dielectric Elastomers

The area of energy scavenging has received a great deal of attention in the past few decades and is now growing into a promising area for commercial development. However, most of the techniques which are being effectively applied to date as described above utilize stiff, brittle materials. In order to develop energy harvesting devices which will be comfortably worn during harvesting of biological energy, further development into soft, polymer type materials will be vital.

2.2.1 Dielectric elastomers as "Smart Muscles"

One type of EAP which exhibit very large strains are the dielectric elastomers (DE). The concept of the dielectric elastomer was first introduced over a decade ago by Pelrine [76], in which the deformation of elastomeric dielectrics undergoing high electric fields were modeled and experimentally verified. These initial investigations provided the basis for the development of actuators which can act very similarly to natural muscles.

Dielectric elastomers are extremely elastic materials with high electrical permittivity which are electromechanically coupled through an electrostatic effect. A DE device is created by placing compliant electrodes on both sides of a dielectric elastomer film, forming a variable capacitance device. When this elastomer capacitor is exposed to an electric field, an electrostatic stress (or Maxwell stress, σ_M) is induced. This Maxwell stress, which is due to an electrical load, causes the elastomer to experience a mechanical strain. In certain configurations, DE can easily undergo strains that are much greater than 100%, and DE generators operate best at low frequencies, making them well suited to harvesting gross human motions which occur at frequencies less than 5 Hz.

While this type of motion is typically non-linear and can be difficult to model, it provides muscle-like performance that cannot be realized with more traditional devices. Because of this, numerous studies over the past ten years have demonstrated that DE holds promise for mimicking human muscles [77-83]. A recent review on the challenges and opportunities for DE use in upper limb prosthetics applications makes it clear that there are still a number of difficulties with the size weight and strength of DE for actuation applications [84]. Although there are still many hurdles to be overcome, as described earlier, there are a large number of medical applications which could benefit from energy harvesting, and as research addresses

many of these issues, the potential for incorporation of this type of material into self-powered biomedical systems is very promising [82, 85].

2.2.2 DE as sensors/energy harvesters

As stated above, as a result of the Maxwell effect, strain is developed in a DE capacitor when it is placed in an induced electric field. The opposite effect, that a strain will induce an electric field is also possible. The capacitance of two electrode plates separated by a dielectric is not only dependent on the permittivity of the dielectric, but also on the surface area and thickness of the dielectric; therefore the capacitance is a function of the geometry of the device. When a compliant material is used, the capacitance of the device becomes a function of material strain. It is this variation of capacitance due to mechanical strain which provides a means for mechanical energy to be converted into electrical energy. When a strained device is subjected to an electric field, a charge forms across the device. When the mechanical force is removed, the material returns to its original shape, resulting in a lower capacitance. The excess charge accumulated on the capacitor, due to the mechanical energy inputted to the device during stretching, can now be stored as electrical energy. This cycle of stretching, charging, relaxation and discharge can be used to convert mechanical energy into electrical energy. During the discharge phase, electrical energy is removed from the device, resulting in a net loss of mechanical energy, leading to structural damping [9].

Since 2008, the use of dielectric elastomers for harvesting energy come to the forefront [32, 86], and since this time, the use of DE materials as energy harvesters has been expanding to encompass a wide range of applications. To date, investigations into DE energy harvesting include environmental energy harvesting from sources such as ocean waves, water currents [87] and wind [88], as well as human motion including heal strikes [89], and knee bending [32, 33].

DE energy harvesting Examples

Many examples of research into the use of DE energy harvesters are now available. Experiments on actual ocean buoys [86] demonstrated that this type of device should be able to generate the necessary energy for low power applications currently employed on ocean buoys. All these preliminary investigations indicated that for low frequency and high strain, the potential for energy generation using DE is favorable.

Recent published results of energy harvesting attempts have demonstrated current energy harvesting trends for DEGs. Three different types of materials are represented in of Table 2.3, the first is an acrylic VHB 4910, without pre-stress treatment, the second is the same material with a pre-stress treatment, and the third is a silicone dielectric with corrugated plated silver electrodes. It has been demonstrated that DE materials are capable of generating reasonable amounts of energy without detrimental degradation of the material when strain rates of 15% are used (see Table 2.3) [90].

Table 2.3: Recent energy harvesting results using dielectric elastomers

Reference (Year)	Material	Movement	Energy (mJ)	Poling voltage
[32] (2008)	Acrylic	Planar/knee joint	0.1	210 V
	Acrylic	Planar/knee joint	1.74	1000 V
[33] (2010)	Acrylic	Tubular/knee joint	0.5	1000 V
[91] (2010)	Acrylic w/ pre-stress	Linear Strain 41%	0.6	650 V
	Acrylic w/ pre-stress	Linear Strain 35%	5.87	2800 V
[90] (2009)	Polypower	Linear Strain 5%	11.2	1200 V
	Polypower	Linear Strain 15%	94.5	1800 V

Although larger strains (15—35%) could be used for higher power output, this carries the risk of an increased incidence of electrical breakdown within the element due to the decrease in thickness of the DE material. When a 15% strain is used, 94.5 mJ of energy was produced by the

'free' mechanical motion. The first three entries of Table 2.3 are most pertinent for our proposed research because they demonstrate the only other published work explicitly describing DE energy harvesting of knee joint energy during walking. Given that human walking is at about 1 Hz, the amount of power (energy per unit time) that can be harvested in these experiments are encouraging but research is definitely needed to increase the energy harvesting capacity of these DE devices.

2.2.3 Recent DE Technological Advancements

There have been many recent innovations in dielectric elastomer technology which have created an ideal atmosphere for the introduction of DEGs into the medical field. Recent critical advancements include:

- Development of high permittivity silicone dielectrics [92, 93] which provide greater performance and increased energy density.
- Increased availability of graphene based materials for inexpensive compliant electrodes [94, 95]. Graphene is a material that can sustain current densities six orders of magnitude higher than that of copper, and reconciles such conflicting qualities as brittleness and ductility. The widespread interest in the development of graphene and carbon nanotubes has paved the way for highly conductive, flexible films which could be directly applied to DE materials [96].
- Fault tolerant self-clearing electrodes using carbon nanotubes [97, 98] which allow for self healing of DE devices when small areas of dielectric breakdown occur, increasing the durability of the material during charge and strain.
- Dielectric elastomer switches which allow for the elimination of many of the solid state switching devices which may normally be required [85]
- Compliant patterned electrodes for greater control of the DE surface area pattern [99].

- Self-priming DE harvesters which can be started with a very small voltage which increases to the necessary level using a secondary DE primer built into the original device [100], eliminating the need for an external power supply.
- Roll to roll automation of low temperature graphene screen printing on flexible polymers [101] providing a means to mass produce complex flexible DE devices with much of the circuitry incorporated into the device.

Each of these technological innovations provides breakthroughs in one or more of the following three areas: simplicity, reliability, and cost. These recent developments provide the basic building blocks for the development of lightweight, wearable DEGs.

2.2.4 Current Challenges to DE application to energy harvesting

Although there are many convincing reasons to use DE materials, there are several issues which still need to be addressed before their widespread use in biomechanical applications will be practical. These include material issues stemming from the non-linear behavior of the dielectric and the high conductivity/flexibility requirements of the compliant electrodes, electromechanical issues such as rupture, dielectric breakdown, and electromechanical instability. Physiological issues must also be addressed, such as how to attach the device to a limb and control the device such that the muscles do not experience adverse effects, as well as safety issues surrounding the use of a high voltage device in a wearable application.

2.3 Beneficial use of Damping induced by Energy harvesting

Just as large scale energy generation may have unintended consequences on its environment, so too, energy harvesting devices can affect the surrounding host structures. One of the ways in which energy harvesting devices modify their surroundings is through the introduction of mechanical stiffness and damping induced by the conversion of mechanical

energy in to electrical energy. Recent work in several areas has begun to address the dynamic effects that energy harvesting can potentially have on host structures through the introduction of dampin g[102-104]. One especially promising area that will be addressed here is that of biomechanics, specifically as applied to walking.

2.3.1 Beneficial Energy Harvesting During Walking

Walking requires a complex combination of bones, muscle and tendons working in coordination with the central nervous system to generate upright bipedal motion. Unlike the walking gait of other bipeds, the human stride occurs with relatively straight legs, causing the center of mass (c.m.) to move up and down, constantly converting kinetic and potential energy as the c.m. pivots about the planted foot [105]. During standing the goal is to provide stability by maintaining the center of gravity above the support base, however, walking requires the deliberate movement of the c.m. beyond the planted foot, causing the c.m. to accelerate as it "falls" forward. As a result of this motion, 80% of the human walking gait is performed with only one foot planted [106]. During this time, the non-planted leg is being lifted off the ground (push-off phase), rotated forward and then placed down in front of the c.m. to "catch" the upper body and move it forward over the planted foot. This type of motion involves careful coordination of the leg's position and velocity using the muscle groups around the hip, knee and ankle joints. In order to generate the desired trajectory, both acceleration and deceleration of the leg are required at different points in the stride. This is demonstrated in Figure 2.1 by observing how the velocities change direction several times throughout each stride. Consider a stride, such as that shown in Figure 2.1 which begins when the toe lifts off the ground. For about 60% of the stride, beginning when heel contact (HC – the red line on figure) is made with the ground, the leg is in stance mode, and the knee must be relatively stiff to allow the knee to support the weight of

the upper body. During this time, the knee angle changes very slowly and very little power is required by the muscles acting on the knee. Once the toe lifts off of the ground (Toe Off which occurs at beginning and end of cycle in figure), the knee must raise up to allow clearance for the foot to swing under the body, this is when the majority of the power to the knee is required. Throughout the rest of the swing phase, the knee must dissipate energy as it prepares for the heel to strike the ground once again, and only minimal power is needed at the knee [107].

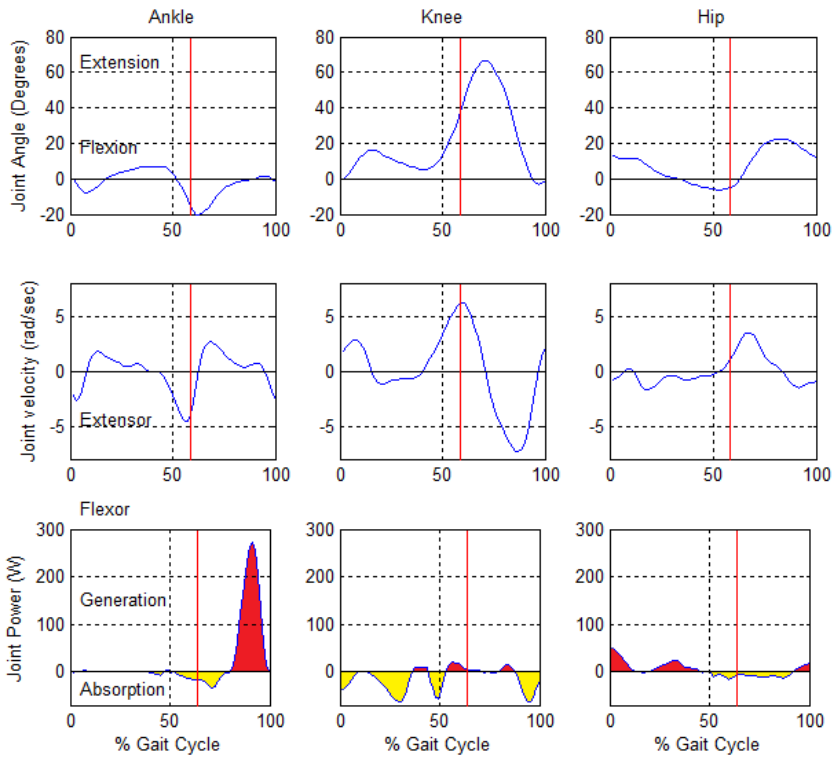

Figure 2.1: Characteristic joint motions (generated from data in [10]). Positive work highlighted in red; negative work highlighted in yellow. (toe off shown with red line)

This dissipation of energy requires the muscles at the different joints to perform "negative work," which simply means that rather than inputting kinetic energy into the system, the muscles are working to remove kinetic energy from the system. Although this negative work is similar to passive damping in that it dissipates energy primarily to heat, it differs in that while passive

dampers do not require additional energy to function, the negative work done by muscles requires a metabolic expenditure similar to that of positive work [23]. The prevalence of negative power after toe off (TO) illustrates the rational for developing a mechanism to collect and store the energy dissipated by the knee during the swing phase of the stride. If even a portion of the swing phase energy were able to be stored for use in the next stride, the overall energy required to drive an assisted knee would be greatly reduced. If a device which converts unwanted mechanical energy into electrical energy were worn, a portion of the negative work which is normally completed by the leg muscles could be performed by this device through the storage of the electrical energy in a battery or capacitor.

This concept is the principle behind beneficial energy harvesting, also called *mutualistic* energy harvesting by Li, et al. [108] who borrows the concept of regenerative braking on a hybrid electric vehicle to describe this idea. In regenerative braking mechanical energy which is normally lost to heat through friction is converted into electrical energy and stored for later use. Just as regenerative braking does not harvest energy during acceleration or cruising because that would increase the combustion energy required, so too, beneficial energy harvesting does not attempt to harvest energy when the muscles are performing positive work.

Observation of the power output at each lower limb joint demonstrates that both positive and negative work are being performed by the muscles during each stride, however, the amount of negative work done as a percentage of the total work performed by each joint is not the same. When the measured work done at the knee is considered from Figure 2.1, the negative work consists of over 90% of the total work done, whereas, with the ankle, it is much lower (28% for the hip and 19% for the ankle) [10]. This occurs because the muscle group near the knee joint

expend additional effort removing energy which was introduced into the system by the muscle groups near the hip and ankle joints.

It is the aim of beneficial energy harvesting to convert and store only the mechanical energy which is normally dissipated by the muscles when the leg is slowing down. Therefore, the knee joint is selected as the appropriate joint to perform energy harvesting. By doing so, it is possible to generate electricity without increasing the metabolic energy requirement to the wearer.

There are currently several teams working independently on the concept of selectively harvesting energy from the knee joint. Li , as mentioned earlier, is developing an electromagnetic generator which is controlled in order to selectively engage and disengage the clutch as the wearer is moving, so as to only harvest energy during the negative work phase of the stride. The control system operates using a combination of angular position and velocity to determine the appropriate times to connect the clutch. The efficiency of the harvesting system will therefore be a function of the sum of the transmission and generator efficiencies. This device uses a mechanical leg brace to attach to the wearer and it is designed to harness fairly large quantities of electricity (25 W during fast downhill climbing) by able bodied wearers [23, 108].

Another team, Andrysek et al. [12], is also developing an energy generation device utilizing the same principle. Their research focuses on the control of an energy harvesting knee joint incorporated into a prosthetic leg for transfibular amputees. This device also uses a combination of position and angular velocity to control an energy harvester during the swing phase of the stride. However, while their device is similar to Li's in that it is comprised of a motor and gear system at the knee, it is unique because since it is intended to operate on a transfemoral prosthesis, it is designed act in three different states: The electrical load state

provides the maximum amount of energy generation while providing moderate damping, the short circuit state which provides little generation, but creates a highly damped situation (necessary for the stance phase of walking), and the disconnected state in which there is no energy harvesting occurring and the associated damping of the knee is low. Preliminary testing of their energy harvesting device was encouraging. When walking at a comfortable pace, the three test subjects could generate around 2W with the generator running constantly, and 0.57-1.36 W using adaptive (beneficial) damping. Walking at a fast pace, the same test subjects could generate 1.0-1.6 W using adaptive damping [12]. Results from both of the researchers indicate that beneficial energy harvesting human motion is a promising means to harvest energy.

2.3.2 Issues within current beneficial energy harvesting technology

While there have been many advances in the area of beneficial energy harvesting during the last decade, there are still many challenges to be faced. Devices which harvest rotational displacements due to human motion such as the PowerWalk are limited due to their reliance on electromagnetic generators, which tend to be stiff, bulky, and relatively heavy. There is a large amount of hardware required to convert rotational energy to electrical energy, and although the actual design is compact, it still requires additional effort to carry this weight at the knee. Tests of metabolic requirements revealed that when worn without harvesting energy, the presence of the device on the wearer added 60 W of required metabolic power to the average metabolic power required for walking to increase from 307 W to 367 W [23]. The mechanical power required to simply overcome the inertia of the system was measured to be as much as 2/3 of the power required for the operation of the device [23].

Another concern with this type of device is the noise level associated with the device. When used, the system contains many mechanical connections which create a continual noise

whenever the device is active. For applications where devices would potentially be used by a large number of people, or in applications where stealth is required, the noise generated by the devices may prohibit their regular use.

Finally, as with many mechanical energy harvesting devices, there is a large mechanical impedance disparity between human tissue and the device itself. In order for a wearable device to be comfortable for the wearer, and have the most efficient transmission of energy, the mechanical properties of the wearer and the device must be similar. Obviously a system made up of rotating shafts, gears and clutches would have very different mechanical properties from the muscles, tendons, ligaments and other tissue associated with human motion. Other, more compliant materials, such as thin-film piezoelectric devices, which are designed to be more flexible do not have the energy density of an electromagnetic generator, therefore, an efficient, soft energy harvester is required which can convert rotational motion to electrical energy.

Using the information gathered from the various sources presented above, the research described in this dissertation seeks to further develop the understanding of the fundamental relationships between dielectric elastomer energy harvesting and its induced damping, and to apply this to the beneficial harvesting of walking energy. This research lays the foundation necessary for the development of dielectric elastomer biomimic devices which will provide a means for coordinating both controlled damping and energy harvesting. This document describes the development of this research through analytical modeling, simulation and experimental testing.

3 Dielectric Elastomer Characterization

3.1 Introduction

The initial objective of this research is to model the energy harvested by a DE generator as a function of the following system parameters: dielectric properties, elastomer and electrode material properties, charge voltage and device geometry. Because of their composite electromechanical design, modeling DE devices requires a multifaceted approach. Not only must the mechanical behavior of the DE polymer be characterized for a given configuration, establishing the stress within the dielectric as a function of the strain. But in order, to estimate the energy harvested as a result of the electromechanical coupling, the mechanical constitutive relation must also be related to the electric field developed across the dielectric, providing a means to model the electromechanical coupling within the system.

In this chapter, a modified non-linear, time-independent, hyperelastic model is developed and experimentally verified which incorporates the effect of boundary conditions induced by the compliant electrodes in a manner that has not previously been modeled. In this section, a brief introduction is provided pertaining to the composition of dielectric elastomers and their existing models. Concerns related to these models are discussed, and an improvement to the model is proposed. Subsequent sections of this chapter describe the modified electromechanical model developed and its application to energy harvesting.

Dielectric elastomer composition

As described in section 2.2.1, dielectric elastomers are electromechanical devices comprised of highly elastic dielectric polymers with a compliant conductive material adhered to either side (Figure 3.1).

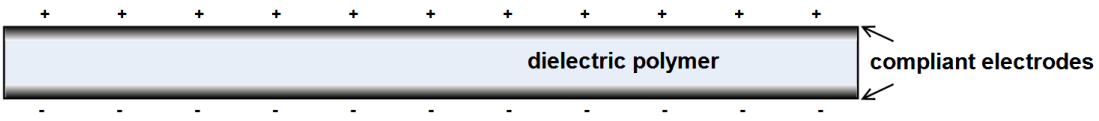

Figure 3.1: Cross section of DE material

This arrangement leads to a composite material with mechanical behaviors that differ from either the dielectric polymer or the compliant electrode alone. Numerous electrode materials are currently used in DE applications including carbon grease [109], graphene [95, 99], silver ink [98, 110, 111] and corrugated metal [90, 112]. Each compliant electrode material has its own mechanical behavior which affects the response of the DE device when operating. In fact, it will be demonstrated in this chapter, that even when uncharged the mechanical properties of the electrode material affect the stress distribution resulting from an external strain.

This composite behavior also influences the electrical behavior of DE devices in several ways. First, as will be described in section 3.4.2, the capacitance of the device is directly related to the surface area of the electrodes and the thickness of the dielectric. Therefore, the relationship between an externally imposed strain and the device's capacitance is greatly influenced by the composite nature of the device. In addition, when an electrical load is placed upon the DE material (designated by the +/- charge on the electrodes in Figure 3.1), the mechanical response to the electrical loading depends on the mechanical properties of both the dielectric polymer and the electrodes. This effect is demonstrated to be significant enough that the behavior of the electrodes should be included in the model of the electromechanical behavior of dielectric elastomers.

Hyperelastic modeling of dielectric elastomers

Early modeling of dielectric elastomers used a linear representation of the stress strain behavior, assuming that when acting as either an actuator or sensor, the material would undergo

small strains [9]. However, as the use of DE is expanded to energy harvesting, its ability to experience large deformations while being nearly incompressible became important as it provides effective conversion of large mechanical strain into electrical energy, requiring the development of nonlinear constitutive relations. For this reason, recent modeling of DE energy harvesters has included several hyperelastic models [91, 113, 114]. Yet, in looking at the electromechanical coupling for a uniaxial thin film DE harvester, it is clear that the current models and assumptions neglect the effect of the electrode material and therefore are unable to fully describe the behavior of the device. The following section provides a description of current hyperelastic models as applied to dielectric elastomers and describes the insufficiency of these models while introducing an improvement to the model which will be developed in this chapter.

Current hyperelastic modeling of the constitutive stress strain equations for dielectric elastomers is summarized as follows. For isotropic, homogeneous and incompressible hyperelastic materials, the Cauchy stress tensor describing the principal stresses is defined by the Finger formula [115]:

$$\sigma = -p + 2\left(\frac{\partial W}{\partial I_1}F - \frac{\partial W}{\partial I_2}F^{-1}\right) \tag{3.1}$$

where W is the strain energy density, which is dependent on the principal invariants of the left hand Cauchy-Green deformation gradient tensor (also known as the *Finger tensor*), $\mathbf{F} = \begin{bmatrix} \lambda_1 & 0 & 0 \\ 0 & \lambda_2 & 0 \\ 0 & 0 & \lambda_3 \end{bmatrix}$ [115], where λ_i are the principal stretch ratios, and p is the volumetric pressure without any shear component (called hydrostatic pressure, it is the pressure which leads to a volumetric change without any change in the shape of a compressible material).

When the following invariant definitions are imposed:

$$I_1 = \lambda_1^2 + \lambda_2^2 + \lambda_3^2 = \sum_{i=1}^{3} \lambda_i^2$$

$$I_2 = \lambda_1^2\lambda_2^2 + \lambda_2^2\lambda_3^2 + \lambda_1^2\lambda_3^2 = \sum_{ij=1}^{3} \lambda_i^2\lambda_j^2 \qquad \text{(3.2a-c)}$$

$$I_3 = \lambda_1^2\lambda_2^2\lambda_3^2 = \prod_{i=1}^{3} \lambda_i^2$$

the stress formula can be reduced to:

$$\sigma_i = \lambda_i \frac{\partial W}{\partial \lambda_i} - p \qquad \text{(no summation on the index) (3.3)}$$

Note that the nominal stress, s_i, which is related to the true stress by: $\sigma_i = s_i \bullet \lambda_i$, is sometimes used in the literature in place of the true stress, resulting in: $s_i = \frac{\partial W}{\partial \lambda_i} - \frac{1}{\lambda_i} p$.

As with eq. (3.1), this stress formula which serves as the basis for hyperelastic modeling, contains three distinct parameters: the directional stretch ratio, λ_i, the strain energy density function, W, and the hydrostatic pressure, p, each of which depends on the given geometric boundary conditions of the dielectric elastomer generator. The first term, λ_i, is the principle directional stretch ratio, which describes the relationship between the original dimension and the modified dimension after a change in state occurs: $\lambda_i = \frac{x_i}{x_{i0}}$. The second term, the strain energy density function, *W,* describes the relationship between the strain energy density of a material and its deformation gradient. Careful selection of *W* is necessary for development of an accurate stress model for the material, as its choice affects how closely the stress model predicts the actual response of the material. Many models have been developed for different hyperelastic materials, ranging from synthetic polymers to biological tissue [116], additional models have also been developed which specifically describe dielectric elastomer applications [113]. Three of the most

prominent models which have been used for modeling DE generator, Neo-Hookean, Mooney-Rivlin, and Yeoh [117], are included in this investigation.

The classic Mooney-Rivlin model for hyperelastic materials still provides a close correlation with many of the materials which are currently used in DE generators. This model uses a strain energy function based on the first and second invariants of the Finger tensor, and as with all of the strain energy density functions presented here, the model relies on empirically determined material parameters, C_i [32, 90, 91, 116]:

$$W = C_1(I_1 - 3) + C_2(I_2 - 3) \tag{3.4}$$

Substituting this strain energy density function into eq. (3.3) results in the Mooney-Rivlin stress formula:

Mooney-Rivlin
$$\sigma_i = \lambda_i \frac{\partial W}{\partial \lambda_i} - p = 2(\lambda_i^2 C_1 - \frac{C_2}{\lambda_i^2}) - p \tag{3.5}$$

Another hyperelastic material model often employed for dielectric elastomer modeling is the Yeoh model [91, 116, 118]. This model uses only the first invariant, however, unlike the Mooney-Rivlin model, it includes higher-order terms:

$$W = C_1(I_1 - 3) + C_2(I_1 - 3)^2 + C_3(I_1 - 3)^3 \tag{3.6}$$

Substituting this strain energy density function into the stress formula results in the following:

Yeoh
$$\sigma_i = \lambda_i \frac{\partial W}{\partial \lambda_i} - p = 2C_1\lambda_i + 4C_2\lambda_i(I_1 - 3) + 6C_3\lambda_i(I_1 - 3)^2 - p \tag{3.7}$$

When small strains are expected, a truncated version of these models utilizes only the first invariant, and results in the Neo-Hookean model [115, 116, 119, 120]:

$$W = C_1(I_1 - 3) \tag{3.8}$$

Similar to the linear model described previously, the Neo-Hookean model provides a linear estimation of the material response, and can be used in materials where only small strains are expected. Here C_1 is related to the material shear modulus (for silicone, the shear modulus is often in the range of 10 KPa) [115]:

$$C_1 = \frac{G}{2}. \tag{3.9}$$

The resulting strain energy density function is:

$$W = \frac{G}{2}\left(\lambda_1^2 + \lambda_2^2 + \lambda_3^2 - 3\right) \tag{3.10}$$

Resulting in a simplified Neo-Hookean stress formula:

Neo-Hookean $$\sigma_i = \lambda_i \frac{\partial W}{\partial \lambda_i} - p = G\lambda_i^2 - p \tag{3.11}$$

The final term in the stress formula, the hydrostatic pressure, *p,* describes how the boundary conditions affect the internal pressure of a material undergoing deformation. This term must be found for a specific strain energy density function and device configuration. An uncharged DE generator in uniaxial tension experiences no constraint in the x_3 direction (ie. $\sigma_3 = 0$), so the hydrostatic pressure is found by substituting the strain energy density function into the stress formula and then solving for p based on the σ_3 stress requirement (see Appendix A for complete development of this process). Using this process the hydrostatic pressure for each of the models described above is found and back substituted into the stress formula, resulting in the following stress strain constitutive relations:

Neohookean model: $$\sigma_i = G\lambda_i^2 - G\lambda_3^2 \tag{3.12}$$

Mooney-Rivlin Model ; $$\sigma_i = 2\left(\left(\lambda_i^2 C_1 - \frac{C_2}{\lambda_i^2}\right) - \left(\lambda_3^2 C_1 - \frac{C_2}{\lambda_3^2}\right)\right) \quad (3.13)$$

Yeoh model: $$\sigma_i = 2\left(\lambda_i^2 - \lambda_3^2\right)\left(C_1 + 2C_2\left(I_1 - 3\right) + 3C_3\left(I_1 - 3\right)^2\right) \quad (3.14)$$

These constitutive relationships are defined in terms of the material parameters and stretch ratio in each direction. At this point standard hyperelastic modeling assumes that the material is isotropic, and therefore simplified boundary conditions can be developed to express the strain behavior of the material in the each of these directions. As a composite material made up of both a hyperelastic dielectric polynomial and electrode materials of differing elasticity, DE devices do not function in such a simplified manner. In initial investigations indicated that the geometric boundary condition modeling have a large effect on the accuracy of the calculations, and for this reason, it was determined that a more comprehensive model would need to be developed based on hyperelastic modeling which takes into consideration the mechanical effect of the electrodes on the DE material.

It is the goal of the first objective of this research to develop a modified hyperelastic model which takes into consideration the effects of the compliant electrode material on the hyperelastic behavior of the dielectric elastomer material. To begin, the mechanical behavior of a thin film DE undergoing uniaxial tension will be modeled through the novel use of a boundary coefficient incorporated into the stretch ratio relations. Experimental measurements of the DE behavior for several different electrode materials are used to validate the results found. Following the development of the mechanical model, a similar technique will be employed to form and validate a model of the electromechanical behavior of the device. This modeling provides a significant improvement over the current models because it provides a means to

distinguish between different electrode materials, providing a more accurate assessment of the energy harvesting capability of each device.

3.2 Empirical modeling of dielectric elastomer boundary conditions

Dielectric elastomers are capacitive devices composed of an elastomeric dielectric with compliant electrodes (see Figure 3.1). The electrical response of the device is coupled to its mechanical behavior, and therefore accurate mechanical modeling of the nonlinear material is critical for correctly modeling the electrical energy harvested. A mechanical model of the device is presented in section 3.3 based on the boundary condition modeling developed here. The mechanical model is followed in section 3.4 by the development of an electromechanical model based on the coupled mechanical and electrical response of the device to a given external force and electric field loading.

A DE generator exposed to uniaxial tension while being electrically loaded can be considered as a hyperelastic material undergoing stress in two axes, as in Figure 3.2, where σ_1 represents the tension generated by an external force in the x_1 direction, and σ_M represents the Maxwell stress induced by an electric field in the x_3 direction. This section focuses on the stress-strain relationship of the uncharged composite DE materials, while the additional electromechanical effects dues to the Maxwell stress will be described in greater detail in section 3.4.3.

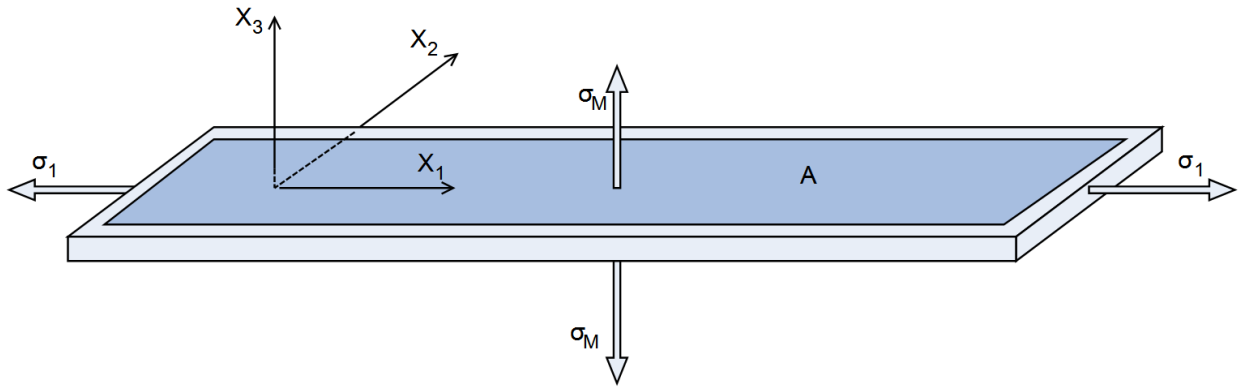

Figure 3.2: Uniaxial DEG orientation

Several different models have been developed to describe the mechanical behavior of the composite DE material, however they fail to take into consideration how the mechanical properties of the electrode material impose additional constraints on the dielectric polymer as it stretches. In what follows, we first overview several of the mechanical models currently used to predict the mechanical behavior of the viscoelastic dielectric material used, and then propose new modeling based on non-classical boundary conditions determined by the electrode material selection. For the uniaxial modeling performed here, the conventional orientation shown in Figure 3.2 will be used, with the actuation strains occurring in the x_1 direction, and the electric field in the x_3 direction.

3.2.1 Boundary condition considerations

The materials used as the dielectric elastomer are generally incompressible, requiring that the total overall volume will remain the same regardless of the strains developed. For a thin film DEG with uniaxial tension in the x_1 direction, the response in the x_2 direction depends on the boundary conditions of the film. When the clamped ends (shown in bold in Figure 3.3a) are fixed and there is no external constraint on the material in the x_2 direction, the edges exhibit 'pull-in' at the center of the film, creating a concave curve to the material. Figure 3.3 compares this true response of the material (a), with the two idealized limiting cases, resulting in either zero stress (b) or zero strain (c) in the x_2 direction. Three electrode materials mentioned earlier will be utilized during this investigation, powdered graphene, carbon grease and corrugated silver. Each one displays pull-in behavior to a varying degree.

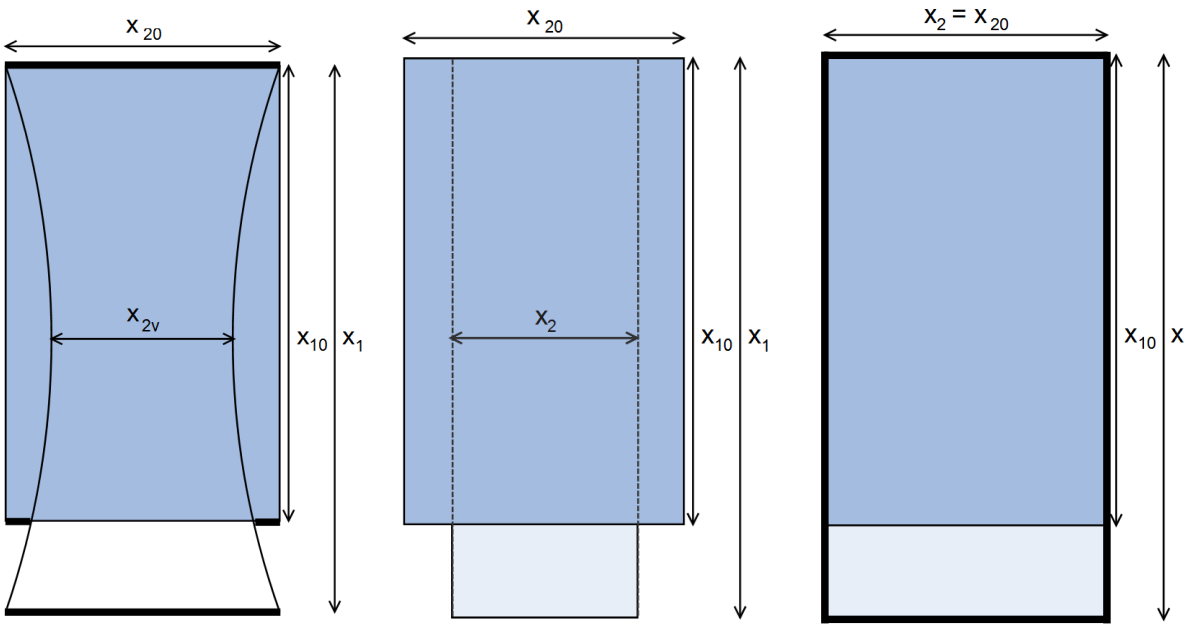

a) Actual response **b) Unconstrained width** **c) Constrained width**

Figure 3.3: Possible modeling conditions for strain in the x_2 direction

The pull-in which occurs when a thin film DE is stretched is usually simplified for the sake of modeling. This is done by assuming one of the two limiting boundary condition shown above.

Unconstrained boundary condition: The unconstrained boundary condition models the assumption of zero stress in the x_2 direction. This boundary condition can be most readily applied when the electrode material is very compliant, such as in the case when graphene powder is dusted over the surface. Utilizing this assumption, the strain in the x_2 direction is modeled as a uniform strain along the entire edge of the film.

Fully constrained boundary condition: For some DE materials, the fully constrained boundary condition is more appropriate. In this boundary condition, the strain in the x_2 direction is very small, and the resulting stretch ratio is $\lambda_2 = 1$, which implies that only the thickness of the film changes directly as a result of the strain in the x_1 direction. In order for this assumption to be

properly applied, either the aspect ratio must be very long (ie $x_2 << x_1$) or the edges of the film must be constrained to provide the stress necessary to prevent pull-in [91, 120]. This assumption will clearly result in a larger decrease in the thickness of the material than the zero stress condition.

Partially constrained: While the above limiting conditions are very important in developing an understanding of the mechanical behavior of elastomers, most material configurations do not precisely result in either of these conditions, but rather behave as in Figure 3.3a. For this reason, a constraint model, which will be described in the following section, has been developed to describe the behavior of configurations which do not exhibit the limiting boundary conditions.

3.2.2 The stretch ratio

As described in section 3.1, the stretch ratios relate the current material dimensions to the original dimensions:

$$x_i = \lambda_i x_{i0} \tag{3.15}$$

These stretch ratios are required to satisfy both the incompressibility assumption of the polymer ($\lambda_1\lambda_2\lambda_3 = 1$) and the constraints placed on them by the boundary conditions. The relationship between the stretch ratios in each direction will take different forms depending on the boundary conditions described. The following section details the development of the invariants and the stretch ratios for both of the limiting boundary conditions described followed by a general formulation accounting for the pull-in effect discussed earlier.

Unconstrained width ($\sigma_2 = 0$): When the completely unconstrained width assumption is applied, the stress in the x_2 direction is zero, and the following stretch ratio relations are developed [116]:

$$\lambda_1 = \lambda,\ \lambda_2 = \frac{1}{\sqrt{\lambda}},\ \lambda_3 = \frac{1}{\sqrt{\lambda}} \tag{3.16}$$

Note that λ is denoted as the stretch ratio in the x_1 direction under a uniaxial stretch test. These stretch ratios indicate that stretching an unconstrained material results in a proportional reduction in both the thickness and the width of the material. Imposing the invariants of the Finger function for the uniaxial, incompressible DE film with uniform width gives:

$$\begin{aligned} I_1 &= \lambda^2 + \frac{1}{\lambda} + \frac{1}{\lambda} \\ I_2 &= \lambda + \frac{1}{\lambda^2} + \lambda \\ I_3 &= \lambda^2 \left(\frac{1}{\lambda}\right)\left(\frac{1}{\lambda}\right) = 1 \end{aligned} \qquad (3.17 \text{ a-c})$$

It will be shown later that utilizing these invariant relations, the principal stresses, σ_i, can be determined using the stress formula (eq. 3.3).

Constrained width ($\lambda_2 = 1$): Considering the uniform width boundary condition (constant x_2), the incompressibility requirement provides the following stretch ratio relations:

$$\lambda_1 = \lambda,\ \lambda_2 = 1,\ \lambda_3 = \frac{1}{\lambda} \qquad (3.18)$$

Here we see that uniaxial stretch of a fully constrained DE material results in a thinner dielectric material than the unconstrained case. This will be demonstrated in later sections to result in a larger increase in the capacitance compared to the unconstrained case, leading to greater energy harvesting capability. For this case, invariants of the Finger function for the uniaxial, incompressible DE film with uniform width become:

$$\begin{aligned} I_1 &= \lambda^2 + 1 + \frac{1}{\lambda^2} \\ I_2 &= \lambda^2 + \frac{1}{\lambda^2} + 1 \\ I_3 &= \lambda^2 \left(\frac{1}{\lambda^2}\right) = 1 \end{aligned} \qquad (3.19)$$

Partially constrained width: The ideal conditions described above are limiting cases which are not experienced by most DE material configurations, and so as part of the first objective of this research, a model is developed which includes the mechanical effects of the electrode behavior on the composite DE material. This will provide a description of materials whose behavior is between that of the unconstrained and the fully constrained condition. Partial constraint of the width can either be externally imposed, such as through the use of elastic constraints along the edge of the width of the film specifically designed to prevent pull in [91] , or internally imposed through the structure of the film or electrodes. One example of an internally imposed constraint is the commercially available PolyPower DE film, manufactured by Danfoss [90, 121]. This DE material uses a silicon dielectric and a plated silver electrode. The polymer has a special corrugated shape in the x_1 direction, allowing stretch only in that direction, while keeping its approximate width in the x_2 direction (Figure 3.4).

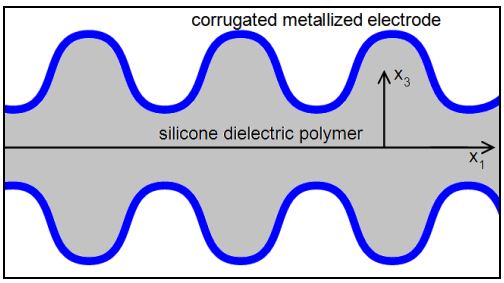

Figure 3.4: Cross sectional view of Polypower DE material

This behavior allows for the use of highly conductive, but rigid metals for the electrodes. Through our experimental observation of the PolyPower film as it is charged, it is clear that although the width is constrained, it still experiences slight pull in behavior in the x_2 direction. To model this condition, a representation of the stretch ratios is developed which describes the behavior of the limiting conditions while expressing the partially constrained condition. To begin with, an empirical parameter is defined: the boundary constraint coefficient, κ, which describes

the influence of the particular boundary condition constraint in the x_2 direction. The value of κ is defined within the range of $0 \le \kappa \le 1$, with $\kappa = 0$ corresponding to an unconstrained width (Figure 3.3b), and $\kappa = 1$ corresponding to a fully constrained width (Figure 3.3c). κ is defined such that the stretch ratio developed in the x_2 direction using κ is essentially an "average" stretch ratio developed from the linear interpolation between the two limiting boundary conditions described in eqs. (3.16) and (3.18).

$$\lambda_{2avg} = \frac{x_{2avg}}{x_{20}} = \sqrt{\frac{1-(1-\lambda)\kappa}{\lambda}} \tag{3.20}$$

which relates to an average width, x_{2avg} , corresponding to a surface area, $x_1 x_{2avg}$, that is equivalent to the surface area actually generated as a result of the pull in behavior (Figure 3.5).

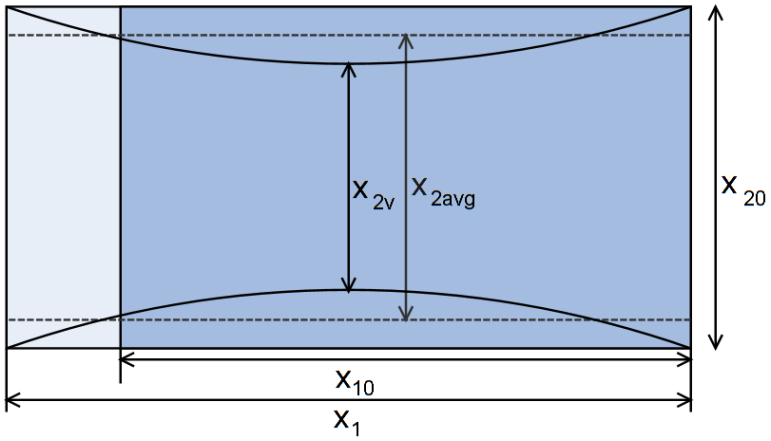

Figure 3.5: Illustration of average width, x_{2avg}, with the actual pull in condition

In order to express this average stretch ratio, each side of the pull in behavior is estimated as a parabola shown in Figure 3.6. The selection of a parabola as the edge shape function was chosen based on observations of the actual devices under strain, and the need for a function which will be readily described in terms of *measureable values*: the stretched length, x_1, and the width at the vertex (the location where the film is at its minimum) of the parabola, x_{2v}. To begin with, the

equation of the parabola is described using the stretched length, x_1, and the change in the width at the vertex , Δx_2.

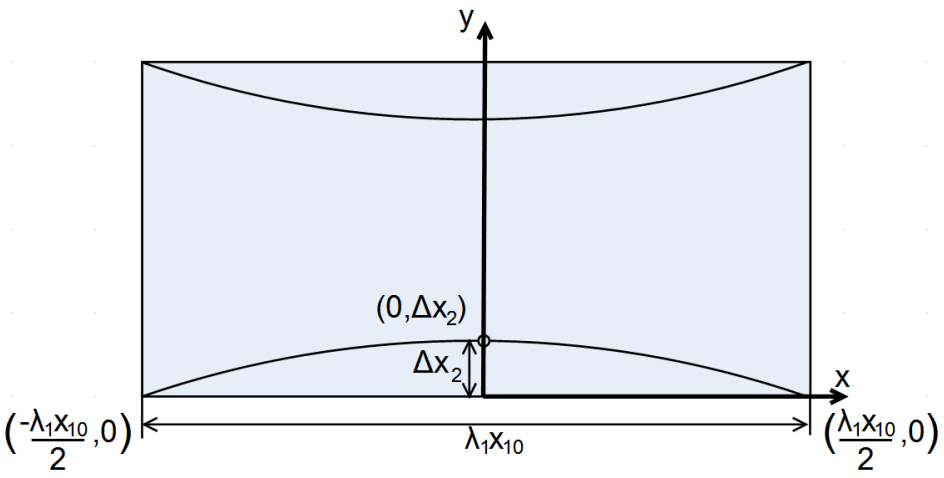

Figure 3.6: Points used to calculate the quadratic equation describing the pull in condition of the DE material

Based on the location of these three points, the quadratic equation describing the pull in curve as a function of x_1 becomes:

$$x_2 = \frac{4\Delta x_2}{\lambda_1^2 x_{10}^2} x^2 + \Delta x_2 \tag{3.21}$$

This equation, describing the shape of the pull in, is then integrated to determine the average change in the width, Δx_{2avg}.

$$\Delta x_{2avg} = \frac{\int_{-\frac{x_1}{2}}^{\frac{x_1}{2}} \left(\frac{4\Delta x_2}{\lambda_1^2 x_{10}^2} x^2 + \Delta x_2 \right) dx}{\lambda_1 x_{10}} = \frac{2\Delta x_2}{3} \tag{3.22}$$

Redefining Δx_2 in terms of measureable values, the original width, x_{20}, and the width at the vertex, x_{2v}, $\Delta x_2 = \frac{1}{2}(x_{20} - x_{2v})$ results in:

$$\Delta x_{2avg} = \frac{1}{3}(x_{20} - x_{2v}) \tag{3.23}$$

The average change in the width, Δx_{2avg}, is used to find the average width, $x_{2avg} = x_{20} - 2\Delta x_{2avg}$, as shown in Figure 3.5. The average width becomes:

$$x_{2avg} = \frac{1}{3}\left(x_{20} + 2x_{2v}\right) \tag{3.24}$$

using this average width, the average stretch ratio can be determined as a function of the measurable values x_{20} and x_{2v}:

$$\lambda_{2avg} = \frac{x_{2avg}}{x_{20}} = \frac{1}{3}\left(1 + 2\frac{x_{2v}}{x_{20}}\right) \tag{3.25}$$

This can be rewritten in terms of the stretch ratio at the vertex, λ_{2v}, leading to a relationship between the average stretch ratio and vertex stretch ratio:

$$\lambda_{2avg} = \frac{1}{3}\left(1 + 2\lambda_{2v}\right) \tag{3.26}$$

Equating this average stretch ratio with the original definition in terms of κ (Eq. 3.20), results in an expression for κ in terms of the measureable values described earlier, x_{20}, x_{2v} and λ:

$$\kappa = \frac{1}{\lambda - 1}\left(\lambda\left(\frac{x_{20} + 2x_{2v}}{3x_{20}}\right)^2 - 1\right) = \frac{1}{\lambda - 1}\left(\frac{\lambda}{3^2}\left(1 + 2\frac{x_{2v}}{x_{20}}\right)^2 - 1\right) \tag{3.27}$$

The significance of the above relationship is that it allows for empirical determination of κ based on experimental data, as all of the parameters on the RHS of eq. 3.27 are experimentally measureable.

The average width can also be written in terms of κ, providing a conceptualization of the pull in behavior based on the boundary coefficient:

$$x_{2avg} = x_{20}\sqrt{\frac{1 - (1 - \lambda)\kappa}{\lambda}} \tag{3.28}$$

These equations (3.27 and 3.28) provide a means to understand the relationship between the physical behavior of a thin film DEG undergoing uniaxial strain, and the mathematical model based on idealized boundary conditions.

Using this approach, the stretch ratios for uniaxial stretch in the x_1 direction, are defined in terms of λ and κ:

$$\lambda_1 = \lambda$$
$$\lambda_2 = \sqrt{\frac{1-(1-\lambda)\kappa}{\lambda}} \qquad (3.29\text{ a-c})$$
$$\lambda_3 = \frac{1}{\sqrt{\lambda(1-(1-\lambda)\kappa)}}$$

A general expression of the uniaxial invariants of the stress function becomes:

$$I_1 = \lambda^2 + \frac{1-(1-\lambda)\kappa}{\lambda} + \frac{1}{\lambda(1-(1-\lambda)\kappa)}$$
$$I_2 = \lambda(1-(1-\lambda)\kappa) + \frac{1}{\lambda} + \frac{\lambda}{(1-(1-\lambda)\kappa)} \qquad (3.30\text{ a-c})$$
$$I_3 = \lambda^2\left(\frac{(1-(1-\lambda)\kappa)}{\lambda}\right)\left(\frac{1}{\lambda(1-(1-\lambda)\kappa)}\right) = 1$$

For uniaxial DE materials experiencing partial constraint of the width (such as PolyPower), this formulation allows for a more accurate approximation of the actual constraint condition. This relationship can be used to model the entire range of boundary conditions between the unconstrained and fully constrained conditions, based on the choice of κ, therefore, it can be considered a general form and is used throughout the hyperelastic modeling which is performed in this project.

Experimental verification of the general stretch ratio

As described in section 3.2.1, while undergoing strain in the x_1 direction, the DE material in the x_2 direction does not retain its original shape, but rather, it takes on a nonlinear curve. The extent of this effect defines the boundary constraint condition, where a non-constraining electrode material such as graphene will have a smaller κ, and produce a more pronounced nonlinear curve than a more rigid electrode material such as corrugated silver plating. In order to quantify the effect that each electrode material had on the pull-in effect, a mechanical test stand was developed to record the geometry of the film as a function of stretch ratio. The mechanical components of the test stand are described here, while the description of the electrical portion is deferred for section 3.4.

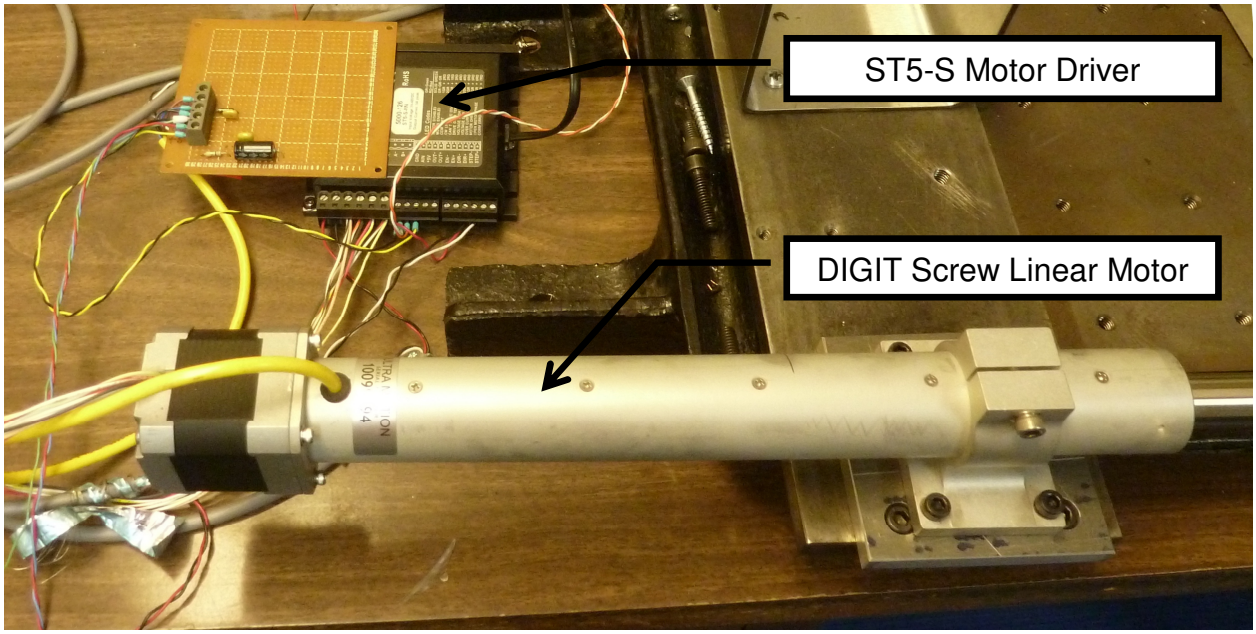

Figure 3.7: Linear motor and driver

The mechanical portion of the test stand was comprised of an instrumented linear motor with a built-in linear potentiometer, and a force gauge. The linear motor was computer controlled via a National Instruments data acquisition card (NI USB 6210) using a custom LabVIEW program (see Appendix C). The linear motor used was the DIGIT linear motor by Ultra Motion

LLC. It was comprised of an 8 inch stroke lead screw linear shaft driven by a NEMA 17 stepper motor. It also contained potentiometer feedback used for both position control of the motor and extension measurements. The motor was driven using the ST5-S driver, modulated through the analog input channel.

Force load cells

The force measurements were made using several different full-bridge thin beam load cells from Omega. Depending on the magnitude of the anticipated maximum force, one of the following load cells was utilized: 2 lb (LCL-816G), 5 lb (LCL-005), or 10 lb (LCL-010). A fixture (Figure 3.8) was utilized to house the strain gauge load cells which constrained the measuring beam to an S bend deformation. This fixture was designed to be used either with one side fixed (a), or inline between two links (b); for the uniaxial test stand the fixed configuration was used.

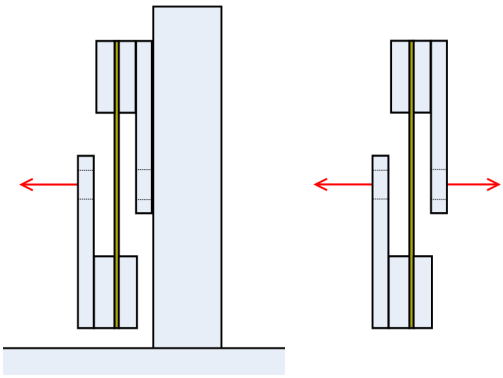

Figure 3.8: S-bend strain gauge force transducer: a) fixed and b) in-line
Thin beam transducer (shown in yellow) in the center bends in S shape as load is increased.

Three different electrode materials were investigated using the uniaxial fixture; a description of how they were each constructed and their mechanical properties can be found in Appendix D. The fixture shown in Figure 3.9 was used to restrain the elastomer DE film during the tests. It was designed to hold the DE polymer without slipping, while also assuring that a constant

electrical connection was maintained between the DE electrodes and the output wires without rupturing the film. The fixture was made of three layers of 1/4 inch polycarbonate plates, which are diagrammed in the cross section in Figure 3.9, and can be seen from above in the photo in Figure 3.10. The DE film is wrapped and sandwiched between the polycarbonate plates and clamped in place using non-conducting nylon screws. In addition to the DE film, on the bottom layer, the electrical wire contacts the electrode material on only one of the sides of the film, with an additional acrylic film to hold it in place, and prevent pinching of the DE material.

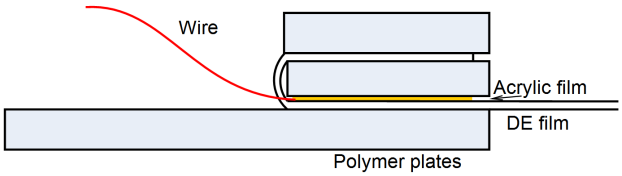

Figure 3.9: Cross section of DE film fixture.

The fixture on the opposite side of the film is similar, except that the wire and acrylic contact the opposite electrode of the DE film.

This test stand was developed to precisely control the stretch of a thin film DE using a LabVIEW program to control the position of the linear motor and record the position of the moving end of the DE film. Its operation can be seen in Figure 3.10, where the material in (a) is in its unstretched position, corresponding to a stretch ratio of one, $\lambda = 1$. Figure 3.10b provides a visual representation of the pull-in exhibited when the devices is strained to a stretch ratio of $\lambda = 1.27$, as determined by comparison of the linear motor potentiometer readings in the unstretched and stretched positions.

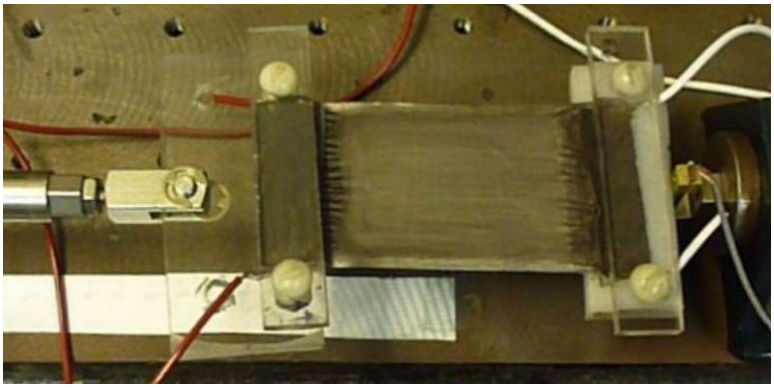

a) unstretched condition (λ=1)

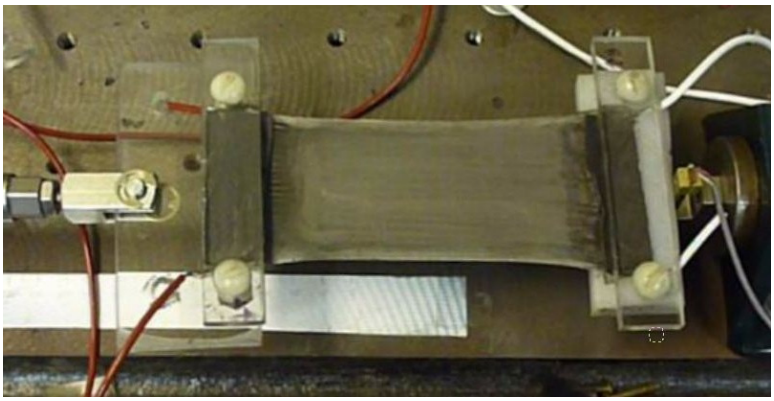

b) stretched (λ=1.27)

Figure 3.10: Pull in behavior of silicone elastomer with graphene electrodes

Measurement of the values required to experimentally determine κ was performed as follows. Images of the material in the unstretched position and the stretched position were captured for a given stretch ratio. The two images were superimposed upon one another. Figure 3.11 demonstrates the result of this process for the two images shown in Figure 3.10.

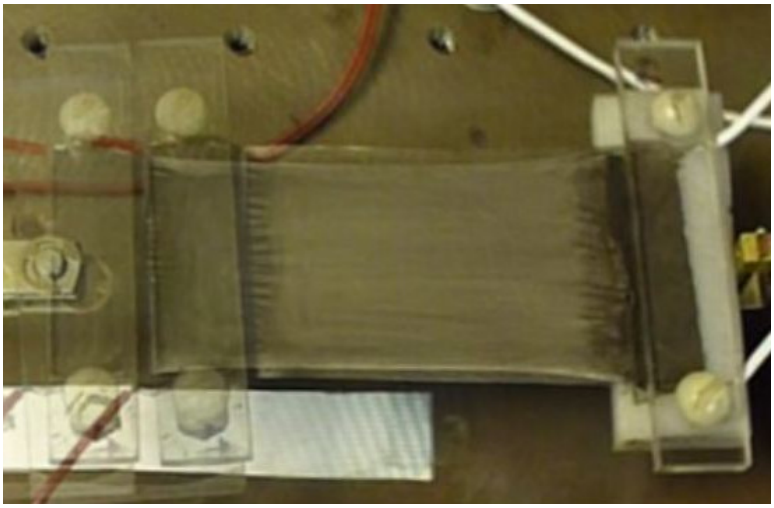

Figure 3.11: Superimposed images of unstretched (λ=1) & stretched (λ=1.27) graphene DE film

With the two images superimposed on one another, it was then possible using an onscreen measurement tool to measure the width for each condition. In this case, a simple freeware program called Screen RULER developed by Delphi Programming was used. Its use can be seen in Figure 3.12, where it is being used to measure the width of the stretched material at the midpoint (x_{2_v}).

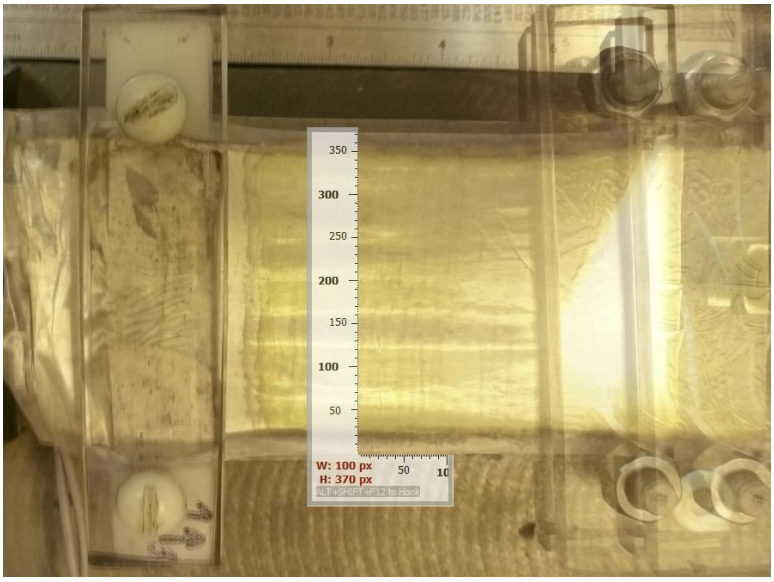

Figure 3.12: Pixel measurement of stretched (λ=1.27) width of PolyPower DE film (stretched image is superimposed on image of unstretched material)

The measurements, made in pixels, were calibrated to centimeters using a known distance, the length between the mounting bolts on the fixture, as seen in Figure 3.13.

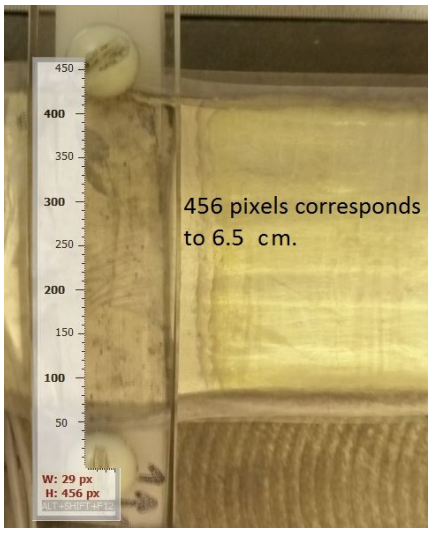

Figure 3.13: Pixel to cm calibration based on known constant measurement (distance between bolts on fixture)

Utilizing these measurements, it was possible to estimate the value of κ for a given configuration based on eq. (3.27). Using the three materials presented here, the following values of κ were found for each material:

Table 3.1: Boundary coefficient and average width stretch ratio for DE films

Compliant electrode material	Stretch ratio (λ)	Boundary coefficient (κ)	Average width stretch ratio (λ_{2avg})
Graphene	1.27	0.169	0.907
Carbon Grease	1.19	0.230	0.938
PolyPower	1.08	0.639	0.987
	1.17	0.634	0.973
	1.27	0.638	0.961

The consistency of κ throughout the operational range was observed for PolyPower at several different stretch ratios. These results confirmed that the boundary coefficient is relatively constant over the operational range. Based on these results, the following constraint coefficients were adopted for the remaining calculations: $\kappa_g = 0.169, \kappa_{cg} = 0.230, \kappa_p = 0.637$.

The development of the boundary coefficient for use in describing the behavior of the uniaxial DE is significant, as it provides a new means to characterize the stress, strain and electromechanical behaviors of the device in terms of the composite construction including both elastomer and electrode material. In section 3.3, the stretch ratios developed based on these boundary conditions will be used to expand the currently available models of hyperelastic materials for the use with uniaxial DE films. Following the derivation, this concept will be applied to the electromechanical behaviors of DE to develop a general expression for the varying capacitance of a charged DE undergoing uniaxial strain which can be utilized regardless of the constraint condition of the x_2 direction.

3.3 Modified hyperelastic constitutive relations

With the designation of the boundary constraint coefficient, κ, a definition of the principal stresses is established for a thin film DE undergoing uniaxial tension which includes the effects of the compliant electrode. Incorporating κ into the constitutive relations described earlier, eqs. (3.12) through (3.14), formulations for the stress in the x_1 and x_2 directions, σ_1 and σ_2, in terms of the stretch ratios for each of the hyperelastic models are presented here.

Neohookean model: The general stress strain relations in terms of λ_1, λ_3 for the modified NeoHookean (MN) model are:

$$\begin{aligned} \sigma_1^{MN} &= G\lambda_1^2 - G\lambda_3^2 \\ \sigma_2^{MN} &= G\lambda_2^2 - G\lambda_3^2 \end{aligned} \tag{3.31}$$

incorporating the stretch ratio terms provided in eq. 3.29 results in the stress / stretch ratio relation for the general case:

$$\sigma_1^{MN}\sigma_2^{MN} = G\left(\lambda^2 - \frac{1}{\lambda\left(1-(1-\lambda)\kappa\right)}\right)$$
$$\sigma_2^{MN} = G\left(\frac{\left(1-(1-\lambda)\kappa\right)}{\lambda} - \frac{1}{\lambda\left(1-(1-\lambda)\kappa\right)}\right) \tag{3.32}$$

when the limiting values of κ are used, the following equations result:

Unconstrained ($\kappa = 0$)
$$\sigma_1^{MN} = G(\lambda^2 - \frac{1}{\lambda})$$
$$\sigma_2^{MN} = 0 \tag{3.33}$$

Constrained ($\kappa = 0$)
$$\sigma_1^{MN} = G(\lambda^2 - \frac{1}{\lambda^2})$$
$$\sigma_2^{MN} = G(1 - \frac{1}{\lambda^2}) \tag{3.34}$$

Mooney-Rivlin model: The general stress strain relations for the modified Mooney-Rivlin (MM) model are:

$$\sigma_1^{MM} = 2\lambda^2\left(C_1 + \frac{C_2\left(1-(1-\lambda)\kappa\right)}{\lambda} + \frac{C_2}{\lambda\left(1-(1-\lambda)\kappa\right)}\right) - \frac{2\left(C_1 + C_2\lambda^2 + \frac{C_2\left(1-(1-\lambda)\kappa\right)}{\lambda}\right)}{\lambda\left(1-(1-\lambda)\kappa\right)}$$
$$\sigma_2^{MM} = 2\left(1-(1-\lambda)\kappa\right)\left(C_1 + C_2\lambda^2 + \frac{C_2}{\lambda\left(1-(1-\lambda)\kappa\right)}\right) - \frac{2\left(C_1 + C_2\lambda^2 + \frac{C_2\left(1-(1-\lambda)\kappa\right)}{\lambda}\right)}{\lambda\left(1-(1-\lambda)\kappa\right)} \tag{3.35}$$

when the limiting values of κ are used, the following equations result:

Unconstrained ($\kappa = 0$)
$$\sigma_1^{MM} = 2(\lambda^2 - \frac{1}{\lambda})(C_1 + \frac{C_2}{\lambda})$$
$$\sigma_2^{MM} = 0 \tag{3.36}$$

Constrained ($\kappa = 0$)
$$\sigma_1^{MM} = 2(\lambda^2 - \frac{1}{\lambda^2})(C_1 + C_2)$$
$$\sigma_2^{MM} = 2(1 - \frac{1}{\lambda^2})(C_1 + C_2\lambda^2) \tag{3.37}$$

Yeoh model: The general stress strain relations for the modified Yeoh (MY) model are:

$$\sigma_1^{MY} = 2\left(\lambda^2 - \frac{1}{\lambda\left(1-(1-\lambda)\kappa\right)}\right)\left(\begin{array}{l} C_1 + 2C_2(\lambda^2 + \frac{1}{\lambda\left(1-(1-\lambda)\kappa\right)} + \frac{\left(1-(1-\lambda)\kappa\right)}{\lambda} - 3) \\ \quad + 3C_3(\lambda^2 + \frac{1}{\lambda\left(1-(1-\lambda)\kappa\right)} + \frac{\left(1-(1-\lambda)\kappa\right)}{\lambda} - 3)^2 \end{array}\right)$$

$$\sigma_2^{MY} = 2\left(\lambda\left(1-(1-\lambda)\kappa\right) - \frac{1}{\lambda\left(1-(1-\lambda)\kappa\right)}\right)\times \tag{3.38}$$

$$\left(\begin{array}{l} C_1 + 2C_2(\lambda^2 + \frac{1}{\lambda\left(1-(1-\lambda)\kappa\right)} + \frac{\left(1-(1-\lambda)\kappa\right)}{\lambda} - 3) \\ \quad + 3C_3(\lambda^2 + \frac{1}{\lambda\left(1-(1-\lambda)\kappa\right)} + \frac{\left(1-(1-\lambda)\kappa\right)}{\lambda} - 3)^2 \end{array}\right)$$

when the limiting values of κ are used, the following equations result:

Unconstrained ($\kappa = 0$)

$$\begin{aligned} \sigma_1^{MY} &= 2(\lambda^2 - \frac{1}{\lambda})(C_1 + 2C_2(\lambda^2 + \frac{2}{\lambda} - 3) + 3C_3(\lambda^2 + \frac{2}{\lambda} - 3)^2) \\ \sigma_2^{MY} &= 0 \end{aligned} \tag{3.39}$$

Constrained ($\kappa = 1$)

$$\begin{aligned} \sigma_1^{MY} &= 2(\lambda^2 - \frac{1}{\lambda^2})(C_1 + 2C_2(\lambda^2 + 1 + \frac{1}{\lambda^2} - 3) + 3C_3(\lambda^2 + 1 + \frac{1}{\lambda^2} - 3)^2) \\ \sigma_2^{MY} &= 2(1 - \frac{1}{\lambda^2})(C_1 + 2C_2(\lambda^2 + 1 + \frac{1}{\lambda^2} - 3) + 3C_3(\lambda^2 + 1 + \frac{1}{\lambda^2} - 3)^2) \end{aligned} \tag{3.40}$$

These sets of equations provide a general formula relating the stretch ratio of the thin film in the x_1 direction, λ, to the generated stresses in each of the three directions. The coefficients for each of these models can be found through experimental measurements, and in many cases they are available in the literature [117]. For the research presented here, coefficients, C_1, C_2, C_3, are found from experimental data with model curve fitting for each material and geometry investigated.

Experimental validation of the modified hyperelastic model

The choice of hyperelastic model used for the silicone DE generator analysis is made based on empirical data. In order to confirm the modeling, the uniaxial test stand described in section 3.2.2 is used to measure the change in the axial force, F_1, when a thin film DE harvester is stretched in the x_1 direction. The force and extension data collected using the linear motor test stand are curve fitted to the models developed, in order to determine which model best fits the response of the DE material.

Force vs. stretch ratio models

The uniaxial experimental test setup described in section 3.2.2 returned force and extension measurements. In order to compare these results with the stress modeling developed in section 3.3, the relationship between the force and the stress was required. Recalling that force is proportional to the stress relative to the cross sectional area of the film, which changes as the material is stretched, this proportionality was found based on the stretch ratio for each of the constraint conditions (eqs. 3.16, 3.18 and 3.29). In all cases, the force relative to the stress written in terms of the initial width and thickness of the DE film and the stretch ratio is:

$$F_1 = \sigma_1 \frac{x_{20} x_{30}}{\lambda} \tag{3.41}$$

Comparison curves of the best fit curves for the force in the x_1 direction due to a prescribed stretch ratio using both an unconstrained (graphene) and a constrained (PolyPower) electrode material were generated. The overall fit for both of these constraint conditions along with the r^2 values can be seen in Figure 3.14.

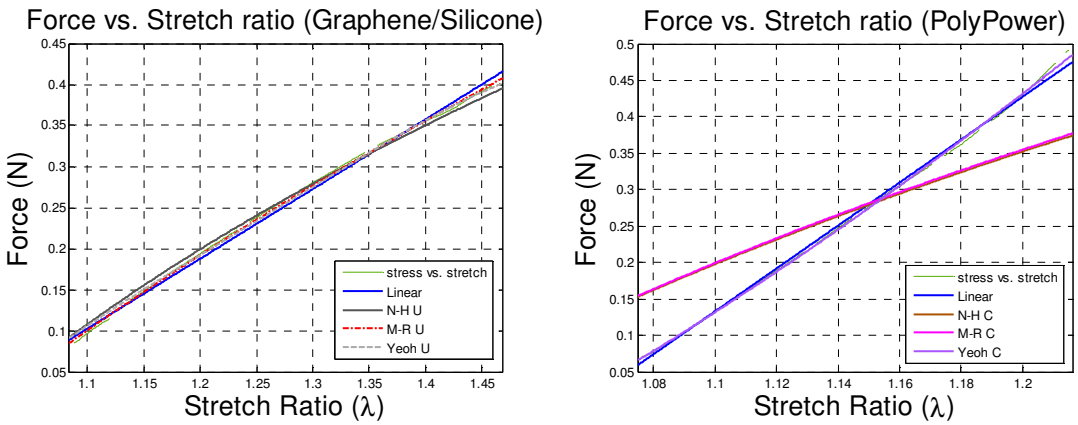

Model	r^2
Neo-Hookean	0.984
Mooney-Rivlin	0.9996
Yeoh	0.9994

Model	r^2
Neo-Hookean	0.8387
Mooney-Rivlin	0.8385
Yeoh	0.9988

Figure 3.14: Curve fits for force-stretch models

For the materials which are considered unconstrained (those with $\kappa < 0.5$), both the Mooney-Rivlin and the Yeoh models resulted in comparable results, however, for the material considered constrained ($\kappa > 0.5$), only the Yeoh model matched the experimental data well. As a result of these comparisons, the Yeoh model was selected as the model of choice, and the coefficients for each of the materials were found experimentally for use in all of the subsequent modeling.

Boundary coefficient sensitivity

The general form of the uniaxial Yeoh stress strain model is rather cumbersome compared to the limiting cases, therefore, the sensitivity of the Yeoh model to the constraint conditions was investigated to determine to what extent variation in κ would affect the coefficients of the $\sigma_1 \, vs. \lambda_1$ curve generated using the modified Yeoh model from empirical data. Our numerical experience indicated that the original form would cause curve fitting difficulty, therefore, division by the denominator terms is avoided by moving it to the left hand side, producing the following formulation of the general Yeoh model:

$$\sigma_1\lambda^3\left(1-(1-\lambda)\kappa\right)^3 = 2\left(\lambda^3\left(1-(1-\lambda)\kappa\right)-1\right)\begin{pmatrix} C_1\lambda^2\left(1-(1-\lambda)\kappa\right)^2 \\ +2C_2\left(\lambda^4\left(1-(1-\lambda)\kappa\right)^2+\lambda\left(1-(1-\lambda)\kappa\right)+\lambda\left(1-(1-\lambda)\kappa\right)^3-3\lambda^2\left(1-(1-\lambda)\kappa\right)^2\right) \\ +3C_3\left(\lambda^3\left(1-(1-\lambda)\kappa\right)+1+\left(1-(1-\lambda)\kappa\right)^2-3\lambda\left(1-(1-\lambda)\kappa\right)\right)^2 \end{pmatrix} \quad (3.42)$$

In this new form, it is possible to determine the coefficients, C_1, C_2, C_3, by curve fitting experimental stress - strain data for a specific material configuration. By comparing curves generated from the same data for several values of κ within the range of $0<\kappa<1$, it is determined that the model coefficients are not affected by the choice of κ. Plots of these curves are shown for both graphene (representing the unconstrained width) and PolyPower (representing the constrained width) in Figure 3.15.

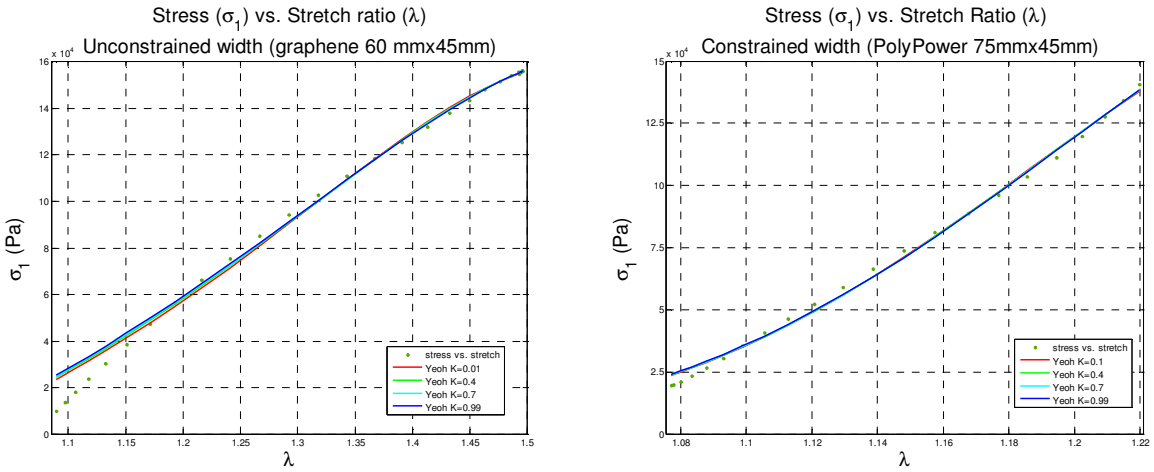

Figure 3.15: Sensitivity of axial stress to variation of κ in the model with different electrode material: left -- graphene; right -- Polypower (dotted line on each represents experimental data).

In both cases, the resulting curves demonstrate that the stress in the x_1 direction is insensitive to the constraint condition. However, brief investigation of the effect of κ in the x_2 direction indicates that stress in this direction is sensitive to the choice of κ, suggesting that the width and

the thickness are influenced by the constraint imposed by the electrode material. Based on this, the constraint coefficient, κ, will be used throughout this work in modeling geometric sensitive values such as capacitance and Maxwell stress in which the change in width and thickness of the device have a large effect. However, for stress strain relationship modeling in the x_1 direction, the limiting cases ("unconstrained" - $\kappa = 0$ and "constrained" - $\kappa = 1$) will be used as they greatly simplify the calculations without loss of accuracy.

At this point a novel formulation for the constitutive relations of a uniaxial dielectric elastomer has been developed to model the mechanical behavior of a composite hyperelastic silicone material. The behavior of other hyperelastic materials such as the acrylic often used in dielectric elastomer research may include additional non-linear behaviors which have not been necessary in this modeling. A summary of several other nonlinear behaviors which may need to be included when expanding this model have been included in Appendix A.

In the subsequent sections of this chapter, the electromechanical coupling of the device will be investigated using the mechanical relations described. Going forward, due to the addition of the electromechanical coupling in the following section, the stress due to mechanical strain will be referred to as $\sigma_{i(mech)}$, and the total stress, including both the mechanical and the electrical stimulus will be referred to using the general notation: σ_i.

3.4 Electromechanical behavior

While the hyperelastic nature of the DE is notable, the true significance of the dielectric elastomer is found in its electromechanical properties. Because the mechanical properties of dielectric elastomers directly affect their electrical properties such as capacitance and electrostatic stress, they exhibit extraordinary electromechanical coupling behaviors which can be harnessed in many different ways. As described in section 2.2.2, dielectric elastomers can be

used electromechanically as actuators, sensors and energy harvesting devices. The following section details the electromechanical modeling which arises from the mechanical model previously developed in section 3.3.

Beginning with a description of how the states of the DE device can be described by the work done on/by the DE system in terms of electrical and mechanical conjugate pairs, a derivation of the capacitance and electrostatic stress behavior of a thin film DE which includes the boundary coefficient is developed. Using these concepts, the constitutive relations for the electromechanical coupling of the DE device is developed. Next, these concepts are applied to the DE energy harvesting process for the constant charge cycle. Finally, the work conjugate operation maps are used to describe the electromechanical behavior of DE materials when used as energy harvesters and estimate their energy harvesting capacity.

3.4.1 Work conjugate pairs

Work conjugate pairs can be used to describe the electromechanical coupling of dielectric elastomers [122-124]. In DE energy harvesting, mechanical stretch energy is converted into electrical energy, and the work done in each can be described based on their work conjugate variables. For mechanical stretch, the force (F) and extension (x) conjugate pair is used to describe the mechanical state, and the electrical work is described by the voltage *(V)* and charge *(Q)* conjugate pair (which corresponds to the normalized terms of electric field *(E)* and electrical displacement *(D)* conjugate variables).

The coupling between these two conjugate pairs can be developed based on the useful work in the electromechanical system, referred to as the Helmholtz free energy of the system, $\mathbf{A}$ [122]. The total free energy of this system includes the mechanical and the electrical energy, and it can be described as a function of extension and charge, ie. $\mathbf{A}(x_1, Q)$. The variation of this

function can be written in terms of these parameters as: $\delta \mathbf{A} = F\delta x_1 + V\delta Q$, using differential calculus, it relations for both the mechanical force and the voltage as:

$$F = \frac{\partial \mathbf{A}(x_1, Q)}{\partial x_1}, \; V = \frac{\partial \mathbf{A}(x_1, Q)}{\partial Q}. \tag{3.43}$$

For a thin film DE device, the free energy function is modeled by a variable capacitance parallel plate capacitor, as will be described in section 3.4.3.

An example of a theoretical work conjugate pair is presented in Figure 3.16. Observation of work conjugate curves can be used to understand the behavior of DE energy harvesting and the limiting factors which affect the amount of energy which can be harvested.

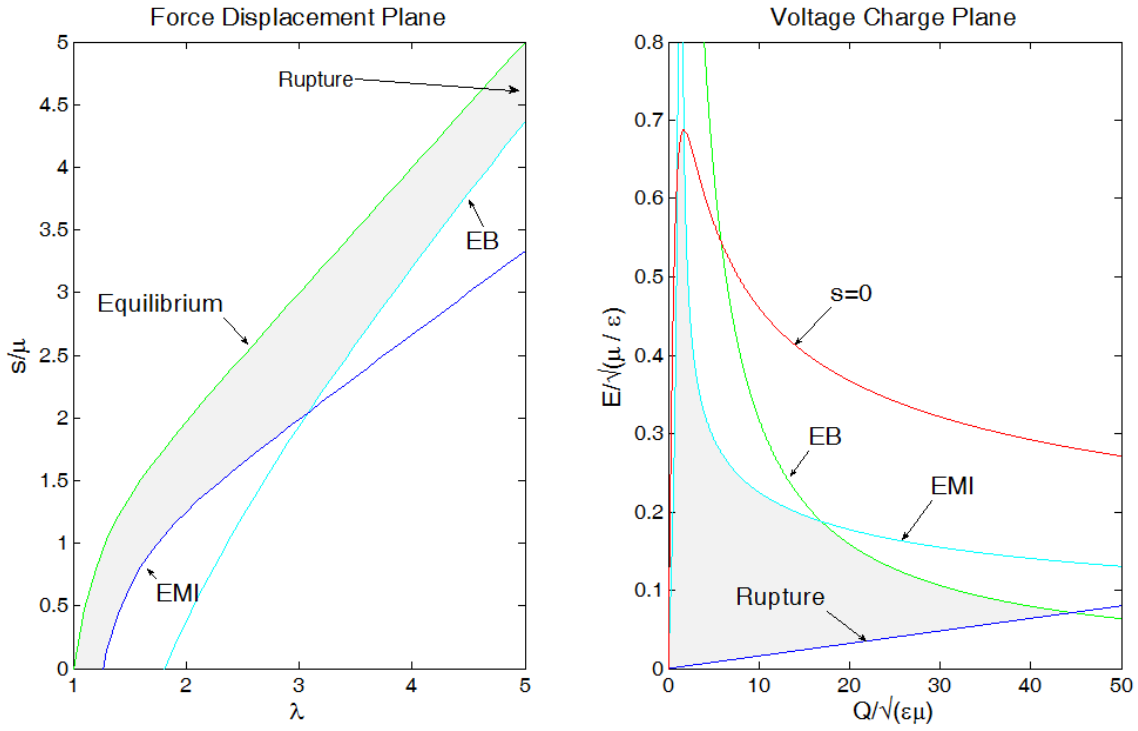

Figure 3.16: Theoretical operational range of a general DE based on its failure modes (plots recreated based on information from [124])

Figure 3.16 shows the operational range of a DE generator based on each of the following failure modes: the maximum strain that the elastomer can experience before rupture, the dielectric breakdown electric field strength (EB), and electromechanical instability (EMI). In order to

operate properly, the motion of the device must remain with these limits, reducing the maximum possible energy harvesting. In addition to the failure modes described, the maximum energy harvested is also reduced by losses in the system due to internal damping of the elastomer and parasidic losssess in the electrical circuit. In the following sections, the operational map for DE energy harvesting will be developed for both of the limiting constraint conditions based on the hyperelastic modeling and the electromechanical coupling of the device.

3.4.2 Capacitance modeling of dielectric elastomer generators

A dielectric elastomer is essentially a variable capacitor which is formed by placing compliant electrodes on either side of a dielectric elastomer film (the dark area in Figure 3.2 above). The capacitance of the device changes as the material stretches and relaxes as a function of both the geometry (the modeling of which was described in the previous section) and the dielectric constant based on the following relationship:

$$C = \frac{\varepsilon A}{x_3} \tag{3.44}$$

where ε is the permittivity of the dielectric, A is the surface area of the electrodes, $A = x_1 x_2$, and x_3 is the thickness between electrodes. The permittivity can be written as: $\varepsilon = \varepsilon_0 \varepsilon_r$ where ε_0 is the dielectric constant of a vacuum (8.85×10^{-12} F/m), and ε_r is the relative permittivity of the material. For the polymers under investigation, the relative permittivity have the following values:

Table 3.2: Relative permittivity of common DE dielectric polymer materials.

Material	Relative permittivity, ε_r
Acrylic (VHB 4910)	4-5 [125]
Silicone	3-8 [93, 126]

The capacitance is also directly related to the charge and the bias voltage as: $C = \frac{Q}{V}$. Substituting this relation into 3.44, the charge is expressed as a function of bias voltage and thickness:

$$Q = \frac{\varepsilon A}{x_3} V \tag{3.45}$$

Boundary condition modeling

As stated previously, dielectric elastomers are capacitors with the unique feature that as they undergo mechanical strain, the capacitance of the device changes based on the stretching and thinning out of the elastomer material. The relationship between the stretch ratio and the resulting capacitance of the DEG can be determined based on hyperelastic modeling of the dielectric polymer. Using the boundary constraint coefficient, the capacitance relative to the stretch ratio in the x_1 direction is be determined in this section for the general situation, it is then be reduced to the limiting width constraint conditions.

Recalling that the capacitance of the DE is proportional to the area of the electrodes divided by the thickness of the dielectric, the capacitance can be related to the unstretched dimensions of the DE by the stretch ratios:

$$C = \varepsilon \frac{A}{x_3} = \varepsilon \frac{x_1 x_2}{x_3} = \varepsilon \frac{(x_{10}\lambda_1)(x_{20}\lambda_2)}{x_{30}\lambda_3} = \varepsilon \frac{x_{10}x_{20}}{x_{30}} \frac{\lambda_1 \lambda_2}{\lambda_3} \tag{3.46}$$

For a given initial geometry, assuming constant dielectric permittivity, ε, the change in capacitance is solely a function of the stretch ratios. Using the stretch ratio terms derived in section 3.2, the general formula for the capacitance using (3.45) is:

$$C = \varepsilon \frac{x_{10}x_{20}}{x_{30}} \frac{\lambda \frac{\sqrt{1-(1-\lambda)\kappa}}{\sqrt{\lambda}}}{\frac{1}{\sqrt{\lambda}\sqrt{1-(1-\lambda)\kappa}}} = \varepsilon \frac{x_{10}x_{20}}{x_{30}} \lambda\left(1-(1-\lambda)\kappa\right) \tag{3.47}$$

Recalling that κ can be found as a function of the device materials and geometry, the capacitance can then be predicted using this model for a given stretch ratio.

Once the general relationship has been found, this equation can be tailored to either of the limiting constraint conditions. For the unconstrained width condition, $\lambda_1 = \lambda$, $\lambda_2 = \frac{1}{\sqrt{\lambda}}$, $\lambda_3 = \frac{1}{\sqrt{\lambda}}$, the capacitance becomes:

$$C_u = \varepsilon \frac{x_{10} x_{20}}{x_{30}} \frac{\lambda \frac{1}{\sqrt{\lambda}}}{\frac{1}{\sqrt{\lambda}}} = \varepsilon \frac{x_{10} x_{20}}{x_{30}} \lambda \tag{3.48}$$

For the fully constrained width condition, $\lambda_1 = \lambda, \lambda_2 = 1, \lambda_3 = \frac{1}{\lambda}$, the capacitance becomes:

$$C_c = \varepsilon \frac{x_{10} x_{20}}{x_{30}} \frac{\lambda}{\frac{1}{\lambda}} = \varepsilon \frac{x_{10} x_{20}}{x_{30}} \lambda^2 \tag{3.49}$$

As expected, many materials used in a DEG will not naturally fall into either of these constraint conditions, however, because of the simplicity of these formulas, when the material behavior is close to that of the limiting case, these simplified forms can be utilized.

Experimental capacitance verification of capacitance modeling

Experimental values of the DE's capacitance were measured as the thin film was stretched. The test setup was the same as that described in section 0. The unconstrained electrode material used was the graphene powder, and the constrained electrode material was the PolyPower silver electrodes. The modeling of the capacitance was based on a thin film silicone polymer with a reported dielectric permittivity, $\varepsilon = 3.1$, and thickness, $x_{30} = 80\,\mu m$ [121]. The length and width of each material are stated in the respective figures, as well as the constraint

condition, κ, which for each case was determined using the procedure described in section 3.2.2. During this test, the capacitance of each material was measured as it was stretched in discrete increments. These experimental results were then compared with the experimental values determined using eqs. (3.47) through (3.49).

The comparison of the experimental data with the modeling is shown for two different constraint conditions, unconstrained graphene (Figure 3.17) and constrained PolyPower (Figure 3.18). It is important to note that the operational stretch ratio range is different for both of the electrode materials. The graphene electrode is operating from unstretched ($\lambda = 1$) to a stretch ratio of $\lambda = 1.6$, whereas, the PolyPower is designed to be functional within a much lower stretch range (30% max, but 15% suggested), therefore, it is only tested to a stretch ratio of $\lambda = 1.2$.

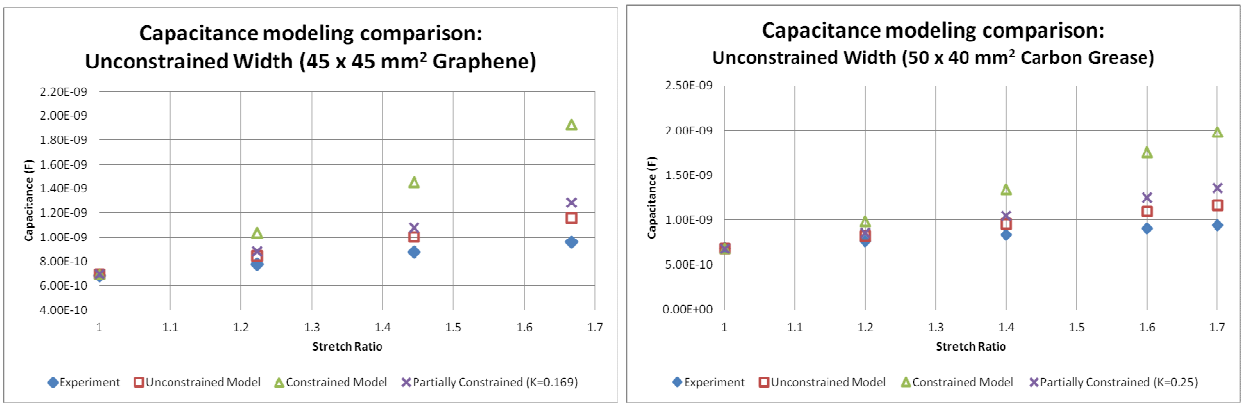

Figure 3.17: Capacitance for thin film with unconstrained width a) graphene b) carbon grease

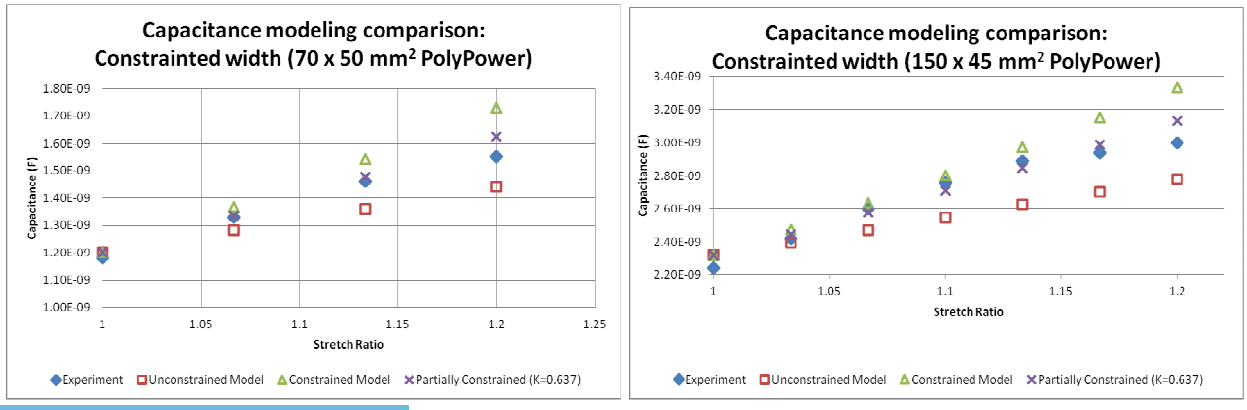

Figure 3.18: Capacitance for thin film with constrained width, second figure shows effect of doubling the length of the active area.

Based on these results, it is clear that both graphene and carbon grease behave as unconstrained electrode materials, however, the unconstrained model is still not properly predicting the capacitance over the entire operational stretch range.

As demonstrated in Figure 3.17, the standard parallel plate capacitance model does not accurately describe the capacitance as a function of stretch ratio for the graphene and carbon grease electrode materials. As the stretch ratio increases, the measured capacitance is increasingly lower than the modeled capacitance. This discrepancy demonstrates an important failure mode of dielectric elastomer compliant electrodes: cracking within the electrode material. It is well documented that when there is a difference between the elastic modulus of the elastomer material and the electrode material, there is a high risk of cracks developing in the electrodes[110, 127]. These cracks will cause the resistance within the electrode material to increase, resulting in decreased capacitance and eventually failure of the device.

Like the carbon grease and graphene DE, the PolyPower DE also experiences cracking when stretched beyond its operational limit. Because of the stiffness of the metallic electrodes, this cracking will occur quickly and render the device unusable. For this reason, tests on the PolyPower material were only performed to a 20% strain, and within this range exhibited little cracking behavior. The reduction in electrode surface area was empirically modeled as an exponentially decaying term, $e^{-\beta(\lambda-1)}$ based on the nature of the failure, in which cracks appear to increase exponentially with stretch, where the coefficient, β, was found from measurements. These coefficients (which can be seen in Figure 3.19) were similar for both the graphene and the carbon grease electrodes, with β ranging from 0.4 to 0.5.

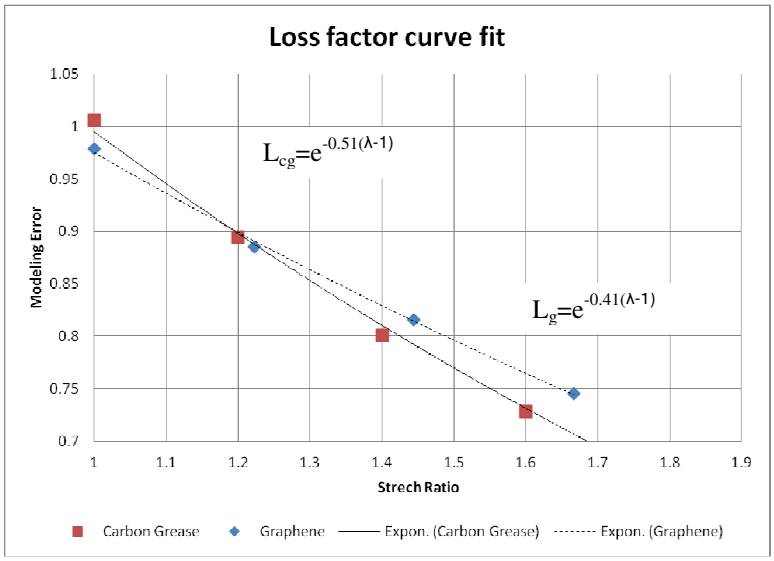

Figure 3.19: Loss factor curve fit from modeling error ratio for carbon grease DE and graphene DE

Using each of exponential curve fits from the data, a loss factor was determined for each material. When this loss factor was included in the capacitance modeling, the predicted values closely matched the experimental values, as shown in Figure 3.20.

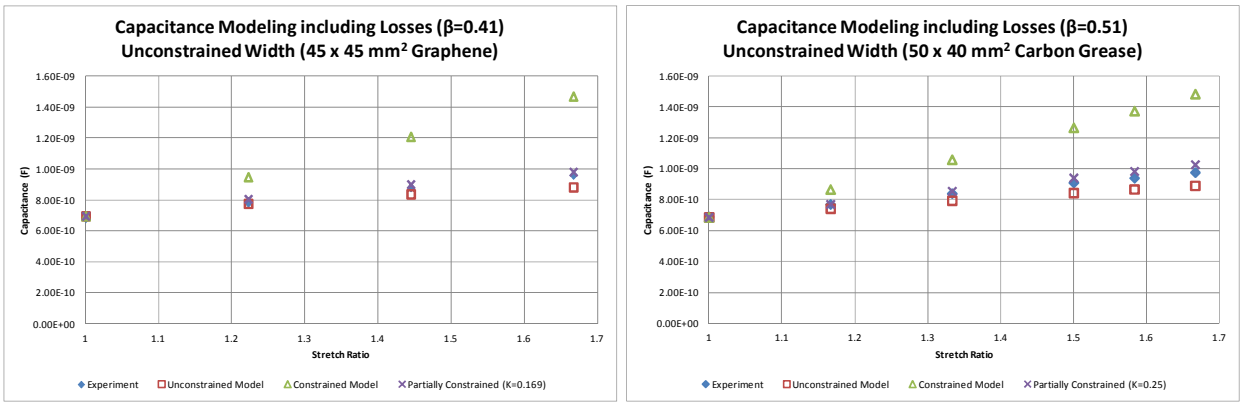

Figure 3.20: Capacitance modeling including losses due to cracking for a) graphene and b) carbon grease

This loss factor was generated for each compliant electrode material and integrated into the modeling based on the materials used.

The variable capacitance of the DE demonstrated above plays a very important role in the electromechanical behavior of the device, and by establishing the relationship between the capacitance and the stretch ratio, the capacitance can be used to estimate the mechanical effects

of a charge placed across the dielectric polymer as a function of stretch. The electromechanical coupling between the electric field and the stress generation in the polymer occurs because of the attractive force of unlike charges located on opposite sides of the polymer dielectric. This electrostatic stress, is directly related to the charge carrying capacity of the device (quantified by the capacitance) and hence this understanding of the capacitance is vital to understanding the electromechanical modeling which will be demonstrated in the following section.

3.4.3 Electrostatic Maxwell stress

Dielectric elastomer energy harvesting utilizes the stresses which are generated when a parallel plate capacitor is placed within an electric field. The Maxwell stress, also termed electrostatic stress, is caused by the force of opposite charges attracting one another from opposite parallel plates. Another stress also associated with a parallel plate dielectric placed within an electric field is the electrostrictive stress. The electrostrictive stress is related to changes in the dielectric properties of the polymer due to polarization effects. Unlike the Maxwell stress, which is developed on the electrodes located outside of the dielectric material the electrostrictive stress develops within the material itself. For the dielectric polymers under investigation, the electrostrictive stress is much smaller than the Maxwell stress, and is assumed to be negligible [111], therefore, the electromechanical coupling of the DE harvesters is modeled based on the Maxwell stress alone.

The Maxwell stress developed by an electric field is directly related by the dielectric constant:

$$\sigma_M = -\varepsilon E^2 \tag{3.50}$$

The derivation of σ_M can be demonstrated using the electrical and mechanical work conjugate pairs introduced previously in section 3.4.1. The DE device under investigation is considered a

variable size parallel plate electrode which experiences constant charge during stretching. The relationship between the voltage and the charge across the electrodes is related to the capacitance as stated in eq. (3.45), which can be written in terms of the displacements:

$$V = \frac{x_3}{\varepsilon x_1 x_2} Q \tag{3.51}$$

Utilizing the stretch ratios associated with the constraint conditions described in section3.2, voltage can be written in terms of x_1 for the unconstrained (V_u), constrained (V_c), and general (V) case:

$$\begin{aligned} V_u &= \frac{Q}{\varepsilon}\frac{x_3}{x_1 x_2} = \frac{Q}{\varepsilon}\frac{x_{30}}{x_{10}x_{20}}\frac{1}{\lambda} = \frac{Q}{\varepsilon}\frac{x_{10}}{x_1} \\ V_c &= \frac{Q}{\varepsilon}\frac{x_3}{x_1 x_2} = \frac{Q}{\varepsilon}\frac{x_{30}}{x_{10}x_{20}}\frac{1}{\lambda^2} = \frac{Q}{\varepsilon}\frac{x_{10}^2}{x_1^2} \\ V &= \frac{Q}{\varepsilon}\frac{x_{30}}{x_{10}x_{20}}\frac{x_3}{x_1 x_2} = \frac{Q}{\varepsilon}\frac{x_{30}}{x_{10}x_{20}}\frac{1}{\lambda\left(1+(\lambda-1)\kappa\right)} \\ &= \frac{Q}{\varepsilon}\frac{x_{30}}{x_{10}x_{20}}\frac{1}{\left(\lambda+(\lambda^2-\lambda)\kappa\right)} = \frac{Q}{\varepsilon}\frac{x_{30}}{x_{10}x_{20}}\frac{1}{\left(\frac{x_0}{x_1}+\left(\left(\frac{x_0}{x_1}\right)^2-\frac{x_0}{x_1}\right)\kappa\right)} \end{aligned} \tag{3.52}$$

These definitions for voltage are then substituted into eq. (3.43), integrating both sides with respect to charge and holding displacement constant, $\int \partial \mathbf{A}(x_1, Q) = \int V \partial Q$, results in the following free energy functions:

$$\begin{aligned} \mathbf{A}_u(x_1, Q) &= \frac{Q^2}{2\varepsilon}\frac{x_{30}}{x_{10}x_{20}} \\ \mathbf{A}_c(x_1, Q) &= \frac{Q^2}{2\varepsilon}\frac{x_{30}}{x_{10}x_{20}}\frac{x_{10}^2}{x_1^2} \\ \mathbf{A}(x_1, Q) &= \frac{Q^2}{2\varepsilon}\frac{x_{30}}{x_{10}x_{20}}\frac{1}{\left(\frac{x_0}{x_1}+\left(\left(\frac{x_0}{x_1}\right)^2-\frac{x_0}{x_1}\right)\kappa\right)} \end{aligned} \tag{3.53 a-c}$$

Returning this function to eq. (3.43) provides a constraint specific equation for the pressure with respect to displacement and charge:

$$F_u = \frac{Q^2}{2\varepsilon}\frac{x_{30}}{x_{10}x_{20}}x_{10}\ln\left(x_1\right)$$
$$F_c = \frac{-Q^2}{\varepsilon}\frac{x_{30}}{x_{10}x_{20}}\frac{x_{10}^2}{x_1^3} \tag{3.54a,b}$$

resulting in the force relationship for the DE device undergoing uniaxial strain.

Considering any of the constraint conditions and then rewriting it in terms of stress, $\sigma = \frac{F}{x_2 x_3}$, and electric field, $E = \frac{V}{x_3}$, where the electric field is related to the voltage and thickness of the material, results in the equation for Maxwell stress above:

$$\sigma_c = \frac{F_c}{x_2 x_3} = \frac{-\left(\frac{\varepsilon \cancel{x_1} \cancel{x_2}}{\cancel{x_3}}\left(E\cancel{x_3}\right)\right)^2}{\varepsilon}\frac{\cancel{x_3}}{\cancel{x_2}\cancel{x_3}\cancel{x_1}\cancel{x_2}}\frac{\cancel{x_1}^2}{\cancel{x_1}^3} = -\varepsilon E^2 \tag{3.55}$$

Therefore, the relationship between the electrical charge and the Maxwell stress can be written in terms of the bias voltage and dielectric thickness [32]:

$$\sigma_M = -\varepsilon\left(\frac{V}{x_3}\right)^2 \tag{3.56}$$

Recall from Figure 3.2 that the Maxwell stress acts only in the direction perpendicular to the electrode surface area, (the x_3 direction) and that this is the only stress experienced in that direction. Therefore, the relationship between the electrical charge and the stress in the x_3 direction can be written in terms of the bias voltage and dielectric thickness [32]:

$$\sigma_{3M} = \sigma_M = -\varepsilon\left(\frac{V}{x_3}\right)^2 \tag{3.57}$$

When the capacitance is known, the charge can be determined and the Maxwell stress can also be found as a function of the surface area of the electrodes.

$$\sigma_{3M} = \sigma_M = -\frac{1}{\varepsilon}\left(\frac{Q}{x_1 x_2}\right)^2 \tag{3.58}$$

Providing a useful description of the Maxwell stress for the case of constant charge, which will be used throughout this analysis.

Electrostatic pressure coupling in x_1 direction

To model the effect of the Maxwell stress generated on the surface of the DE in the x_3 direction, a similar methodology is employed as was used to determine the hydrostatic pressure due to a mechanical strain. To differentiate the stretch ratio due to the Maxwell stress from that due to the mechanical strain, a new stretch ratio term $\tilde{\lambda}_i$, the Maxwell stretch ratio, is defined. The Maxwell stretch ratio describes the change in the displacement of the film which occurs as a result of the Maxwell stress generated due to a charge across the DE film (which acts as a capacitor), independent of any mechanical stretch. For simplicity, we first examine the Maxwell stress purely due to the electric field with $\lambda = 1$. Once this relationship is established, the analysis is expanded to include strains due to mechanical stresses, where $\lambda \neq 1$.

In establishing the Maxwell stretch ratios, $\tilde{\lambda}_1$, $\tilde{\lambda}_2$, and $\tilde{\lambda}_3$ in terms of κ, the following assumptions about the electromechanical behavior of the material are imposed:

- First, because the test setup utilizes position control in the x_1 direction to isolate the Maxwell stress, the position in the x_1 direction is fixed and there can be no additional stretch due to the Maxwell stress, i.e., $\tilde{\lambda}_1 = 1$.

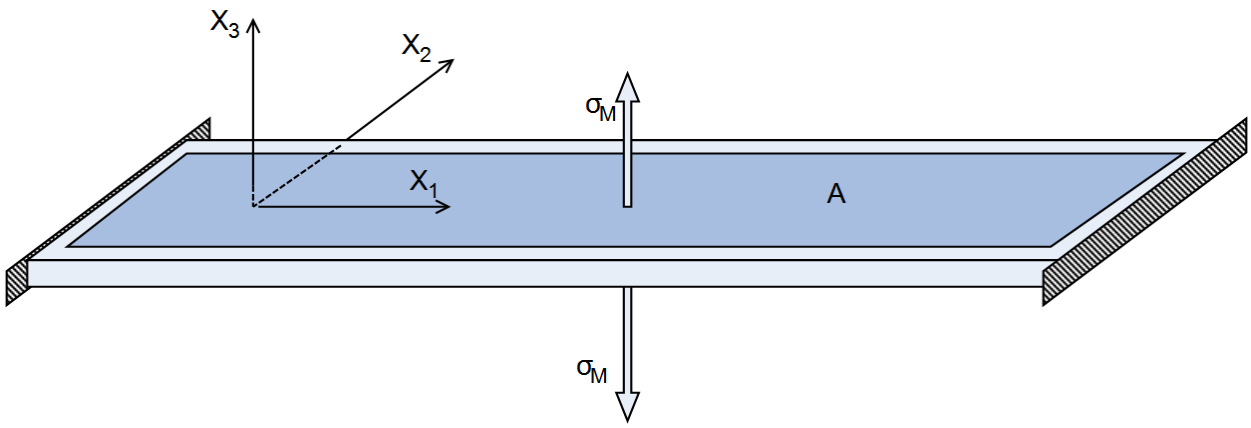

Figure 3.21: DE film fully constrained in x_1 direction undergoing stress in x_3 direction due to Maxwell stress

- Secondly, σ_3 is assumed to be equal to the Maxwell stress, thus allowing σ_M to be incorporated into the stress formula, $\sigma_{3M} = \tilde{\lambda}_3\left(\partial W/\partial\tilde{\lambda}_3\right) - p = \sigma_M$.

The Maxwell stretch ratios and electrostatic pressure constitutive relation will be determined for the general case through the investigation of the limiting cases.

Electrostatic pressure in x_1 direction for fully constrained width

In modeling the Maxwell stretch ratios and electrostatic pressure constitutive relations, the limiting boundary conditions are first considered to provide an understanding of how the general equations should be developed. The fully constrained condition provides the most direct relationship between the Maxwell stress and the stress in the x_1 direction. For this constraint condition, as demonstrated in Figure 3.22, the x_1 and x_2 directions are both constrained, so that there is no stretch in either direction.

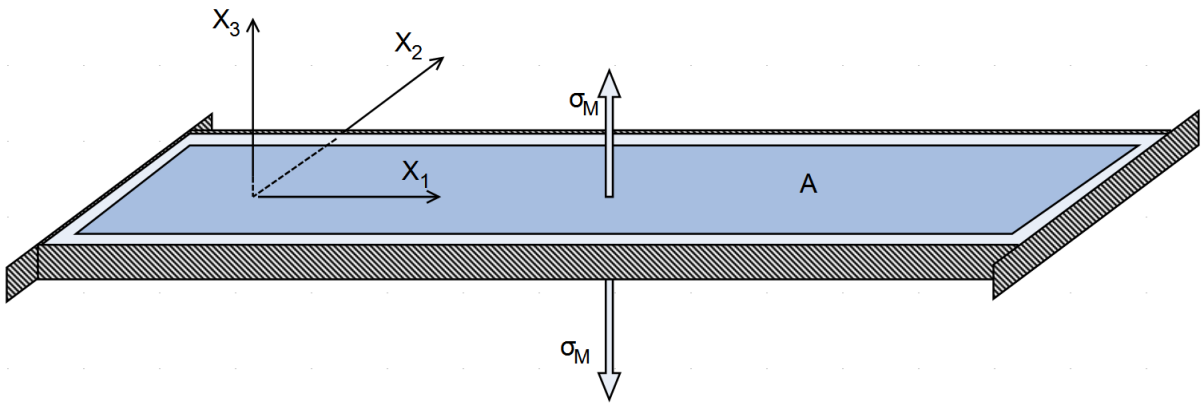

Figure 3.22: DE film fully constrained in both x_1 and x_2 directions

Assuming that the Maxwell stress is evenly distributed across the surface of the film, and taking advantage of the incompressibility of the hyperelastic polymer, this configuration results in a situation similar to a rigid box, in which stresses are generated in all directions, as a result of the Maxwell stress, σ_M , in the x_3 direction as demonstrated in Figure 3.23.

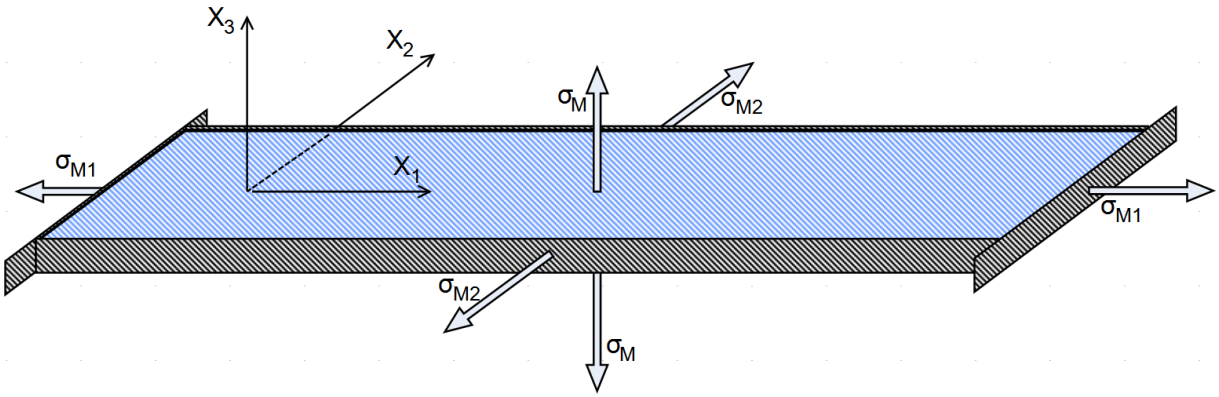

Figure 3.23: Conceptualization of DE film enclosed by rigid constraints.
(Idealized fully constrained width condition)

Incorporating this idealized condition into the model results in the following stretch ratios:

$$\tilde{\lambda}_1 = 1,\ \tilde{\lambda}_2 = 1,\ \tilde{\lambda}_3 = 1 \tag{3.59}$$

This results in perfect transmission of the Maxwell stress to each edge of the film, indicating that the stress in the measurement direction (x_1) is equivalent to the Maxwell stress generated by the

capacitor [125]. Therefore, for the situation where there is no mechanical strain, the dimensions remain constant, and the stress in the x_1 direction resulting from the Maxwell stress simplifies to:

Constrained
$$\sigma_{1M} = \sigma_{3M} = \sigma_M = -\varepsilon\left(\frac{V}{x_{30}}\right)^2 = -\frac{1}{\varepsilon}\left(\frac{Q}{x_{10}x_{20}}\right)^2 \tag{3.60}$$

Electrostatic pressure in x_1 direction for unconstrained width

The unconstrained boundary condition presents a slightly more complex situation, since the stretch ratio in the x_2 direction is unknown.

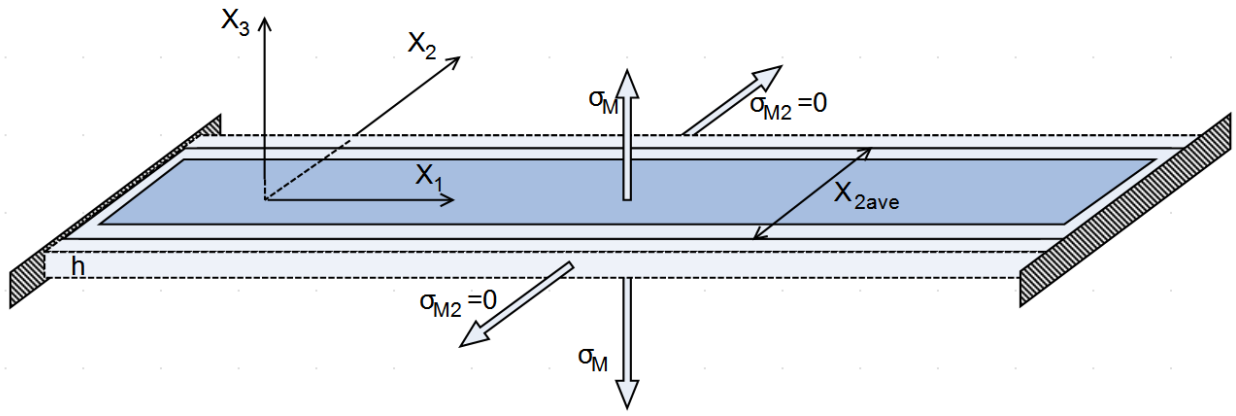

Figure 3.24: Conceptualization of DE film with no constraint in x_2 direction. (Idealized unconstrained width condition)

However, since there is no stress generated in the x_2 direction, $\sigma_2 = 0$, it is still possible to determine the stress in the x_1 direction. Recalling that the x_1 direction is fixed, the stretch ratios become:

$$\tilde{\lambda}_1 = 1,\ \tilde{\lambda}_2 = \tilde{\lambda},\ \tilde{\lambda}_3 = \frac{1}{\tilde{\lambda}} \tag{3.61}$$

Utilizing the Yeoh hyperelastic model for the unconstrained width, the stress equations become:

$$\sigma_{1M} = \tilde{\lambda}_1 \frac{\partial W}{\partial \tilde{\lambda}_1} - p = 2C_1\tilde{\lambda}_1 + 4C_2\tilde{\lambda}_1\left(\tilde{\lambda}_1^2 + \tilde{\lambda}_2^2 + \tilde{\lambda}_3^2 - 3\right) + 6C_3\tilde{\lambda}_1\left(\tilde{\lambda}_1^2 + \tilde{\lambda}_2^2 + \tilde{\lambda}_3^2 - 3\right)^2 - p$$

$$= 2C_1 + 4C_2\left(1 + \tilde{\lambda}^2 + \frac{1}{\tilde{\lambda}^2} - 3\right) + 6C_3\left(1 + \tilde{\lambda}^2 + \frac{1}{\tilde{\lambda}^2} - 3\right)^2 - p$$

$$\sigma_{2M} = \tilde{\lambda}_2 \frac{\partial W}{\partial \tilde{\lambda}_2} - p = 2C_1\tilde{\lambda}_2 + 4C_2\tilde{\lambda}_2\left(\tilde{\lambda}_1^2 + \tilde{\lambda}_2^2 + \tilde{\lambda}_3^2 - 3\right) + 6C_3\tilde{\lambda}_2\left(\tilde{\lambda}_1^2 + \tilde{\lambda}_2^2 + \tilde{\lambda}_3^2 - 3\right)^2 - p = 0 \quad \text{(3.62 a-c)}$$

$$= 2C_1\tilde{\lambda} + 4C_2\tilde{\lambda}\left(1 + \tilde{\lambda}^2 + \frac{1}{\tilde{\lambda}^2} - 3\right) + 6C_3\tilde{\lambda}\left(1 + \tilde{\lambda}^2 + \frac{1}{\tilde{\lambda}^2} - 3\right)^2 - p = 0$$

$$\sigma_{3M} = \tilde{\lambda}_3 \frac{\partial W}{\partial \tilde{\lambda}_3} - p = 2C_1\tilde{\lambda}_3 + 4C_2\tilde{\lambda}_3\left(\tilde{\lambda}_1^2 + \tilde{\lambda}_2^2 + \tilde{\lambda}_3^2 - 3\right) + 6C_3\tilde{\lambda}_3\left(\tilde{\lambda}_1^2 + \tilde{\lambda}_2^2 + \tilde{\lambda}_3^2 - 3\right)^2 - p = \sigma_M$$

$$= 2C_1\frac{1}{\tilde{\lambda}} + 4C_2\frac{1}{\tilde{\lambda}}\left(1 + \tilde{\lambda}^2 + \frac{1}{\tilde{\lambda}^2} - 3\right) + 6C_3\frac{1}{\tilde{\lambda}}\left(1 + \tilde{\lambda}^2 + \frac{1}{\tilde{\lambda}^2} - 3\right)^2 - p = \sigma_M$$

In order to utilize these equations to find σ_1, both the hydrostatic pressure and the stretch ratio, $\tilde{\lambda}$, must be found. The hydrostatic pressure can be found as a function of $\tilde{\lambda}$ and σ_M by using the stress equation in the x_3 direction:

$$p = 2\frac{1}{\tilde{\lambda}}\left(C_1 + 2C_2\left(1 + \tilde{\lambda}^2 + \frac{1}{\tilde{\lambda}^2} - 3\right) + 3C_3\left(1 + \tilde{\lambda}^2 + \frac{1}{\tilde{\lambda}^2} - 3\right)^2\right) - \sigma_M \quad \text{(3.63)}$$

which, when substituted into the stress formula, eq. (3.3), results in:

$$\sigma_{1M} = 2\left(1 - \frac{1}{\tilde{\lambda}}\right)\left(C_1 + 2C_2\left(1 + \tilde{\lambda}^2 + \frac{1}{\tilde{\lambda}^2} - 3\right) + 3C_3\left(1 + \tilde{\lambda}^2 + \frac{1}{\tilde{\lambda}^2} - 3\right)^2\right) + \sigma_M$$

$$\sigma_{2M} = 2\left(\tilde{\lambda} - \frac{1}{\tilde{\lambda}}\right)\left(C_1 + 2C_2\left(1 + \tilde{\lambda}^2 + \frac{1}{\tilde{\lambda}^2} - 3\right) + 3C_3\left(1 + \tilde{\lambda}^2 + \frac{1}{\tilde{\lambda}^2} - 3\right)^2\right) + \sigma_M = 0 \quad \text{(3.64ac)}$$

$$\sigma_{3M} = \sigma_M$$

At this point, it is possible to determine the stretch, $\tilde{\lambda}$, which occurs as a result of the charge placed across the electrodes using eq. (3.64 b). The value of $\tilde{\lambda}$, which results from a constant Maxwell stress is named the equilibrium stretch ratio, because it describes the stretch of

the material as it is experiencing a constant charge. In order to find $\tilde{\lambda}$, eq. (3.64 c) must be rewritten in terms of $\tilde{\lambda}$ using eq. (3.60), which results in:

$$\sigma_{3M} = \sigma_M = -\frac{1}{\varepsilon}\left(\frac{Q}{x_{10}x_{20}\tilde{\lambda}_1\tilde{\lambda}_2}\right)^2 = -\frac{1}{\varepsilon}\left(\frac{Q}{x_{10}x_{20}}\right)^2 \frac{1}{\tilde{\lambda}^2} \tag{3.65}$$

The above result in then substituted into eq. (3.64 b) and numerical root finding is utilized to determine the equilibrium stretch ratio for the given conditions. Using the equilibrium stretch ratio, the effective stress in the x_1 direction due to the Maxwell stress, σ_{1M}, (called the *effective Maxwell stress*) is determined using eq. (3.64a).

Electrostatic pressure in x_1 direction for the general uniaxial DE

The general case represents the situation where neither of the simplifying assumptions associated with the limiting cases applies. The stretch ratios associated with this condition can be described using the constraint condition coefficient, κ, defined in section 3.3. However, because the position in the x_1 direction is now fixed, the subsequent Maxwell stretch ratios are defined as the linear interpolation between the two limiting cases:

$$\tilde{\lambda}_1 = 1,\ \tilde{\lambda}_2 = \tilde{\lambda} + (1-\tilde{\lambda})\kappa,\ \tilde{\lambda}_3 = \frac{1}{\tilde{\lambda} + (1-\tilde{\lambda})\kappa} \tag{3.66}$$

which can be compared with the mechanical stretch ratios defined in eq. (3.29).

Using these Maxwell stretch ratio definitions, the stress generated in the x_1 direction can be defined as a function of κ by considering the stress in the x_2 direction. When the width of the DE film is partially constrained, σ_2 is no longer zero, therefore, it contributes to the transmission of the stress in the x_1 direction, yet because the width is not fully constrained, the stretch ratio is not known, this results in an underdetermined system:

$$\sigma_{1M} = 2\tilde{\Gamma} - p$$
$$\sigma_{2M} = 2\left(\tilde{\lambda} + (1-\tilde{\lambda})\kappa\right)\tilde{\Gamma} - p \neq 0 \qquad \text{(3.67 a-c)}$$
$$\sigma_{3M} = 2\frac{1}{\tilde{\lambda} + (1-\tilde{\lambda})\kappa}\tilde{\Gamma} - p = \sigma_M$$

where:

$$\tilde{\Gamma} = \left(C_1 + 2C_2\left(1 + \left(\tilde{\lambda} + (1-\tilde{\lambda})\kappa\right)^2 + \frac{1}{\left(\tilde{\lambda} + (1-\tilde{\lambda})\kappa\right)^2} - 3\right) + 3C_3\left(1 + \left(\tilde{\lambda} + (1-\tilde{\lambda})\kappa\right)^2 + \frac{1}{\left(\tilde{\lambda} + (1-\tilde{\lambda})\kappa\right)^2} - 3\right)^2 \right)$$

which can also be written in terms of the first invariant defined in terms of the Maxwell stretch ratio, $I_1 = \sum_{i=1}^{3} \tilde{\lambda}_i^2$, as: $\tilde{\Gamma} = \left(C_1 + 2C_2(I_1 - 3) + 3C_3(I_1 - 3)^2\right)$, and the Maxwell stress defined in terms of the Maxwell stretch ratio is: $\sigma_M = -\frac{1}{\varepsilon}\left(\frac{Q}{x_{10}x_{20}}\right)^2 \frac{1}{\left(\tilde{\lambda} + (1-\tilde{\lambda})\kappa\right)^2}$.

If additional measurements are taken to determine the position, x_2, after the Maxwell stress is applied to a material of a known constraint condition, then the equilibrium stretch ratio, $\tilde{\lambda}$, can be found by comparing x_2 before and after charging. Based on this, it is possible to determine directly the stress in the x_1 direction, due to the Maxwell stress using the stress equations above. In the absence of experimental data, another approach involves linearly interpolating $\tilde{\lambda}$ based on the stretch ratios of the limiting cases, $\tilde{\lambda}_c, \tilde{\lambda}_u$ where $\tilde{\lambda}_c = 1$ and $\tilde{\lambda}_u$ is found using the technique described in the previous section. Once the interpolated $\tilde{\lambda}$ is found, it is returned back to the stress equations, where the hydrostatic pressure is found using (3.67c) to be: $p = 2\frac{1}{\tilde{\lambda} + (1-\tilde{\lambda})\kappa}\tilde{\Gamma} - \sigma_M$ which results in the following description of the effective Maxwell stress in the x_1 direction:

$$\sigma_{1M} = 2\left(1 - \frac{1}{\tilde{\lambda} + (1-\tilde{\lambda})\kappa}\right)\tilde{\Gamma} + \sigma_M \tag{3.68}$$

where $\tilde{\Gamma}$ and σ_M are defined in eq. (3.67) above. As the first method requires additional information which was not available, the alternate method was utilized, and eq. (3.68) was used to find σ_{1M}, the stress generated in the x_1 direction as a function of the Maxwell stress.

Electromechanical stretch ratio coupling

When a DE device is undergoing a uniaxial strain in the x_1 direction in addition to the Maxwell stress, the total stress can be determined based on the combined effects of both the mechanical stress (section 3.3) and the Maxwell stress (section 3.4.3). For the general uniaxial thin film DE in tension experiencing constant charge, the Maxwell stress is determined based on the geometry resulting from the product of the stretch ratios.

$$\sigma_M = -\frac{1}{\varepsilon}\left(\frac{Q}{x_{10}x_{20}}\frac{1}{\lambda_1\tilde{\lambda}_1\lambda_2\tilde{\lambda}_2}\right)^2 \tag{3.69}$$

where the stretch ratios are determined based on the constraint conditions of the devices. The electromechanically coupled Maxwell stress formulations will be discussed here for the limiting cases.

Constrained Maxwell stress

Recalling that the stress is equivalent in the x_1 and x_3 directions for the fully constrained case ($\kappa = 1$), the product of the stretch ratios is $\lambda_1\tilde{\lambda}_1\lambda_2\tilde{\lambda}_2 = \lambda \times 1 \times 1 \times 1$, and the effective Maxwell stress in the x_1 direction becomes:

$$\sigma_{1M} = -\frac{1}{\varepsilon}\left(\frac{Q}{x_{10}x_{20}\lambda}\right)^2 = -\frac{1}{\varepsilon}\left(\frac{Q}{x_{10}x_{20}}\right)^2\frac{1}{\lambda^2} \quad \text{(Constrained)} \tag{3.70}$$

This result may at first seem counter-intuitive, as it appears to contradict the original description of Maxwell stress as a function of voltage: $\sigma_M = -\varepsilon\left(\frac{V\lambda}{x_{30}}\right)^2$. However, it is important to note that in the constant charge case, the voltage itself is not constant, but rather, is varying inversely to λ^2. Therefore when the charge is kept constant, the reduction in voltage due to the stretch results in a net increase in the effective Maxwell stress [125]. Once the effective Maxwell stress is found, the total stress in the x_1 direction becomes the sum of the mechanical stress and the effective Maxwell stress.

Unconstrained Maxwell stress

When the product of the stretch ratios for the unconstrained condition, $\lambda_1\tilde{\lambda}_1\lambda_2\tilde{\lambda}_2 = \lambda\times 1\times\frac{1}{\sqrt{\lambda}}\times\tilde{\lambda}$, is utilized, the Maxwell stress is found in the x_3 direction:

$$\sigma_M = -\frac{1}{\varepsilon}\left(\frac{Q}{x_{10}x_{20}\sqrt{\lambda}\tilde{\lambda}}\right)^2 = -\frac{1}{\varepsilon}\left(\frac{Q}{x_{10}x_{20}}\right)^2\frac{1}{\lambda\tilde{\lambda}^2} \quad \text{(Unconstrained)} \tag{3.71}$$

This term now specifies the Maxwell stress perpendicular to the mechanical motion, and the stretch ratio due to the effect of the Maxwell stress, $\tilde{\lambda}$, will need to be found in order to determine the effective Maxwell stress in the x_1 direction. As described previously, this can be accomplished in the unconstrained case based on the condition that the stress in the x_2 direction is zero utilizing eq. (3.64b). Once the equilibrium stretch ratio due to the Maxwell stress , $\tilde{\lambda}$, is found, the effective Maxwell stress in the x_1 direction can be determined.

General Maxwell stress

When the product of the stretch ratios for the unconstrained condition are utilized,

$\lambda_1\tilde{\lambda}_1\lambda_2\tilde{\lambda}_2 = \lambda\times 1\times\sqrt{\frac{1+(\lambda-1)\kappa}{\lambda}}\times\left(\tilde{\lambda}+(1-\tilde{\lambda})\kappa\right)$, the Maxwell stress is found in the x_3 direction:

$$\begin{aligned}\sigma_M &= -\frac{Q^2}{\varepsilon\left(x_{10}x_{20}\lambda\times 1\times\sqrt{\frac{1+(\lambda-1)\kappa}{\lambda}}\times\left(\tilde{\lambda}+(1-\tilde{\lambda})\kappa\right)\right)^2} \\ &= -\frac{1}{\varepsilon}\left(\frac{Q}{x_{10}x_{20}}\right)^2\frac{1}{\lambda\left(1+(\lambda-1)\kappa\right)\left(\tilde{\lambda}+(1-\tilde{\lambda})\kappa\right)^2}\end{aligned} \tag{3.72}$$

This provides a comprehensive means for determining the Maxwell stress when the equilibrium stretch ratio due to the Maxwell stress, $\tilde{\lambda}$, is known (either experimentally or through estimation). Using σ_M and $\tilde{\lambda}$, the effective Maxwell stress in the x_1 direction, σ_{1M}, can be found directly from eq. (3.64a). Once stresses due to both the mechanical strain and the electrical charge are known, the total stress in the x_1 direction is found as the sum of the mechanical stress, $\sigma_{1(mech)}$, and the effective Maxwell stress, σ_{1M}:

$$\sigma_1 = \sigma_{1(mech)} + \sigma_{1M} \tag{3.73}$$

3.4.4 Experimental Measurements of force due to Maxwell stress

The experimental measurement of the force in the x_1 direction generated by the Maxwell stress was performed using the test stand described in section 3.2.2. In order to charge the DE device to the required voltage, a power supply circuit was developed to provide up to 3500 V of electricity to the DE device, and then discharge the device while measuring the power dissipated. The following section describes the power supply circuit, its control and the results of the measurements.

A simple schematic of the circuit used to supply the high voltage power and control the discharge is compared in Figure 3.25 with the hardware used(the DE capacitor is shown in the

middle of the circuit diagram, but not shown in the image of the actual circuit). The power supply charges the DE capacitor when the first switch is closed, and discharges the capacitor when the second switch is closed.

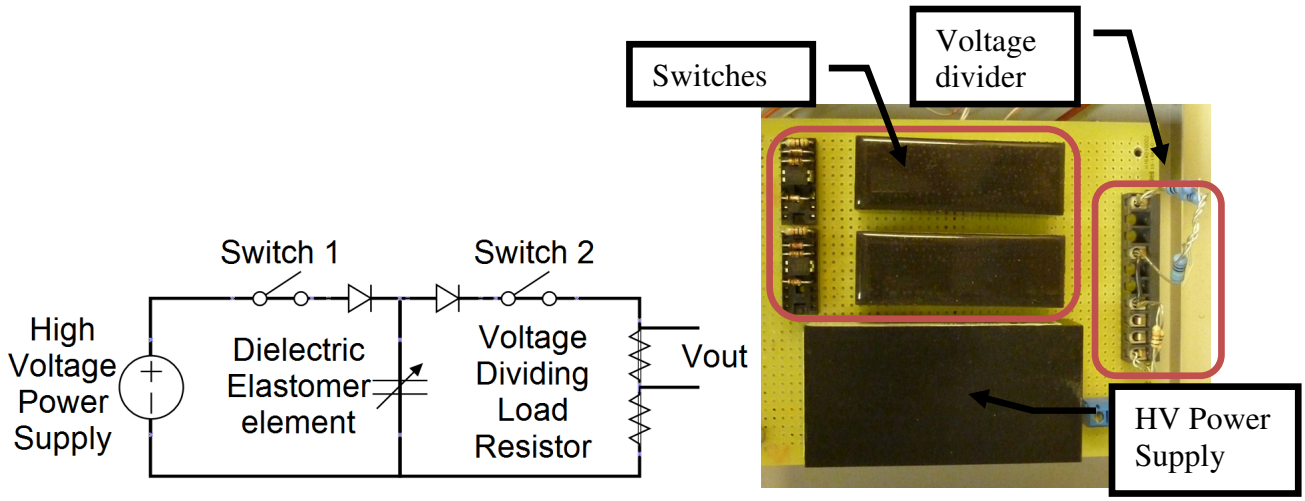

Figure 3.25: Energy harvesting circuit schematic and hardware.

In addition to the dielectric elastomer itself, this circuit contained three computer regulated high power devices which: a high voltage power supply, and two switches. A voltage divider was also included in order to output a low voltage signal related to the discharge voltage. This signal was collected by the DAQ board through LabVIEW. The resistances used for the voltage divider could be changed between tests, and were selected based on the maximum voltage discharge expected. Each of the components of the circuit were carefully selected to be able to withstand the high voltage requirements of the DE harvester.

The high voltage power supply was calibrated by comparing the input voltage to the power supply with its voltage output. The power supply response was found to be linear according to the following calibration curve: $V_{Signal\,in} = 0.0011 V_{HVout} + 0.0073$. This curve was used to control the voltage input signal to the circuit based on a desired voltage profile by a LabVIEW VI which was imbedded in the operating code for the entire test setup (see Appendix C for LabVIEW code).

Using this test stand, the force in the x_1 direction as a result of the Maxwell stress was determined by measuring the force required to stretch the film to a specified stretch ratio when it was both uncharged and charged. The force generated as a result of the Maxwell stress was found by measuring the change in the forcing the x_1 direction as a result of the electrical loading, as demonstrated in Figure 3.26.

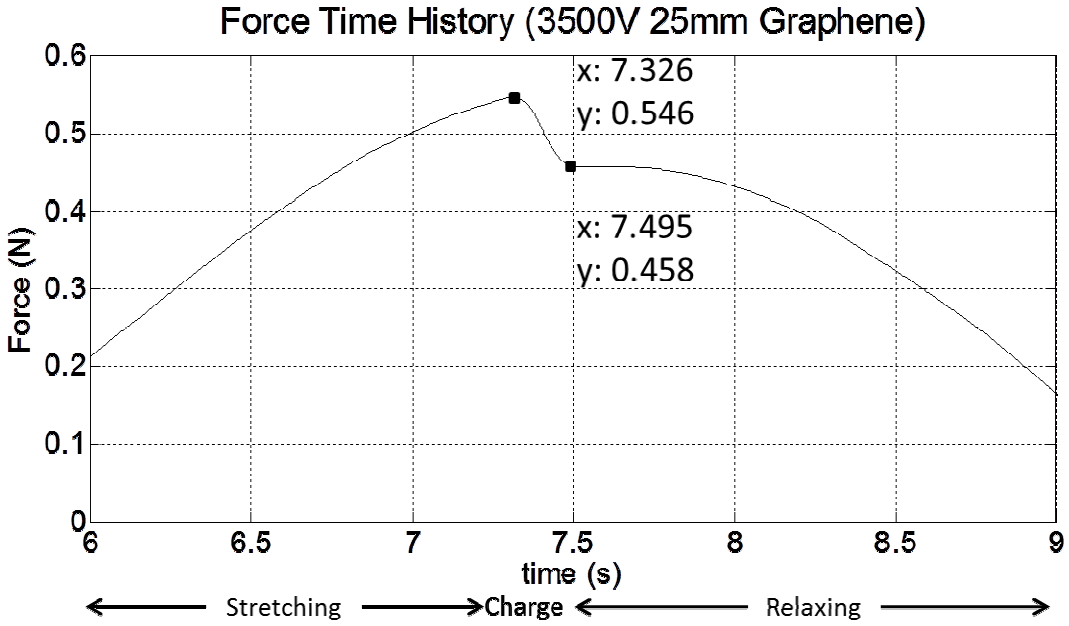

Figure 3.26: Measured force in x_1 direction due to Maxwell stress.

As expected, the Maxwell stress generated across the surface in the x_3 direction resulted in a decrease in the tension measured in the x_1 direction. This was caused by the relaxing of the material in the x_1 and x_2 directions as the material was squeezed together in the x_3 direction. Comparison of the Maxwell stress modeled using eq. (3.72) and measured experimentally is found in Table 3.3.

Table 3.3: Comparison of calculated and measured force generated in x_1 direction from Maxwell stress due to charge.

Device Properties				Force induced by Maxwell stress (N)			
				Predicted			Experimental
DE electrode material	Charge voltage (V)	Boundary coefficient K	λ	our model	K=0	K=1	
Graphene	3500	0.169	1.50	0.077	0.034	0.473	0.088
Carbon Grease	3500	0.230	1.60	0.051	0.021	0.265	0.060
Polypower	3500	0.639	1.23	0.192	0.054	0.304	0.130
Polypower	2250	0.639	1.23	0.070	0.024	0.127	0.0718

In this table, the force estimated by the modified hyperelastic model using the measured κ value is shown along with the force estimated using the limiting cases. When these predicted values are compared with the measured force generated for each material, the results demonstrate the importance of the constraint condition in the hyperelastic DE model. When the unconstrained boundary condition is assumed, the force generated by the Maxwell stress is consistently underestimated, and when the constrained case is assumed, the force is greatly over estimated. Without the boundary condition effects incorporated into the model, the effects of the Maxwell stress cannot be accurately estimated.

The charge and discharge loading duration is another important behavior issue for the DE material. Although the electrical time constant for the material is fairly small (around $\tau = 1e^{-4}s$ for carbon grease and graphene, and as small as $\tau = 1e^{-6}s$ for PolyPower), the mechanical behavior of the material still exhibited a time delay between loading and full application of the effective Maxwell stress, see Figure 3.26.

This charging lag was observed both for the uniaxial thin film devices as seen above, and for the devices attached to the knee joint which will be discussed in section 4.4.2. This behavior was observed in all three different electrode materials investigated. For single layer thin film DE devices on the uniaxial tests stand, the lag was observable both on the force time history

curves and on slow motion video of the material. It was measured to be between 0.16-0.18 s for each materials. Both the force generated as a result of an electrical charge on the DE material, and the time lag measured experimentally will be incorporated in to the model of the device behavior presented in section 4.4.

3.4.5 Energy Harvesting Calculations

Using the experimentally validated electromechanical model, the Maxwell stress equation (3.72) will now be applied to the constant charge DE energy harvesting cycle in order to calculate its energy harvesting capability. As described in section 2.2.2, a dielectric elastomer stores elastic mechanical energy when stretched. If that DE experiences an electric field while stretched, then during relaxation a portion of the stored mechanical energy is converted into electrical energy through the electrostatic behavior of the device. This electrical energy can then be collected and stored for use in other applications. The following section demonstrates how the energy harvested by the Maxwell stress (the difference between the electrical energy before and after relaxation) can be determined based on the DE material properties and operating procedure.

Description of the energy harvesting cycle

DE energy harvesting can be accomplished using a constant electric field, a constant voltage, a constant current or a combination of the three. The constant current method is most straightforward to perform, and as it was used exclusively throughout this research, it is described in detail here. The constant current DE energy harvesting cycle begins with the DE device pre-stretched to an initial configuration (Figure 3.27 a). When the mechanical stretch is applied (Figure 3.27 b), the capacitance increases based on the geometric changes to the dielectric, $C = \varepsilon \frac{A}{x_3}$. At this point (Figure 3.27 c), a charge, $Q = CV$, is placed on the electrodes

of the device by an electric field, *E*. As described in equations 3.56 and 3.58, the induced Maxwell stress due to this charge can be written either in terms of charge, voltage or electric field:

$$\sigma_M = -\frac{1}{\varepsilon}\left(\frac{Q}{x_{10}x_{20}\lambda_1\lambda_2\tilde{\lambda}_1\tilde{\lambda}_2}\right)^2 = -\varepsilon\frac{V_c^2}{x_{30}\lambda_3\tilde{\lambda}_3} = -\varepsilon E^2 \tag{3.74}$$

where x_{30} is the initial thickness of the dielectric, λ_3 is the stretch ratio of the thickness of the dielectric polymer, and V_c, is the voltage applied across the DE film at maximum stretch, $V_c = \frac{x_3}{\varepsilon A}Q$. At this point (Figure 3.27 d), the capacitor is discharged, allowing the excess charge to flow into an external storage device such as a battery or capacitor.

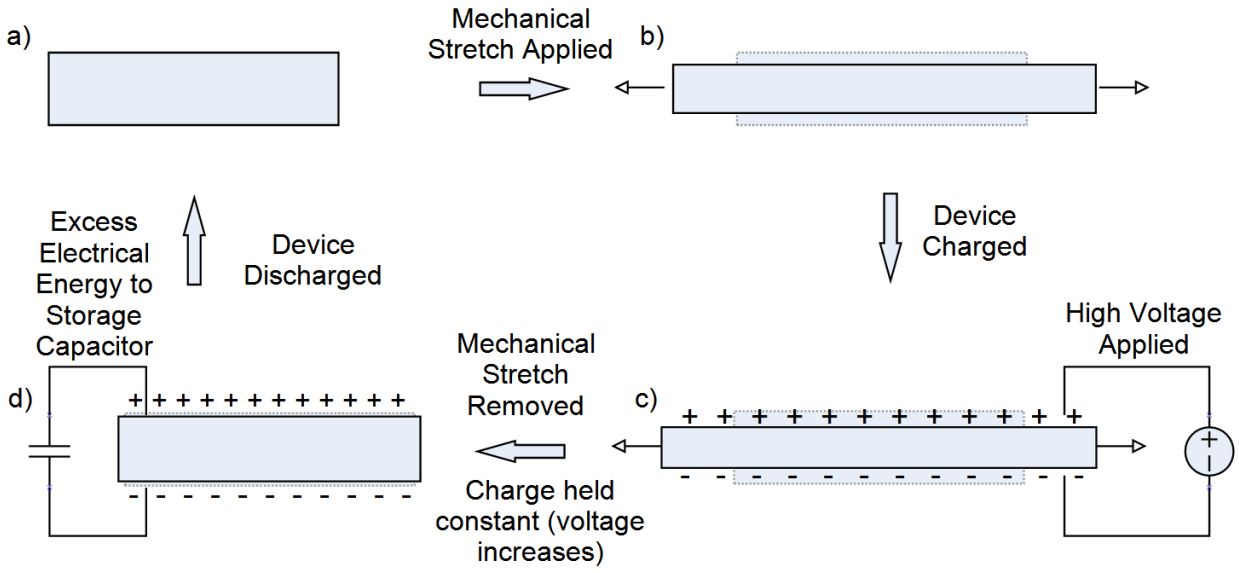

Figure 3.27: DE energy harvesting cycle

Figure 3.28 provides a comparison of the electric field generated across the DE capacitor for each of the states described. As can be seen, the constant charge method results in an increase in the electric field as the device relaxes from state **c** to state **d**.

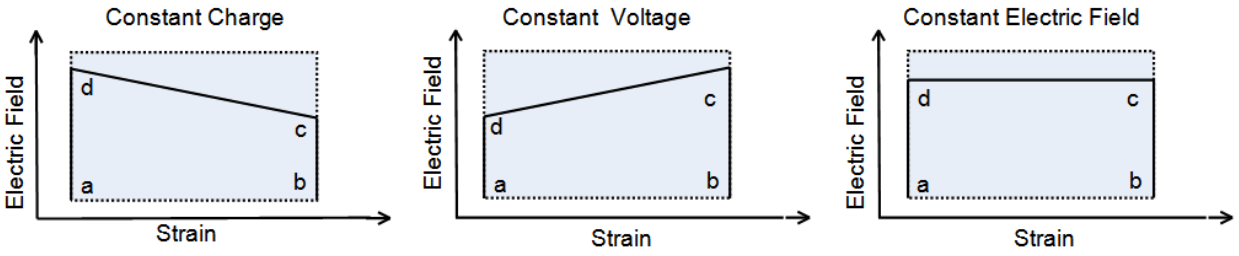

Figure 3.28: Electric field profile for different electrical loading conditions

This electric field variation directly affects the Maxwell stress generated in the x_3 direction of the DE as described in eq. (3.74). A sketch of how the Maxwell stress varies as a function of stretch ratio during the harvesting cycle in Figure 3.29 includes both the increase in the electric field as the DE is relaxed (c→d) and the decrease as the device is discharged (d→a).

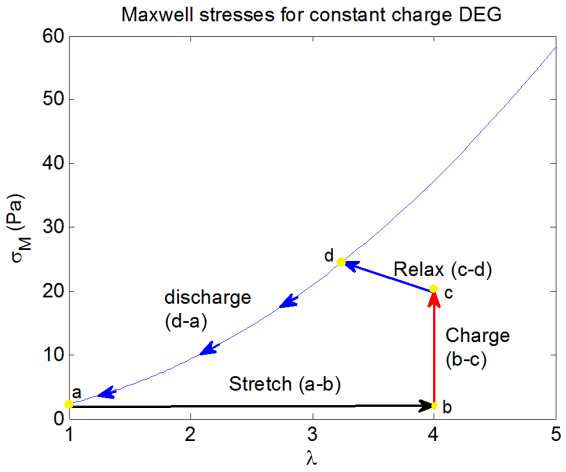

Figure 3.29: Maxwell stress during constant current energy harvesting cycle.

Observation of the changes in the Maxwell stress provides insights into the behavior of the material due to the energy harvesting process. The initial state of the material is specified by the pre-load which is placed on the DEG. During the mechanical stretching phase (a→b), there is no charge across the capacitor, so the Maxwell stress is zero. When the capacitor is charged (b→c), the Maxwell stress increases according to the eq. (3.74), while the stretch ratio is held constant. Next, the stretch is released (c→d), and because the charge is held constant while the

material is relaxed to its original shape, the Maxwell generated between the electrodes increase due to the decrease in the surface area of the electrodes. As the material is discharged, the Maxwell stress decreases along the equilibrium curve of the material, as seen in Figure 3.29, causing further increase in the thickness of the material, and subsequent reduction in the capacitance until the material returns to its original equilibrium state.

Operational maps of DE energy harvesting

The amount of energy harvested using a DEG depends on the material properties of both the elastomer and the electrodes, the electrical circuit configuration, and electrical and mechanical losses. When the energy harvesting states are mapped using either the mechanical or electrical work conjugate pairs described in section 3.4.1 mechanical or electrical conjugate pairs, an operational map of the energy harvesting process is generated. Figure 3.30 demonstrates the use of operational maps to quantify the constant charge DE energy harvesting cycle, where the states (a,b,c,d) refer to the states shown in Figure 3.27.

These operational maps demonstrate the electromechanical behavior of the device, where the extension / force and charge / voltage planes represent equivalent operations, and points on the mechanical plane can be mapped to corresponding points on the electrical plane.

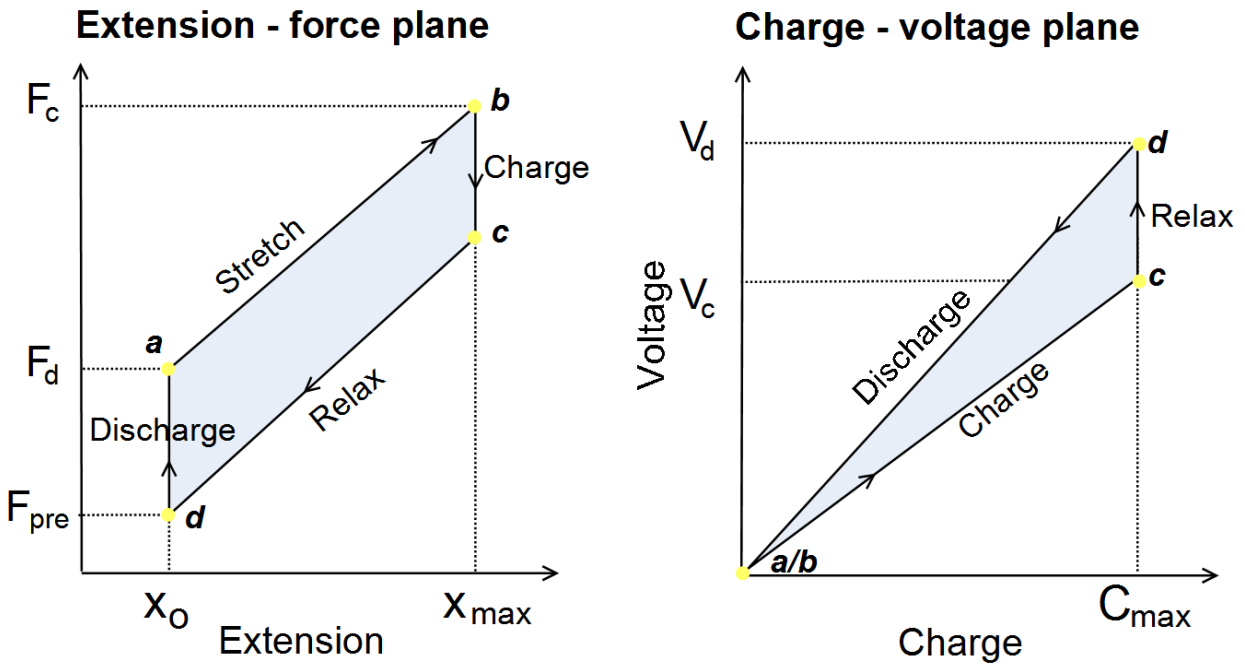

Figure 3.30: Operational maps for constant charge energy harvesting

Since each of these operational maps describes the behavior of work conjugate pairs, the work done on the system during one cycle is the area within the curve. The clockwise path of the harvesting cycle on the extension / force plane demonstrates the total mechanical work which is performed on the system and the counter clockwise path on the charge / voltage plane demonstrates the electrical work removed from the system [122]. In a perfect operating cycle, with no losses, the area within each of these curves should be identical, indicating that all of the mechanical work is transformed into electrical energy.

Energy harvesting modeling

In the following section, derivation of the maximum energy harvesting capability for the constant charge configuration is demonstrated based on the stretch ratio definitions provided in section 3.2.2. Using the variables for thickness. x_3, and area, $A = x_1 x_2$, the electrical potential energy stored in a parallel plate capacitor is:

$$U_{elec} = \frac{x_3}{2\varepsilon A} Q^2 \tag{3.75}$$

An intuitive understanding of the effects of different parameters can be developed based on the derivative of this term [128], $dU_{elec} = \frac{x_3}{\varepsilon A} Q\, dQ + \frac{1}{2\varepsilon A} Q^2 dx_3 - \frac{x_3}{2\varepsilon A^2} Q^2 dA$. First, as the charge across the electrode is increased, more energy is required to place more like charges on the electrodes. Secondly, as the thickness increases, more energy is required to separate the unlike charges, and finally, the negative sign in the third term shows that the electrical energy will decrease with an increase in surface area, as similar charges are further away from each other

For the constant charge harvesting cycle, taking into account the incompressibility of the elastomer (ie, $x_3 A = 1$ and $A dx_3 + x_3 dA = 0$), the change in thickness can be written in terms of the change in area: $dx_3 = -\frac{x_3}{A} dA$, which allows the change in the electrical energy to be rewritten as:

$$dU_{elec} = -\frac{x_3}{\varepsilon A^2} Q^2 dA = -2U_{elec} \frac{1}{A} dA \text{, where } dQ = 0 \tag{3.76}$$

Since the charge is kept constant, the change in electrical potential energy is due solely to the mechanical change in the geometry of the device, which demonstrates the constant charge DE energy harvesting behavior described in Figure 3.28. The energy required to charge the device decreases during stretching due to the addition of mechanical energy, and during relaxation the charge is kept constant, so the mechanical energy which was stored in the device as a result of the stretch is converted into electrical energy as the like charges are forced closer together during the relaxation (c → d) via the Maxwell effect.

The maximum amount of energy harvested can be calculated by observing the increase in the electric potential energy of the capacitor as the material relaxes from point c to point d.

($U_{harvest} = -\Delta U = -(U_c - U_d)$) The relationship between the energy at charge (U_c) and at discharge (U_d) can be found by integrating both sides of the equation above [120], $\int_{U_c}^{U_d} \frac{1}{U_{elec}} dU_{elec} = -2\int_{A_c}^{A_d} \frac{1}{A} dA$ resulting in:

$$U_d = U_c \left(\frac{A_c}{A_d} \right)^2 \text{ or } U_c = U_d \left(\frac{A_d}{A_c} \right)^2 \tag{3.77}$$

As described earlier, the electric field will be at its maximum after relaxation (d), therefore, the energy at this point can also be described as:

$$U_d = \frac{x_3}{2\varepsilon A} Q^2 = \frac{1}{2} \varepsilon A x_3 E_{\max}^2 = \frac{1}{2} \varepsilon \forall E_{\max}^2 \tag{3.78}$$

where $\forall = x_1 x_2 x_3$ is the volume of the elastomer. This results in the following relationship for the theoretical maximum energy harvested as a function of the DE surface area at charge (A_c) and discharge (A_d):

$$U_{harvest} = \frac{1}{2} \varepsilon \forall E_{\max}^2 \left(1 - \left(\frac{A_d}{A_c} \right)^2 \right) \tag{3.79}$$

where the maximum electric field, $E_{\max}$, occurs at discharge. Recalling that $\sigma_M = -\varepsilon E^2$, the energy harvested can be rewritten in terms of the Maxwell stress at discharge and the stretch ratios due to both mechanical (λ) and electrical $(\tilde{\lambda})$ strain:

$$U_{harvest} = \frac{1}{2} \forall \sigma_M \left(1 - \left(\frac{\chi_{10}\chi_{20}\lambda_{1d}\lambda_{2d}\tilde{\lambda}_{1d}\tilde{\lambda}_{2d}}{\chi_{10}\chi_{20}\lambda_{1c}\lambda_{2c}\tilde{\lambda}_{1c}\tilde{\lambda}_{2c}} \right)^2 \right) = \frac{1}{2} \forall \sigma_M \left(1 - \left(\frac{\lambda_{1d}\lambda_{2d}\tilde{\lambda}_{1d}\tilde{\lambda}_{2d}}{\lambda_{1c}\lambda_{2c}\tilde{\lambda}_{1c}\tilde{\lambda}_{2c}} \right)^2 \right) \tag{3.80}$$

Substituting the general stretch ratios from eq. (3.29) and (3.66), results in the following general equation for the energy harvested as a function of

$$U_{harvest} = \frac{1}{2}\forall\sigma_{Md}\left(1-\frac{\lambda_d\left(1-\left(1-\lambda_d\right)\kappa\right)\left(\tilde{\lambda}_d+\left(1-\tilde{\lambda}_d\right)\kappa\right)^2}{\lambda_c\left(1-\left(1-\lambda_c\right)\kappa\right)\left(\tilde{\lambda}_c+\left(1-\tilde{\lambda}_c\right)\kappa\right)^2}\right) \tag{3.81}$$

Where the terms λ_c and λ_d are the mechanical stretch ratios at charge and discharge, the $\tilde{\lambda}_c$ and $\tilde{\lambda}_d$ terms are the stretch ratios due to the Maxwell stress at charge and discharge. The Maxwell stress, σ_{Md} is the stress at discharge, found using eq. (3.72) .

For each of the limiting constraint conditions eq. (3.81) becomes:

$$\text{constrained:} \quad U_{harvest} = \frac{\forall}{2\varepsilon}\left(\frac{Q}{x_{10}x_{20}\lambda_d}\right)^2\left(1-\left(\frac{\lambda_d}{\lambda_c}\right)^2\right)$$

$$\text{unconstrained:} \quad U_{harvest} = \frac{\forall}{2\varepsilon}\left(\frac{Q}{x_{10}x_{20}\sqrt{\lambda_d}\tilde{\lambda}_d}\right)^2\left(1-\frac{\lambda_d}{\lambda_c}\frac{\tilde{\lambda}_d^2}{\tilde{\lambda}_c^2}\right) \tag{3.82 a,b}$$

where Q is constant throughout the relaxation phase and can be determined by the charging voltage and λ_c and $\tilde{\lambda}_c$. For the fully constrained condition, this results in:

$$U_{harvest} = \frac{\forall\varepsilon}{2}\left(\frac{\lambda_c^2 V_c}{\lambda_d x_{30}}\right)^2\left(1-\left(\frac{\lambda_d}{\lambda_c}\right)^2\right) \tag{3.83}$$

providing an estimate of the energy harvested based solely on the material properties of the device, the charge and discharge stretch ratios and the initial voltage placed across the DE capacitor.

Experimental Results from energy harvesting

For mechanical stretch, the extension / force conjugate pair can either be modeled, or directly generated from the measured data. The electrical values necessary to generate a voltage / charge curve were not able to be measured with the test setup used, therefore, the electrical work conjugate curve is generated only using modeling of the voltage and charge based on the basic

electrical theories shown in section 3.4.2. These curves were developed using the modified Yeoh hyperelastic model which included the boundary coefficient for each material as listed in Table 3.1.

Figure 3.31 shows the work conjugate curves for each of the materials under investigation. On this figure, the operation map of a single energy harvesting cycle is plotted on both planes for carbon grease, graphene and Polypower materials. These figures include operational maps developed based on modeling (red lines) compared with the experimental results for the same operating conditions for the mechanical plane only (blue line).

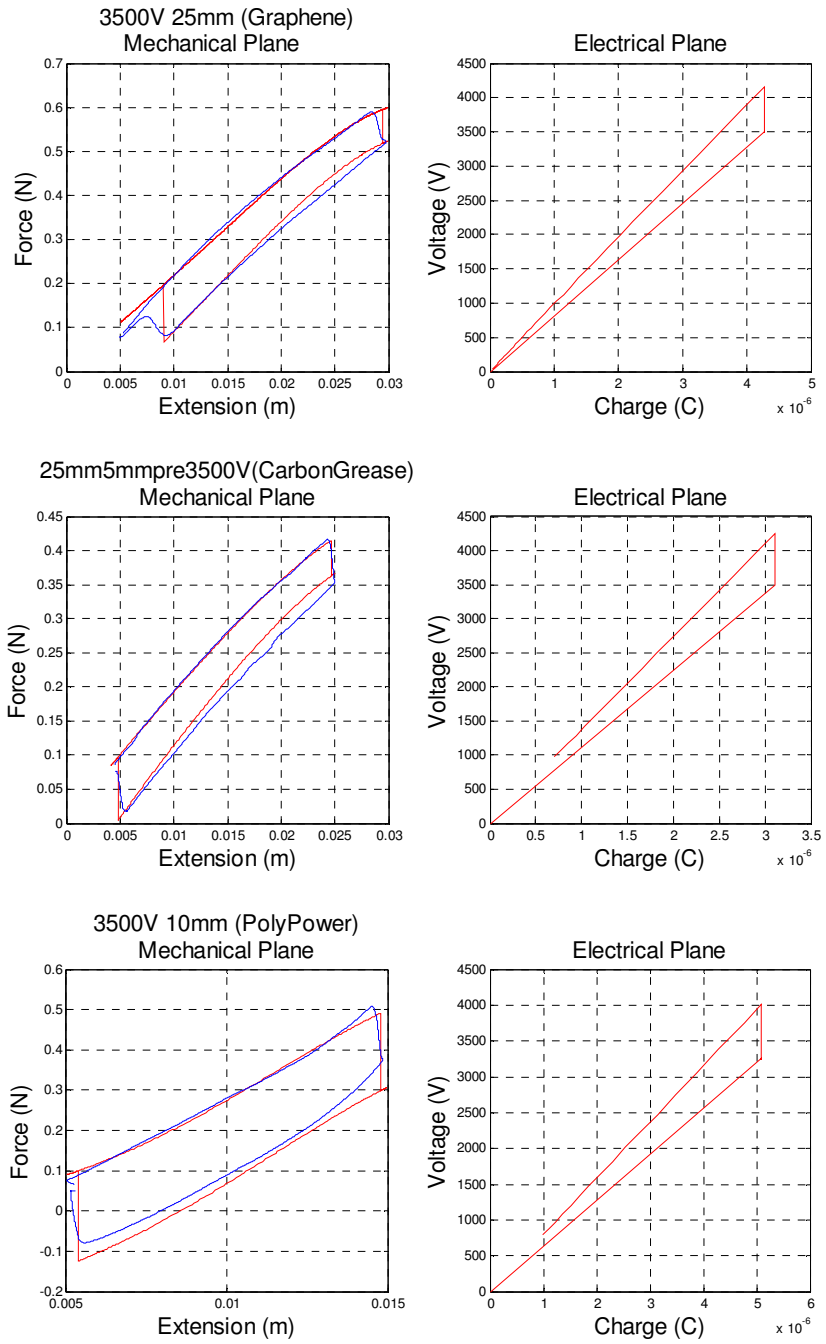

Figure 3.31: Operational maps of DE energy harvesting; red modeled, blue experimental

Utilizing these curves along with the modeling presented above, there are three theoretical methods and one experimental method for estimating the energy harvested by a uniaxial DE operating at a known strain and charge voltage. The first two methods utilize the

operation maps depicted in Figure 3.30, and include calculations based on the area within the mechanical or electrical conjugate pair maps. The third method is based on eq. (3.83). Comparison of the area within the modeled operational curves and the experimental measurements of work for each device is provided in Table 3.4.

Table 3.4: Comparison of harvested energy (J): estimates and experimental results

DE Material	λ	Calculated (mJ)			Experimental (mJ)
		Operational Map		U_h Estimate	force / displacement
		force / displacement	charge / voltage		
Graphene	1.5	2.051	1.476	1.101	2.412
Carbon Grease	1.6	1.372	1.169	0.734	1.678
Polypower	1.23	1.947	1.958	1.493	1.735
Polypower (2250V)	1.23	0.707	0.838	0.545	0.843

It is important to note when comparing these results that each material experienced a different stretch ratio. In the case of the carbon grease, this was due to a slightly different size film length and for the Polypower, this was due to mechanical limitations of the device that limited the maximum strain of the device to 15% (recommended for long life application) to 30% (failure expected after small number of cycles). Although its stretch ratio is nearly 30% less than that of graphene or carbon grease, as demonstrated in Table 3.3, the Polypower generates a larger Maxwell stress, therefore, the energy harvested in case is fairly similar. For each material, the energy harvest estimate from eq. 3.82 slightly underestimates the actual energy which is removed from the system as measured by the area within the experimental force / displacement curve, however the comparison of the force displacement operational maps shows a close correlation between the experimental and modeled curves. The available electrical energy for collection can also be determined by observing the discharge curve for the DE device when it does not

experience any mechanical stretch compared to the discharge curve for the same DE device when it has undergone a mechanical stretching and relaxation cycle.

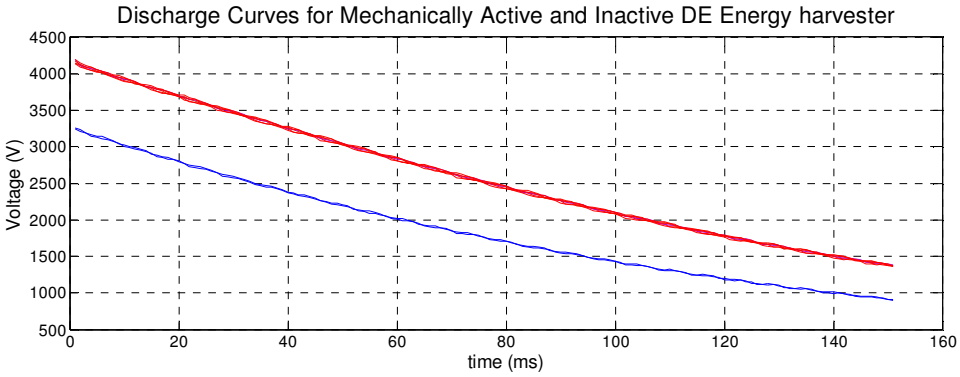

Figure 3.32: Comparison of discharge curve for graphene DE energy harvester charged at 3500V without mechanical stretch (blue) and with 25 mm of mechanical stretch (red)

Discharge curves such as these serve to confirm that the electromechanical energy conversion which is measured from the mechanical side does in fact result in a subsequent increase in the electrical energy in the circuit which is available for storage and use in other electrical applications such as those described in Table 1.3.

3.5 Summary

Based on both the mechanical and electrical principles of a dielectric elastomer, a model was developed for a uniaxial thin film which incorporates the boundary conditions presented by the electrode material, the hyperelastic nature of the elastomer material and the electrostatic behavior of a variable capacitance thin film capacitor. This model was demonstrated for use with three different electrode materials on a similar dielectric elastomer.

This novel modeling of the boundary constraint imposed on the dielectric elastomer due to its composite nature provides a means to distinguish between different electrode materials when modeling the electromechanical behavior of the device. This modeling also provides a means to theoretically describe the effect of mechanically modifying a DE device in order to

produce a larger boundary constraint condition, and therefore increase the energy harvesting capability [129].

In the following chapter, the model developed will be applied to the investigation of the effects of energy harvesting on both a uniaxial thin film DE energy harvester and a DE harvester located across the knee joint.

4 Mechanical behaviors induced by DE energy harvesting

4.1 Introduction

Damping within a structure results from the removal of energy from the system. This energy removal can occur through numerous means, most often it is the result of dissipation to the environment in the form of sound, mechanical plastic deformation, chemical process, etc. resulting in heat dissipation, which can lead to wasted energy and undesirable consequences. For energy harvesting applications, the structural damping of the system can also be altered by the transformation of energy into another usable form through energy harvesting. The evaluation of the damping induced by energy harvesting was first introduced for piezoelectric devices in the works by Lesieutre [130] and Liang [131, 132], which were developed based on the analysis of structural damping resulting from dissipation due to shunt resistance circuits described by Hagood [133].

While many DE polymers, such as silicone, do not exhibit viscoelasticity themselves, and therefore, the hyperelastic models developed in section 3.3 do not contain an explicit damping term (see Appendix A for alternate time dependence modeling), when used as an energy harvester, it is necessary to quantify the damping effect on the material as a result of the energy harvesting. Several techniques for quantifying the damping induced by DE energy harvesters will be developed to identify the role energy harvesting plays in the dynamic behavior of a DE harvester.

The objective of this chapter is to examine the conceptual principles behind the behavior of hyperelastic DE energy harvesting and to develop an understanding of the fundamental relationship between the energy harvested and the mechanical damping induced by this energy conversion. In section 4.2 a means for describing the damping characteristics of hyperelastic

materials undergoing energy harvesting is developed first by reviewing viscous and hysteretic models for damping. For both of these models, stress strain relationship will be provided along with equivalent damping coefficients which can provide a means to model the damping in a standard equation of motion. After that, the use of rheological terms and dynamic mechanical analysis will be discussed with respect to DE energy harvesting. Finally, the *harvesting factor*, which is another damping quantification that was first used by Liang [131] will be introduced for use with DE energy harvesting.

Subsequent sections of this chapter will describe the empirical validation of a damping model for uniaxial DE energy harvesters, as well as development of a knee joint test stand which is used to demonstrate the Maxwell stresses and resulting stiffness and damping modifications due to the energy harvesting. Finally, an oscillation model will be described which quantifies the damping changes for the knee joint as it experiences controlled charge and discharge of a DE device in different positions and orientations. The tools developed in this chapter will then be applied to the human walking gait cycle in chapter 5, specifically investigating the kinetic effects of DE energy harvesting on the knee joint during the swing phase.

4.2 Review of damping models

4.2.1 Viscoelastic damping

Viscoelastic materials are those which behave both elastically (energy storage) and viscously (energy dissipation). The following section demonstrates the use of viscoelastic damping in modeling the behavior of this type of material. The response of viscoelastic materials to cyclical loading is modeled using a stress / strain relationship which reflects both their elastic and viscous behavior. One of the simplest and most prevalent models of the stress strain behavior is the Kelvin–Voigt model, which represents the mechanical behavior using spring and dashpot

elements, working in parallel with one another. As such, it is comprised of two material terms, the first describing the stiffness of the material (Young's modulus), E, which is proportional to strain, and the second describing the damping, E^*,which is proportional to the strain rate:

$$\sigma = E\varepsilon + E^* \frac{d\varepsilon}{dt} \tag{4.1}$$

This simple model is able to characterize the behavior of many linear viscoelastic materials, and for more complex systems involving nonlinear performance, higher order spring and damping terms may be incorporated into the model for improved results.

In the case of viscoelastic damping, the velocity-dependent damping of the material response is represented by a damping force which is the product of the damping coefficient, c, and the extension rate, $\dot{x}$:

$$d_v = c\dot{x} \tag{4.2}$$

The behavior of the system associated with DE energy harvesting can thus be quantified through the addition of the damping coefficient into the equation of motion.

$$m\ddot{x} + c\dot{x} + kx = f(t) \tag{4.3}$$

which, using standard notation can be written in terms of the damping ratio, ζ, and natural frequency, ω_n, $\ddot{x} + 2\zeta\omega_n\dot{x} + \omega_n^2 x = \omega_n^2 u(t)$.

Energy methods can be used to relate the equivalent damping term to the DE harvesting parameters, following the method presented by Graf [134], who investigated a piston style DE harvester – damper. The amount of energy dissipated through conventional damping of an oscillating system in terms of c can be written by integrating the damping force with respect to displacement, the damping power, $P_v = d_v \cdot \dot{x}(t)$ over one cycle:

$$U_D = \oint P_v \, dx = \int_0^{\frac{2\pi}{\omega}} d_v \dot{x} \, dt = \int_0^{\frac{2\pi}{\omega}} (c\dot{x})\, \dot{x} \, dt \tag{4.4}$$

When this is evaluated assuming a harmonic response, $x = \mathrm{x}_0 \cos(wt + \phi)$, the damping energy for one cycle is:

$$U_D = \pi c \omega \mathrm{x}_0^2 \tag{4.5}$$

Equating the damping energy over one cycle with the harvested energy from eq. 3.82:

$$U_D = U_{harvest} \quad \Rightarrow \quad \omega \pi c \mathrm{x}_0^2 = \frac{1}{2} \varepsilon \forall E_{\max}^2 \left(1 - \left(\frac{A_d}{A_c}\right)^2\right) \tag{4.6}$$

results in a relationship for the equivalent damping coefficient due to DEG energy harvesting:

$$c = \frac{\varepsilon \forall E_{\max}^2}{2\omega \pi \mathrm{x}_0^2} \left(1 - \left(\frac{A_d}{A_c}\right)^2\right) \tag{4.7}$$

The damping induced by DEG energy harvesting depends on the material properties: the permittivity and the total volume as well as operating conditions such as: the maximum electric field and the ratio of maximum to minimum area of the device. It is also inversely proportional to the frequency of oscillation, ω, indicating that c will decrease for larger frequencies.

4.2.2 Hysteretic damping

Unlike the viscoelastic analysis above, many materials exhibit an internal damping which is not frequency dependent. Modeling of this behavior requires an alternate method of characterizing the damping. The following section will describe a hysteretic damping model which is regularly used in the analysis of frequency independent damping.

Materials which exhibit both energy storage and energy dissipation, but do not show evidence of a frequency dependent response can be modeled using a hysteresis model which is similar to the Kelvin–Voigt model, where the damping is proportional to the frequency of loading:

$$\sigma = \mathrm{E}\varepsilon + \frac{\tilde{\mathrm{E}}}{\omega}\frac{d\varepsilon}{dt} \tag{4.8}$$

Employing an approach similar to the modeling of viscous damping, an equivalent hysteretic damping term can also be found. However, unlike viscoelastic damping, the damping force is inversely proportional to frequency, ω. Defining the hysteretic damping coefficient as: $h = \omega c$, results in the following damping force:

$$d_h = \frac{h}{\omega}\dot{x} \tag{4.9}$$

The damping associated with DE energy harvesting can be quantified through the addition of the damping coefficient into the equation of motion.

$$m\ddot{x} + \frac{h}{\omega}\dot{x} + kx = f(t) \tag{4.10}$$

If this is compared with standard notation for viscous damping, $\ddot{x} + 2\zeta\omega_n\dot{x} + \omega_n^2 x = \omega_n^2 u(t)$, an equivalent damping ratio, ζ_h, can be written in terms of the damping coefficient: $\zeta_h = \frac{h}{2\omega_n \omega m}$.

Utilizing the relationship between the natural frequency and the stiffness, $k = m\omega_n^2$, and assuming oscillation at the natural frequency, $\omega \cong \omega_n$, the damping ratio can be expressed as:

$$\zeta_h = \frac{h}{2k} \tag{4.11}$$

where the damping coefficient, h, can be found from experimental measurements, or estimated based on the DE energy harvesting parameters.

Just as with the viscoelastic model, the damping effects due to energy harvesting can be quantified based on the energy harvested for a single cycle. When the damping hysteretic force is used, the relationship for the hysteretic damping coefficient due to DEG energy harvesting becomes:

$$h = \frac{\varepsilon \forall E_{\max}^2}{2\pi x_0^2}\left(1-\left(\frac{A_d}{A_c}\right)^2\right) \tag{4.12}$$

As expected, for hysteretic damping models, the damping induced by DEG energy harvesting is independent of the frequency of oscillation, and depends only on device material properties and geometry.

Utilizing the technique developed in section 3.4.5, the general form of the damping coefficient for the uniaxial DE harvester written in terms of the boundary constraint coefficient, κ, is:

$$h = \frac{\varepsilon \forall E_{\max}^2}{2\pi x_0^2}\left(1-\frac{\lambda_d\left(1-\left(1-\lambda_d\right)\kappa\right)\left(\tilde{\lambda}_d+\left(1-\tilde{\lambda}_d\right)\kappa\right)^2}{\lambda_c\left(1-\left(1-\lambda_c\right)\kappa\right)\left(\tilde{\lambda}_c+\left(1-\tilde{\lambda}_c\right)\kappa\right)^2}\right) \tag{4.13}$$

For the two limiting conditions of interest for the uniaxial DE, fully constrained $\kappa = 1$ and unconstrained $\kappa = 0$, the hysteretic damping coefficient becomes:

$$\begin{aligned} h_C &= \frac{\varepsilon \forall E_{\max}^2}{2\pi x_0^2}\left(1-\left(\frac{\lambda_d}{\lambda_c}\right)^2\right) \\ h_U &= \frac{\varepsilon \forall E_{\max}^2}{2\pi x_0^2}\left(1-\frac{\lambda_d}{\lambda_c}\left(\frac{1}{\tilde{\lambda}_c}\right)^2\right) \end{aligned} \tag{4.14}$$

This formulation provides the ability to estimate the damping of a DE energy harvester based completely on the DE material and operating parameters.

4.2.3 Rheology (dynamic mechanical analysis)

The hysteretic damping model described above can be further developed through the use of Dynamic Mechanical Analysis (DMA). DMA uses the rheological (flow) properties of solids over a wide range of operating conditions (temperature and frequency) to describe the elasticity and damping of the material.

Elastic materials respond immediately to an applied stress, resulting in a stress response that is in phase with the applied stress. Purely viscous materials respond very differently to an applied stress, resisting the strain linearly with time, resulting in a strain response to an applied stress that is 90° out of phase. When a viscoelastic material undergoes sinusoidal loading there will be a temporal phase shift, Δt, between the input and the response of the material. This phase shift will lie between 0 and 90°, depending on whether the elastic or viscous behavior of the material dominates. An example of this behavior is seen in the time history stress and strain curves in Figure 4.1. Measurement and analysis of this phase shift is the basis of dynamic mechanical analysis.

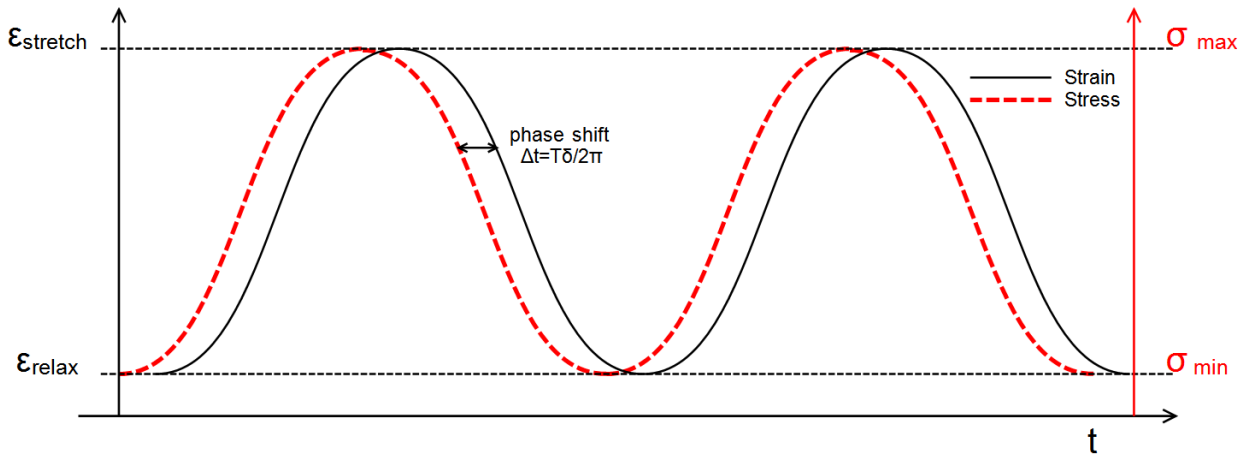

Figure 4.1: Scaled stress and strain time history curves for viscoelastic material

For a given stress, $\sigma(t) = \sigma_0 \sin(2\pi\omega t)$, the strain can be written in terms of the phase angle, δ, $\varepsilon(t) = \varepsilon_0 \sin(2\pi\omega t - \delta)$. Therefore, the relationship between the phase shift and the phase angle becomes: $\delta = \Delta t \omega = \frac{2\pi\Delta t}{T}$. The phase angle (also known as the loss angle) provides a dimensionless measure of the viscoelastic damping of a material, and the tangent of this angle, $\tan\delta$ is often used to describe the internal or "mechanical damping" of a system. For example a completely elastic solid will exhibit no phase shift regardless of the frequency, resulting in

$\tan\delta = 0$, and on the opposite end of the spectrum, a liquid will have an increasingly large phase shift as the frequency increases, leading to $\tan\delta \to \infty$. Modeling of hysteretic damping described in the previous section can be used in conjunction with the phase shift measurements to quantify the damping of the material.

As in the hysteretic model, the damping is proportional to the frequency of loading:

$$\sigma = \mathrm{E}\boldsymbol{\varepsilon} + \frac{\tilde{\mathrm{E}}}{\omega}\frac{d\boldsymbol{\varepsilon}}{dt} \tag{4.15}$$

When a sinusoidal input of frequency ω is considered, eq. 4.8 results in a damping coefficient that is no longer proportional to velocity, but rather acts similarly to a force that is proportional to the displacement while still being in phase with the velocity:

$$\sigma = \left(\mathrm{E}' + i\mathrm{E}''\right)\boldsymbol{\varepsilon} \tag{4.16}$$

resulting in a complex stiffness, E^*, in which the real part, E', corresponds to the energy storage of the material and the imaginary part, E'', relates to the energy loss of the material (note that the primes distinguish terms and do not denote derivatives). The phase shift can be represented using a complex stiffness term, $\mathrm{E}^* = \mathrm{E}' + i\mathrm{E}''$, which is written in terms of the storage modulus, E', and the loss modulus, E''. The loss angle and the stiffness are related to one another by the ratio of the loss modulus over the storage modulus:

$$\tan\delta = \frac{\mathrm{E}''}{\mathrm{E}'} \tag{4.17}$$

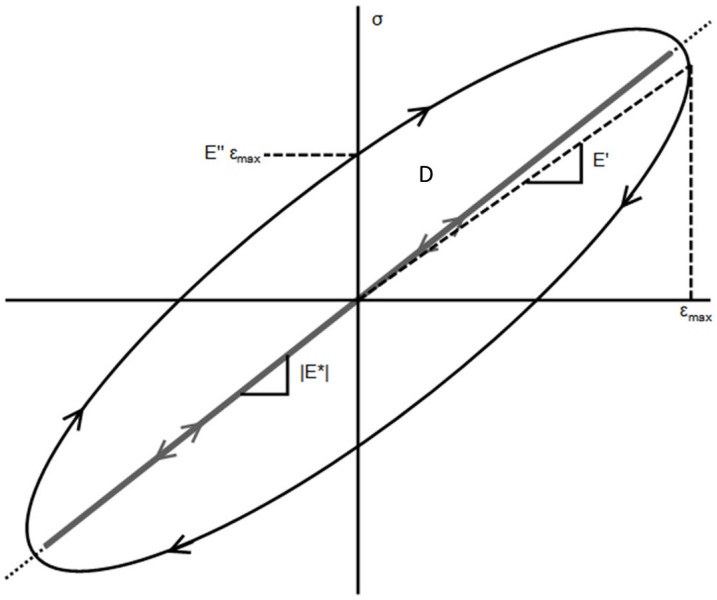

Figure 4.2: Stress vs. strain for linear viscoelastic material undergoing oscillatory load [135].

The stress strain diagram in Figure 4.2 provides some insight in to the nature of hysteresis damping and how it relates to rheological material properties. In purely elastic materials (represented by the gray line), the stress strain curve of a material undergoing cyclical loading within the elastic range follows an identical loading and unloading path; however in materials with internal damping (the black curve), the loading and unloading paths of the stress strain curve are different. The difference between the loading and unloading paths demonstrates that not all of the energy added to the system during loading is recoverable during unloading as it would be for a completely elastic material, and the area within the curve, often referred to as D, is equivalent to the unrestored energy or energy dissipation.

The components of the complex stiffness can be determined from the curve shown in Figure 4.2 as well. The magnitude of the complex stiffness, $|E^*|$, is simply the slope of the line drawn through the tips of the curve. The storage modulus, E', denoting the energy stored elastically within the material, is the slope of the line drawn from the origin to the maximum

strain. Finally, the loss modulus is related to the maximum strain at the initial stress: $\sigma(0) = \boldsymbol{\varepsilon}_{\max} \mathrm{E}''$ [135].

Through the use of time history and the stress strain curves, it is possible to develop a description of the mechanical damping occurring within a viscoelastic material. Measurements of this type are often performed over a range of frequencies and temperatures to get a full picture of the material behavior. Dynamic mechanical analysis (DMA) involves the measurement of E' and $\tan\delta$ over a specified frequency and/or temperature range, and provides a means to characterize the damping and the elasticity of a material over a wide range of operating conditions [136].

The complex stiffness is also commonly written in terms of the loss factor, η, as such: $m\ddot{x} + k(1 + i\eta)x = 0$. In traditional electromechanical systems without energy harvesting, the loss factor is equivalent to the dissipation factor, η_d. With the introduction of energy harvesting, the loss factor must also include the energy collected from the system by the harvester. In order to quantify the damping induced by energy harvesting, Liang and Liao [132] developed the *energy harvesting factor*, η_h, which is similar in form to the loss factor in that it defines the ratio of energy removed from the system relative to the overall energy stored in the system:

$$\eta_h = \frac{\Delta U_h}{2\pi U_{\max}} \tag{4.18}$$

where the distinction from η_d is that the ΔU_h describes the energy harvested from the system and stored for later use, rather than the energy that is dissipated.

By combining η_h with the energy dissipation term, the dissipation factor, η_d (eq. 4.20), the resulting damping associated with the system can be modeled as the superposition of η_h and η_d:

$$\eta = \frac{\Delta U}{2\pi U_{\max}} = \frac{U_h + U_d}{2\pi U_{\max}} = \eta_h + \eta_d \tag{4.19}$$

As the loss factor, η, describes the ratio of the energy removed from the system relative to the total energy in the system, it is equivalent to $\tan\delta$, eq (4.17), and can be related to the hysteresis curve:

$$\tan\delta = \eta = \frac{\Delta U}{2\pi U_{\max}} = \frac{D}{\pi \sigma_{\max} \varepsilon_{\max}} \tag{4.20}$$

where ΔU is the change in energy, or the energy lost during one cycle. Recall from Figure 4.2, that ΔU can be found from the total area within the stress/strain curve, D, and describes the amount of energy dissipated from the system. For systems with low levels of damping (generally, $\eta < 0.2$), there is an approximate relationship between the viscous damping ratio, $\tan\delta$ and the hysteretic loss factor: $\tan\delta = \eta = 2\zeta = \frac{h}{k}$. This relationship is not surprising as it embodies the original definition of the storage modulus, $\tan\delta = \frac{E''}{E'}$, but it does present a unique opportunity to define $\tan\delta$ in terms which will be found both experimental and analytically throughout this research. Additionally, this relationship provides an alternative description of the hysteretic damping coefficient which can be measured based on the stress strain curve for a single cycle:

$$h = \frac{Dk}{\pi \sigma_{\max} \varepsilon_{\max}} \tag{4.21}$$

where $k = E'$, and is found experimentally as the slope of the curve.

In summary, the concepts of oscillatory energy harvesting, hysteresis and rheology can be brought together, to develop both theoretical and empirical relationships for frequency independent damping as described in eqs. (4.13) and (4.21) respectively. By combining the

frequency independent equivalent damping coefficient from eq. (4.21) with the operation of a DE energy harvester, a theoretical framework for describing the energy harvesting of repetitive mechanical motion through cyclic electrical loading of dielectric elastomers is developed. Defining the energy harvesting damping coefficient in this way provides a means to describe the mechanical response of the system resulting from energy harvesting.

Recall that the purpose of this chapter is to describe the conceptual principles behind the behavior of hyperelastic DE energy harvesting in order to develop a relationship between the energy harvested and the mechanical damping induced by this energy removal. This will be accomplished by building on the background ideas presented, to generate a theoretical description of the stiffness and damping behavior of an active DE energy harvester. This will be accomplished first for a uniaxial thin film similar to that described in chapter 3, followed by a thin film DE harvester operating on a biofidelic knee joint ergometer.

Additionally, the performance of a knee joint energy harvester will be modeled and tested as it undergoes standard gait motion. Experimentation for this work utilizes a combination of the linear motor test stand previously described in chapter 3 and a biofidelic knee joint test stand which will be described in section 4.4. It has been found for the configurations investigated, that there is an observed change in both the stiffness and the damping behavior of the system as a result of this electromechanical coupling. For both configurations, the theoretical estimates of the damping from eq (4.12) are compared with the empirical values found using eq (4.21). Based on these results, the effect on the mechanical behavior due to the electromechanical coupling of the Maxwell stress generated on the DE material during charged relaxation is modeled and empirically demonstrated.

Finally, a simulation of the effects of this behavior on the motion of the knee joint is developed based on free oscillation of the knee joint test stand. This simulation is used to estimate the expected behavior of the knee joint during the swing phase of a device with an active DE energy harvester attached.

4.3 Uniaxial thin film energy harvester

4.3.1 Uniaxial DE harvesting: Stiffness

In section 3.4.5, the constant charge DE energy harvesting cycle was illustrated, noting the pattern of mechanical and electrical loading on the electromechanical device as mechanical energy is transformed into electrical energy. Building on that description, the following section describes the effects that this cycle has on two key mechanical parameters of the material: the stiffness and the damping. After describing the behavior, experimental verification will be provided for the uniaxial thin film DE device.

When an elastic material (such as silicone) undergoes a sinusoidal displacement, $\tan\delta$ is very small, and the stress within the material very closely follows the input. An uncharged DE generator is also highly elastic, and will respond in a similar fashion. With reference to the first half of the period of the oscillation for the DE material response simulated in Figure 4.3, when the device is charged at its maximum strain, the Maxwell stress induced on the material will cause a decrease in the internal stress of the material in the x_1 direction as specified in eqs. (3.70) and (3.71), this effect is seen by the decrease in the stress at the point of the charge.

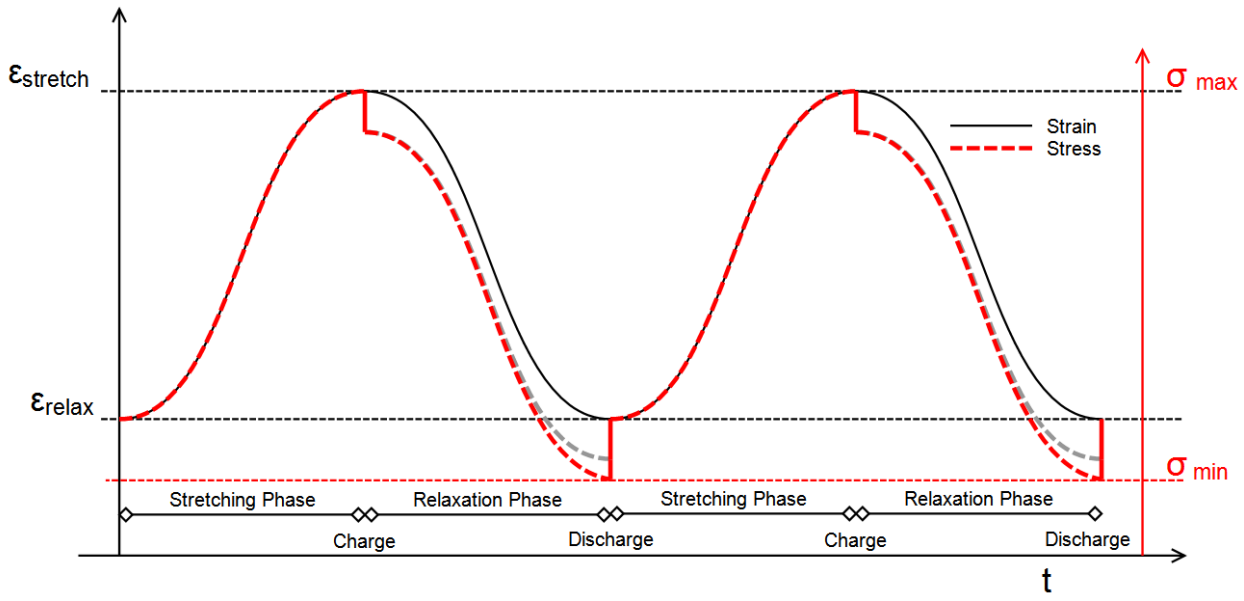

Figure 4.3: Scaled x_1 stress and strain time history curves for uniaxial hyperelastic DE energy harvesting.

As the material is relaxed back to its original stretch, the stress does not reduce proportionally to the strain (as simulated by the gray dashed line). Instead, as the material relaxes, the thickness increases, the cross-sectional area decreases, and for a constant charge, the subsequent Maxwell stress on the material increases in the 3 direction, causing the stress in the lateral direction to decrease even more. When the device is discharged, the Maxwell stress on the material is removed, and the material returns back to its original stress and the cycle repeats itself. This cycle holds describes to the mechanical behaviors which are modified by the electromechanical coupling of a DE energy harvester and will be explored in the following two sections.

When a thin film DE device is charged and the charge is held constant while relaxing as described in Figure 3.27, the Maxwell stress affects the material in the following ways: the tensile stress within the material decreases, and the effective stiffness of the material decreases. As demonstrated in Figure 4.3 above, for a single layer DE device in tension, the Maxwell stress generated from powering the device at a constant charge serves to increase the stiffness of the

material. This increase in stiffness is caused by the stretch dependency of the Maxwell stress. Based on equations 3.70 and 3.71, it is clear that regardless of what the constraint condition is, the equivalent Maxwell stress generated in the x_1 direction will decrease with increasing stretch ratio: for an unconstrained material it is proportional to $\frac{1}{\lambda}$ and, for a fully constrained material, it is proportional to $\frac{1}{\lambda^2}$. Since the Maxwell stress in the material serves to decrease the overall tensile stress, the effective result of the Maxwell stress is to increase the amount of force required with increasing stretch, effectively increasing the stiffness of the material. This behavior is demonstrated both through modeling and experimental measurements in the following section.

Experimental results: stiffness

The change in the stiffness due to the variable Maxwell stress described above can be observed both in the force-time history plots, as described in Figure 4.3, and in the force/extension plots. Comparison between the expected time history shown in Figure 4.3 and the measured response is demonstrated in Figure 4.4.

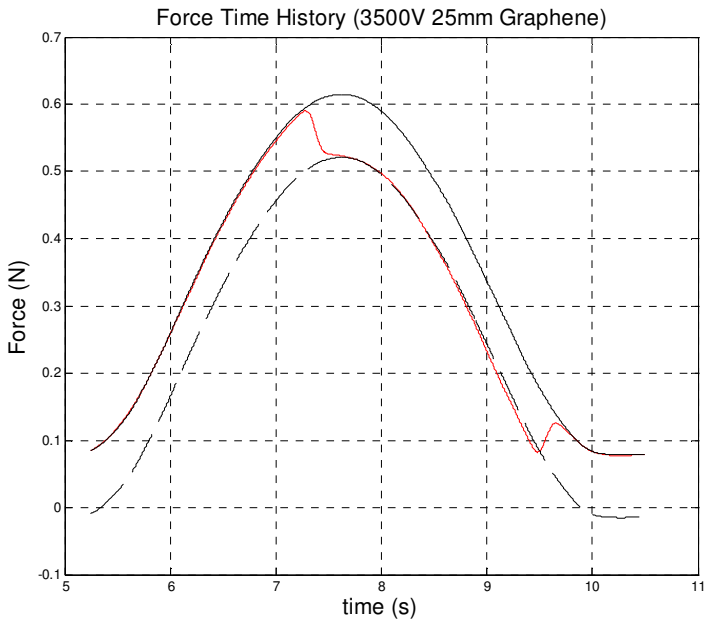

Figure 4.4: Time history of experimental force measurements: charged (red) and uncharged (black). (dotted black line is proportional to stretch for visual comparison of charged relaxation curve)

The reduction in the total force due to an increase in the Maxwell stress as the stretch decreases is the difference between the red line and the black dashed line. Although the behavior is rather slight, it is measurable, and as DE materials increase in their performance, (either through material changes such as increasing the dielectric permittivity or the effective size of the electrodes or through experimental parameters such as charge voltage) this behavior will become more pronounced.

The effect of the Maxwell stress on the stiffness of the material can also be demonstrated by observing the change in the slope of the force/extension curve shown in Figure 4.5. This figure shows this behavior in the same material using a plot of two force/extension relaxation curves overlaid on top of another. In this figure, the light blue curve is the relaxation curve which is not experiencing Maxwell stress, and the orange curve is the relaxation curve of a charged DE device. The slight increase in the slope can be seen for the charged relaxation curve, demonstrating the increase in the effective stiffness of the device.

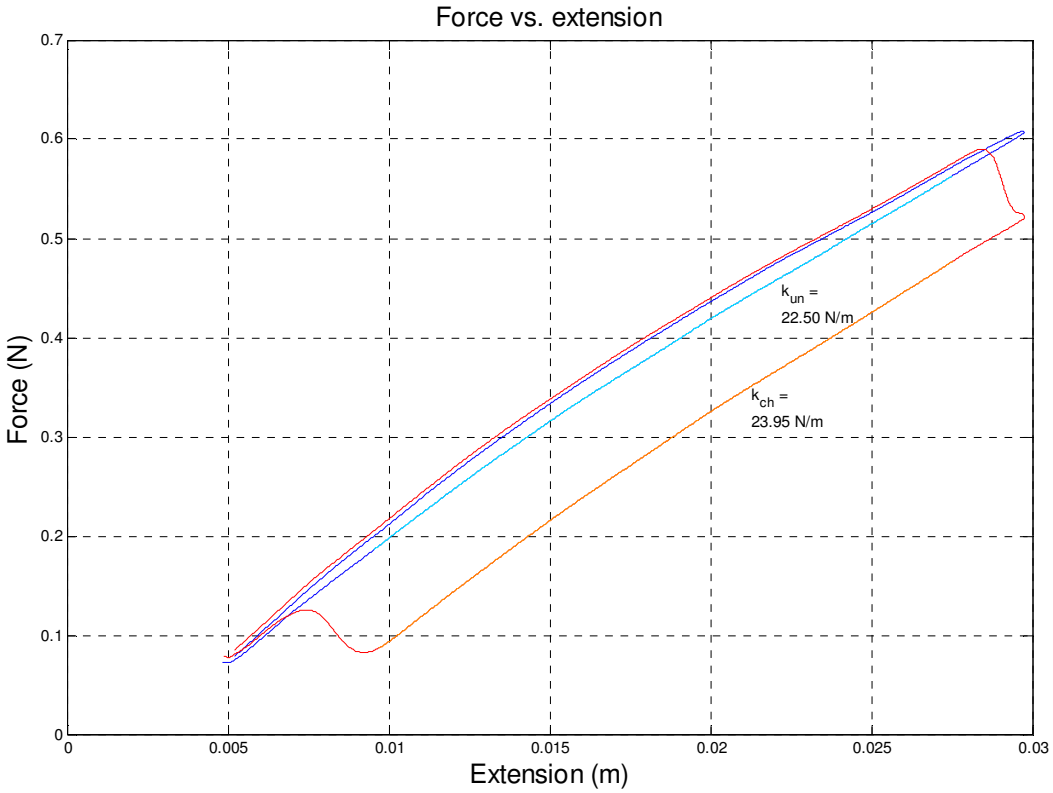

Figure 4.5: Comparison of force / extension curve of a Graphene uniaxial DE during stretch and relaxation: charged (red/orange) and uncharged (blue/light blue), (V_c = 3000V)

The charging of the DE device causes the Maxwell stress to be generated across the DE device as described in section 3.4.3. As expected, this stress results in a change in the stiffness of the material. When the DE film is charged at the point of maximum stretch, and then discharged at the point of minimum stretch, the effective stiffness of the material during relaxation does indeed go up. This is due to the variation of the Maxwell force which is generated in the DE as the stretch is decreased. As the material is relaxed, the Maxwell force will increase, increasing the slope of the force / extension curve. However, it is important to note that when used as an energy harvester, the DE material is stretched when uncharged and will not experience this increase in stiffness during stretching.

For each of the materials characterized, this increase in the stiffness of the material was measured experimentally and also simulated using the Maxwell stress models developed in 3.4.3. The results are provided in Table 4.1.

Table 4.1: Stiffness (N/m) of uncharged and charged DE devices (experimental and modeled)

Material	Max Stretch (m)	Modeled Stiffness (N/m)				Experimental Stiffness (N/m)			
		0V	3500V	Δk	% increase	0V	3500V	Δk	% increase
Graphene	0.025	22.2	25.4	3.2	14.4%	22.5	23.95	1.45	6.4%
Carbon Grease	0.025	17	20.3	3.3	19.4%	17.3	19.31	2.01	11.6%
PolyPower	0.01	47.45	51.1	3.65	7.7%	41.8	43.5	1.7	4.1%

The change in the measured stiffness for each of the materials undergoing energy harvesting demonstrates an increase in the stiffness ranging from 4.1% for polypower to 11.6% for carbon grease. Comparison between the measured and modeled values shows that the modeled response overestimates the increase in stiffness by 3 to 8%, but still captures a similar trend.

The results demonstrated here are significant because they suggest the possibility of using coordinated energy harvesting to modify the stiffness of the material when it is advantageous to do so, leading the way for smart materials which can be controlled to modify the mechanical behavior of a system while harvesting energy.

4.3.2 Uniaxial DE harvesting: Damping

As described in section 3.4.5, mechanical energy loss in a system exhibits itself through a clockwise hysteresis loop on the extension/force plane, where the area within the loop is directly related to the mechanical energy which is removed from the system. Figure 4.6 shows this behavior in a DE harvester using a plot of two force/extension curves overlaid on one another. In this figure, the black curve demonstrates relaxation for an uncharged silicone / graphene DE device which is not experiencing Maxwell stress, and the red curve is a relaxation curve of a

charged DE device. The uncharged curve (black) encompasses only a small area, indicating that there is very little energy loss in the system, however, in the charged case, where mechanical energy is transformed into electrical energy and then removed from the system, the area within the curve increases substantially. This large increase in the area of the charged relaxation curve, demonstrates the increase in the effective damping due to energy harvesting.

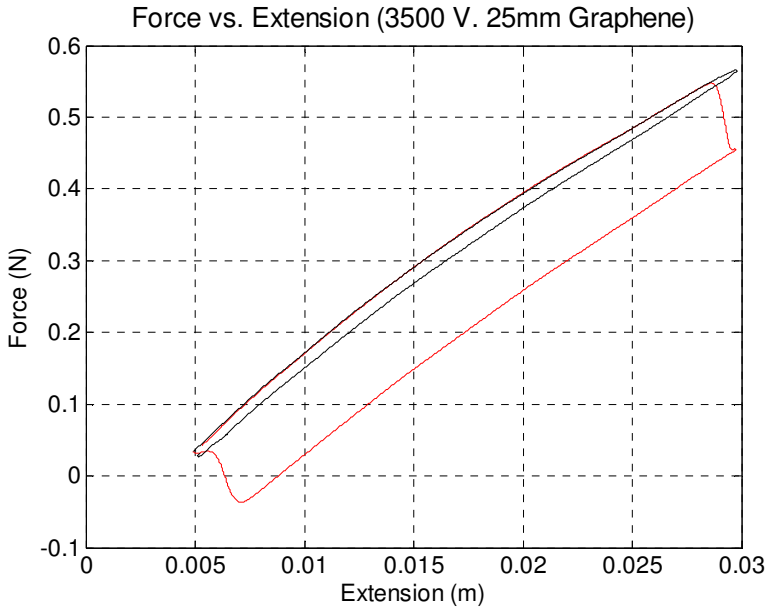

Figure 4.6: Force / extension curve from experimental force meas.: charged (red) and uncharged (black).

This behavior is important because it demonstrates how the electromechanical coupling of a dielectric elastomer harvester is directly related to damping in the system.

Damping coefficient: As described in section 4.1, the damping coefficient for a DE device using hysteretic modeling can be estimated based on the geometric, mechanical and electrical properties of the material. Recalling that for the constant charge condition demonstrated in Figure 3.28, the maximum electric field occurs at discharge, eq. (4.14) can be written in terms of the Maxwell stress at discharge, σ_{Md}, resulting in:

$$h = \frac{\varepsilon \forall E_{\max}^2}{2\pi x_0^2}\left(1-\left(\frac{A_d}{A_c}\right)^2\right) = \frac{\forall \sigma_{Md}}{2\pi x_0^2}\left(1-\left(\frac{A_d}{A_c}\right)^2\right) = \frac{\varepsilon \forall \left(\frac{\lambda_c^2 V_c}{\lambda_d x_{30}}\right)^2}{2\pi x_0^2}\left(1-\left(\frac{A_d}{A_c}\right)^2\right) \quad (4.22)$$

where x represents the amplitude of the mechanical motion.

Using this estimate, damping coefficients were estimated for each of the three electrode materials investigated (Table 4.2). Measurements of the damping coefficient were also made based on the measured energy within the hysteresis loop. Applying the relationship between the damping coefficient and the area within the mechanical plain from eq (4.21) to the force extension curve, where $k = \frac{F_{\max} - F_{\min}}{x_{\max} - x_{\min}}$ results in:

$$h = \frac{\Delta D}{\pi (x_{\max} - x_{\min})^2} \quad (4.23)$$

where ΔD is the difference between the area of the hysteresis curve without energy harvesting and when energy harvesting is performed. Comparison between the estimated and measured damping due to energy harvesting values for each of the electrode materials is provided in Table 4.2.

Table 4.2: Damping coefficient, h, as a result of energy harvesting. estimated and measured, for DE electrode materials

DE Material	Voltage (V)	Calculated (N/m)	Experimental (N/m)
Graphene	3500	0.8511	1.239
Carbon Grease	3500	0.5887	1.032
Polypower	3500	5.335	5.66
Polypower	2250	1.948	2.77

Observation of these results confirms several assertions concerning the expected damping of a DE generator:

1. Devices which experience greater Maxwell stress, due to electrode boundary constraints and material properties will also induce increasingly damped behavior in the material.
2. Increased bias voltage directly affects the level of damping experienced by the material during energy harvesting. This is expected as the amount of energy converted through electromechanical coupling is strongly affected by the bias voltage.

4.4 Mechanical behavior modification due to knee joint DE harvesting

Once the effect of energy harvesting on the mechanical properties of the thin film DE material has been described, this provides a means to quantify how it affects the behavior of a human knee joint when energy harvesting is performed while being worn on the knee joint. A laboratory knee joint motion simulator was developed to duplicate the angular motion that a healthy knee will undergo during a gait cycle. The device is similar in form to a human knee with a kinematic linkage attached to a linear motor to provide the desired profile for different strides (walking, running, climbing stairs etc.). The DE generator was attached to this device and allowed to operate over a standard operating range based on the specified gait speed and simulated terrain. This mechanism provided a means to characterize the amount of energy harvested from as well as allow for the development of electrical loading patterns. The following section describes the test stand and its use in measuring the behavior of a thin film DE harvester undergoing energy harvesting, along with the modeling developed based on the experimental results collected.

4.4.1 Biofidelic Knee Joint Test Stand

Until this point, the mechanical behavior of the DE material has been investigated for the material itself, however, an important component of the behavior of the DE device is how it affects its surroundings, specifically in this case, the torque, stiffness and damping at the knee

joint. In order to investigate this, an instrumented knee joint test stand was developed to mimic the behavior of a human knee joint during walking. This test stand was designed to operate in two different modes: prescribed profile mode (position control with force measurements) and free oscillation mode (initial condition prescribed, unforced oscillation with acceleration measurements). The development and use of both of these modes will be described in this section along with the results and analysis based on each of these modes of operation. As described earlier, in order to investigate the behavior of a DE energy harvester operating on the knee joint during walking, a biofidelic knee joint test stand was developed. This test stand was built to mimic the normal behavior of the knee during a typical walking gait cycle and was instrumented to measure several important quantities including, force, displacement, and acceleration. This section will include an anatomical description of the test stand, an explanation of its different operating modes and the orientations of the DE material followed by details of how the key concepts of capacitance, stretch ratio and Maxwell stress transmission were determined.

Anatomy of the knee joint test stand

In order to demonstrate the dynamic effects of the DEG energy harvester, an anatomically accurate knee joint test stand was developed. The structural components of the test stand were comprised of artificial members formed in the shape of the distal end of a Femur bone, the patella, and the proximal end of the Tibia/fibula pair. This bone portion can be seen as the highlighted area in Figure 4.7.

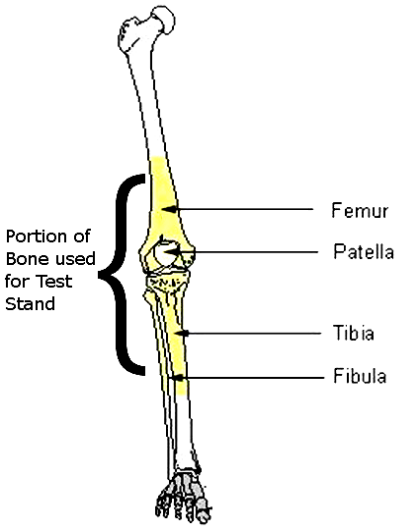

Figure 4.7: Lower limb with bone structure included in test stand highlighted in yellow.

The structural members were supported by plastic ligaments which were attached via screws and provided a range of motion for the knee similar to that of a healthy knee joint. The patella was held in place by a silicone strip designed to mimic the behavior of the patellar ligament, allowing the patella to move relative to the femur as it would in a normally functioning knee joint. To replicate the shape of the muscles surrounding the knee, molded silicone with padding was fixed to the bones both above and below the knee joint.

Figure 4.8: Knee Joint test stand with silicone ligaments and flesh; a) flexed, b) extended

It is important to note that these molds were only designed to provide the approximate shape of the muscles and they were not designed to activate as ordinary muscles. All motion of the knee was controlled by forces applied at the distal end of the tibia portion.

The entire structure was supported from the femur bone. The cut surface of the bone was fixed at 45 degrees to a solid test stand, allowing the lower limb the mobility to rotate through its normal range of motion. Over the bone, muscle and ligament structures, an additional layer of silicone film was placed on the entire structure to create a surface which the DE device was placed on. The test stand before placement of the DE device is shown in Figure 4.8.

Several key locations on the test stand such as the axis of rotation and the areas of maximum stretch were also determined. Although the axis of rotation of the knee joint does move slightly during the motion of the knee, there is evidence to suggest that the motion of the knee can be modeled as two independent axes (flexion-extension and longitudinal), with relatively fixed axes of rotation [137-139]. The axis of rotation was determined using an anthropomorphic ratio of the location of the flexion-extension axis of rotation for the human knee joints relative to the anterior femoral shaft (the front edge of the femur bone) and the posterior-medial femoral condyle (the interior projection at the distal end of the femur) [137]. The location was confirmed through observation of video of the knee motion, and is shown in the photograph of the knee joint in Figure 4.9. Knowledge of location of the axis of rotation allowed for the determination of key dimensions which were necessary for analysis of the test results.

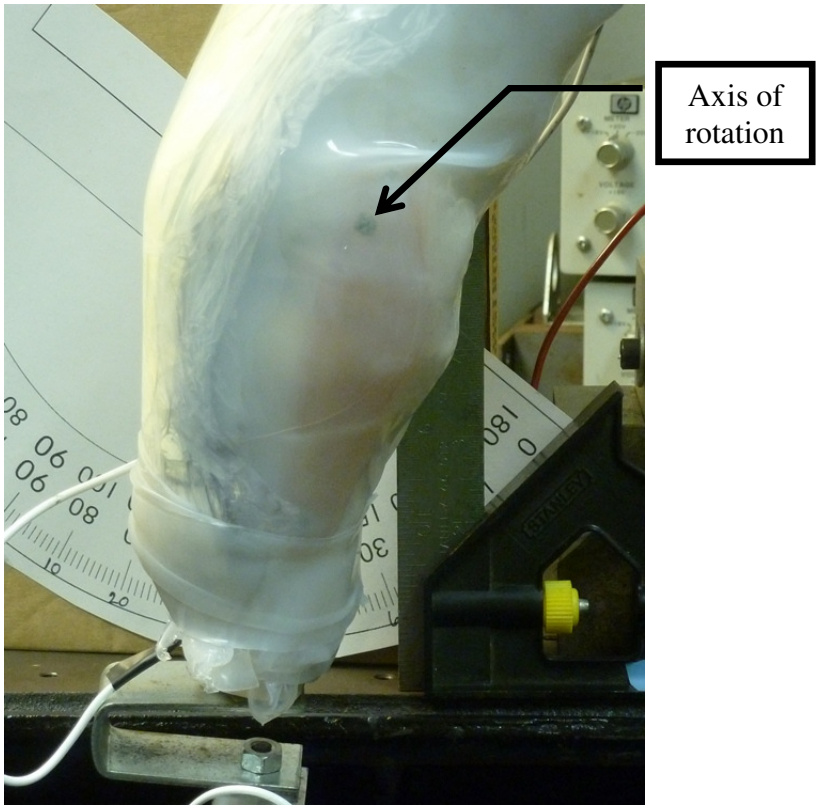

Figure 4.9: Location of axis of rotation

Figure 4.10 illustrates the measurements of the radius of the patella during flexion and extension as well as the pendulum length of the tibia portion with the masses attached.

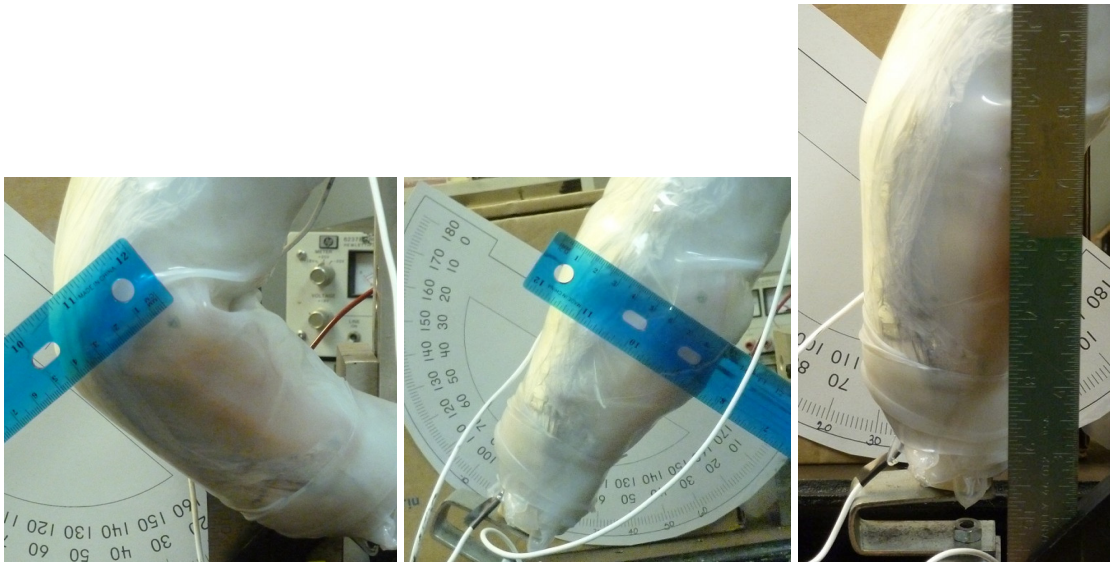

Figure 4.10: Measurements of test stand dimensions relative to axis of rotation (top: flexion and extension; bottom: length of pendulum).

With the determination of the axis of rotation, the knee joint test stand was prepared for the different test configurations described in the following section.

Knee joint test stand configurations

Two different types of tests were performed using the knee joint test stand. The first involved position control and torque measurements (similar to the DE film tests described in section 3.2), and the second involved free oscillation with acceleration measurements.

Torque / angular displacement test stand: The torque / angular displacement test was performed using the linear motor to drive a link attached to a pin through the tibia/fibula section. The linear motor was the same stepper motor with an internal linear potentiometer as was used in the thin film testing, with a force transducer mounted between the motor actuator and the link arm in the inline configuration shown in Figure 3.8b. The test stand in both flexion and extension is shown in the Figure 4.11 below.

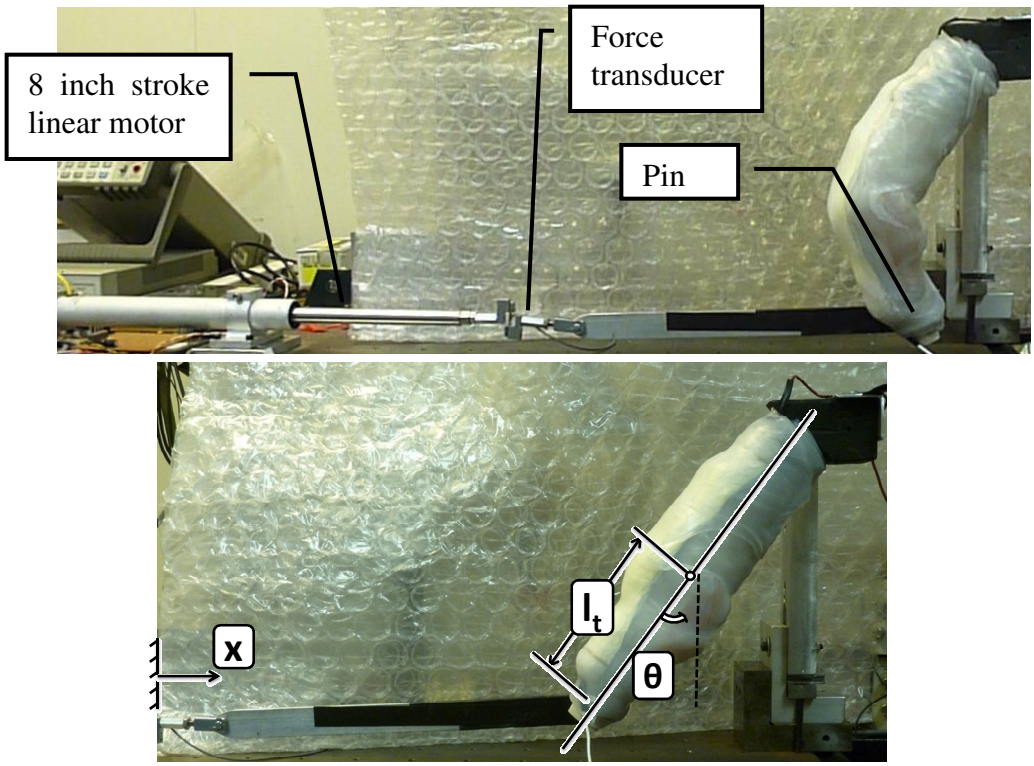

Figure 4.11: Force / displacement measurements; top: flexion, bottom: extension (θ=0)

The angular position of the knee was controlled using a proportional controller assimilated into the LabVIEW code operating the test stand (see Appendix C). The relationship between the desired angle and the linear displacement was found relative to the initial position of the linear motor when the knee joint was fully extended, x_0, and the distance from the axis of rotation of the knee to the pin in the tibia, l_t:

$$x = x_0 - 2l_t \sin\left(\frac{\theta}{2} + \frac{\pi}{4}\right)\sin\left(\frac{\theta}{2}\right) \tag{4.24}$$

This kinematic transformation from linear to angular displacement was developed based on the assumption that the angle of the link arm from horizontal is very small throughout the motion of the knee joint. The nearly horizontal orientation of the link arm can be seen at the limits of its motion during the flexion and extension of the knee joint in Figure 4.11. Using the inverse of eq. 4.24, the angular displacement data was calculated using measurements from the force transducer and potentiometer as:

$$\theta = \cos^{-1}\left(\frac{x - x_0}{l_t} + \frac{1}{\sqrt{2}}\right) - \frac{\pi}{4} \tag{4.25}$$

Using the angle and the linear force measurements, the torque was found directly using the following relation:

$$\tau = F\, l_t \sqrt{\left(1 - \left(\frac{x - x_0}{l_t} + \frac{1}{\sqrt{2}}\right)^2\right)} \tag{4.26}$$

The instrumented test stand developed allowed for the determination of the relationship between the torque and the angular displacement of the knee joint when it was exposed to DE energy harvesting across the joint.

Free oscillation test stand: The free oscillation test stand used a modification of the knee joint test stand in which the link between the tibia and the linear motor is removed, and an optional weight was attached to the end of the tibia/fibula section. Additional weights were added or removed as shown in Figure 4.12, and the value was selected based on the desired dynamic behavior of the device.

When used in this configuration, the acceleration of the tibia was measured rather than the torque. This data was collected using a simultaneous combination of three methods: a uniaxial accelerometer, a tri-axial accelerometer and video measurement. The accelerometer measurements provided both a time history of the behavior used to measure the reaction to the Maxwell stress, and frequency response information utilized to determine the stiffness and damping of the device. Additionally, the video measurements were post-processed to provide angular displacement data.

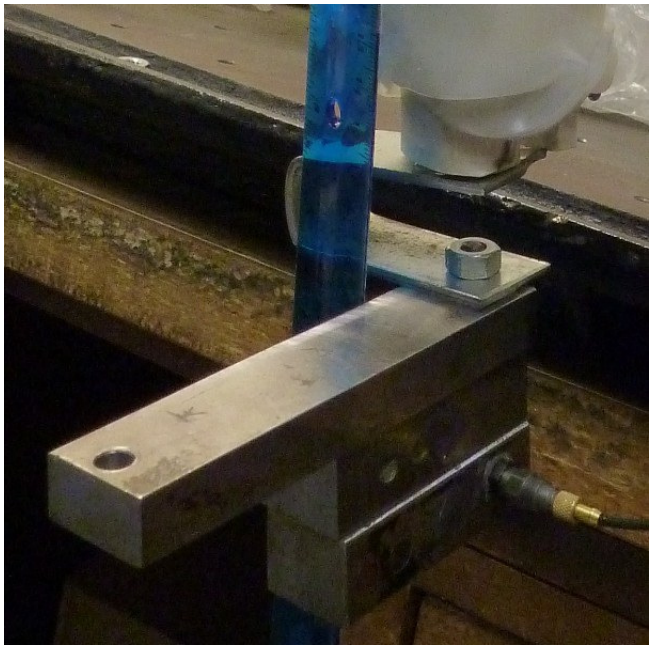

Figure 4.12: Weights used for oscillatory testing of knee joint (top = 0.28kg, middle = 0.18 kg, bottom = 0.177 kg)

The free oscillation knee joint test stand was used to measure the Maxwell force generated by charging the DE. These measurements were performed using the test stand without weights (the rotational stiffness and damping of the test stand without weights were: $k_r = 2.5\frac{N \cdot m}{rad}$ and $\zeta_r = 0.11$). The unweighted test stand had an approximate mass moment of inertia of 0.0037 kg-m^2. The response of the tibia portion was measured through both the accelerometer and video measurements to determine the acceleration and maximum displacement of the limb when experiencing an impulsive force due to the Maxwell stress.

Free vibration energy harvesting: To investigate energy harvesting during cyclical motion similar to that during walking, the test stand was fitted with additional weights. Figure 4.12 shows the mounting of these weights on the end of the tibia portion of the tests stand as they were used for the free vibration tests. The addition of 0.64 kg at the end of the tibia portion resulted in a mass moment of inertia of 0.028 kg-m^2. The dynamic behavior of the knee joint was also influenced by the silicone ligaments and tissue which were placed around the synthetic bone. The rotational stiffness and damping of the test stand were determined experimentally to be approximately: $k_r = 3.5\frac{N \cdot m}{rad}$ and $\zeta_r = 0.07$. These results were compared with published ranges of knee joint stiffness and damping based on experimental measurements on human subjects. The initial experimental data on human subjects were reported in [140], where the initial data were later corrected in [141]. Note that our values are for a prototype model, while the data reported in [141] were obtained from experiments on a human subject. In order to compare our measured values with those reported in [141], we employed a dimensional similarity analysis using

$\zeta_r = \frac{c_r}{2\sqrt{k_r I}}$ as the pi group. It was found that our measured damping ratios corresponded well with the damping ratios calculated based on the range of data in [141] for all age groups.

DE device placement on the knee joint

Once the test stand itself was developed, a methodology for mounting of the DE material was developed which involved placing a folded DE film, wrapped in a thin layer of silicon dielectric, along the surface of the test stand. PolyPower DE film has an active stretch length of 0.2 m, and can be cut to the desired width. In the tests presented here, a 1.1 m wide sheet the film was used. Once the film was cut, the electrode material from the edges were etched away using sodium hypochlorite (bleach) to prevent shorting. The width of the film was then folded in half consecutive times until the device has the following dimensions: 0.2 m x 0.07 m. The active film was then completely wrapped by a thin protective silicon film, and the wire leads were attached using conductive tape to the opposite sides of the film. This device was then held in place by a thicker 1 mm sheet of silicone which mimicked the knee brace which would house the DE energy harvester on a human wearer.

Utilizing this attachment method, two different DE placement conditions were used during the knee joint testing:

i. the DE placed in front of the knee over the patella

ii. the DE placed behind the knee, along the hamstring tendons.

The placement of each of these can be seen in Figure 4.13. Each of these positions provided a different operational behavior, allowing for greater flexibility in how the device was implemented within the walking cycle.

Figure 4.13: DE film placement on the knee joint test stand; left -- front of knee joint, right -- back of knee joint.

Before placing the DE device on the knee, the capacitance of the folded DE device was measured at rest in a horizontal, unstretched position. After this, the device was wrapped in a thin sheet of silicone and placed on the knee in the unstretched position (extension for a DE located on the front of the knee, see Figure 4.13.a, and flexion for a device located on the back of the knee). The device was attached to the knee by wrapping a 1 mm sheet of very compliant silicone (fabricated using TC-5005 3 part silicon with 30% relaxer compound from BJB Enterprises). The capacitance was then measured at both extension and flexion. These measurements at the extensions, along with the unstretched capacitance became the benchmark values from which the stretch ratio, λ, of the DE material were determined. Recalling that for the Polypower DE attached to the knee joint test stand, the fully constrained limiting case was used ($\kappa = 1$), the stretch ratio determined here was equivalent to the mechanical stretch ration, λ, as described in section 3.2.2.

Capacitance as a function of joint angle

Measurements of the capacitance of a DE device relative to the knee joint angle were taken on both the knee joint test stand and on a human knee. The results of these tests confirmed that over the range of interest, the capacitance increased linearly with the joint angle. Results of these measurements can be seen in Figure 4.14. Note that the tests were run with different size PolyPower DE devices and that the nearly 16 time reduction in the capacitance of the device on the human knee is because the surface area of the device was also about 16 times less than that of the device on the test stand.

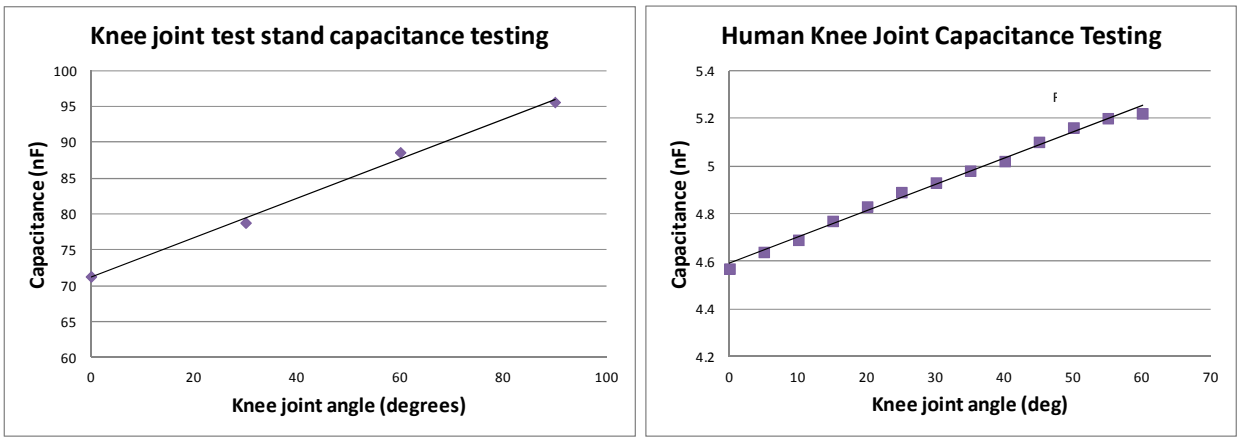

Figure 4.14: DE capacitance relative to knee joint angle for measurements made: a) on the knee joint test stand (approx dimensions: 0.2m x 1.1 m) b) on a human knee (approx dimensions: 0.2m x 0.065 m).

Based on these measurements, the capacitance of the DE devices used were assumed to be linearly increasing with joint angle within the normal range of motion.

Stretch ratio values determined from capacitance measurements

The capacitance was measured at each of the critical loading positions (ie, fully flexed and fully extended) and these values, along with the material properties and geometric dimensions, were used to estimate the stretch ratio of the material for a given length and width DE of the device. This estimation was performed as follows: first, the capacitance was estimated

for an unstretched device with the prescribed dimensions. Next, a function in terms of λ was developed for the capacitance modeled using the general constraint condition (eq. 3.47), relates capacitance joint angles. Finally, the first root for $\lambda > 1$ was found using the function defined. This value was then returned and used as the stretch ratio related to a given angle based on the extension and flexion capacitance measurements. This calculation was very important for it formed the means for determining the stretch ratio of the material at any position based on the capacitance measurement.

4.4.2 Transmission of Maxwell stress to joint moment.

Joint moment model

The electromechanical response of the DE device attached to the knee is similar to the behavior observed during the initial thin film investigations (see section 3.2). However, attachment to the knee joint introduces new constraints to the mechanical effect of charging the device. In order to replicate the behavior of the DE harvester attached to the knee joint, the following assumptions are imposed on the model of the behavior of the DE mounted to the knee joint:

1. The larger, folded DE device behaves similarly to the narrower samples of material used in the uniaxial testing.
2. The PolyPower DE device held in place by the silicone sheet behaves in the fully constrained uniaxial configuration.
3. The silicone wrap causes all forces transmitted from the DE to the knee through shear contact forces with the surface of the tests stand.

4. The stiffness of the DE device is much smaller in magnitude than the stiffness of the bone and any deformation of the bone itself is considered negligible, therefore, the only effect of the DE is a bending movement generated about the knee joint.
5. Very little stretching of the DE material occurs in the area covering the patella, significant stretching of DE occurs above and below, as demonstrated in Figure 4.15.

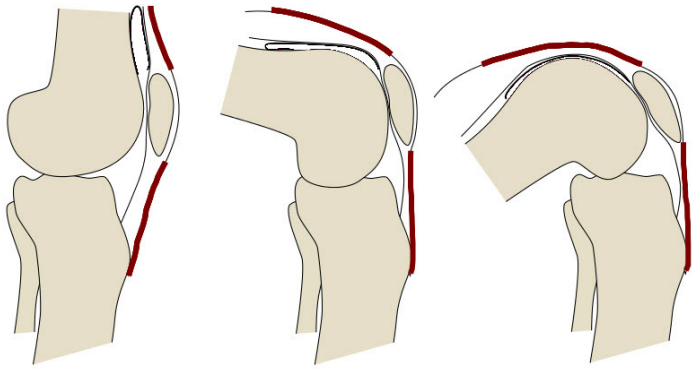

Figure 4.15: Stretching above and below the patella

Based on these modeling assumptions, the relationship between the electrical conditions (capacitance and voltage) and the joint torque generated was developed as follows.

First, the approximate capacitance of the DE device at the specified angle was estimated. Since, the capacitance of the DE device relative to joint angle was found to be linear within the extension to flexion operating range, the capacitance at the specified angle was determined using linear interpolation of the capacitance measurements at extension and flexion. Based on this capacitance, the stretch ratio, λ, of the material was found and the effective Maxwell stress generated in the x_1 direction (along the knee ligament) was calculated based on the completely constrained model described by eq. 3.70. Because the stress was applied evenly across the entire surface of the material, the force was described proportionally to its length (Force / length of material (N/m)). Based on this unit length force, the moment about the knee joint was determined by assuming that the force is transmitted as a shear force, acting on the surface of the

test stand, where the distance from the leg surface to the axis of rotation was determined empirically for both the fully extended and the fully flexed conditions. Based on this moment, the force acting on the link was found using the vertical distance from the joint to the link mounting location, assuming that the link remain completely horizontal during the entire range of motion under consideration. The MATLAB code used to implement this process is found in Appendix C.

Experimental measurements of the effects of the Maxwell stress

The moment generated about the knee joint due to the Maxwell force was determined experimentally using two different methodologies which utilized the configurations of the knee joint test stand described in section 4.4.1. The first method determined the moment by measuring the change in the force required to hold the knee joint in a fixed position using the linear motor link. The second method utilized the knee joint in its free oscillation mode. The knee joint was placed at rest in its equilibrium position, and the angular acceleration generated due to charging the DE was used to estimate the moment generated about the joint. In what follows, each of these methods is described in greater detail along with a demonstration of the measured data.

Fixed position measurements

The moment generated about the knee joint due to the Maxwell stress was measured for the knee joint in both its fully flexed and fully extended positions. To provide the most accurate measurements, these tests were run with the knee joint completely stationary before and after charging. The force required to hold the knee joint at its prescribed location was measured before and after charging occurred. A sample of these measurements can be seen in Figure 4.16 for of a DE device located on the front of the knee joint which was charged to 3000 V. This figure demonstrates the behavior of the device in both the flexed (a) and extended positions (b). The

force reported here was directly measured using the force transducer located between the linear motor and the link as shown in Figure 4.11, and was directly related to the moment at the knee joint required to position the knee.

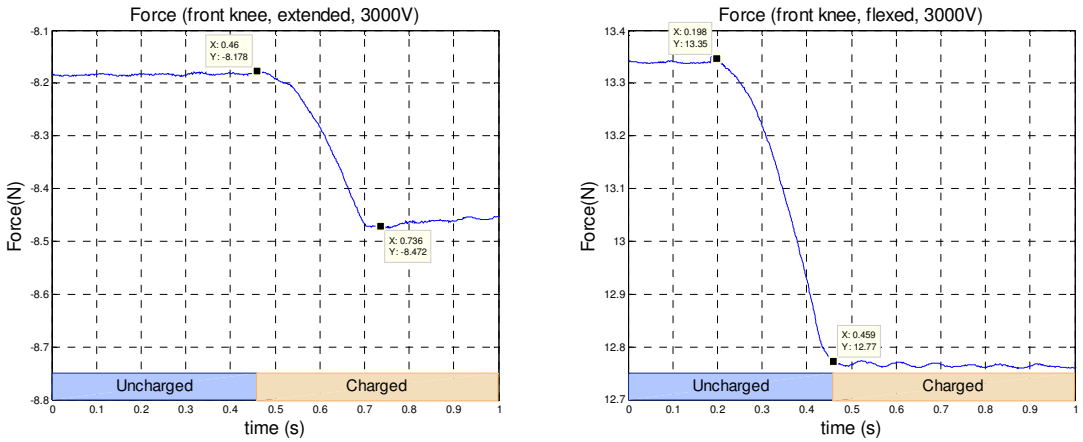

Figure 4.16: Force measured due to Maxwell stress.
a) knee joint flexed b) knee joint extended

In order to interpret these results, it must be noted that the force required to maintain the desired knee location is position dependent. In the flexed position the link is in compression, pushing the shank in the counter-clockwise direction to generate the required angular position. In the extended position, the link is in tension, pulling the shank in the counter-clockwise direction about the knee joint. In both cases, the response of the knee to the charged DE is a moment in the clockwise direction, creating a compressive force on the linear motor link, causing the force measured to become more negative. In the case of the flexed knee, this has the effect of decreasing the magnitude of the force required to hold the joint in position, similar to the uniaxial response described in section 3.4.3. In the case of the extended knee, the already negative force becomes more negative, with the effect of increasing the magnitude of the resultant force. This behavior will be investigated in greater detail when the stiffness of the knee joint undergoing DE energy harvesting is described in section 4.4.3.

In addition to the direction of the force, its magnitude at each of the positions is important as well. In the flexed position the DE material is stretched relative to the extended position, causing the thickness to decrease and the Maxwell stress, which is inversely dependent on the thickness as described in eq. (3.56), to increase as well. This behavior is clearly seen by comparison of the magnitude of the decrease in the force at the link, where the force measured at flexion is nearly twice that of the force measured at extension. Considering that the perpendicular distances from the linkage applied force to the knee joint during flexion and extension are $d_f = 0.12m$ and $d_e = 0.09\,m$, the moment generated in flexion is over three times that generated in extension, underscoring the importance of understanding the effect of orientation on the moment generated when charging a wearable DE device.

Finally, observation of the loading behavior of the knee joint test stand also exhibit a time delay similar to that described for the uniaxial load, where regardless of the DE device position, the delay ranges from 0.2 – 0.23 s. That these delays are slightly longer than those for the film tests could be because of a larger DE device being used, or it could be an additional delay due to the mechanical coupling of the knee joint itself.

Free Oscillation force measurements

Based on the free oscillation test described in section 4.4.1, acceleration measurements from both the tri-axial and the uniaxial accelerometer were utilized along with video data to quantify the effect of the Maxwell stress generated during charging of the DE energy harvester. Because the effects of the Maxwell stress are very small, the multiple readings were helpful in confirming the behavioral trends (apart from anomalies or noise).

Acceleration measurements from the tangential (y) direction tri-axial accelerometer and the uniaxial accelerometer were recorded as the DE device located on the front of the knee was charged as shown overlaid in Figure 4.17.

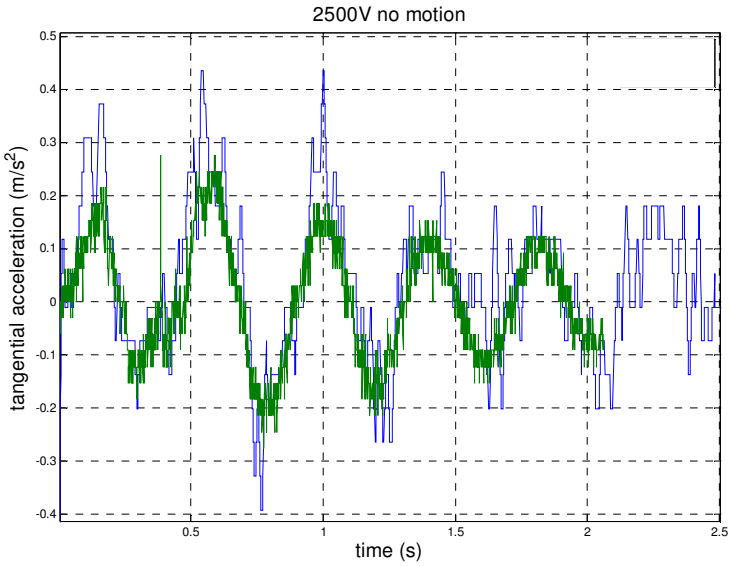

Figure 4.17: Response of the shank to the Maxwell stress generated due to a 2500V charge on the DE harvester (blue: Y axis of tri-axial accelerometer , green: uniaxial accelerometer)

The shank was at rest when a 2500V charge was applied at t=0, and the resulting acceleration and subsequent oscillatory motion is clearly demonstrated in the figure. Because of the careful calibration of the tri-axial accelerometer (blue), its amplitude was considered accurate and were utilized for the determination of the moment generated by the Maxwell stress. The moment was determined based on the tangential acceleration, the location of the accelerometer and the moment of inertia of the shank: $M = \frac{a_t}{l_{accel}} I$ (the moment of inertia had been calculated theoretically and then confirmed via experimental validation).

Along with the acceleration, the angular displacement of the knee joint due to the moment was measured using the video measurements. During the maximum displacement on the

first oscillation, the shank moved in the positive (ccw) direction approximately 0.85° (shown by the red line) from the stationary equilibrium point (shown by the blue line).

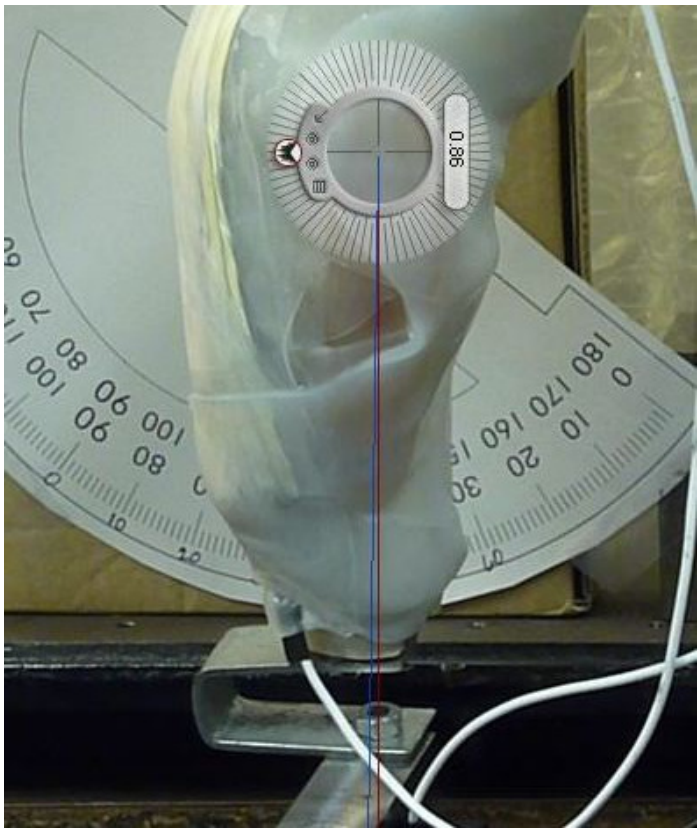

Figure 4.18: Angular displacement of the knee joint due to the Maxwell stress during 2500 V charge of the DE.

The information provided by these measurements, was utilized in the development of the oscillation simulation which will be described in detail in section 4.5.

Maxwell stress comparison

Measurements were performed to determine the moment about the knee joint based on the Maxwell stress for a DE energy harvester placed on the front of the knee joint using both the torque / theta method and the oscillation method. In Table 4.3 the moment calculated about the knee joint due to the Maxwell effect using the methodology described in section 4.4.2 is compared with the moments measured.

Table 4.3: Knee Joint moment due to Maxwell Stress, modeled vs. experimental

Knee joint orientation	Constraint	Voltage	Modeled (N m)	Experimental (N m)
Extended	Fixed	3000	0.033	0.028
Flexed	Fixed	3000	0.071	0.066
Relaxed (vertical)	Free	2500	0.045	0.054

As expected from Figure 4.16, the moment generated when the knee joint is extended is smaller than that of the moment generated in the flexed position. This comparison, provides confirmation that the model is able to predict the moment generated about the knee as a function of the knee joint position.

Energy harvested measurements

The Maxwell stress has a direct effect on the energy harvesting capability of the DE device. The energy harvested was measured by comparing the area within the mechanical operational map of the uncharged and charged DE material, using a methodology similar to that shown in section 3.4.5. The energy harvested by the DE harvester used in this research is shown with the energy harvesting of the other results available in the literature in Table 4.4.

Table 4.4: Comparison of knee joint DE energy harvesters

	Date	Electrode material(s)	Minimum Capacitance	charge voltage	Energy harvested (experimental) (J)
Jean-Minstral	2010	carbon grease	62 pF	200 V	1.22 uJ
				1000 V	32.6 uJ
		carbon grease/silver	60 pF	200 V	1.68 uJ
				1000 V	42.5 uJ
		silver/carbon grease	72 pF	200 V	1.69 uJ
				1000 V	35.1 uJ
Slade	2012	EAP roll		500 V	3.13 uJ
Presented Research	2013	PolyPower front of knee	75 nF	3000 V	84.6 mJ
		PolyPower Back of knee	75 nF	3000 V	16.5 mJ

When compared with previous knee joint DE harvesting attempts, the amount of energy harvested is substantially higher. This is due to the much larger surface area vs. thickness (as demonstrated by the minimum capacitance) and higher charging voltage which is possible when testing on a non-living test stand rather than a human subject.

4.4.3 Mechanical behavior modification due to knee joint DE harvesting

The biofidelic knee joint was used next to aid in the understanding of the effects of DE energy harvesting on the knee joint during walking. The physical phenomena associated with each of these mechanical behaviors relative to the electrical stimulus are described here, followed by experimental results and a description of the simulation used to model the mechanical response.

Stiffness: The charging of the DE device causes a Maxwell stress to be generated within the DE device as described in section 3.4.3. This stress in turn results in a change in the stiffness of the material, as was demonstrated for the uniaxial thin film DE in Table 4.1. This change in the stiffness of the DE film also affects the effective stiffness of the knee joint, where the location of the DE device and the timing of the charge/discharge cycle dictates whether there is an increase or decrease in this effective stiffness. When the DE film is charged at the point of maximum stretch, and then discharged at the point of minimum stretch, the effective change to the stiffness of the knee joint during relaxation is reduced. This is due to the variation of the Maxwell force which is generated in the DE as the stretch is decreased. However, when the DE film is charged at the point of minimum stretch, and then discharged at maximum stretch, the effective change to the stiffness of the knee joint increases, effectively requiring increased force for the same motion.

Damping: The hysteretic damping coefficient due to energy harvesting can be estimated using eq. (4.14). When applying constant charge electrical loading to the knee joint during relaxation, the maximum electric field, which occurs at discharge, can be written in terms of the charge voltage, V_c, as $E_{\max} = \frac{\lambda_c^2 V_c}{\lambda_d x_{30}}$. Also, the amplitude of the oscillation, which was written as x_0 for the uniaxial test, is written for the angular rotation in terms of the angle at which the DE device is charged and discharged (θ_c, and θ_d, respectively). The amplitude is considered half of the total joint rotation, therefore, $\theta_0 = \frac{\theta_c - \theta_d}{2}$. This results in the following definition for the rotational damping for the constrained case due to energy harvesting:

$$h_r = \frac{\varepsilon \forall}{2\pi \left(\frac{\theta_c - \theta_d}{2} \right)^2} \left(\frac{\lambda_c^2 V_c}{\lambda_d x_{30}} \right)^2 \left(1 - \left(\frac{\lambda_d}{\lambda_c} \right)^2 \right) \tag{4.27}$$

This provides a means to estimate the damping which the material will experience as a result of the energy harvesting for a specific condition.

Unlike the DE material itself which does not exhibit much internal damping, the knee joint is highly damped. This can be observed by comparing the small area within the operating loop of the uncharged uniaxial DE film shown in Figure 4.6 with the large area within the operating loop of the torque / theta curve for the unpowered devices shown in Figure 4.19. In Figure 4.19, the behavior of the knee joint alone is compared with the behavior with an unpowered DE device mounted to it, demonstrating that there is a large increase in the stiffness of the knee joint, but only a moderate increase in the damping when the uncharged DE device is placed on the joint.

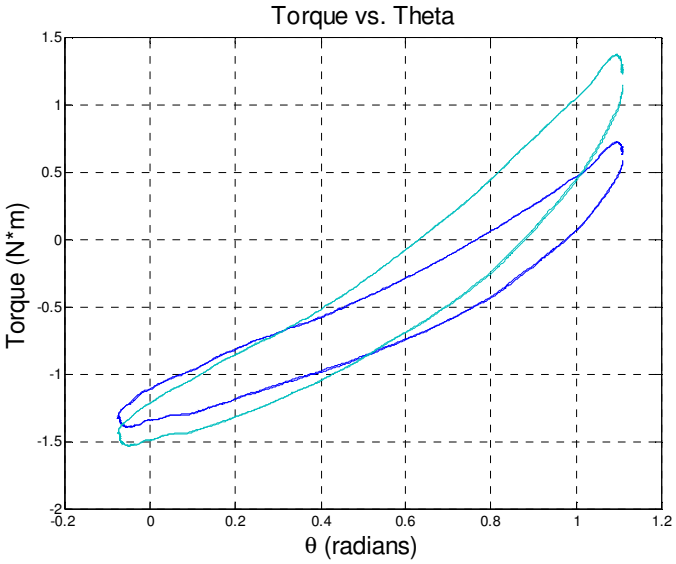

Figure 4.19: Comparison of the knee joint test stand behavior alone (dark blue) and with the unpowered DE device mounted on the front of the knee (light blue)

The damping induced by the DE energy harvesting was measured by comparing the damping coefficient for both charged and uncharged operations. The damping coefficient is found using the area of the hysteresis loop and the maximum and minimum extension based on eq (4.23), following the method described in section 4.3.2. When the energy harvesting induced damping term is added to the mechanical damping of the knee and uncharged harvester, the total damping experienced at the knee joint can be determined. In the following section, the damping of the knee joint itself for a given configuration is compared with the damping for the powered device.

Experimental results

The stiffness and damping of the knee joint were measured for the two different locations described in section 4.4.1: in front of the knee (front) and behind the knee (back). The DE device in the front position was tested with two different loading conditions as well: charging at flexion and charging at extension. For each set of tests, a representative curve is presented with a detailed description of how the curve demonstrates the effects of the energy harvesting on the stiffness of the knee joint.

Case 1: DE material located on front of knee joint, charging occurs at flexion

The first location/charging orientation is that of a DE device located in front of the knee joint with charging occurring at flexion and discharge at extension. In this configuration, the device is charged at its maximum stretch and discharged after undergoing relaxation. It will be seen from the results presented that this arrangement represents a charge and discharge timing scheme which is effective for energy harvesting, and also for beneficial mechanical effects.

Figure 4.20 compares the torque vs. angular displacement curves for the knee joint test stand for a test run with the DE harvester located on the front of the knee, with and without energy harvesting. The red curve demonstrates the behavior of the knee joint with an inactive, uncharged DE device located on it, and the blue curve demonstrates the behavior of the test stand with the same device performing energy harvesting. The DE material is charged at maximum flexion, relating to the maximum extension. The knee joint is then moved through a controlled swing phase cycle based on measured gait data from [142] until the knee joint reaches the maximum extension point, represented by the minimum extension. At this point, the DE is discharged, the electrical energy is removed from the system, and the knee continues to travel through the second half of the gait cycle, ending at the fully flexed position where the motion began.

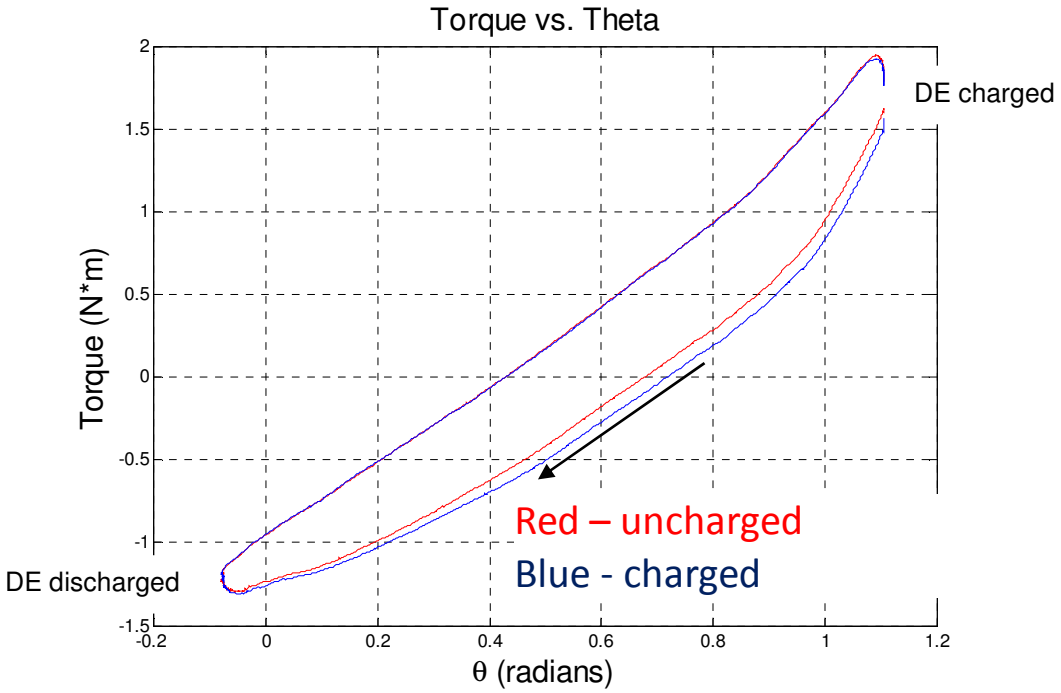

Figure 4.20: Knee joint behavior for energy harvesting DE located on Front of knee; uncharged (red), charged at flexion (blue); arrow indicates direction from charging to discharging

Stiffness results: By observing the slope of the curves, using a technique similar to that used in section 4.3.1, it can be determined that when charged the stiffness of the knee joint is lower than the stiffness of the knee during same motion with uncharged DE. The behavior of the lower portion of the curve for the charged and uncharged device can be compared with a similar behavior measured for the uniaxial test results. When the uniaxial DE was charged, the measured stiffness of the thin film itself in the x_1 was increased, however, when located on the front of the knee joint, this behavior has the overall effect of decreasing the rotational stiffness of knee itself.

Damping results: Direct observation of the curve makes it clear that during energy harvesting, additional mechanical energy is removed from the system as demonstrated by the increased area within the hysteresis loop in Figure 4.20. Comparing the curves presented here, there is a 13.5% increase in the damping as a result of the DE energy harvesting that was performed.

Case 2: DE material located on back of knee joint, charging occurs at extension

Another DE configuration which is possible for energy harvesting knee joint motion is placement the DE film on the back of the knee joint and then charge the device during extension, when it is fully stretched and then discharge it after flexing, when the device is relaxed. This timing is appropriate for both energy harvesting, and for producing a beneficial effect. The results of operating the DE energy harvester in this configuration are shown in Figure 4.21

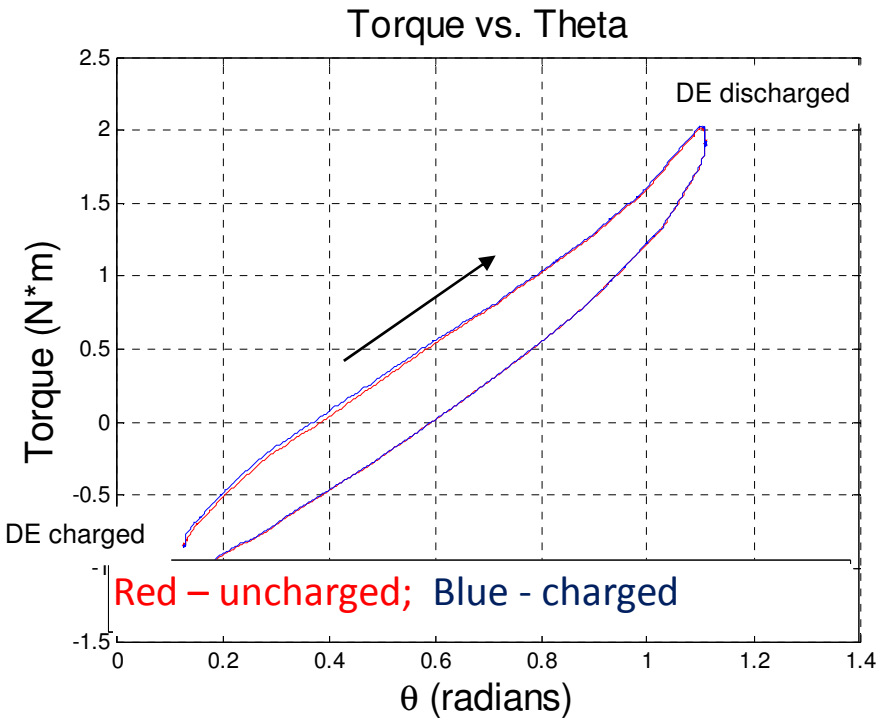

Figure 4.21: Knee joint behavior for energy harvesting DE located on Back of knee; uncharged (red), charged at extension (blue); arrow indicates direction from charging to discharging

Stiffness results: Although the effect is very small, there is a measurable decrease in the stiffness of knee behavior during charge than when the knee is performing the same motion with uncharged DE. As described earlier, this is to be expected because the orientation of the knee joint is such that the device is stretched when charged (extension for a device located on the back of the knee), and as it relaxes, the moment due to the Maxwell stress increases as the capacitance

increases. However, it is much less pronounced than in the first case because the geometry is such that the original moment generated is less in the extended position.

Damping results: Once again, the effect is small, however, as evidenced by the blue line, representing the charged DE response which is slightly outside of the uncharged response, the damping does increase when the DE material is relaxed while charged compared to when it is uncharged.

These effects confirm that placing a DE harvester on the back of the knee joint such that it is stretched while the knee is in extension and relaxed in flexion does result in beneficial energy harvesting behavior. These results indicate that back of the knee placement should be considered as a viable choice for beneficial energy harvesting from walking.

Case 3: DE material located on front of knee joint, charging occurs at extension

In order to confirm that change in stiffness is due to the coordination of location and charge timing, a third location/charging orientation was investigated. In this orientation, the DE harvester was once again located at the front of the knee, however, rather than being charged from flexion to extension (ie the lower portion of the curve), it was charged from extension to full flexion (the upper portion of the curve). It is important to note that this corresponds to a situation where the DE harvester is being charged during extension rather than relaxation which represents actuation / sensor performance rather than energy harvesting. This behavior can be explained by traversing the energy harvesting cycle in Figure 3.27 backwards, with the voltage applied at d), and then removed at c) when the electrical potential is lower than it was at charge, essentially putting energy into the mechanical system.

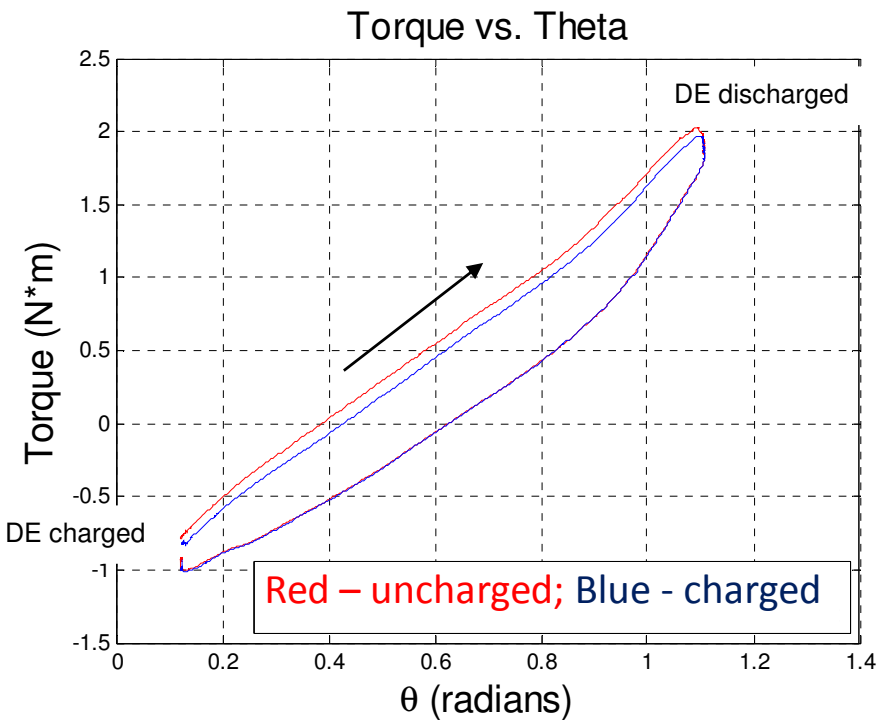

Figure 4.22: Knee joint behavior for energy harvesting DE located on Front of knee; uncharged (red), charged at extension (blue); arrow indicates direction from charge to discharge

Stiffness results: Once again, the change in the stiffness from the uncharged stretch to the charged stretching was small, however, the rotational stiffness of the knee during charge of DE is slightly higher than the stiffness of the knee during same motion with uncharged DE, this is due to the decrease in the Maxwell stress as the material is stretched while being charged.

Damping results: The change in the damping is much more pronounced than the change in the stiffness. Comparison of the uncharged (red) curve and the charged (blue) curve, makes it clear that the area within the charged DE loop is smaller, demonstrating that the damping decreases when a charged DE device is stretched. This result agrees with the expected behavior of a DE material under these conditions and reiterates the fact that stretching while charged is not an effective energy harvesting scheme.

Summary of effects of energy harvesting on joint stiffness /damping

An overview of the knee joint stiffness results are shown in Table 4.5 for each of the conditions demonstrated above. This table compares the rotational stiffness measured on the knee joint test stand with the DE energy harvester when uncharged and charged to 3000V for both front and back placement and for charging while relaxed and stretched.

Table 4.5: Comparison of translational knee joint stiffness for uncharged and charged DE test stand trials.

Location	Charge	Voltage (V)	k_r (N-m/rad)
Front of knee	Flexion/relaxation	0	2.425
	Flexion/relaxation	3000	2.406
Back of knee	Extension/relaxation	0	2.501
	Extension/relaxation	3000	2.455
Front of knee	Extension/stretching	0	2.624
	Extension/stretching	3000	2.627

The results of these tests demonstrate that when energy harvesting is correctly performed using knee joint motions, it has the overall effect of decreasing the stiffness at the knee. The physiological effects of this behavior will be investigated further in Chapter 5.

Summary of the damping calculations also demonstrate the predicted behavior. The first two configurations result in both active energy harvesting, and also lead to an increase in the damping of the system as expected by the removal of energy from the system. The third condition, results in a substantial decrease in the damping of the system, which corresponds with the increase of mechanical energy, generated by adding electrical energy to the system rather than harvesting mechanical energy.

Table 4.6: Comparison of translational knee joint damping for uncharged and charged DE test stand trials.

Location	Charge	Voltage (V)	h_r (N-m/rad)	%
Front of knee	Flexion/relaxation	0	0.57	13.5%
	Flexion/relaxation	3000	0.65	
Back of knee	Extension/relaxation	0	0.58	3.8%
	Extension/relaxation	3000	0.60	
Front of knee	Extension/stretching	0	0.69	-16.3%
	Extension/stretching	3000	0.58	

Recall from Figure 4.19 that the knee joint without a DE device has its own internal damping, which was designed to correspond to that of the human knee joint. Comparison of knee joint response with and without the uncharged DE provides a means to find the total additional stiffness and damping due to both the uncharged DE device itself and the energy harvesting. This method is used in the following section to quantify the mechanical effects of the DE energy harvester on the knee joint through a oscillatory model, and then in subsequent sections apply the joint reaction torques about the knee for varying electrical parameters.

4.5 Simulation of damped swing phase knee joint

A simulation of the behavior of the device attached to a knee joint was developed using a one degree of freedom, angular equation of motion whose behavior was defined by empirically determined parameters. This knee joint simulation will act as a platform to observe the effect of changing electrical parameters such as dielectric permittivity and bias voltage. A description of the model, followed by experimental validation will be explained in this chapter. In chapter 5, this model will be mapped to the swing phase of the walking cycle and it will be used to estimate the change in the behavior of the knee joint, in order to determine the effect of DE energy harvesting on the joint reaction moments of the wearer.

4.5.1 Damping Simulation: Free oscillation waveform

As described previously, the DE energy harvesting affects the stiffness and mechanical damping of the host system. During the swing phase, this behavior can be observed, not only through the force/extension curves described in the previous section, but also through the vibration response of the knee joint when the device is selectively activated. A dynamic model of the knee joint test stand has been developed, using the measurements described previously. The purpose of the model is to verify the behavior of the DE energy harvester on the test stand, and provide a means to apply the force/extension results to the swing phase of the walking gait. These results will then be used to estimate the physiological behavior on a human knee joint for increased energy harvesting capabilities. To this end, the model was designed to include the significant behaviors of the knee without focusing on minute behavioral anomalies of the test stand itself. As the swing phase involves the lower leg undergoing a pendulum type motion, rotating primarily about the knee, a free oscillation of the knee joint test stand is utilized.

A one degree of freedom state space model of the free angular vibration based on the motion measurements from the knee joint test stand was developed using the following set of equations:

$$\begin{aligned} u_1 &= \dot{\phi} \\ u_2 &= \ddot{\phi} = \frac{-k\left(\phi - \phi_0\right) - c\dot{\phi} + M_M}{I} \end{aligned} \tag{4.28}$$

where k and c were selected based on empirical measurements of the knee joint test stand, and M_M is the moment due to the Maxwell stress. This moment is determined based on the force generated by the Maxwell stress and the effective distance from the link connection point on the tibia and the knee joint, $M_M = F_M \bullet D$. The force generated by the Maxwell stress F_M is modeled

for the fully constrained condition: $F_M = \varepsilon \frac{x_{20} V^2}{x_{23} \lambda} R_{EL}$, where λ is found as a linear function of angle based on the endpoint stretch ratios, which were found experimentally using capacitance measurements, and R_{EL} is the ratio of the effective length of the DE material relative to the entire stretched length. The distance D is the perpendicular distance from the measurement location to the knee joint. The oscillation simulation was performed numerically in MATLAB based on this model using the ODE23 built-in function which applies the 2nd and 3rd order Runga-Kutta formulas to numerically solve the system of ODEs from eq. 4.28.

The behavior of the model was tuned to closely resemble the measured behavior of the knee joint test stand, as seen in Table 4.7

Table 4.7: Comparison of damped oscillation characteristics for test stand and model

	ω_d (rad/s)	k_r (N-m/rad)	ζ_r
Experimental	12.06	3.65	0.06
Model	12.02	3.59	0.07

The loading due to the charging of the DE was performed in a bang-bang style, where M_M was turned on at maximum stretch and off at the minimum stretch. The occurrence of minimum and maximum stretch was determined based on the angular velocity's vicinity to zero. The MATLAB code used to implement this oscillation simulation can be found in Appendix C.2, and the results of the simulation for the Polypower DE device charged at 3000V can be seen in Figure 4.23.

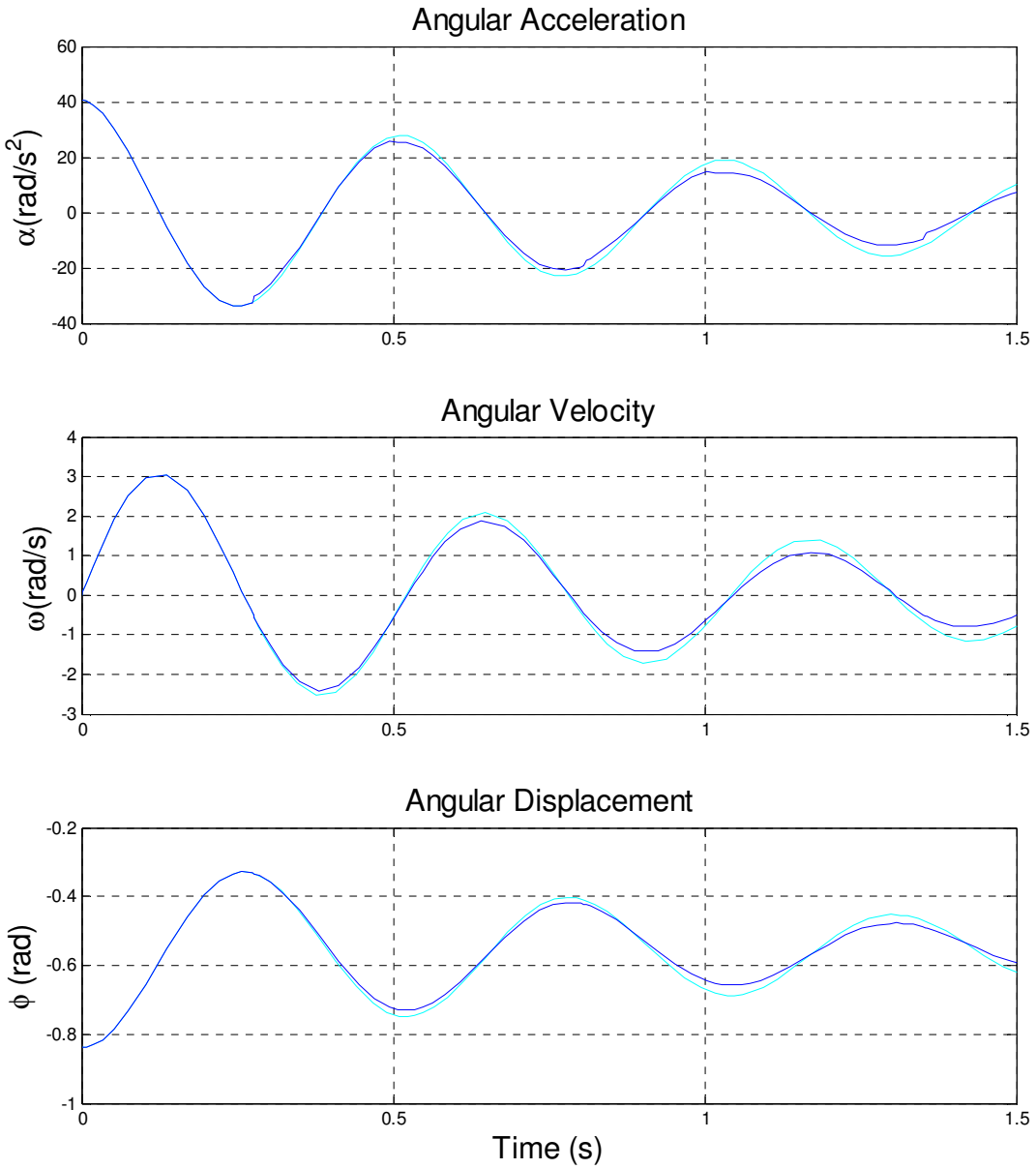

Figure 4.23: Oscillation Simulation Response due to 3000V energy harvesting (uncharged DE – light blue, charged DE – dark blue)

The effects of the Maxwell stress are most pronounced in the acceleration curve, as seen in Figure 4.24, which shows a close up of the acceleration due to the first charge and discharge cycle.

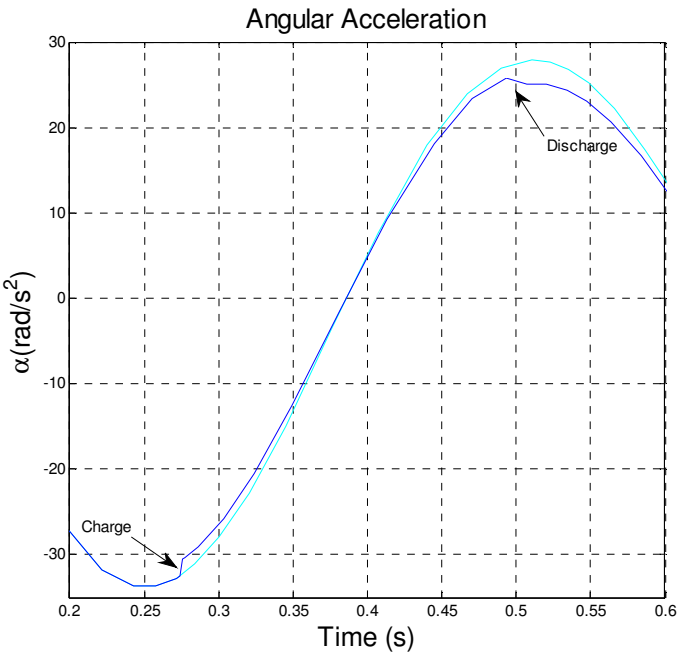

Figure 4.24: Close up of first charging and discharging cycle of the oscillation simulation. (uncharged DE – light blue, charged DE – dark blue)

The effects of DE energy harvesting can also be seen in the simulated velocity and displacement curves, where the moment generated by the Maxwell stress results in an increase in the damping, and a decrease in the damped natural frequency. The change in the damping and frequency of oscillation were found from the simulated angular position results using the values demonstrated in Figure 4.25.

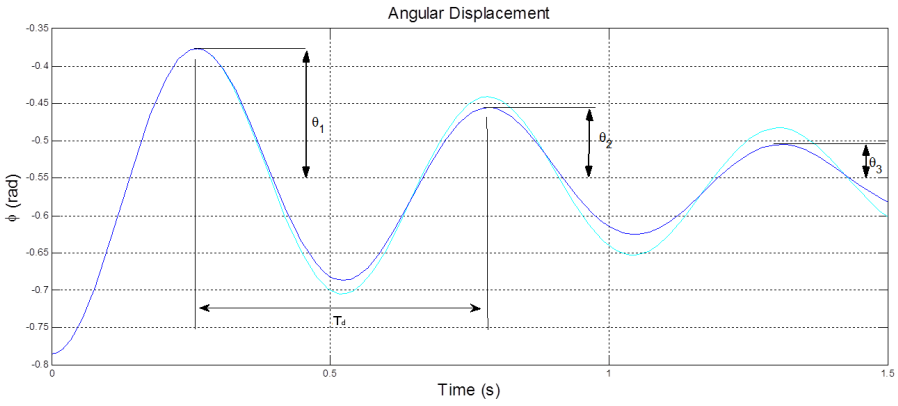

Figure 4.25: Simulated angular displacement as used for calculating ζ and ω_d.

The damping was found using the logarithmic decrement of the amplitude of the peaks for each subsequent oscillation: $\varsigma = \ln\left(\frac{\theta_i}{\theta_{i+1}}\right)$, and the damped natural frequency was found using the period between subsequent peaks: $\omega_d = \frac{2\pi}{T_d}$. Using ω_d along with the mass moment of inertia, the modified stiffness could be found: $k = I\omega_d^2$. This is then used with the damping ratio to find the equivalent hysteretic damping coefficient: $h = 2\varsigma k$. The equivalent damping ratio determined from the simulation could then be compared with the values measured on the knee joint test stand.

4.5.2 Comparison of damping calculations and experimental measurements

The angular hysteretic damping coefficient, h_r measured from the Force/Extension tests is compared with the DE energy harvesting calculation from eq. (4.27) and oscillation simulation describe above in Table 4.8.

Table 4.8: Rotational hysteretic damping coefficient, h_r, for DE energy harvester (V_c=3000V, A=1.1 m).

	h_r
Extension / force curve	0.222
Energy calculation	0.1763
Oscillation simulation	0.1093

Once the equivalent hysteretic damping coefficient is known, it can be used to determine other key parameters such as the loss factor, or $\tan\delta$, which allows a means to compare the behavior of an active DE energy harvester to that of standard viscoelastic materials.

4.6 Summary

The purpose of this objective was to demonstrate that the transformation of mechanical energy to electrical energy from a system using a DE energy harvester has a quantifiable effect

on the mechanical behavior of the system. This was demonstrated initially through measurements of the force vs. extension of a uniaxially activated DE thin film, and then further developed through force vs. extension and free oscillation measurements of a biofidelic knee joint ergometer. For both situations, the hysteretic damping coefficient was determined as a function of the electrical and mechanical parameters which govern the maximum energy harvested from the device. For the knee joint, an oscillatory simulation of the knee joint was also developed which incorporated both the internal damping of the knee joint, and the behavior of the knee joint. The significance of these results will be developed in Chapter 5, as the biokinetic effects of changes in the stiffness and damping of the energy harvester are further developed.

5 Beneficial DE energy harvesting during walking

5.1 Introduction

The previous chapters have shown that the level of energy harvesting is a function of geometry, electrical loading conditions and material properties. In addition, a method for relating the energy harvested to damping has been developed, providing a means for managing the damping due to energy harvesting within a structure using coordinated electrical loading. The purpose of the final objective of this research is to use a musculoskeletal model of the lower body to investigate the possibility of limiting the metabolic expenditure required to harvest energy from walking through careful coordination of the electrical loading of a DE energy harvester with the mechanical motion of the walking stride. The results of this empirically based modeling are significant as they present a description of how DE materials can be used in conjunction with knee joint kinetics to effectively harvest energy and establish the feasibility of beneficial energy harvesting during walking using a wearable, electroactive smart material.

This chapter begins by describing the kinematics and dynamics of the healthy walking gait cycle. Based on the kinetics of the lower limbs during walking, it is clear that the knee joint is the most promising for applying beneficial energy harvesting. Therefore, understanding the behavior of the knee provides the means to synchronize the DE harvester operation with the rotation of the knee joint. This coordination is demonstrated through the mapping of the DE loading pattern onto a plot of the intersegmental kinetics of the knee joint. This timing is determined by incorporating the information about DE harvesting developed during the previous two objectives with an investigation of lower limb kinetics during walking. Based on this information, electrical loading patterns for a DE generator placed in several orientations across the knee joint are developed which selectively energize the device such that harvesting occurs

when it is beneficial to the wearer. Using these, the preferred location, orientation and electrical loading pattern of the device will be determined.

Two suitable loading patterns are evaluated based on the kinematic conditions, and the behavior of the most promising is modeled using a biomechanical model which has been developed to simulate the knee going through the gait cycle. This biofidelic model, which determines the energy expenditure of the knee during the charged phase of the DE energy harvesting cycle, is developed using the results from the test stand described in section 4.4, and publicly available human walking gait data. Employing this model, the expected energy expenditure is simulated for increasing energy harvesting based on two key electrical parameters, permittivity and charge voltage. Comparison of the energy expenditure estimations demonstrate the effectiveness of carefully timed DE harvesters for performing beneficial energy harvesting.

5.2 Bipedal motion: the walking gait cycle

5.2.1 Knee joint kinematics during walking

Human bipedal walking occurs in a cyclical fashion, where most people walk in a very repeatable manner. The patterns in this motion have been measured for a large number of healthy individuals, and normal gait patterns have been determined for healthy individuals depending on age and gender. The similarities between the majority of people's gait make it possible to use a normal gait baseline profile to compare the effects of modifications to the gait which may occur either through internal influences such as muscular or neurological dysfunctions, or through external influences such as a heavy backpack, a foot orthotic or a knee brace.

Generation of these normative kinematic curves comes from empirical measurements; several different techniques can be used for this type of motion, ranging from direct joint

kinematic measurements using goniometers and accelerometers, to global position measurements using markers and vision systems. In all cases, the final result is a joint angle path profile which can be used to determine the position, velocity and acceleration of the segments as a function of time. Figure 5.1 shows a normal knee joint profile, plotting the knee position and velocity as a function of gait cycle. The phases of the walking cycle (stance and swing phase), along with key events (heel strike and toe off) are shown for the right leg relative to the knee joint kinematics.

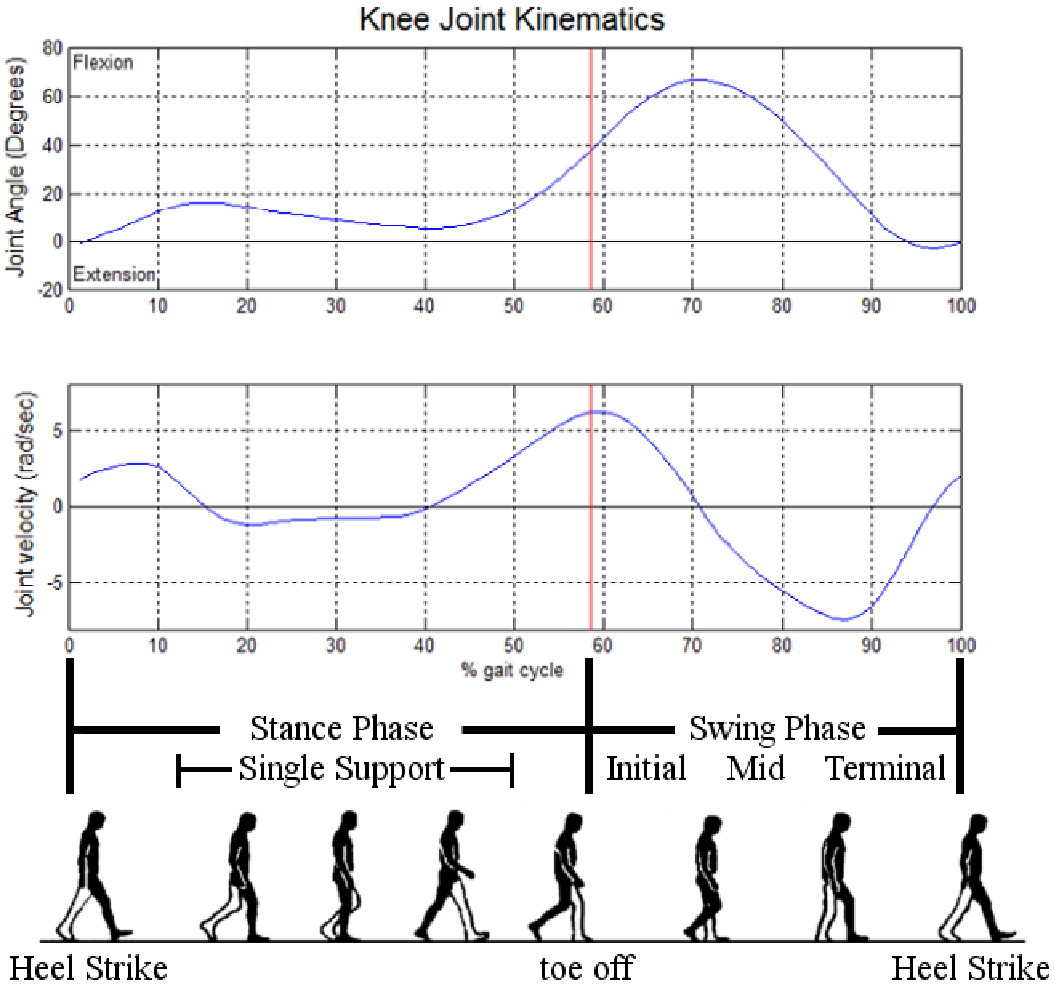

Figure 5.1: Knee joint angular position and velocity for one cycle of the walking gait (generated from data in [10]).

An understanding of the knee joint kinematics is essential for the research presented here. Recalling that the energy harvesting capacity of a DE energy harvester is directly related to the

stretch which it experiences, it is clear that the knee joint position profile will play a very important role in determining how to coordinate the timing of the electrical loading of the device. Because of the large stretch requirement, it is clear that the charging of DE device must occur during the swing phase of the gait cycle, when the knee joint experiences a very large flexion followed by an extension of over 60°. Selection of the location of the DE material as described in section 4.4, either across the front or the back of the knee joint, will further dictate whether the energy is harvested during the flexion or the extension of the knee joint.

5.2.2 Potential, kinetic and metabolic energy during walking

Walking is a cyclical motion that involves a series of kinematic events which occur at regular intervals. When the overall motion of the body is considered in terms of the energy of the center of mass, the relationship between the kinetic and potential energy can be used to help understand the distinctions between walking and other types of bipedal motion.

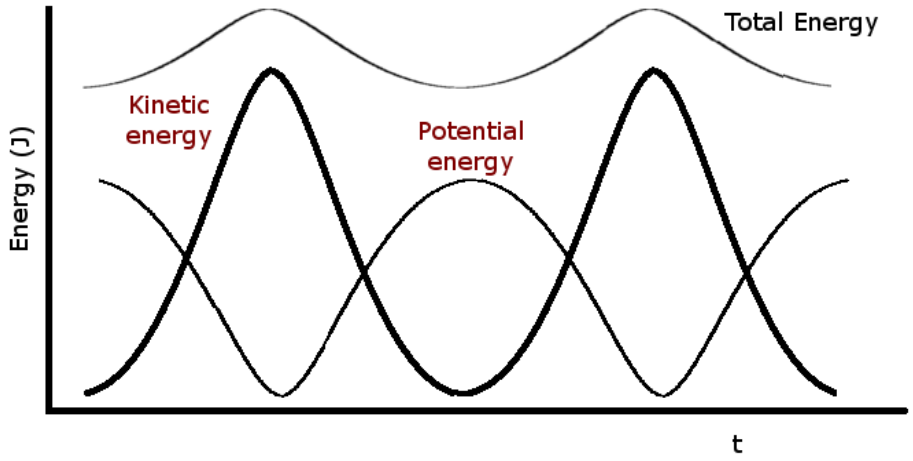

Figure 5.2: Comparison of kinetic and potential energy of the center of mass during walking

In walking, unlike running, jumping, skipping etc., kinetic and potential energy are out of phase, similar to a pendulum, as shown in Figure 5.2. Consequently, there is a constant conversion of kinetic energy to potential and back again, which greatly increases the efficiency

of walking, as the kinetic energy is transferred and stored as potential energy as the height of the center of mass (c.m.) increases, and is then returned back to kinetic energy as the c.m. moves to its minimum point. However, unlike a conservative pendulum, where the total energy of the system remains constant, in walking, only a portion of the kinetic energy is stored as potential energy and with each stride, the total energy of the system oscillates as kinetic energy of the c.m. is absorbed by the muscles, and then muscular activity increases the energy of the c.m. again [143]. In addition to the energy of the c.m., since the body does not act as a single rigid body, but as a system of many segments, there is a large amount of internal work that is done within the body. The muscles must expend a large amount of work in speeding up and slowing down the individual limbs in order to create the forward motion of the c.m [142]. This internal work done by the muscles is significant, as it plays an important role in the overall work done by the muscles during walking, and it indicates that there is a large amount of metabolic energy expended by the muscles to absorb kinetic energy of the limbs which could potentially be harvested.

5.2.3 Joint dynamics during walking

The internal work done by the muscles is a very important concept in the development of a beneficial DE energy harvester. All work done by the muscles, whether it involves energy generation or energy absorption requires metabolic expenditure by the muscles, therefore, it is the overall magnitude of the power required, regardless of whether is positive or negative work which determines the energy expenditure of the muscles and the overall efficiency of the motion.

Concentric muscle contractions occur when the moment generated by the muscles in the same direction as the velocity of the limb. The net power of concentric contractions are considered positive. Conversely, when the moment generated by the muscle contraction is in the opposite direction of the velocity of the limb, an eccentric muscle contraction is performed, and the net power is negative. Figure 5.3 highlights the period during the walking gait cycle when the muscles are contracting concentrically vs. eccentrically. It is important to note that during the majority of the gait cycle, the knee joint muscles are contracting eccentrically, and hence, negative work is being performed.

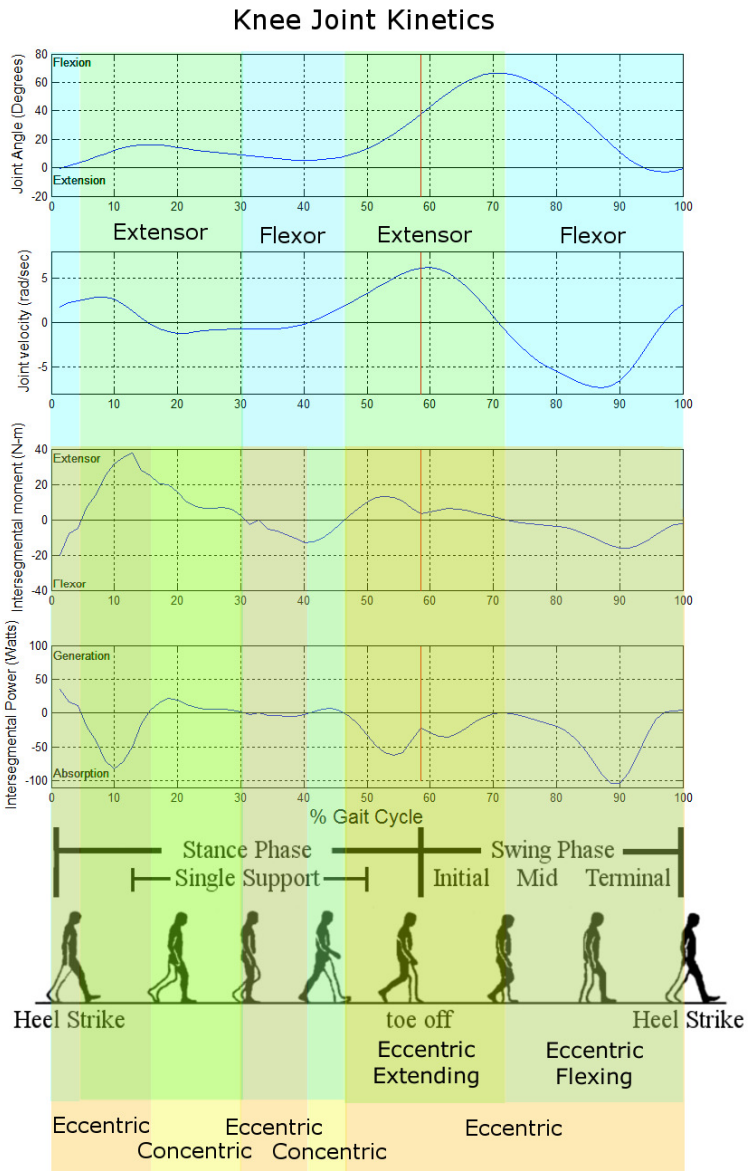

Figure 5.3: Knee joint kinetics; (generated from data in [10]). extensor moments highlighted in green, flexor moments in blue; concentric loading highlighted in orange, eccentric loading in red.

While knee kinematics and kinetics are very important for understanding the behavior of the muscles while undergoing an action, the most important variable for determining the functional role of the muscles is the mechanical power [144]. This is because the power profile incorporates both the forces acting on a specified joint (or the forces within specific muscles) and the direction in which the motion is occurring. The power profile is generated through the

combination of the kinematic and kinetic data, where the power is the scalar value found by multiplying the angular velocity by the moment, $P = \omega M$. Once the power profile is known, integration over a specified portion of the cycle to find the work done by the muscles during that motion provides a single variable which can be used to gauge specific functions during the gait cycle [144]. For example, integrating the ankle power during the last 20% of the gait cycle results in a very large positive energy during that time, indicating that the muscles are undergoing concentric loading, therefore, mechanical energy is being generated by these muscles and then transferred across the ankle joint into the leg segment. On the contrary, the muscles associated with knee joint during this same period of time are undergoing eccentric loading, resulting in a net negative energy over this same period of time, signifying that much of the energy that was transferred through the knee is now being absorbed by the knee joint [142].

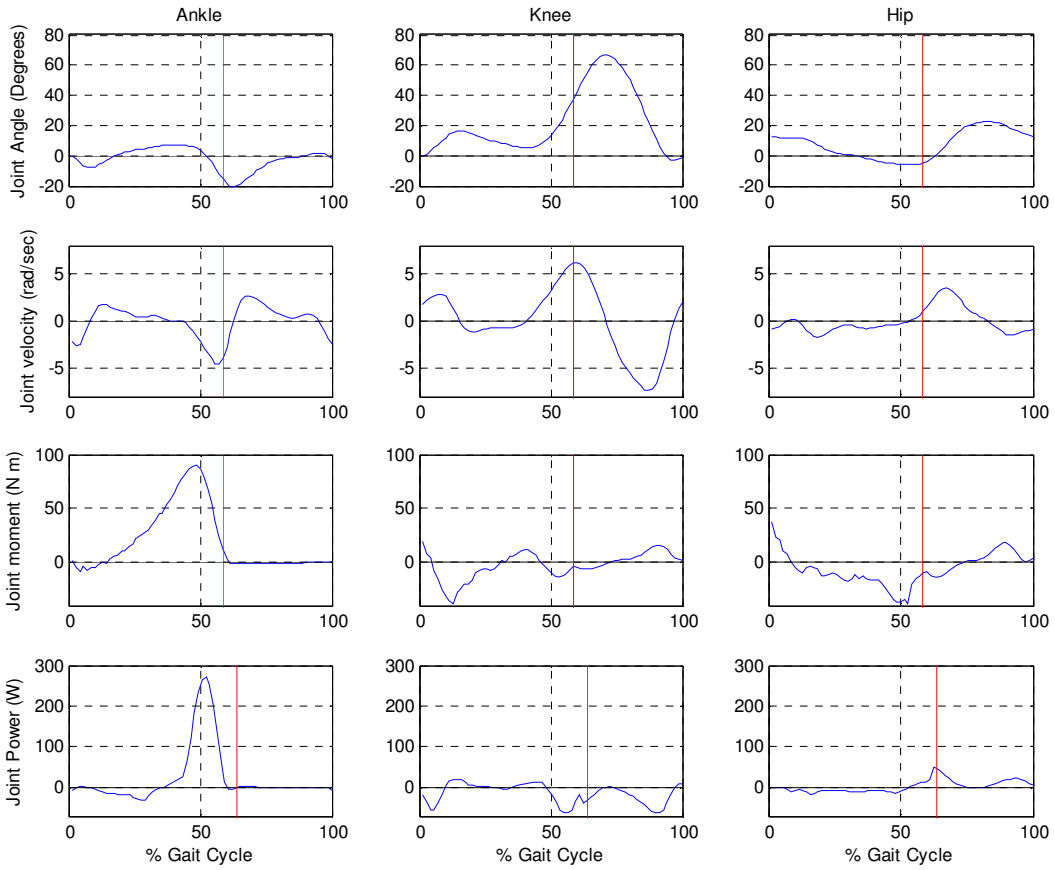

Figure 5.4: Characteristic joint motions (generated from data in [10]). The redline refers to toe off as shown in Figure 5.1.

The power profile provides a helpful tool for evaluating the possibility for beneficial energy harvesting. Since muscles expend metabolic energy whether they are acting concentrically or eccentrically, an external device which reduces the magnitude of the power over any period in time will reduce the overall energy requirement. Therefore, when the muscles are working eccentrically, absorbing energy to slow down motion, external damping which absorbs unwanted energy leads to a decrease in the energy requirement during that portion of the gait cycle. This is the foundation for beneficial energy harvesting, which coordinates the removal of energy from the joint to align with periods of large negative work, reducing the overall energy requirement of the muscles during that time.

Comparison of the ankle, knee and hip power profiles in Figure 5.4 shows that during the swing phase of the gait cycle, only the knee is predominantly undergoing negative work. This is consistent with the overall behavior of the knee compared to the ankle and hip, where the intersegmental power at the knee is predominantly negative. In fact, the knee only performs 4% of the positive work during walking, with the hip contributing 43% and the ankle 53% [143]. Clearly, the primary role of the knee throughout the entire gait cycle is to stabilize the motion of the lower leg by transferring and absorbing energy across the knee joint, making it an ideal candidate for beneficial energy removal. Equipped with this analysis of normal knee joint behavior, the investigation now turns to how to utilize this motion for beneficial energy harvesting.

5.3 Beneficial energy harvesting

The idea behind beneficial energy harvesting comes from the study by Liang [132] of piezoelectric energy harvesters and their role in structural damping, which built on the work of Hagood [133]. It was further developed by Li et al. with the introduction of the Bionic-Power exoskeleton which uses a clutch controlled DC generator to time the conversion of energy so that it only harvested energy when it is beneficial to the motion [23]. The research presented here builds on these ideas with the primary distinctions being the means for providing energy harvesting and the amount of energy predicted to be harvested. Rather than a stiff articulating device which has the potential to harvest large amounts of energy (> 20W) during big motions such as climbing down hills, the DE generator, is a soft elastomer base fabric is used to harvest energy in the range of 0.1 – 2.0 W during every day motion. The goal of this research is to demonstrate that it is in fact, feasible to use dielectric elastomer energy harvesters for collecting energy from human motion in a manner that provides beneficial damping.

As described in section 2.3.1, in order for energy harvesting to be beneficial to the wearer, the conversion and storage of mechanical energy must be carefully aligned with the lower limb kinematics and kinetics described in the previous section in such a way that energy is only removed from the system when the muscles are expending energy to absorb energy to control the motion of a limb segment.

Based on the required electrical loading patters of a DE energy harvester, as described in Figure 3.27, two possible DE energy harvesting loading cycles are mapped onto the human walking stride in Figure 5.5. The mapping is performed by taking into consideration the required conditions for beneficial DE energy harvesting including: large angular displacement, eccentric muscular activation and DE charge at stretch and discharge after relaxation. Based on these requirements, two different electrical loading patterns were determined, one for each of the mounting locations described in section 4.4.3.

The first loading pattern represents energy harvesting for a knee joint located on the front of the patella. In this orientation, the DE is fully relaxed when the knee is extended and is stretched when the knee is flexed. The second curve displays the loading cycle for a DE device placed along the back of the knee joint, in this case, the DE is relaxed when the knee is in flexion and stretched when the knee is in extension. In both figures, the green portion of the curve shows when the DE material is stretched, and the pink area shows where it is relaxed. In both cases, the device is charged at the specific point in the stride when the stretch of the DE is at its maximum, and then is discharged after the material has relaxed.

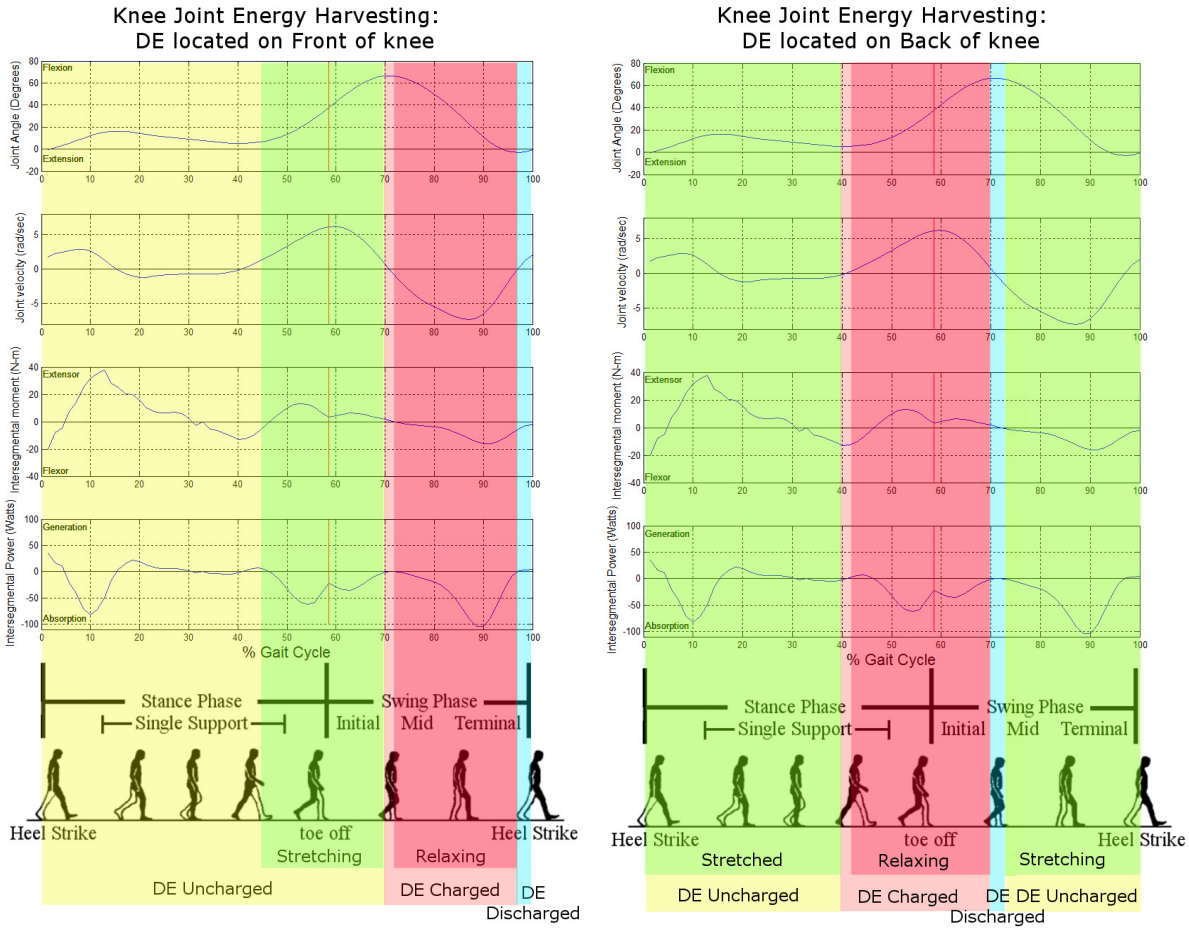

Figure 5.5: Mapping of DE energy harvesting to the swing phase of the walking stride for DE harvesting device located on front and back of the knee (generated from data in [10]).

Both of these loading patterns could be utilized to perform beneficial energy harvesting, however, further investigation of the intersegmental power indicates that the negative work done by the knee during the mid and terminal swing phases is substantially higher than that in the initial swing phase. In addition to this, the very high peak in the ankle intersegmental power just before toe off (Figure 5.4) suggests that a large amount of energy is transferred from the ankle to the knee during this time, and high levels of damping may adversely affect the knee moment during that time. For these reasons, it is determined that a DE positioned on the front of the knee is the preferred location for the primary source of beneficial energy harvesting, with a DE located on the back of the knee used as a back-up or auxiliary device. Based on this assessment,

investigations into beneficial energy harvesting throughout the rest of this work focuses on DE devices located on the front of the knee joint.

5.4 Simulations of the effects of DE energy harvesting on walking

In order to estimate the effects of the DE energy harvesting process on the biomechanics of the knee, the knee joint behavior without a DE energy harvester is compared with the response of the knee when undergoing energy harvesting. This comparison is completed using a two-part simulation which involves 1) a biologically based model of the knee joint behavior based on measurements of a healthy gait cycle and 2) a joint dynamics simulation utilizing the stiffness and damping representation of the energy harvesting develop from the pendulum oscillation model described in section 4.5. The interaction of the different components involved in this process can be seen from the flowchart in Figure 5.6. This flow chart demonstrates the major tasks associated with the biokinetic simulation. It begins with both experimental inputs and material properties (parameter inputs). The experimental inputs are used with a musculoskeletal model, which will be described in section 5.4.1, to determine the inverse dynamics of a healthy gait cycle. The parameter inputs will define all of the necessary material properties and boundary conditions for the oscillation simulation, described previously in section 4.5, which provides an estimation of the changes in the stiffness and damping due to the DE energy harvesting. Finally, results from both of these are combined in the knee joint simulation model to estimate the knee joint power requirements during the swing phase of the gait cycle, which then can be used to describe the relationship between intersegmental power and DE energy harvesting.

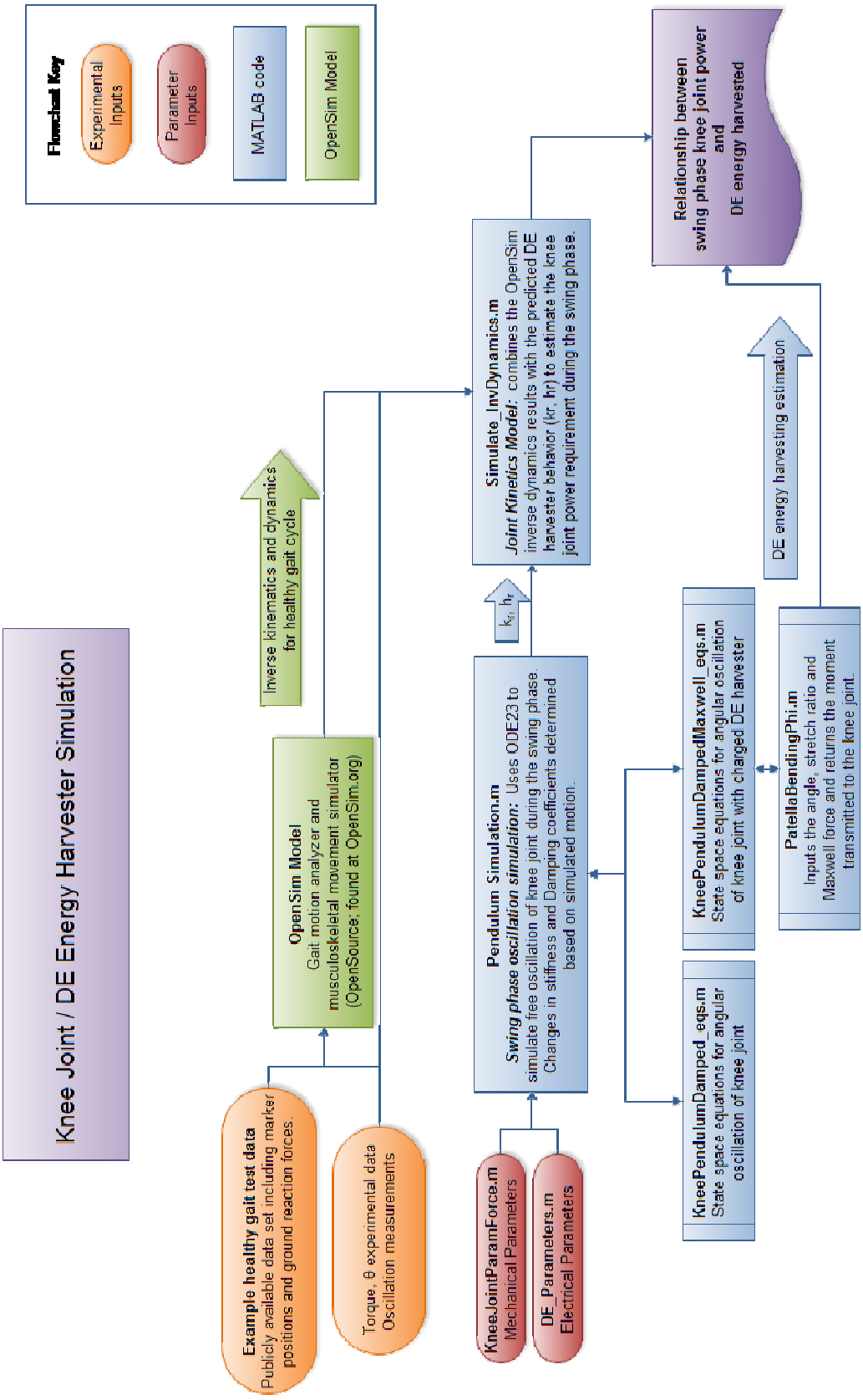

Figure 5.6: Flowchart of the knee joint DE harvesting model

The process depicted here utilizes a open source musculo-skeletal model called OpenSim and a series of MATLAB codes based on the modeling described in chapters 3 and 4. The OpenSim model will be described in next section, and the MATLAB joint simulation will be described in the succeeding section. Following these descriptions, in section 5.5, simulated results for increased energy harvesting based on improvements to key electrical parameters will be presented to demonstrate the feasibility of beneficial energy harvesting using soft wearable electroactive materials such as DE.

5.4.1 Musculo-skeletal OpenSim model

OpenSim is a biomechanical modeling and simulation program developed by the National Center for Simulation in Rehabilitation Research. It provides a common platform for creating and simulating musculoskeletal models within a wide range of biomechanical fields including rehabilitation, orthopedics, robotics, and ergonomics. In order to simulate the effects of energy harvesting on human motion, OpenSim 3.0 is used to provide baseline joint torque values and to verify a joint dynamics model developed in MATLAB to predict the changes in the joint torques of the knee joint as a result of different levels of energy harvesting using the DEG.

The OpenSim simulations are performed using a scaled measurement based model of the lower body (Gait2354_Simbody) and a set of marker data for a single, representative test subject (this data is available as part of the OpenSim package). The basic biomechanical model is comprised of bodies, joints, forces and markers. The muscles are individually modeled as specially defined forces which have prescribed attachment points and dynamic behavior. Figure 5.7a,b show the muscles associated with extension and flexion of the knee.

The process for determining the joint motions and moments involves first scaling the model based on the size of the subject from whom the marker data was recorded, using the

distance between two specified markers. The static marker data provided in Gait2354_Simbody contains marker locations for the lower limbs of a 72.5 kg person undergoing a normal gait cycle. The scaled model then utilizes the distances from statically measured marker locations (which are associated with externally visible anatomical landmarks) to the internal anatomical coordinate systems relating to each segment (see Figure 5.7c for the coordinate systems relating to the left hip, knee and subtalar joints, where the z axis (green) is perpendicular to the sagittal plane, and the y axis (yellow) is oriented along the represented bone segment).

The movement marker data is then transformed through inverse kinematics to determine the relative movement between segments, and hence the relative joint angles between them. This data is provided in three dimensions, however, for many of the joints in the body which behave as pin joints, there is a primary axis of rotation within which most of the movement occurs. In the case of the knee joint, the predominant rotation occurs about the z axis as flexion and extension within the sagittal plane.

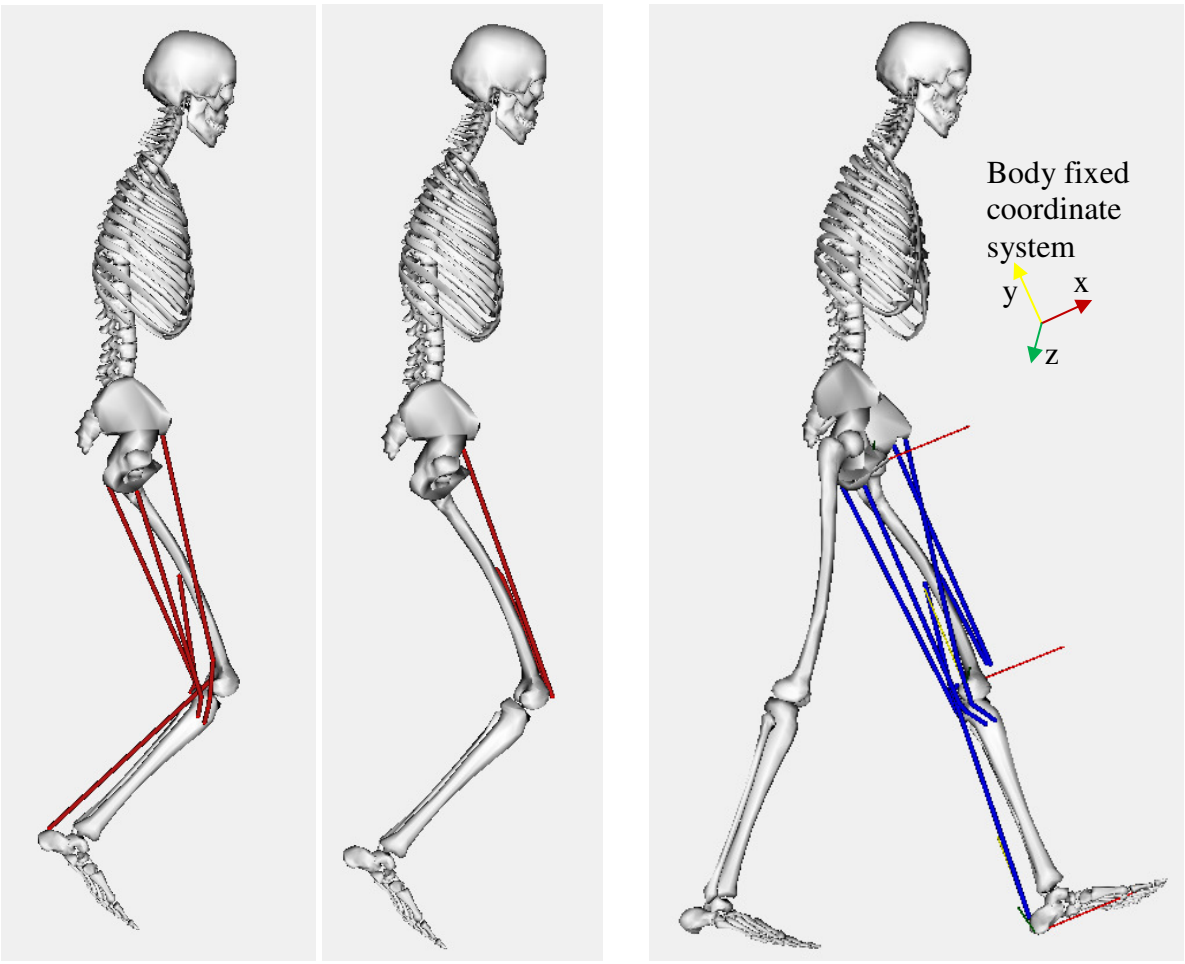

a) knee extensors **b) knee flexors** **c) left knee joint at full extension**

Figure 5.7: OpenSim Muscle Groups associated with knee motion (software screenshot)
a), b) Shown just before knee swing phase begins, t=0.965s; c) shown at heel contact, t=1.2s

Once the kinematics of the motion has been established, ground reaction forces which were measured along with the marker data can be used to perform inverse dynamics calculations which provide the joint reaction forces and moments related to each limb segment. This process generates the characteristic kinetic profiles of each of the lower limb joints (similar to the intersegmental moments displayed in the third row of Figure 5.4).

These profiles provide the baseline for the analysis of the effects of the energy harvesting DE located at the knee joint. In order to compare the energy expended by the knee with active DE harvesting to that of a normal knee, the behavior of the DE is coupled to the measured

moment in OpenSim using a built in force called a bushing force. A bushing force in OpenSim is specifically designed to model forces which are a function of displacement and velocity. It is comprised of a force which is applied at a specified location and is defined in terms of linear and rotational stiffness and damping terms which can be defined in all 3 directions. In modeling the DE harvester, the bushing force is positioned at the knee joint and it is defined based on the relative motion between the femur and the tibia, with full extension occurring at $\theta = 0$, hyperextension at $\theta < 0$. and flexion at $\theta > 0$. The translational forces are all defined as zero, and the rotational stiffness and damping terms are applied to the bushing force model in the z direction, corresponding to the flexion and extension motion of the knee (See Appendix C for the OpenSim bushing force code). The values used for the rotational stiffness and damping terms defined in the bushing force were found using the oscillation model described in Section 4.5 (also see Appendix C: Pendulum_Simulation.m).

In the OpenSim model, the joint loading is locally applied to the knee joint, and the effects are not transmitted to any of the other joints due to this external load. For much of the gait cycle, especially during the stance phase, this assumption may not be valid, as there is a clear dynamic link to the ground reaction forces from the ankle, to the knee and hip. However, for the front located energy harvesting scheme (Figure 5.5 a), the DE is active during the swing phase of the gait cycle, and throughout this phase, the energy transfer from the knee to the ankle is negligible. Therefore, the OpenSim model is considered appropriate for analysis during this phase. A comparison of the intersegmental moment generated at the knee due to normal walking with and without an uncharged DE device are shown in Figure 5.8.

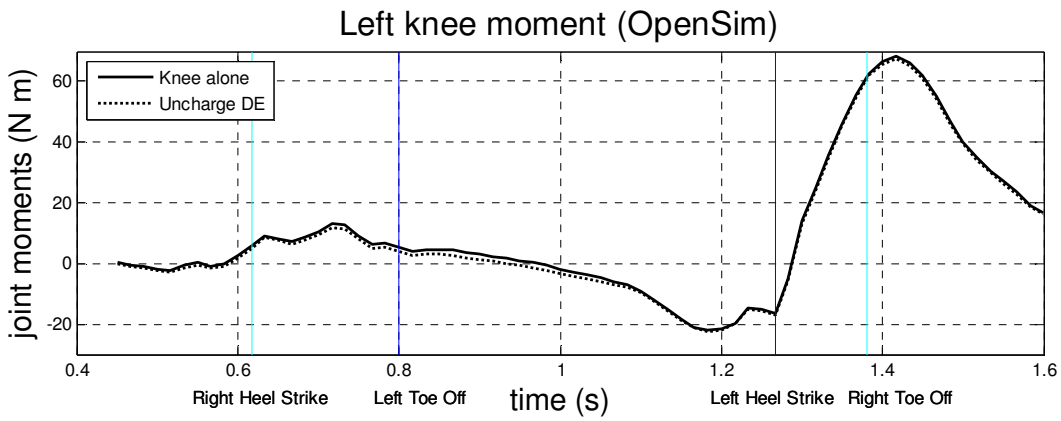

Figure 5.8: OpenSim moment calculations for the healthy knee (from measurements) and the same knee with a DE generator (from modeling)

It can be seen by comparison between this figure and Figure 5.3, that the effect of the uncharged DE device are most prominent during times of eccentric loading, and a close inspection reveals that the time from 0.9 s to 1.2 sections, which corresponds to the extension part of the swing phase, the proposed duration of the DE charge.

5.4.2 Joint Loading simulation

The rotational stiffness and damping coefficients used to define the bushing force in OpenSim are constant with time, so it is not possible to use this force to model the discrete mechanical loading due to the Maxwell stress generated during charging and discharging. Therefore, a MATLAB based joint kinetics model has been developed to determine the knee joint intersegmental moment due to a charged DE throughout the entire walking cycle. This model was based on the methodology used in OpenSim and was verified for both the stiffness and damping components. Using this methodology, the moment generated by the DE was found in the joint dynamics model as a summation of the moment caused by the stiffness and the damping induced by the device:

$$M_{k_r} = k_r \theta$$
$$M_{c_r} = c_r \dot{\theta} \tag{5.1}$$
$$M_{DE} = M_{k_r} + M_{c_r}$$

The loading moments calculated using the MATLAB joint dynamics model are compared with the OpenSim loading moments in Figure 5.9. The sold red and dashed black lines are nearly identical, verifying that joint dynamics model of the DE device is equivalent to the OpenSim bushing force model.

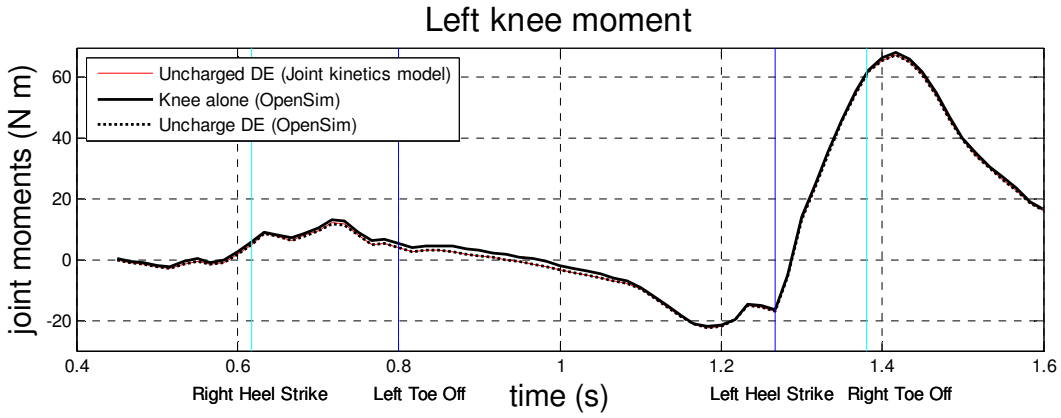

Figure 5.9: Comparison of OpenSim results with MATLAB joint dynamics simulation for moment due to stiffness and damping applied at the knee joint.

The DE harvester behavior is modeled in two parts; the first segment corresponds to the uncharged behavior of the DE harvester and relates to the mechanical properties of the device. The second component is associated with the charged behavior of the device and it relates to the electromechanical coupling during energy harvesting. The transition between the unloaded and loaded conditions is determined based on time, since the time at which the DE material should be charged and discharged is known a priori. At the onset of the extension portion of the swing phase, when the knee joint flexion is at its peak, the stiffness and damping coefficients for the model are modified to reflect the behavior of the charged device. At the end of the swing phase, before the left heel strike occurs, the stiffness and damping coefficients are returned to their

original values, corresponding to the uncharged DE device. Therefore, the additional loading experienced by the knee joint due to the DE device is defined as such:

$$M_{DE} = \begin{Bmatrix} t < t_c & M_{k_{DEbaseline}} + M_{c_{DEbaseline}} \\ t_c \le t \le t_d & M_{k_{DEactive}} + M_{c_{DEactive}} \\ t > t_d & M_{k_{DEbaseline}} + M_{c_{DEbaseline}} \end{Bmatrix} \tag{5.2}$$

and the total moment at the knee joint becomes the summation of the measured intersegmental knee kinetics and the moment due to the DE device: $M_{KneeTotal} = M_{Knee\,Kinetics} + M_{DE}$.

This joint dynamics model provides a means to quantify the energy requirement at the knee joint to operate a DE harvester. Recall that the intersegmental power profile can be found using the velocity and moment profiles. With the estimation of the moments, only the velocity profile needs to be determined. Since this analysis seeks to determine the change in the energy expenditure at the knee joint when the kinematic profile remains unchanged, the velocity profile is found by differentiating the original joint angles. Multiplying each point on the velocity and moment curves together over the gait cycle results in a power profile. By integrating the power profile, during the swing phase, the energy absorbed by the knee during extension is determined. This energy term can then be used to characterize the effect of different levels of DE energy harvesting, the more energy which is harvested from the system, the less energy expended by the muscles at the knee to slow down the motion of the leg as it swings through its pendular trajectory. In the following section, extrapolation of the behavior for new DE materials with increased electrical performance will be simulated to investigated the feasibility and benefit of selective DE energy harvesting during the swing phase.

5.5 Extrapolation of energy harvesting capabilities to joint dynamics

The joint dynamics model described above allows for the calculation the energy absorbed by the knee during the swing phase, providing the means for quantification of the effect of the DE energy harvester on the knee. As described in section 5.2, the larger the negative energy at the joint during a motion, the more work must be done by the muscles to absorb energy while controlling the motion of the limbs. The objective of this research is to demonstrate the change in the energy expenditure at the knee joint due to DE harvesting, and to verify that it is feasible to use DE energy harvesting at the knee in a way that reduces the energy expenditure of the knee muscles.

This objective is accomplished by modeling the effects of increasing DE parameters which increase the energy harvesting capability of the device using the joint dynamics model described in section 5.4. In order to isolate the electromechanical behavior of the device from the purely mechanical behavior, the simulations are performed changing only electrical parameters. This means that the simulations are run keeping the mechanical properties of the DE device fixed and assuming that the kinematic profile remains the same, essentially asking the question: what is the change in the energy expenditure for a person walking with their normal gait profile as the energy harvesting increases due to changes in the electrical parameters alone?

Electrical parameters of a DE energy harvester which can be modified without affecting the mechanical properties of the device include the charging voltage (V) and the permittivity (e) of the dielectric. Both of these parameters have been found to have a significant effect on DE energy generation [91]. The charging voltage is a loading parameter which is dependent on the charging power supply, and its maximum value is limited by the breakdown voltage of the dielectric elastomer [124]. The permittivity is a material property of the dielectric elastomer, and

it is determined by the structure of the elastomer used, to date, a number of different fillers have been proposed to increase the permittivity of the device [93]. Other parameters which increase the energy harvesting capability of the device, such as material pre-stretch, or multiple layers, directly affect the mechanical properties of the device and will not be address in this investigation.

In order to simulate the effect of charge voltage (V) and permittivity (e) on the behavior of a DE device during energy harvesting, the oscillation model developed in section 4.5 was used to estimate the damping coefficient, h_r and stiffness, k_r, over a range of values. For each parameter selection, the values of the coefficients were incorporated into the joint dynamics model described in section 5.4.2, which simulated the changes in the device during the portion of the swing phase when the DE device was electrically charged while DE underwent relaxation.

5.5.1 Effect of voltage on energy harvesting and biomechanical energy expenditure

As described in eq. (3.83), the energy harvesting potential of a DE device is directly related to the square of the charging voltage, and should therefore also have a direct affect on the behavior of the DE material. It can be seen from Table 5.1, that as the voltage increases, the damping also increases and the stiffness decreases, these behaviors are consistent with the results measured on the knee joint test stand in section 4.4.3 for a DE device during energy harvesting.

Table 5.1: Extrapolated Behavior due to increase in charge voltage based on oscillation curve

	Voltage	ς	ω_d (rad/s)	h_r (N-m/rad)	k_r (N-m/rad)
Expt.	No DE		12	0.424	2.474
	nocharge	0.0785	11.8831	0.5719	3.686
Oscillation Model	2000	0.0766	11.9952	0.5592	3.6502
	3000	0.0864	11.9774	0.6287	3.6394
	5000	0.1225	11.8852	0.8947	3.5836
	7000	0.1965	11.7675	1.3909	3.513
	9000	0.3065	11.1615	1.8825	3.1605

10000	0.3066	10.6528	1.6902	2.8789

Each of these conditions are incorporated in to the joint dynamics model through superposition of the change in the damping or stiffness parameter to the healthy knee joint moment. The values of the parameters used in the joint dynamics model are found in Table 5.2.

Table 5.2: Input values for the joint dynamics model as a function of charge votage

voltage	Δh_r (N-m/rad)	Δk_r (N-m/rad)
0	0.114	1.189
2000	0.167	1.176
3000	0.237	1.165
5000	0.503	1.110
7000	0.999	1.039
9000	1.490	0.687
10000	1.298	0.405

When included in the joint dynamics model, the behavior of the DE material was altered during the swing phase extension. This behavior can be observed in the close-up plot of the swing phase moments in Figure 5.10, where the change in the intersegmental moment at the knee due to the charge voltage can be compared to the original response. Based on this modeling, as the voltage (and energy harvesting) of the DE material increases, the magnitude of the negative moment decreases, returning to the moment generated during the normal gait cycle, and then reducing even further. The power curves reveal the same trend, where the negative power at the knee joint decreases with increasing charge voltage.

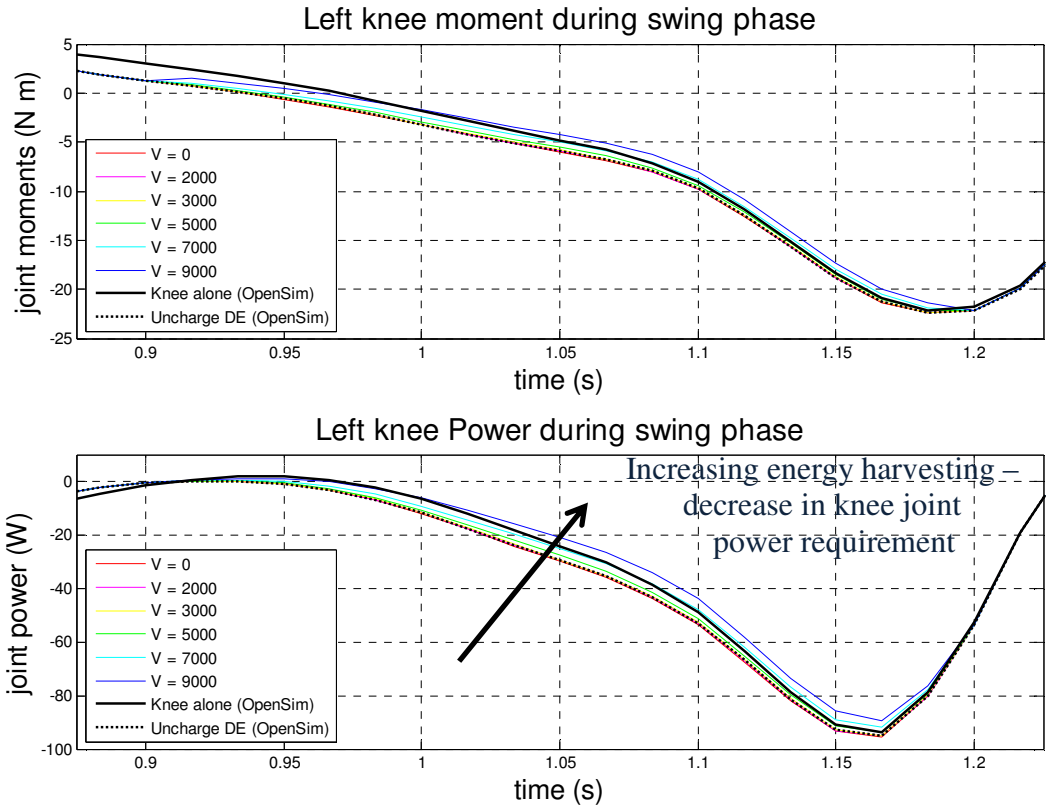

Figure 5.10: Moment and power curves of DE harvester for increasing voltage (e = 3.1)

The power curves displayed in Figure 5.10 can be integrated with respect to time in order to determine the total energy expended by the knee muscles during the swing phase extension.

$$E_{total} = \int_{t_c=0.9}^{t_d=1.2} P(t)\,dt \tag{5.3}$$

Once the total energy expenditure is determined, the difference between the expenditure of the knee without a DE device is compared with the energy expenditure of the knee with devices of increasing charge voltage. Subtracting the energy expenditure of the knee without the DE device quantifies the additional energy expended by the knee joint as a result of wearing the DE device.

$$E_{additional} = E_{total} - E_{total\ no\ DE} \tag{5.4}$$

Table 5.3 and Figure 5.11 both provide a comparison between the additional knee expenditure and the estimated energy harvested.

Table 5.3: Joint Energy expenditure (J) during swing phase compared with DE energy harvested (J) as a function of charge voltage.

Voltage	Joint Energy Expenditure	Additional Knee Joint Energy Expenditure	Energy Harvested
No DE	9.06	n/a	n/a
0	10.11	1.05	0
2000	10.05	0.99	0.05
3000	9.98	0.92	0.11
5000	9.69	0.63	0.30
7000	9.19	0.13	0.60
9000	8.42	-0.65	0.99

Based on these results, it is clear that there is a direct relationship between the amount of energy harvested and the reduction in the energy expenditure during the swing phase extension, which is based on the quadratic relationship between the voltage and the energy harvested. This relationship is clearly seen in Figure 5.11.

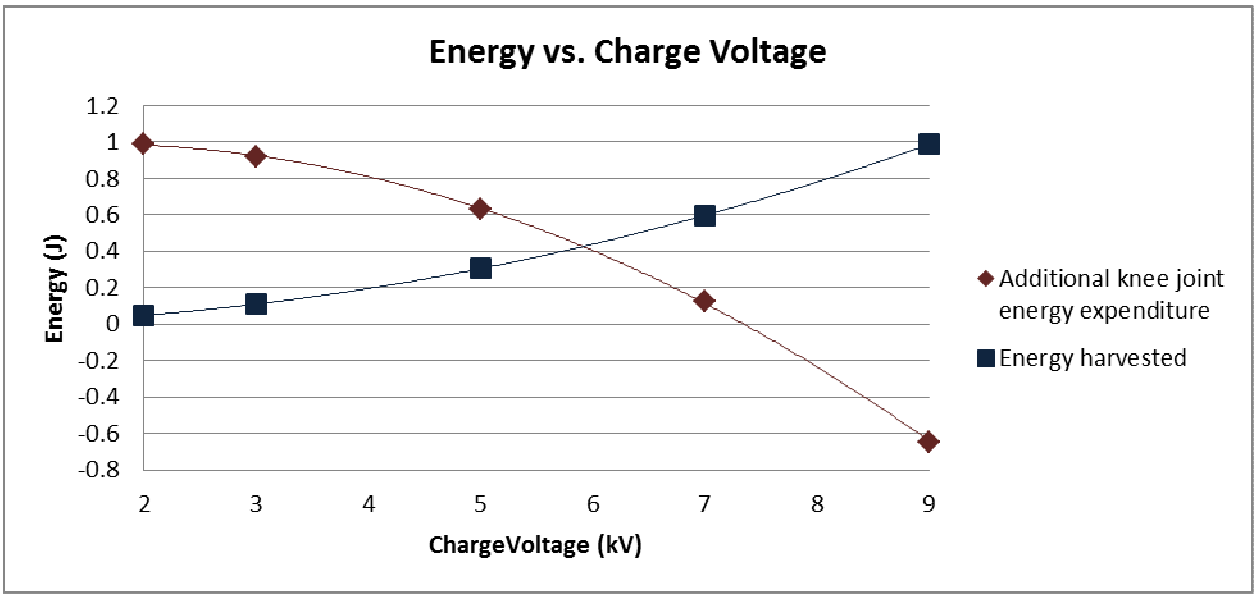

Figure 5.11: Joint Energy expenditure (J) during swing phase compared with DE energy harvested (J) as a function of charge voltage.

The negative additional energy expenditure for the V = 9000V case demonstrates that it is possible for the energy removed from the knee as a result of DE harvesting during the swing

phase extension to reduce the energy expenditure of the muscles below the original energy expenditure for the knee alone. While this does not guarantee that the overall energy biomechanical energy expenditure for the entire gait cycle will be less, it does indicate that there are harvesting conditions for which the energy harvested and overall energy expenditure can be optimized.

5.5.2 Effect of permittivity on energy harvesting and biomechanical expenditure

When a similar analysis is performed for increased permittivity, the results are similar, however, as eq. (3.83) indicates, the energy harvesting is a linear function of permittivity, resulting in an inverse linear relationship between the permittivity and the knee joint energy expenditure.

Table 5.4 shows the response of the charged DE material to increasing permittivity based on the oscillation model.

Table 5.4: Extrapolated Behavior due to increase in permittivity based on oscillation curve.

	e	ς	ω_d (rad/s)	h_r (N/rad)	k_r (N/rad)
Expt.	No DE	0.047787	12.06	0.3922	2.474
	No charge	0.073052	12.0539	0.504	3.686
Oscillation Model	0	0.0694	11.8939	0.5058	3.5889
	3.1	0.0864	11.8805	0.6287	3.5808
	5	0.0979	11.8398	0.7104	3.5563
	11	0.1413	11.7411	1.0124	3.497
	12	0.1491	11.7262	1.0796	3.4884
	13	0.1579	11.7109	1.1364	3.479
	14	0.1671	11.7078	1.199	3.477
	15	0.1768	11.658	1.2631	3.4479
	17	0.1979	11.5516	1.4005	3.3853
	20	0.2336	11.4818	1.6432	3.3445

Table 5.5 demonstrates the changes in the mechanical response of the knee joint to active DE harvesters of increasing efficiency.

Table 5.5: Input values for the joint dynamics model as a function of permittivity

e	Δh_r	Δk_r
0	0.114	1.189
3.1	0.237	1.107
5	0.318	1.082
12	0.687	1.014
15	0.871	0.974
17	1.008	0.911
20	1.251	0.871

Once again, as shown in Figure 5.12, an increase in the permittivity leading to increased energy harvesting results in a decrease in the knee joint power requirement.

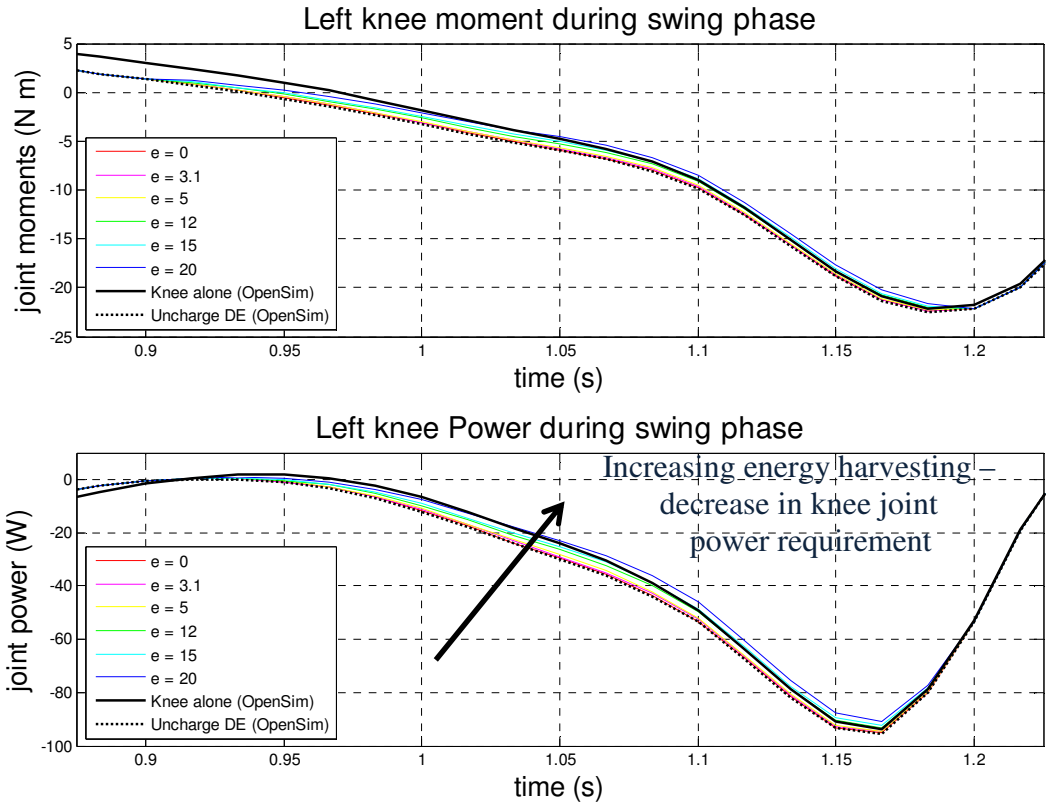

Figure 5.12: Moment and power curves for DE for increasing permittivity (e) (V_c = 3000V)

Finally, Table 5.6 and Figure 5.13 describe the additional energy expenditure at the knee joint as a function of permittivity.

Table 5.6: Joint Energy expenditure (J) during swing phase (t=0.9 – t=1.2 s) compared with DE energy harvested (J) as a function of permittivity (V = 3000v).

e	Total Joint Energy Expenditure during swing phase	Additional knee Joint Energy Expenditure	Energy Harvested
No DE	9.06	n/a	n/a
0	10.04	0.98	0
3.1	9.92	0.86	0.11
5	9.83	0.77	0.18
12	9.44	0.38	0.42
15	9.24	0.18	0.53
20	8.80	-0.26	0.71

The linear relationship between the amount of energy harvested and the reduction in the energy expenditure during the swing phase extension, is detected for both the energy harvested and the reduction in the energy expenditure in Figure 5.13.

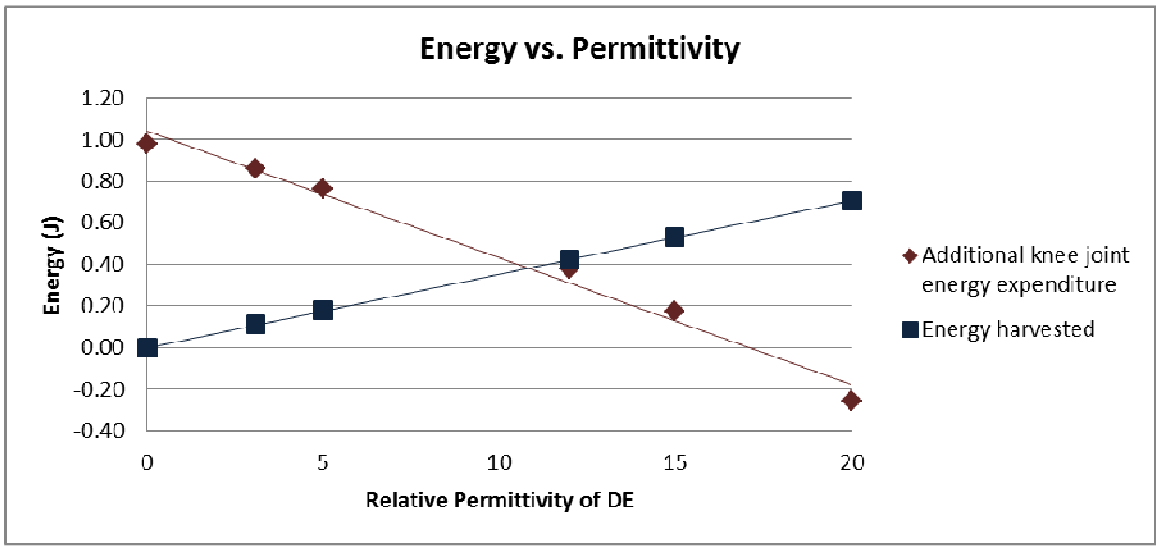

Figure 5.13: Joint Energy expenditure (J) during swing phase compared with DE energy harvested (J) as a function of permittivity.

As with the increased voltage, increasing the permittivity of a DE device both increases the energy harvesting capacity and when properly coordinated with the walking cycle, it also has the potential to decrease the required energy expenditure during the swing phase. Note that once again, it is possible to select values (in this case the e = 20 condition) in which the additional energy expenditure is negative, indicating that there is a net decrease in the expenditure during the swing phase extension.

5.6 Summary

At the completion of objective 3, a model of the damping effects of the DE energy harvester on the joint kinetics and energy expenditure of the human knee during walking has been developed. Analysis of the effect of increasing the energy harvesting through the improvement of two key electrical parameters, charge voltage and permittivity, has demonstrated that beneficial energy harvesting can be achieved such that the overall increase in the energy requirement is reduced as the energy harvested increases. The results of this analysis are significant, as they confirm that it is possible to use soft, wearable active electromechanical devices for beneficial energy harvesting, and that it is possible to design DE energy harvester / electrical loading profiles which reduce the energy expenditure while increasing the energy harvesting output of the harvester.

6 Conclusion

6.1 Overview of work presented

Dielectric elastomer harvesters hold significant promise as wearable energy harvesting devices which, when properly controlled, offer the wearer a comfortable, unobtrusive low power energy source with less fatigue than traditional gait-based energy harvesters. Although there are many different areas of ongoing research within electroactive polymers, there is a very limited amount of research which has been focused on the damping effects of energy harvesting [134], and none to date which has specifically addressed the kinetic effects that this damping has on the wearer of a dielectric elastomer (DE) material based device during energy harvesting. This dissertation presents a novel, interdisciplinary investigation which addresses the potential for the DE energy harvester to be used as a viable, low power source for on-board electronics. Since energy harvesting fundamentally involves harnessing the dissipative energy in a system, this research specifically investigates the damping induced by DE thin film energy harvesters which are affixed to the knee and operated during walking. It addresses this issue through the accomplishment of three objectives: *The characterization of DE uniaxial energy harvesting, the development of a relationship between energy harvesting and damping, and the investigation of the biokinetic effects of beneficial DE energy harvesting during walking.*

The first objective involved a thorough empirical investigation of DE uniaxial thin film behavior. This investigation resulted in an improved hyperelastic model which incorporates the boundary condition effects of the compliant electrode material on the composite DE constitutive relations. This model is implemented through the use of an empirically determined boundary coefficient, κ, which accounts for the effects of the DE compliant electrodes on the material kinematics. This consideration has not been addressed in traditional hyperelastic models. Using

this boundary coefficient, modified constitutive relations were developed for the DE material to calculate the mechanical stress in the longitudinal and lateral directions, σ_1 and σ_2. The improved mechanical model for the uncharged device predicted that, while σ_1 was insensitive to κ and the compliant electrode material properties, σ_2 is strongly influenced by the value of κ. Building upon this by including the effects of κ in the electromechanical constitutive relations of the composite DE indicates that energy harvesting is also influenced by the effect of κ. Therefore, the integration of the boundary coefficient into the electromechanical results in a more comprehensive model for DE energy harvesting.

The second objective was accomplished utilizing the constitutive relations developed through the thin film DE investigation in combination with concepts drawn from oscillatory motion, hysteretic damping and rheology. This was applied to the development of a model of the predicted damping due to the energy harvesting based on the mechanical and electrical parameters of the device. This provided a fundamental relationship between the energy harvested and the mechanical damping induced by this energy removal in the development of a hysteretic equivalent damping coefficient, h, which can be calculated as a function of dielectric permittivity, DE geometry, stretch at charge and discharge and the charge voltage. These results were experimentally verified for both the DE uniaxial stretching, using a thin film test stand, and for DE knee joint stretching, using a biofidelic knee joint test stand developed specifically to exercise the DE material with the same profile it would experience if located on a human knee during walking. The uniaxial test included three different compliant electrode materials: graphene, carbon grease and PolyPower (a corrugated spray deposited silver), and the knee joint test included three different configurations involving the placement of the DE material on the biofidelic knee and the electrical charging cycles: a) DE located on the front of knee / charged

during extension, b) DE located on the back of knee / charged during flexion and c) DE located on the front of knee / charged during flexion. Through the completion of this objective, not only was it was confirmed that it is possible to harvest energy from a knee joint using a DE harvester, but also, both theoretical and experimental methods for determining the damping associated with the harvested energy were developed. Based on these results, it was shown that it is possible to selectively introduce damping into a system through coordinated mechanical and electrical loading of a DE device.

The final objective of this research involved the investigation of the possibility of reducing the metabolic expenditure required to harvest energy from walking through careful coordination of the electrical loading of a DE energy harvester with the mechanical motion of the walking stride. The DE energy harvesting model was mapped to the swing phase of a walking stride in order to determine the most advantageous device placement and electrical loading pattern for beneficial energy harvesting. The resulting effects of energy harvesting on the biomechanics of the knee were determined through the use of the OpenSim platform, an open source biomechanical modeling and simulation program, which utilizes a gait measurement based musculoskeletal model to determine joint motion and loading during walking. This behavior was then estimated for extrapolated energy harvesting predictions based as a function of charge voltage and dielectric permittivity. The extrapolated responses were incorporated into a joint dynamics model which calculated the net energy requirement during active energy harvesting. The results of this modeling clearly establish that it is possible to reduce the energy expenditure requirement of DE energy harvesting by inducing damping during the mid to terminal swing phase.

6.2 Contributions of this work

There are several novel ideas which have been presented in this dissertation. The following describes the most significant contributions from this research.

1. ***Introduction of a boundary coefficient, κ, into the dielectric elastomer constitutive relations.*** The development of the boundary coefficient is notable as it provides a means to apply traditional hyperelastic models to composite DE materials which include compliant electrodes with material properties which differ greatly from the hyperelastic dielectric itself. Besides providing a more comprehensive constitutive relation for DE materials, the modified model also provides a means to directly assess the effects of the electrode material properties on the energy harvesting. This model confirms the experimental investigation of [129] who determined that by stiffening the DE electrode material in the lateral direction, energy harvesting efficiency can be increased.
2. ***Quantification of the mechanical damping effects due to knee joint DE energy harvesting.*** While it has previously been established that the system response to harvesting energy using an electromechanical harvester can be described similarly to dissipation due to damping [133, 134], this work is distinctive in that it specifically applies this concept to the biomechanical behavior of the knee joint. Through this research, it has been established that it is possible to selectively induce damping through coordinated mechanical and electrical loading of a DE device placed on the knee joint.
3. ***Assessment of the knee joint energy expenditure due to mechanical damping effects during swing phase knee joint DE energy harvesting.*** The joint dynamics model developed to determine the effect of DE energy harvesting on the intersegmental power of the knee is significant as it presents a description of how DE materials can be used in

conjunction with knee joint kinetics to effectively harvest energy while limiting the additional biomechanical energy expenditure required for energy harvesting. Results of this model establish the feasibility of beneficial energy harvesting from walking motion using a wearable, electroactive smart material. These results are critical for the development of comfortable, lightweight, wearable rehabilitation devices that can be incorporated into daily living. Successful demonstration of these concepts provides a foundation for applications to a wide range of medical research such as wireless body sensor networks, telerehabilitation and prosthesis development, opening up many technology transfer opportunities between engineering and rehabilitation medicine.

6.3 Recommendations and Future challenges

The work presented here demonstrates the feasibility of using soft wearable electromechanical materials, such as dielectric elastomers, as beneficial energy harvesting devices. While devices such as these hold incredible potential, there are still challenges in key areas such as material properties, control circuitry and manufacturing which must be addressed before widespread adoption of DE energy harvesters can be expected. Many of these issues are actively being investigated by research groups worldwide. Building on the research of others, the following section proposes recommendations on how these emerging research areas can be applied directly to DE knee joint energy harvesting:

1. ***Increased permittivity silicone dielectrics.*** The permittivity of a dielectric describes the amount of energy which can be stored in the material by an applied voltage, and hence is directly related to the efficiency of DE electromechanical conversion. As demonstrated through this research, the permittivity of the dielectric directly affects both the energy harvesting and the beneficial damping of DE knee joint energy harvesting. Therefore, high

permittivity silicone dielectrics, which are currently under development through the use of ceramic fillers such as barium titanate and titanium dioxide, or elastomer blends such as polyurethane and silicone [92, 93] or through temporary electrical modification using corona charging and poling [145, 146] should be employed to provide greater performance.

2. ***Graphene based electrodes.*** Based on the results of the investigations of the compliant electrode influence on the DE, graphene was found to have a lower boundary coefficient, κ, than the other materials investigated indicating that its mechanical behavior has less influence on the behavior of the silicone dielectric. In addition, graphene was also found to be more resistant to losses caused by electrode cracks than carbon grease, suggesting it will result in more robust performance. Therefore, it is recommend that the increased availability of graphene based materials [94, 95] be taken advantage of in the development of inexpensive compliant electrodes for widespread use of dielectric elastomers.
3. ***Fault tolerant self-clearing and patterned compliant electrodes.*** DE devices are still very susceptible to dielectric breakdown leading to shorts across the elastomer. Fault tolerant self-clearing electrodes use carbon nanotubes to self-heal by electrically insulating the short from the rest of the compliant electrode [97, 98]. Additionally, carefully designed patterns can be incorporated in the electrode surface area [99], providing better control of where high voltage charge is located on the device. Incorporating these types of technologies into the compliant electrode will result in increased durability of the material during both mechanical and electrical loading.
4. ***Dielectric elastomer circuit components.*** The high voltage electrical circuits currently used to power and control DE energy harvesters require several large high voltage devices such as switches and a high voltage power supply. These components currently restrict the use of

these types of devices to stationary applications, however current research is addressing this issue in several ways. Dielectric elastomer switches have been developed which allow for the elimination of many of the solid state switching devices which may normally be required [85]. In addition to eliminating large switches, the DE can also potentially eliminate the need for a high voltage power supply by using a dual DE self-priming arrangement By including an additional primer DE device [100] on the back side of the knee joint, or an electret coupled with the DE harvester [147], it would be possible to start with a very low voltage and incrementally increase the voltage until it reaches a value suitable for energy harvesting, eliminating the need for a high voltage external power supply. Implementation of these improvements will allow for miniaturization of the control circuit, allowing for broader application of DE harvesting.

5. ***Dielectric Elastomer Automated production.*** Roll to roll automation of low temperature graphene screen printing on flexible polymers [101] provides a means to mass produce complex flexible DE devices which could potentially include much of the required circuitry to operate the harvesting device. Through the adoption of these types of automated procedures, wearable DE devices should be able to be fabricated at a cost that could make them available for widespread use.

The recommendations above describe ways in which ongoing fundamental research in the area of dielectric elastomers can be applied to the use of dielectric elastomers for harvesting energy from human motion. The following future challenges describe several other areas specifically related to the implementation of DE harvesters in biomedical applications which have yet to be addressed:

Initial swing phase effects. In investigating the damping effect of increasing energy harvesting

through the improvement of DE electrical properties, it was assumed that these parameters could be substantially improved with negligible effects on the mechanical properties of the device. However, these substantial electrical improvements may in fact require a moderate increase in the mechanical stiffness of the device [92, 93]. This change in the mechanical behavior will affect the entire gait cycle as it is not controlled by the electrical load cycling. In this case, the effects of increasing mechanical properties of a DE harvester on the energy expenditure at all joints during the entire gait will be necessary to determine the overall effect on the energy expenditure due to increased energy harvesting.

Dynamics of electrical loading. The effects of the moments generated at the knee joint by the Maxwell stresses produced by a sudden electrical load during charging must be further investigated. These effects may be sufficiently large to require the charging and discharging of the DE to be applied in a controlled manner so as to prevent a sudden jerk of the Maxwell stress generated due to the application of a high voltage.

Fatigue loading effects on failure modes. The repetitive motion which a wearable DE energy harvester experiences warrants a close examination of the fatigue affects over time. Specifically, determining whether dielectric breakdown and elastomer rupture increase with increasing loads, and if so, what is causing the increased failures and how can it be reduced or eliminated.

The beneficial DE energy harvesting presented in this research lay the foundation for future work in the integration of wearable technology using dielectric elastomers with sensing, actuation, and energy harvesting. This research is innovative as it establishes a pathway for the integration of DE energy harvesting into a broad spectrum of fields where comfortable, inconspicuous, wearable devices can be designed to harvest energy in an unobtrusive manner.

APPENDIX A: NONLINEAR MECHANICAL BEHAVIOR OF DE POLYMERS

Some hyperelastic materials, such as many acrylic materials, can also experience several other nonlinear behaviors which may need to be addressed within the modeling. These nonlinear behaviors are mentioned here as they may come up in future testing, however, they are not included in the following work. Stretch stiffening occurs when the curled molecular chains within the polymer get stretched out so that they are no longer able to extend without a much larger stress. This behavior can be modeled using a polymer model which has been in use for rubber materials [122, 129, 148]. The strain energy density function model, for this model includes an experimentally determined material specific term, $J_{\lim}$, which is related to the stretch ratio at which the material begins to stiffen:

$$W = \frac{\mu}{2} J_{\lim} \log\left(1 - \frac{\lambda_1^2 + \lambda_2^2 + \lambda_1^{-2}\lambda_2^{-2} - 3}{J_{\lim}}\right) \tag{A.1}$$

Hyperelastic materials which experience an increase in the viscosity along with the stretch stiffening can also be modeled using the Gent model, by varying the viscosity term, μ, based on experimental measurements [129]. Some dielectric elastomer materials such as VHB 4910 exhibit time dependent strain, therefore, it is often necessary to include the time dependence of the material in the mechanical model. The time dependence can be modeled using quasi-linear viscoelastic method utilizing a Prony series of the following form [111]:

$$C_i^R = C_i^0 \left[1 - \sum_{k=1}^{N} g_k \left(1 - e^{-t/t_k}\right)\right] \tag{A.2}$$

Where the time independent constants, C_i^0, which are found from uniaxial tensile test are modified to reflect the relaxation of the material, and the variables, g_k and t_k are related to the

relaxation curves for the material under investigation. The resulting time dependent constants, C_i^R, can be used in the hyperelastic model developed to incorporate time dependency of the material response. While each of these additional non-linear behaviors presents itself in different hyperelastic materials, the silicone materials used in this research did not strongly exhibit these characteristics and modeling of these was not necessary.

APPENDIX B: HYDROSTATAIC PRESSURE AND STRESS RELATIONS

The strain in each of the three directions using the Neohookean model is found using the stress formula:

$$\begin{aligned}\sigma_1 &= \lambda_1 \frac{\partial W}{\partial \lambda_1} - p = \lambda_1 \frac{G}{2} 2\lambda_1 - p = G\lambda_1^2 - p \\ \sigma_2 &= \lambda_2 \frac{\partial W}{\partial \lambda_2} - p = \lambda_2 \frac{G}{2} 2\lambda_2 - p = G\lambda_2^2 - p \\ \sigma_3 &= \lambda_3 \frac{\partial W}{\partial \lambda_3} - p = \lambda_3 \frac{G}{2} 2\lambda_3 - p = G\lambda_3^2 - p = 0\end{aligned} \tag{B.1}$$

For a DE generator in uniaxial tension, the hydrostatic pressure is found by equating $\sigma_3 = 0$, resulting in:

$$p = G\lambda_3^2 \tag{B.2}$$

which is then substituted in order to provide a formulation for the stress in the x_1 and x_2 directions:

$$\begin{aligned}\sigma_1 &= G\lambda_1^2 - G\lambda_3^2 \\ \sigma_2 &= G\lambda_2^2 - G\lambda_3^2\end{aligned} \tag{B.3}$$

Unconstrained uniaxial Neohookean model

Using the stretch ratios defined for the unconstrained condition, $\lambda_1 = \lambda$, $\lambda_2 = \frac{1}{\sqrt{\lambda}}$, $\lambda_3 = \frac{1}{\sqrt{\lambda}}$, the stress in the 1 and 2 directions becomes:

$$\begin{aligned}\sigma_1 &= G(\lambda^2 - \frac{1}{\lambda}) \\ \sigma_2 &= 0\end{aligned} \tag{B.4}$$

Constrained uniaxial Neohookean model

Using the stretch ratios defined for the unconstrained condition, $\lambda_1 = \lambda,\ \lambda_2 = 1,\ \lambda_3 = \frac{1}{\lambda}$, the stress in the 1 and 2 directions becomes:

$$\begin{aligned} \sigma_1 &= G(\lambda^2 - \frac{1}{\lambda^2}) \\ \sigma_2 &= G(1 - \frac{1}{\lambda^2}) \end{aligned} \tag{B.5}$$

Note that when the width is constrained, it results in a larger stress for a given stretch ratio than when the width is not constrained.

General uniaxial Neohookean model

Recalling that the stretch ratios general for a thin film hyperelastic polymer undergoing uniaxial tension model are defined as: $\lambda_1 = \lambda, \lambda_2 = \frac{\sqrt{1-(1-\lambda)\kappa}}{\sqrt{\lambda}}, \lambda_3 = \frac{1}{\sqrt{\lambda}\sqrt{1-(1-\lambda)\kappa}}$, the stress in the 1 and 2 directions becomes:

$$\begin{aligned} \sigma_1 &= G\left(\lambda^2 - \frac{1}{\lambda\left(1-(1-\lambda)\kappa\right)}\right) \\ \sigma_2 &= G\left(\frac{\left(1-(1-\lambda)\kappa\right)}{\lambda} - \frac{1}{\lambda\left(1-(1-\lambda)\kappa\right)}\right) \end{aligned} \tag{B.6}$$

Hydrostatic pressure using Mooney-Rivlin model

For a DE generator in uniaxial tension, both of the boundary conditions extremes, constrained and unconstrained width, will be considered separately and then the results will be compared with the general formulation.

Unconstrained uniaxial Mooney-Rivlin model

When the width is unconstrained in the 2 direction, the hydrostatic pressure is found by considering the stress in the 1 direction when the stress in the 3 direction is set equal to zero. For the Mooney-Rivlin model this becomes:

$$\sigma_1 = \lambda_1 \frac{\partial W}{\partial \lambda_1} - p = 2(\lambda_1^2 C_1 - \frac{C_2}{\lambda_1^2}) - p = 2(\lambda^2 C_1 - \frac{C_2}{\lambda^2}) - p$$
$$\sigma_3 = \lambda_3 \frac{\partial W}{\partial \lambda_3} - p = 2(\lambda_3^2 C_1 - \frac{C_2}{\lambda_3^2}) - p = 2(\frac{C_1}{\lambda} - \lambda C_2) - p = 0 \quad \text{(B.7 a,b)}$$

Solving for p results in:

$$p = 2(\frac{C_1}{\lambda} - \lambda C_2) \quad \text{(B.8)}$$

which is then back substituted in order to provide the following stress function:

$$\sigma_1 = 2(\lambda^2 C_1 - \frac{C_2}{\lambda^2}) - 2(\frac{C_1}{\lambda} - \lambda C_2) = 2(\lambda^2 - \frac{1}{\lambda})(C_1 + \frac{C_2}{\lambda}) \quad \text{(B.9)}$$

Fully Constrained uniaxial Mooney-Rivlin model

The same process can be completed using the same strain energy function with the boundary condition in which the material is constrained in the 2 direction.

$$\sigma_1 = \lambda_1 \frac{\partial W}{\partial \lambda_1} - p = 2(\lambda_1^2 C_1 - \frac{C_2}{\lambda_1^2}) - p = 2(\lambda^2 C_1 - \frac{C_2}{\lambda^2}) - p$$
$$\sigma_3 = \lambda_3 \frac{\partial W}{\partial \lambda_3} - p = 2(\lambda_3^2 C_1 - \frac{C_2}{\lambda_3^2}) - p = 2(\frac{C_1}{\lambda^2} - \lambda^2 C_2) - p = 0 \quad \text{(B.10 a,b)}$$

Solving for p results in:

$$p = 2(\frac{C_1}{\lambda^2} - \lambda^2 C_2) \quad \text{(B.11)}$$

which is then back substituted to provide a complete formulation:

$$\sigma_1 = 2(\lambda^2 C_1 - \frac{C_2}{\lambda^2}) - 2(\frac{C_1}{\lambda^2} - \lambda^2 C_2) = 2(\lambda^2 - \frac{1}{\lambda^2})(C_1 + C_2) \quad \text{(B.12)}$$

For either boundary condition, a complete stress, strain response of the material is developed in terms of two constants, $C_1$and C_2, which will be found by experimentation.

General uniaxial Mooney-Rivlin model

Using the same process, the general stretch ratios results in a general formulation in terms of κ can be developed for use in a range of partially constrained width conditions:

$$\sigma_1 = \lambda_1 \frac{\partial W}{\partial \lambda_1} - p = 2\lambda^2 \left(C_1 + \frac{C_2\left(1-(1-\lambda)\kappa\right)}{\lambda} + \frac{C_2}{\lambda\left(1-(1-\lambda)\kappa\right)} \right) - p]$$

$$\sigma_2 = \lambda_2 \frac{\partial W}{\partial \lambda_2} - p = 2\left(1-(1-\lambda)\kappa\right)\left(C_1 + C_2\lambda^2 + \frac{C_2}{\lambda\left(1-(1-\lambda)\kappa\right)} \right) - p \qquad \text{(B.13 a-c)}$$

$$\sigma_3 = \lambda_3 \frac{\partial W}{\partial \lambda_3} - p = \frac{2\left(C_1 + C_2\lambda^2 + \frac{C_2\left(1-(1-\lambda)\kappa\right)}{\lambda} \right)}{\lambda\left(1-(1-\lambda)\kappa\right)} - p$$

Solving for p by setting $\sigma_3 = 0$ results in:

$$p = 2\left(\frac{C_1 + C_2\lambda^2 + \frac{C_2\left(1-(1-\lambda)\kappa\right)}{\lambda}}{\lambda\left(1-(1-\lambda)\kappa\right)} \right) \qquad \text{(B.14)}$$

Which is then returned to the first equation in order to provide a complete formulation for the stress as a function of the strain ratio:

$$\sigma_1 = 2\lambda^2 \left(C_1 + \frac{C_2\left(1-(1-\lambda)\kappa\right)}{\lambda} + \frac{C_2}{\lambda\left(1-(1-\lambda)\kappa\right)} \right) - \frac{2\left(C_1 + C_2\lambda^2 + \frac{C_2\left(1-(1-\lambda)\kappa\right)}{\lambda} \right)}{\lambda\left(1-(1-\lambda)\kappa\right)}$$

$$\sigma_2 = 2\left(1-(1-\lambda)\kappa\right)\left(C_1 + C_2\lambda^2 + \frac{C_2}{\lambda\left(1-(1-\lambda)\kappa\right)} \right) - \frac{2\left(C_1 + C_2\lambda^2 + \frac{C_2\left(1-(1-\lambda)\kappa\right)}{\lambda} \right)}{\lambda\left(1-(1-\lambda)\kappa\right)} \qquad \text{(B.15)}$$

as confirmation of this formulation, when the following equation is observed with $\kappa = 0$ or $\kappa = 1$, it reduces to the equations for the limiting conditions shown previously.

Hydrostatic pressure using Yeoh model

For a DE generator in uniaxial tension with a given constraint in the 2 direction, the hydrostatic pressure is found by considering the stress in the 1 direction when the stress in the 3 direction is set equal to zero. Utilizing the Yeoh strain energy density function, $W = C_{10}(I_1 - 3) + C_{20}(I_1 - 3)^2 + C_{30}(I_1 - 3)^3$, the invariants will be evaluated as with the Mooney-Rivlin model based on the stretch ratios defined for the given constraint conditions.

Unconstrained uniaxial Yeoh model

Considering the boundary condition in which the material is unconstrained in the 2 direction, the Yeoh model becomes:

$$\sigma_1 = \lambda_1 \frac{\partial W}{\partial \lambda_1} - p = 2\lambda(C_1 + 2C_2(\lambda^2 + \frac{2}{\lambda^2} - 3) + 3C_3(\lambda^2 + \frac{2}{\lambda^2} - 3)^2) - p$$
$$\sigma_3 = \lambda_3 \frac{\partial W}{\partial \lambda_3} - p = 2\frac{1}{\lambda}(C_1 + 2C_2(\lambda^2 + \frac{2}{\lambda^2} - 3) + 3C_3(\lambda^2 + \frac{2}{\lambda^2} - 3)^2) - p = 0 \quad \text{(B.16 a,b)}$$

Solving for the hydrostatic pressure using the stress in the 3 direction results in:

$$p = 2(\frac{1}{\lambda})(C_1 + 2C_2(\lambda^2 + \frac{2}{\lambda} - 3) + 3C_3(\lambda^2 + \frac{2}{\lambda} - 3)^2) \quad \text{(B.17)}$$

when returned to the stress equation, results in[116, 117]:

$$\sigma_1 = 2(\lambda^2 - \frac{1}{\lambda})(C_1 + 2C_2(\lambda^2 + \frac{2}{\lambda} - 3) + 3C_3(\lambda^2 + \frac{2}{\lambda} - 3)^2) \quad \text{(B.18)}$$

The coefficients for each of these models can be found through experimental measurements, and in many cases they are available in the literature[117].

Fully Constrained uniaxial Yeoh model

For the Yeoh model defined previously experiencing fully constrained with, the stress formula becomes:

$$\sigma_1 = \lambda_1 \frac{\partial W}{\partial \lambda_1} - p = 2\lambda^2 (C_1 + 2C_2(\lambda^2 + 1 + \frac{1}{\lambda^2} - 3) + 3C_3(\lambda^2 + 1 + \frac{1}{\lambda^2} - 3)^2) - p$$
$$\sigma_3 = \lambda_3 \frac{\partial W}{\partial \lambda_3} - p = 2\frac{1}{\lambda^2} (C_1 + 2C_2(\lambda^2 + 1 + \frac{1}{\lambda^2} - 3) + 3C_3(\lambda^2 + 1 + \frac{1}{\lambda^2} - 3)^2) - p = 0 \quad \text{(B.19 a,b)}$$

Solving for p by setting $\sigma_3 = 0$ results in:

$$p = 2\frac{1}{\lambda^2} (C_1 + 2C_2(\lambda^2 + 1 + \frac{1}{\lambda^2} - 3) + 3C_3(\lambda^2 + 1 + \frac{1}{\lambda^2} - 3)^2) \quad \text{(B.20)}$$

which is then back substituted to the first equation in order to provide a complete formulation [91]:

$$\sigma_1 = 2(\lambda^2 - \frac{1}{\lambda^2})(C_1 + 2C_2(\lambda^2 + 1 + \frac{1}{\lambda^2} - 3) + 3C_3(\lambda^2 + 1 + \frac{1}{\lambda^2} - 3)^2) \quad \text{(B.21)}$$

General uniaxial Yeoh model

Using the same process, with the general stretch ratios results in a general formulation in terms of κ which can be used for a range of partially constrained width conditions:

$$\sigma_1 = \lambda_1 \frac{\partial W}{\partial \lambda_1} - p = 2\lambda^2 \Gamma - p$$
$$\sigma_2 = \lambda_2 \frac{\partial W}{\partial \lambda_2} - p = 2\lambda \left(1 - (1-\lambda)\kappa\right) \Gamma - p$$
$$\sigma_3 = \lambda_3 \frac{\partial W}{\partial \lambda_3} - p = 2\frac{1}{\lambda \left(1 - (1-\lambda)\kappa\right)} \Gamma - p = 0 \quad \text{(B.22 a-c)}$$

where:

$$\Gamma = \left(\begin{array}{l} C_1 + 2C_2(\lambda^2 + \dfrac{1}{\lambda \left(1 - (1-\lambda)\kappa\right)} + \dfrac{\left(1 - (1-\lambda)\kappa\right)}{\lambda} - 3) \\ \quad + 3C_3(\lambda^2 + \dfrac{1}{\lambda \left(1 - (1-\lambda)\kappa\right)} + \dfrac{\left(1 - (1-\lambda)\kappa\right)}{\lambda} - 3)^2 \end{array} \right)$$

Solving for p using the second equation results in:

$$p = 2\frac{1}{\lambda \left(1 - (1-\lambda)\kappa\right)} \left(\begin{array}{l} C_1 + 2C_2(\lambda^2 + \dfrac{1}{\lambda \left(1 - (1-\lambda)\kappa\right)} + \dfrac{\left(1 - (1-\lambda)\kappa\right)}{\lambda} - 3) \\ \quad + 3C_3(\lambda^2 + \dfrac{1}{\lambda \left(1 - (1-\lambda)\kappa\right)} + \dfrac{\left(1 - (1-\lambda)\kappa\right)}{\lambda} - 3)^2 \end{array} \right) \quad \text{(B.23)}$$

which is then back substituted to the first equation in order to provide a complete formulation for the stress generated in the 1 direction for a thin film hyper elastic polymer in general uniaxial tension:

$$\sigma_1 = 2\left(\lambda^2 - \frac{1}{\lambda(1-(1-\lambda)\kappa)}\right)\left(\begin{array}{l} C_1 + 2C_2(\lambda^2 + \frac{1}{\lambda(1-(1-\lambda)\kappa)} + \frac{(1-(1-\lambda)\kappa)}{\lambda} - 3) \\ \quad + 3C_3(\lambda^2 + \frac{1}{\lambda(1-(1-\lambda)\kappa)} + \frac{(1-(1-\lambda)\kappa)}{\lambda} - 3)^2 \end{array}\right)$$

$$\sigma_2 = 2\left(\lambda(1-(1-\lambda)\kappa) - \frac{1}{\lambda(1-(1-\lambda)\kappa)}\right)\times \left(\begin{array}{l} C_1 + 2C_2(\lambda^2 + \frac{1}{\lambda(1-(1-\lambda)\kappa)} + \frac{(1-(1-\lambda)\kappa)}{\lambda} - 3) \\ \quad + 3C_3(\lambda^2 + \frac{1}{\lambda(1-(1-\lambda)\kappa)} + \frac{(1-(1-\lambda)\kappa)}{\lambda} - 3)^2 \end{array}\right) \quad \text{(B.24 a-c)}$$

$$\sigma_3 = 0$$

This set of equations provides a general formula relating the stretch ratio of the thin film in the x_1 direction, λ, to the generated stresses in each of the three directions. The coefficients, C_1, C_2, C_3, will be found experimentally for a given material and geometry.

Hydrostatic pressure including the boundary constraint coefficient.

Neohookean model: $$p = G\frac{1}{\lambda(1-(1-\lambda)\kappa)} \quad \text{(B.25)}$$

Mooney-Rivlin Model ; $$p = 2\left(\frac{C_1 + C_2\lambda^2 + \frac{C_2(1-(1-\lambda)\kappa)}{\lambda}}{\lambda(1-(1-\lambda)\kappa)}\right) \quad \text{(B.26)}$$

Yeoh model: $$p = 2\frac{1}{\lambda(1-(1-\lambda)\kappa)}\left(\begin{array}{l} C_1 + 2C_2(\lambda^2 + \frac{1}{\lambda(1-(1-\lambda)\kappa)} + \frac{(1-(1-\lambda)\kappa)}{\lambda} - 3) \\ \quad + 3C_3(\lambda^2 + \frac{1}{\lambda(1-(1-\lambda)\kappa)} + \frac{(1-(1-\lambda)\kappa)}{\lambda} - 3)^2 \end{array}\right) \quad \text{(B.27)}$$

APPENDIX C: MODELING CODE

C.1 Chapter 3 code

MATLAB code: Uniaxial modeling

```
% material properties
e0=8.8541878e-12; % permittivity of vacuum in F/m
epsilon= e*e0;   % permittivity of material in F/m

%% Modeling Results %%%%%%%%%%%%%%%%%%%%%%%%%%%%%%%%%%%%%%%%%%%%%%%%%%%%%%%%
 % variables necessary for modeling
 x_p = x_pre;
 n = NumCycles;
 % Model timing: t over n cycle
 del_t_model=0.01; % time resolution for modeling
 t_model=0:del_t_model:n/f;
 % find the indices for tc and td
 for i=1:length(t_model),
   if((round(t_model(i)*100)/100)==tc),i_on=i+3; end
   if((round(t_model(i)*100)/100)==td),i_off=i-3; end
 end
 %coefficients of the elastomer material (from experimental results)
 c1 = CoeffVal(1); c2 = CoeffVal(2); c3 = CoeffVal(3);

 %% MODEL - Stretch Ratio,
 w = 2*pi*f;
 % Stretch ratio lambda1
 L = @(t) (-(del_x/2)*cos(w*t+phi)+x0+del_x/2)/(disp0+x_offset);
 % displacement of the ACTIVE material only
 s_active = @(t) L(t)*x0_active;
 % displacement of the total polymer material
 s_all = @(t) L(t)*(disp0+x_offset);
 % engineering strain
 strain = @(t) (L(t)-1)*100;
 %% MODEL - Capacitance
 % linear function with respect to L(t) based on the material properties
 %  the constraint condition (K) and the stretch ratio function
 C_eps = @(t)epsilon*x0_active*y0*L(t).*(1+(L(t)-1)*K)/z0;

 % Including loss factor Beta
 C_eps = @(t)epsilon*x0_active*y0*L(t).*(1+(L(t)-1)*K)./z0.*exp(-beta*(L(t)-1));

 %% MODEL - Electrical

 % Time constant based on the total resistance (the device and
 % the load resistance) and the measured capacitance at charge
 DisTimeConst=(R+R_DE+R_DEG)*Cc;

 % charge based on modeled C and measured V
 charge= @(t)((t>=tc).*(t<td))*Vcharge*C_eps(tc) +...
       ((t>=(td)).*(t<=td_end)).*(Vdischarge*C_eps(t).*exp(-1/DisTimeConst*(t-td))) + ...
       (t>td_end).*(Vdischarge*C_eps(t)*exp(-(1/DisTimeConst)*HarvestSec));

 % Voltage based on modeled C and charge
 voltage=@(t) charge(t)./C_eps(t);

 %% MODEL -Yeoh Model for silicone dielectric
 % Yeoh formulation for stresses in 1 direction due to stretch ratio
 s_silicone = @(t) 2*(L(t).^2-1./(L(t).*(1-(1-L(t))*K))) ...
     .*(c1 + c2*2*(L(t).^2+1./(L(t).*(1-(1-L(t))*K))+(1-(1-L(t))*K)./L(t)-3) ...
       + c3*3*(L(t).^2+1./(L(t).*(1-(1-L(t))*K))+(1-(1-L(t))*K)./L(t)-3).^2);
 force_silicone=@(t) s_silicone(t)*y0*z0./L(t);
```

```
%% MODEL - maxwell stresses
% % maxwell stresses due to constant charge Q

% s_maxwell assuming  ***Constrained*** width
if (K==1)
  % when the material is fully constrained, the polymer will act as a rigid volume,
  % and the stress in all directions will be the same as the maxwell stress:
  s_maxwell= @ (t) -((t>=tc).*(t<td))*1/epsilon.*(charge(t)./(x0*y0*L(t))).^2;

% s_maxwell using ***Partially Unconstrained*** width
else
  % when the material is Fully Unconstrained, the polymer will freely stretch
  % in the 2 direction, and the stress in the 2 direction will be zero.
  % 1. Curve fit for c1_u, c2_u, c3_u
  if K==0
    c1_u = c1; c2_u = c2; c3_u = c3;
  else
  % Curve fit for unconstrained material c1_u, c2_u, c3_u

    c1_u = UnCoeffVal(1); c2_u = UnCoeffVal(2); c3_u = UnCoeffVal(3);
  end
  % 2. Find Lm_d by setting sigma2=s_silicone_2 + s_maxwell_3 == 0 using fzero.
            % maxwell stress w/out Lm term in numerator
  s_maxwell_3_mod = @ (Lm) -1/epsilon.*(charge(td)./(x0*y0)).^2*(1/(L(td)*Lm^2));
  s_silicone_2_mod = @ (Lm) 2*(Lm-1/Lm)*(c1_u+2*c2_u*(1+Lm^2+1/Lm^2-...
            3)+3*c3_u*(1+Lm^2+1/Lm^2-3)^2);
  f = @ (Lm) s_silicone_2_mod(Lm) + s_maxwell_3_mod(Lm);
  % find ~L (stretch ratio due to maxwell stress) using root finding
  Lm_0d=fzero(f,1.01);
  % Find Lm for K using linear interpolation between Lm_1 and Lm_0
  Lm_d = 1-(1-Lm_0d)*(1-K);
  % 3. Find Lm_c by setting sigma2(t=tc)=s_silicone_2 + s_maxwell_3 == 0 using fzero.
  % maxwell stress w/out Lm term in numerator
  s_maxwell_3_mod = @ (Lm) -1/epsilon.*(charge(tc)./(x0*y0)).^2*(1/(L(tc)*Lm^2));
  s_silicone_2_mod = @ (Lm) 2*(Lm-1/Lm)*(c1_u+2*c2_u*(1+Lm^2+1/Lm^2-3)…
                                          +3*c3_u*(1+Lm^2+1/Lm^2-3)^2);
  f = @ (Lm) s_silicone_2_mod(Lm) + s_maxwell_3_mod(Lm);
  % find ~Lc (stretch ratio due to maxwell stress) using root finding
  Lm_0c=fzero(f,1.01);
  % Find Lm for K using linear interpolation between Lm_1 and Lm_0
  Lm_c = 1-(1-Lm_0c)*(1-K);

  if (K==0) %define the stress for the fully unconstrained case
    % Maxwell stress term in the 3 direction as a function of both time and Lm
    s_maxwell_3   = @ (t,Lm) -1/epsilon.*(charge(t)./(x0*y0)).^2.*(1./(L(t)*Lm^2));
              % first term in the effective Maxwell stress in the 1 direction
    s_silicone_1   = @ (Lm) 2*(1-1/Lm)*(c1+2*c2*(1+Lm^2+1/Lm^2-3)+…
                                                    3*c3*(1+Lm^2+1/Lm^2-3)^2);

  else %%% general constraint case
    % General Maxwell stress term in the 3 direction as a function of both time and Lm
    s_maxwell_3 = @ (t,Lm) -1/epsilon.*(charge(t)./(x0*y0)).^2.*…
                        (1./(L(t).*(1-(L(t)-1)*K)*(Lm+(1-Lm)*K)^2)); % maxwell stress w/ Lm^2 term
    % first term in the effective Maxwell stress in the 1 direction
    s_silicone_1 = @ (Lm) 2*(1-1/Lm)...
              *(c1+2*c2*(1+(Lm+(1-Lm)*K)^2+1/(Lm+(1-Lm)*K)^2-3)...
              + 3*c3*(1+(Lm+(1-Lm)*K)^2+1/(Lm+(1-Lm)*K)^2-3)^2);
  end
  % complete effective Maxwell stress term in the 1 direction as a function of Lm_c
  s_maxwell_c= @ (t) ((t>=tc).*(t<td)).*(s_silicone_1(Lm_c) + s_maxwell_3(t,Lm_c));
  % complete effective Maxwell stress term in the 1 direction as a function of Lm_d
  s_maxwell_d= @ (t) ((t>=tc).*(t<td)).*(s_silicone_1(Lm_d) + s_maxwell_3(t,Lm_d));

  % Select which condition maxwell stress will be caluclate under
  s_maxwell = s_maxwell_c;
end

% force associated with maxwell stress
```

```
F_maxwell = @(t) s_maxwell(t)*y0*z0./L(t);

% total Stress = silicone stress + maxwell stresses
Stress= @(t) s_silicone(t)+s_maxwell(t);
% force associated with total stress taking into consideration
% change in crosssectional area
F_total = @(t) Stress(t)*y0*z0./L(t);

%% MODEL -Estimated energy harvested
% assuming ***Unconstrained width*** (Variable: Uhu in paper)
EharvestEst_Uh_U=-1/2*x0_active*y0*z0*s_maxwell(td-Del_t)*(1-((Lm_d/Lm_c)^2*(L(td)/L(tc))));
% assuming ***constrained width*** (Variable: Uhc in paper)
EharvestEst_Uh_C=-1/2*x0_active*y0*z0*s_maxwell(td-Del_t)*(1-(L(td)/L(tc))^2);
% Energy harvested using value of Kappa (K)
EharvestEst_Uh=-1/2*x0_active*y0*z0*s_maxwell(td-Del_t)*...
  (1-(L(td)*(1-(1-L(td))*K)*(Lm_d+(1-Lm_d)*K)^2/…
            (L(tc)*(1-(1-L(tc))*K)*(Lm_c+(1-Lm_c)*K)^2)));
% Energy harvested estimation based on modeling operation map area calculations
% Force vs. extension
ForceExtensionArea=polyarea(s_active(t_model)-x0_active,F_total(t_model));
% Voltage vs. charge
ChargeVoltageArea=polyarea(charge(t_model),voltage(t_model));

%% MODEL - Estimated damping coefficient
% Damping coefficient based on Energy Harvested using kapa
h_K = EharvestEst_Uh/(pi*(x0_active*(L(tc)-L(td)))^2);
```

MuPad: Derivation of stresses in terms of kappa

```
reset(): DIGITS:=5:
Defining the Deformation gradient tensor (Finger tensor)
F:=matrix([[L_1,0,0],[0,L_2,0],[0,0,L_3]])
Mooney Rivlin Strain energy density function in terms of invariants
W_M_R:=C_1*(I_1-3)+C_2*(I_2-3)
Definition of invariants
I_1:=L_1^2+L_2^2+L_3^2;
I_2:=L_1^2*L_2^2+L_2^2*L_3^2+L_1^2*L_3^2;
I_3:=L_1^2*L_2^2*L_3^2;


Mooney Rivlin Strain energy density function in terms of stretch ratios (L_1, L_2, L_3)
W_M_R
Stress Formula in terms of stretch ratios (without the hydrostatic pressure term, p which will be added later)
T_M_R[(1)]:=simplify(F[(1,1)]*diff(W_M_R,F[(1,1)]))
T_M_R[(2)]:=simplify(F[(2,2)]*diff(W_M_R,F[(2,2)]))
T_M_R[(3)]:=simplify(F[(3,3)]*diff(W_M_R,F[(3,3)]))
stretch ratios for uniaxial strain with no constraint in Y direction
T_M_R|(L_1=L,L_2=1/sqrt(L),L_3=1/sqrt(L))
stretch ratios for uniaxial strain fully constrained in Y direction
T_M_R|(L_1=L,L_2=1,L_3=1/L)
stretch ratios for general uniaxial strain where K is the constraint condition (0 = unconstrained, 1= fully constrained)
(without hydrostatic pressure term)
T_M_R_K:=T_M_R|(L_1=L,L_2=sqrt(1-(1-L)*K)/sqrt(L),L_3=1/(sqrt(L)*sqrt(1-(1-L)*K)))
K=1 corresponds to the unconstrained condition (without hydrostatic pressure term)
T_M_R_K|K=0
K=1 corresponds to the fully constrained condition (without hydrostatic pressure term)
T_M_R_K|K=1
Hydrostatic Pressure calculation based on assumption that stress in 3 direction is zero
p:=T_M_R_K[3];
expand(T_M_R_K[3]);

General stress strain relationship including hydrostatic pressure
S_M_R_K[1]:=T_M_R_K[1]-p;
S_M_R_K[2]:=T_M_R_K[2]-p;
S_M_R_K[3]:=T_M_R_K[3]-p


Unconstrained stress strain relationship including hydrostatic pressure
S_M_R_0[1]:=Simplify(S_M_R_K[1]|K=0);
S_M_R_0[2]:=Simplify(S_M_R_K[2]|K=0);
S_M_R_0[3]:=Simplify(S_M_R_K[3]|K=0);


Fully constrained stress strain relationship including hydrostatic pressure
S_M_R_1[1]:=Simplify(S_M_R_K[1]|K=1);
S_M_R_1[2]:=Simplify(S_M_R_K[2]|K=1);
S_M_R_1[3]:=Simplify(S_M_R_K[3]|K=1);
```

C.2 Chapter 4 code

LabVIEW: Knee joint test stand controller (front panel followed by block diagram)

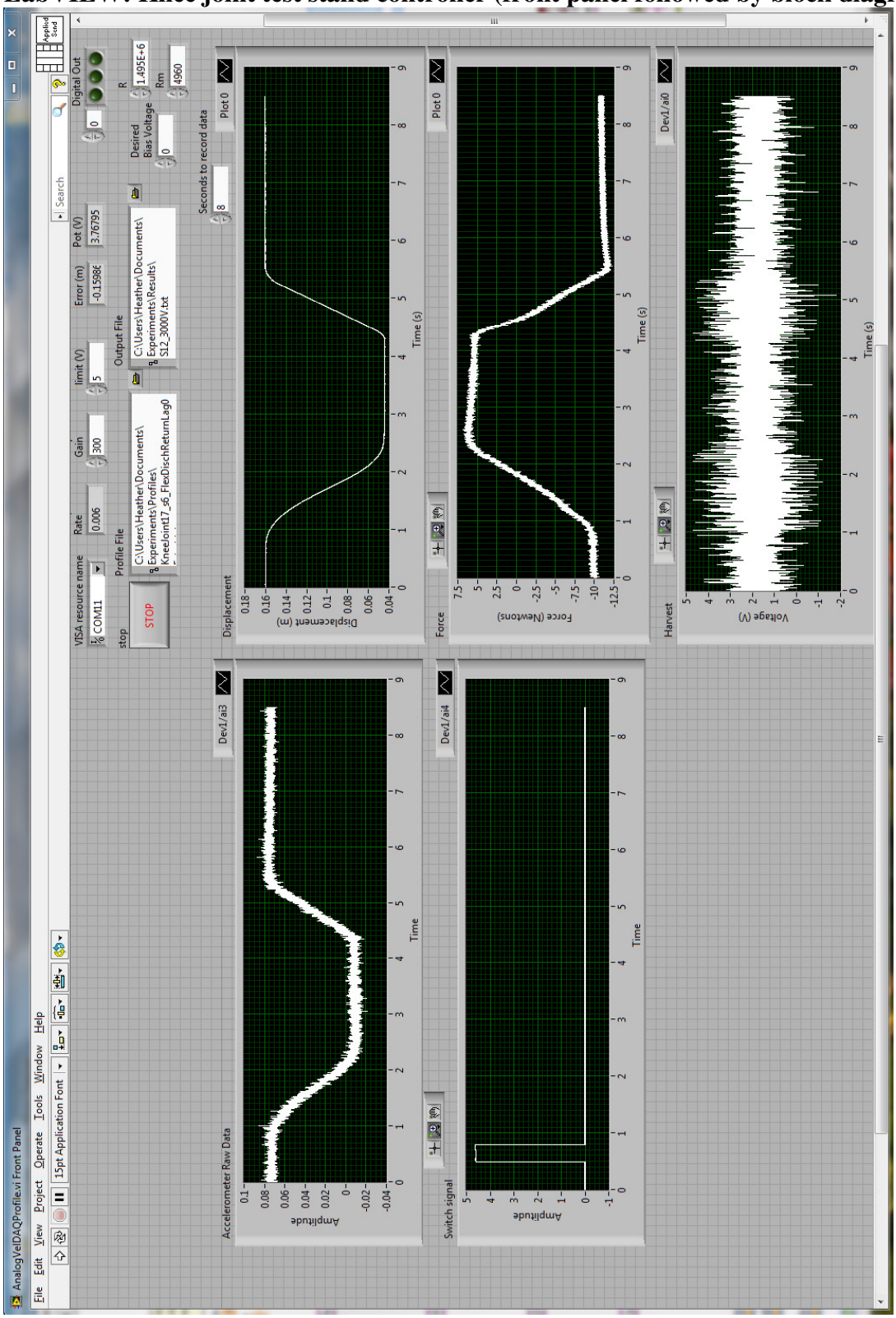

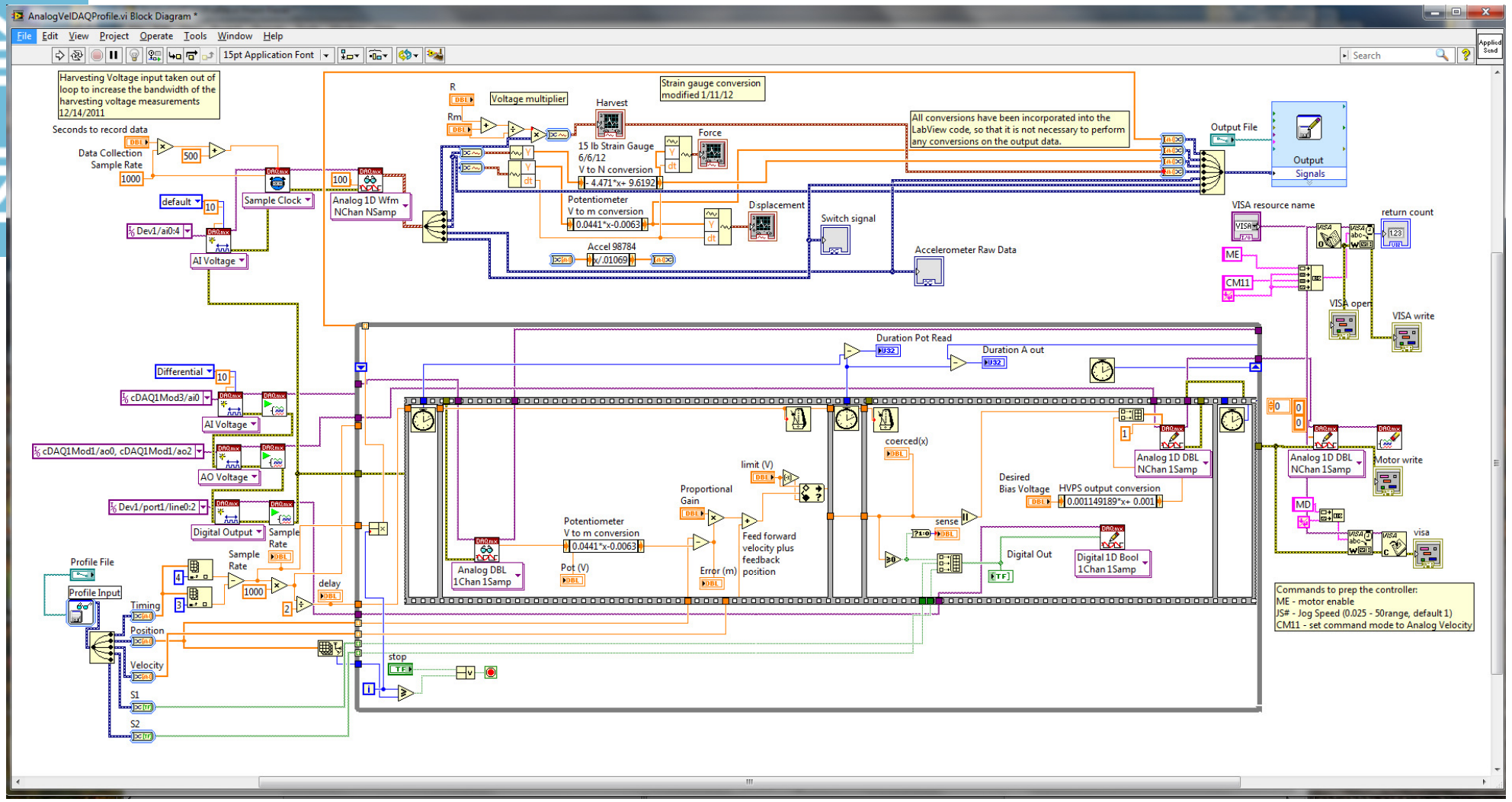

MATLAB: DE Maxwell stress in a knee joint

```
function [M,Fl,a_t,U,h]=PatellaBending(V,CE,CF,K,e,x,y,z,theta,thetaE,thetaF)
% Function file: PatellaBending.m 7/12/2012
% inputs:
%  V= DE charge voltage
%  CE capacitance at extension
%  CF = capacitance at flexion
%  K = boundary constraint condition
%  e = relative permittivity of DE elastomer
%  x = x10
%  y = x20
%  z = x30
%  theta = angle theta measured from fully extended in degrees
%  thetaE = angle of full extension
%  thetaF = angle of full flexion
% Outputs:
%  M = moment at the knee joint
%  Fl = force in the link transmitted through the knee joint
%  a_t = tangential acceleration due to moment about knee joint
%  U = Energy harvesting estimate
%  h = equivalent damping coefficient
%
% suggested parameters for specific tests:
% % % parameters for 5/16 no motion 2500V oscillation
% V= 2500;    % DE charge voltage
% CE = 69.5e-9;  % capacitance at extension
% CF = 85e-9;   % capacitance at flexion
% K=0.639;    % boundary constraint condition
% e=3.1;
% e0=8.8541878e-12;% Universal constant: permitivity of vacuum
% x = 0.2;    % x10
% y = 1.05;    % x20
% z = 8e-5;    % x30
%
% theta=45; % angle theta measured from fully extended in degrees
% thetaE=0;
% thetaF=60;

% parameters for 5/10 Force testing
% V= 9000;    % DE charge voltage
% CE = 74.6e-9;
% CF = 90.2e-9;
% K=0.639;
% e=3.1;
% x = 0.2;
% y = 1.04;
% z = 8e-5;
%
% theta=45; % angle theta measured from fully extended in degrees
% thetaE=5;
% thetaF=56;


%%%%%%%%%%%%%%%%%%%%%%%%%%%%%%%%%%%%%%%%%%%%%%%%%%%%%%%%%%%%%%%%%%%%%%%%%%%%%%%
%% properties of the test stand
e0=8.8541878e-12;% Universal constant: permitivity of vacuum
Lpatela=.035;  % Length of the DE material contacting the patella
LgapE=0.07;   % gap where the DE material does not contact the surface in extension
LgapF=0.12;   % gap where the DE material does not contact the surface in flexion
```

```
DE=0.059;    % distance from the outside surface of the test stand to the axis of rotation of knee joint in extension
DF=0.057;    % distance from the outside surface of the test stand to the axis of rotation of knee joint in flexion
Llink=0.125;  % length of the link

%%%%%%%%%%%%%%%%%%%%%%%%%%%%%%%%%%%%%%%%%%%%%%%%%%%%%%%%%%%%%%%%%%%%%%%
DlinkE = Llink*sind(45+thetaE); % vertical distance of link attachment and knee joint at extension
DlinkF = Llink*sind(45+thetaF); % vertical distance of link attachment and knee joint at flexion
Dlink = Llink*sind(45+theta);  % vertical distance of link attachment and knee joint at specified angle

thetaF_rad = thetaF*pi/180;   % angle at flexion
thetaE_rad = thetaE*pi/180;   % angle at extension
l_t = 0.125;  % length of tibia

% Get all necessary parameters for knee joint free oscillation tests
%  Not all parameters used in this code
[k,m,l,l_a,I] = KneeJointParamForce;
Dlinka = l_a*sind(45+theta);
% effective area, perpendicular distance to the joint and capacitance are
% found for a specific angle based on linear interpolation
Lgap = (LgapF-LgapE)/(thetaF-thetaE) * theta + LgapE;
D = (DF-DE)/(thetaF-thetaE) * theta + DE;
C = (CF-CE)/(thetaF-thetaE) * theta + CE;

% Find the stretch ratio, the equivalent maxwell stress,
%  the force in x1 direction, and the linear force
[myLE,SmE,FmE,PmE]=LfromCap(e,x,y,z,CE,V,K,0);
[myLF,SmF,FmF,PmF]=LfromCap(e,x,y,z,CF,V,K,0);
[myL,Sm,Fm,Pm]=LfromCap(e,x,y,z,C,V,K,0);

% find the moment at the knee joint due to the Maxwell stress
ME=PmE*(LgapE-Lpatela)*DE;
MF=PmF*(LgapF-Lpatela)*DF;
M=Pm*(Lgap-Lpatela)*D;

% find the force in the link transmitted through the knee joint
FlE=PmE*(LgapE-Lpatela)*DE/DlinkE;
FlF=PmF*(LgapF-Lpatela)*DF/DlinkF;
Fl=Pm*(Lgap-Lpatela)*D/Dlink;

% find the tangential acceleration due to moment about knee joint
a_t = Dlinka*M/I;

% find the energy harvested and the hysteretic damping coefficient.
U = x*y*z*e*e0/2*(myLF^2*V/(myLE*z))^2*(1-(myLE/myLF)^2)
h = x*y*z*e*e0/(2*pi*((thetaF_rad-thetaE_rad)/2)^2)*(myLF^2*V/(myLE*z))^2*(1-(myLE/myLF)^2);


function [L,Sm,Fm,Pm]=LfromCap(e,x,y,z,C,V,K,beta)
% Find the stretch ratio based on the surface area and measured capacitance
% of a given material
% INPUTS:
% e = relative permittivity of the dielectric material
% x = initial length
% y = initial width
% z = initial thickness
% C = capacitance
% V = charge voltage (optional, default: V=0)
% K = describes the actuation constraint can be any number between 0 and 1 (optional):
%    K == 0 -> unconstrained uniaxial loading (default)
%    K == 1 -> uniaxial loading constrained in y direction
```

```
% beta = exponential decay of the surface area of the capacitor
%    (optional, default: beta=0)
% OUTPUTS:
% L = ratio vector calculations corresponding to capacitance
% Sm = Maxwell stress for completely constrained condition
% Fm = Maxwell force for completely constrained condition
% Pm = Maxwell force per meter for completely constrained condition

if (nargin<5) error('Not enough inputs'), end
if (nargin<6) V=0; end
if (nargin<7) K=0; end
if (nargin<8) beta=0; end
% Universal constant: permittivity of vacuum
e0=8.8541878e-12;

% capacitance estimate for unstretched device
C0 = e*e0*x*y/z;

% root finding function for capacitance in terms of L
f = @ (L) C-(e*e0*x*y*L*(1+(L-1)*K)/z*exp(-beta*(L-1)));
% figure(400), fplot(f,[0,4]), grid on

% fzero root finding to determine L for given parameters
L=fzero(f,1);

% calculate the Maxwell stress based on
% ***completely constrained condition***
  Sm = e*e0*(V*L/z)^2;
  Fm = Sm*y*z/L;

% find the linear force p of the active material
  Pm=Fm/(x*L*(1+(L-1)*K));
```

MATLAB: Oscillation Simulation

```
function [td,atd,ud,tM,atM,uM]=PendulumMaxwellSimulation(x0,y0,t0,t1,h)
% function [td,atd,ud,tM,atM,uM]=PendulumMaxwellSimulation(x0,y0,t0,t1,h)
% Function file simulates the oscillatory motion of the knee joint in
% free vibration experiencing a disturbance, Fm(t) due to charging the DEG
% written by: Heather Lai, 7/2012
% Inputs:
% x0 = Initial angular position, phi (default: 45 deg)
% y0 = Initial angular velocity, phi-dot (default: 0 deg)
% t0 = start time (s)(default: 0 s)
% t1 = end time (s)(default: 1 s)
% h = step time (s)(default: 0.01 s)
% Outputs:
% td = time vector for damped non perturbed response
% atd = tangential acceleration vector for damped non perturbed response
% ud = angular response matrix for damped non perturbed response
%   [angular position, angular velocity, angular acceleration]
% tM = time vector for damped DEG perturbed response
% atM = tangential acceleration vector for damped DEG perturbed response
% uM = angular response matrix for damped DEG perturbed response
%   [angular position, angular velocity, angular acceleration]
% initialize the default values
if nargin<5, h=0.01; end  % step time (s)
```

```
if nargin<4, t1=1; end   % end time (s)
if nargin<3, t0=0; end   % start time (s)
if nargin<2, y0=0; end   % Initial angular velocity, phi-dot
if nargin<1, x0=-45*pi/180; end  % Initial angular position, phi

% Load knee joint model parameters
[k,m,l,l_a,I,g,c,phi_e] = KneeJointParamForce;

%% solve the Damped system of ODEs using RK4 method for phi and phi-dot
[td, ud] = ode23(@KneePendulumDamped_Eqs,[t0,t1],[x0,y0]);
% find angular acceleration (alpha) by using ODE
for i=1:length(ud), ddt(i,:) = KneePendulumDamped_Eqs(td(i),ud(i,:)); end
alphad = ddt(:,2);

% solve the Damped system WITH MAXWELL STRESS of ODEs using RK4 method
[tM, uM] = ode23(@KneePendulumDampedMaxwell_Eqs,[t0,t1],[x0,y0]);

% find angular acceleration (alpha) by using ODE
for i=1:length(uM), dMdt(i,:) = KneePendulumDampedMaxwell_Eqs(tM(i),uM(i,:)); end
alphaM = dMdt(:,2);

% Convert to tangential acceleration using distance of accelerometer (m)
atd=l_a*alphad;
atM=l_a*alphaM;

%% Plot the results
figure(3000)
subplot(3,1,3),plot(td,ud(:,1),'c',tM,uM(:,1)),grid on,title('Angular Displacement','FontSize',16)
      xlabel('Time (s)','FontSize',16), ylabel('\phi (rad)','FontSize',16),%hold on
subplot(3,1,2),plot(td,ud(:,2),'c',tM,uM(:,2)),grid on,title('Angular Velocity','FontSize',16)
      ylabel('\omega(rad/s)','FontSize',16),%hold on
subplot(3,1,1),plot(td,alphad,'c',tM,alphaM),grid on,title('Angular Acceleration','FontSize',16)
      ylabel('\alpha(rad/s^2)','FontSize',16),%hold on

 %% return result
 uM = [uM alphaM];
 ud = [ud alphad];


function ddt=KneePendulumUndamped_Eqs(t,u)
% The knee joint is modeled as a linear pendulum with both stiffness
% and damping at the knee as well as large angular displacements.
% Inputs:
% t = time (s)
% phi = angle measured from vertical in radians
% phi_dot = derivative of phi wrt time
% Output:
% ddt = vector of derivatives of phi and phi_dot: [dphi_dt;dphi_dotdt];

% Load knee joint model parameters
[k,m,l,l_a,I,g,c,phi_e,kr_mass] = KneeJointParamForce;

% Define equations as two first order equations including the higher order
% mass term.
phi=u(1);   % phi = angular displacement (phi measured from vertical)
phi_dot=u(2); % phi_dot = angular velocity

dphi_dt= phi_dot;
dphi_dotdt= -(k*(phi-phi_e))/I; % original function
```

```
% Populate the return vector
ddt = [dphi_dt;dphi_dotdt];


function ddt=KneePendulumDampedMaxwell_Eqs(t,u)
% ddt=KneePendulumDampedMaxwell_Eqs(t,phi,phi_dot)
% The knee joint is modeled as a non-linear pendulum with both stiffness
% and damping at the knee as well as large angular displacements.
% Maxwell stresses applied at max stretch and removed at minimum stretch
% Inputs:
% t = time (s)
% phi = angle measured from vertical in radians
% phi_dot = derivative of phi wrt time
% Output:
% ddt = vector of derivatives of phi and phi_dot: [dphi_dt;dphi_dotdt];

% Load knee joint model parameters
[k,m,l,l_a,I,g,c,phi_e,kr_mass,vel_switch] = KneeJointParamForce;
% Load DE film parameters
[e,e0,V,x0,y0,z0,K,beta,CE,CF,phiE,phiF]=DE_Parameters;

%define the slope and intercept of the Lambda vs phi relationship
LPhiSlope = 0.1039;
LPhi0 = 1.1187;

phi=u(1);   % phi = angular displacement (phi measured from vertical)
phi_dot=u(2); % phi_dot = angular velocity

% F maxwell Active only from max stretch to discharge at min stretch
if phi_dot<vel_switch && vel_switch<0
  % find the stretch ratio based on phi
  L=LPhiSlope*phi+LPhi0;  % Define L based on experimental/calculated values
  % calculate the Maxwell stress based on***completely constrained condition***
  Fmaxwell=(e*e0*V^2*y0/(z0*L));
  % find the moment about the knee joint caused by Fmaxwell based on the
  % effective area
  [Mmaxwell,a_t]=PatelaBendPhi(phi,L,Fmaxwell);

% F maxwell Active only from MIN stretch to discharge at MAX stretch
elseif phi_dot>vel_switch && vel_switch>0
  % find the stretch ratio based on phi
  L=LPhiSlope*phi+LPhi0;  % Define L based on experimental/calculated values
  % calculate the Maxwell stress based on***completely constrained condition***
  Fmaxwell=(e*e0*V^2*y0/(z0*L));
  % find moment about the knee joint caused by Fmaxwell based on the effective area
  [Mmaxwell,a_t]=PatellaBendPhi(phi,L,Fmaxwell);
else
  % if the DE material is stretching, no Maxwell force is applied
  Fmaxwell = 0; Mmaxwell = 0; a_t = 0;
end
% disp([t a_t Mmaxwell Fmaxwell])

% Define equations as two first order equations including the higher order
% mass term and the Maxwell force term.
% phi = angular displacement (phi measured from vertical)
% phi_dot = angular velocity
dphi_dt= phi_dot;
dphi_dotdt= -(k*(phi-phi_e)+c*phi_dot-Mmaxwell)/I;
```

```
% Populate the return vector
ddt = [dphi_dt;dphi_dotdt];


function [M,a_t]=PatellaBendPhi(phi,L,F)
% Function file: PatellaBendPhi.m 8/1/2012
% finds the moment and tangential acceleration of the knee joint due to a
% maxwell force on a DE film placed on the front of the knee joint.
% Input:
%  phi = knee angle measured in rad from the vertical
%  L = stretch ratio of the DE material
%  F = maxwell force
% Output returns the following values:
%  M - moment at the knee joint
%  a_t - tangential acceleration due to moment about knee joint

% Load necessary parameters for knee joint free oscillation tests
%  (Not all parameters used in this code)
[k,m,l,l_a,I,g,c] = KneeJointParamForce;
% Load DE film parameters
[e,e0,V,x0,y,z,K,beta,CE,CF,phiE,phiF]=DE_Parameters;

theta=phi*180/pi+45; % angle theta measured from fully extended in degrees
thetaE=phiE*180/pi+45;% angle at fully extended (thetaE)
thetaF=phiF*180/pi+45;% angle at fully flexed (thetaF)

Lpatella=.035;    % length of the outside surface of the patela
LgapE=0.07;     % length of gap when leg is in extension
LgapF=0.12;     % length of gap when leg is in flexion
DE=0.059;      % distance from surface to joint axis in extension
DF=0.057;      % distance from surface to joint axis in flexion
Llink=0.125;    % length along tibia from joint axis to the link pin

Dlink = Llink*sind(45+theta); % vertical distance from joint axis to link pin
Dlinka = l_a*sind(45+theta); % vertical distance from joint axis to accel.

% effective area(Lgap) perpendicular distance to the joint(D) and
% capacitance(C) are found for a specific angle based on linear interpolation
Lgap = (LgapF-LgapE)/(thetaF-thetaE) * theta + LgapE;
D = (DF-DE)/(thetaF-thetaE) * theta + DE;

% calculate moment at the knee joint due to the Maxwell stress using the
% ratio of the actual length of the DE film (x0*L) and the effective
% stretching length (Lgap-Lpatela) multiplied by the perpendicular distance
% to the joint(D)
M=F/(x0*L)*(Lgap-Lpatella)*D;

% calculate tangential acceleration due to moment about knee joint
a_t = Dlinka*M/I;
```

C.3 Chapter 5 code

OpenSim OISM model file: bushing force component, DE attached, uncharged

```
<!--INCLUDE DE DEVICE ADDITIONAL KNEE JOINT STIFFNESS AND DAMPING IN THE OPENSIM CODE
                    for control values-->
                <BushingForce name="KneeJointBushing_l">
                    <body_1> femur_l </body_1>
                    <body_2> tibia_l </body_2>
                    <location_body_1> 0.03 -0.04 0.000 </location_body_1>
                    <orientation_body_1> 0.0000  0.0000  0.0000 </orientation_body_1>
                    <location_body_2> 0.0000  0.0000   0.0000 </location_body_2>
                    <orientation_body_2>  0.0000  0.0000  0.0000 </orientation_body_2>
                    <rotational_stiffness> 0.000  0.000 1.1212 </rotational_stiffness>
                    <translational_stiffness> 0.0000 0.000 0.000 </translational_stiffness>
                    <rotational_damping>  0.000  0.000  0.02017 </rotational_damping>
                    <translational_damping> 0.0000 0.000 0.000 </translational_damping>
                </BushingForce>
```

MATLAB file: DE energy harvester on knee joint simulation

```
function [KneeMomentL_total,KneePowerL_active,KneeEnergyL_noDE_swing, ...
                    KneeEnergyL_active_swing,KneeEnergyL_noDE,KneeEnergyL_active] ...
    = Simulate_InvDynamics(DataPath,DataFile,DataFileKinematics, ...
                    kr_baseline,hr_baseline,Kr,Hr,t_c,t_d,legend_text)
% Heather Lai Feb. 2013
% Function Simulate_InvDynamics(DataPath,DataFile,DataFileKinematics,kr_baseline,hr_baseline,Kr,Hr,t_c,t_d,legend_text)
% calculates moments based on a given baseline and active DE stiffness and damping,
% returns the left knee angle, velocity, moment and power curves
% Inputs:
% DataPath - path where the files are located
% DataFile - file names of trials to be investigated. Unmodified model should be first.
% DataFileKinematics - path and file name where kinematic motion file is located
% kr_baseline - baseline stiffness based on oscillation model
% hr_baseline - baseline damping based on oscillation model
% Kr - vector of stiffnesses based on oscillation model for varing parameters
% Hr - vector of hysteretic effective damping coefficients based on oscillation model for varing parameters
% e - vector of possible permittivity values
% t_c - charge time in seconds
% t_d - discharge time in seconds
% legend_text - text for the varing parameters values
% Outputs:
% KneeMomentL_total - vector of moment including active DE
% KneePowerL_active - vector of power curve including active DE
% KneeEnergyL_noDE - integral of power curve without DE
% KneeEnergyL_active - integral of power curve including active DE

% moment of inertial based on anthropomorphic data: I_shank = 0.00214,
% (written in terms of unit mass and leg length)
% and measurements from the subject 1 data: leg length = 0.993m and mass = 72.6 kg
I_shank = 0.1532; % in kg m^2
k_knee = 22.94; % from slope measurements of the model
%define range to search for charge time (based on sample time)
delta = .01;

% read in Joint angle info data from each file
[JointAngles]=dlmread(DataFileKinematics,'\t',12,0);
```

```
tAngles=JointAngles(2:end-1,1);

Fs = 1/mean(tAngles(2:end)-tAngles(1:end-1));  % Sample Frequency
LKneeAngles = JointAngles(2:end-1,18);     % selection of knee joint angles
LKneeRad = LKneeAngles*(pi/180);        % Convert to radians
LKneeomega = derivative(tAngles,LKneeRad)';   % calculate the joint angular velocities

%% OpenSim results for comparison
% read in moment data
[Dynamics_data1]=dlmread(strvcat(strcat(DataPath,DataFile(1,:))),'\t',10,0);
[Dynamics_data2]=dlmread(strvcat(strcat(DataPath,DataFile(2,:))),'\t',10,0);
t(:,2)=Dynamics_data2(:,1);
KneeMomentL(:,1) = Dynamics_data1(:,18);
KneeMomentL(:,2) = Dynamics_data2(:,18);

[Dynamics_data]=dlmread(strvcat(strcat(DataPath,DataFile(1,:))),'\t',10,0);
t(:,1)=Dynamics_data(:,1);
KneeMomentL(:,1) = Dynamics_data(:,18);

L=length(KneeMomentL(:,1)); % find number of frames

%% find the frequency content of LKneeRad
% perform fft on the knee joint angle (with DC offset removed)
Y = fft(LKneeRad-mean(LKneeRad))/L;
f = Fs/2*linspace(0,1,L/2)';
% Find the frequency of the max peak (relate to the natural frequency)
[peak ipeak] = findpeaks(abs(Y(1:end/2)));
[p,i]=max(peak);
iomega = ipeak(i);
omega_n=2*pi*f(iomega);

%% convert hysteretic damping coefficient into the viscous damping coefficient
cr_baseline=hr_baseline/omega_n;

%% loop through all of the different values of e
for j=1:length(Kr)
  % select stiffness and damping
  kr = Kr(j);
  hr = Hr(j);

  %% convert hysteretic damping coefficient into the viscous damping coefficient
  cr=hr/omega_n;

  %% determine the element index related to the charge and discharge times.
  i_c = find(t(:,1)>t_c-delta&t(:,1)<t_c+delta,1);
  i_d = find(t(:,1)>t_d-delta&t(:,1)<t_d+delta,1);

  %% calculate force based on uncharged/charged rotational stiffness
  % calculations using LKneeRad
  % moment of DE on Knee joint due to uncharged stiffness of the device
  Moment_kr_uncharged = zeros(1,length(KneeMomentL(:,1)));
  Moment_kr_uncharged(1:i_c) = kr_baseline*LKneeRad(1:i_c);
  Moment_kr_uncharged(i_d:end) = kr_baseline*LKneeRad(i_d:end);
  % moment of DE on Knee joint due to charged stiffness of the device
  Moment_kr_charged = zeros(1,length(KneeMomentL(:,1)));
  Moment_kr_charged(i_c+1:i_d-1) = kr*LKneeRad(i_c+1:i_d-1);

  %%% for VISCOUS damping coefficient, cr
  % moment of DE on Knee joint due to uncharged damping ratio of the device
  Moment_cr_uncharged = zeros(1,length(KneeMomentL(:,1)));
  Moment_cr_uncharged(1:i_c) = cr_baseline*LKneeomega(1:i_c);
  Moment_cr_uncharged(i_d:end) = cr_baseline*LKneeomega(i_d:end);
```

```
% moment of DE on Knee joint due to charged stiffness of the device
Moment_cr_charged = zeros(1,length(KneeMomentL(:,1)));
Moment_cr_charged(i_c+1:i_d-1) = cr*LKneeomega(i_c+1:i_d-1);

% moment due to DE assuming viscous damping
DEMomentL = (Moment_kr_uncharged + Moment_kr_charged + …
                    Moment_cr_uncharged + Moment_cr_charged)';

% moment profile for knee joint including moment_kr and Zr
KneeMomentL_total(:,j) = KneeMomentL(:,1) + DEMomentL;

%% Knee joint energy / power requirement
% Original power = moment about joint X joint angular velocity
KneePowerL_baseline(:,j) = KneeMomentL(:,1) .* LKneeomega;
% total energy = integral power.
KneeEnergyL_baseline(:,j) = trapz(t(:,1),KneePowerL_baseline);

% Harvesting power = moment about joint X joint angular velocity for
% regular knee and for knee with DE energy harvester
KneePowerL_noDE = KneeMomentL(:,1) .* LKneeomega;
KneePowerL_DE0 = KneeMomentL(:,2) .* LKneeomega;
KneePowerL_active(:,j) = KneeMomentL_total .* LKneeomega;

% find energy during swing phase: energy = integral power.
 KneeEnergyL_noDE_swing = trapz(t(i_c+1:i_d-1,1),KneePowerL_noDE(i_c+1:i_d-1));
 KneeEnergyL_active_swing(j) = trapz(t(i_c+1:i_d-1,1),KneePowerL_active(i_c+1:i_d-1));
KneeEnergyL_noDE = trapz(t(:,1),KneePowerL_noDE);
KneeEnergyL_active(j) = trapz(t(:,1),KneePowerL_active);
end
```

APPENDIX D: DE DESIGN AND MATERIAL PROPERTIES

Fabrication of dielectric elastomers is a quickly developing field, and many new advancements are under development, however, most current research still requires individual fabrication of each device. One of the most challenging aspects of producing dielectric elastomers is fabricating a compliant electrode which allows the device to experience large strains without losing conductivity, while still being connected to the high voltage leads with little electrical resistance. Three different electrode materials were utilized in the analysis of the DE generator, corrugated silver electrodes (PolyPower), graphene, and carbon grease.

Each electrode material was adhered to the same polydimethylsiloxane (PDMS) type silicone dielectric substrate, which is the corrugated polymer manufactured by Danfoss for use in PolyPower. In the case of the graphene and carbon grease, all electrode material was first removed from the surface of the polymer. This polymer was used for each prototype in order to provide comparable substrate for all tests, and has the following properties [149]:

Material Property	Value
Relative Permittivity	3.1
Young's modulus	1.1 Mpa
Density	1.11 g/cm^2
Volume Resistance	> 1014 Ω
Film Thickness	80 µm

PolyPower configuration: Metalized silver electrodes

The DE used most throughout this research was the PolyPower film with ~100 nm thick sputter-based vacuum coated metallic silver electrodes. PolyPower is a commercially available dielectric material made by Danfoss PolyPower A/S. It utilizes the PDMS dielectric polymer with a corrugated geometry described previously with the thin silver electrodes to create a material which is able to elongate up to 30% without cracking the metalized electrodes. The

metalize film has an equivalent modulus of eleasticity of 1 MPa [114]. When the material is stretched past the maximum allowable strain of the flattening of the corrugation, the metal will be strained and cracking will begin. Because of this behavior, all of the tests performed on the PolyPower devices are limited to below the maximum stretch of 30%. Preparation of this material for uniaxial use consisted of cutting the sample to the desired size, and then etching the edges using sodium hypochlorite (bleach) to prevent shorting. Once the sample was ready, it was installed onto the test rig using the test fixture described in the text, and conductive tape and pressure from the fixture compression were used to create an electrical connection between the high voltage wire and the metallic electrodes.

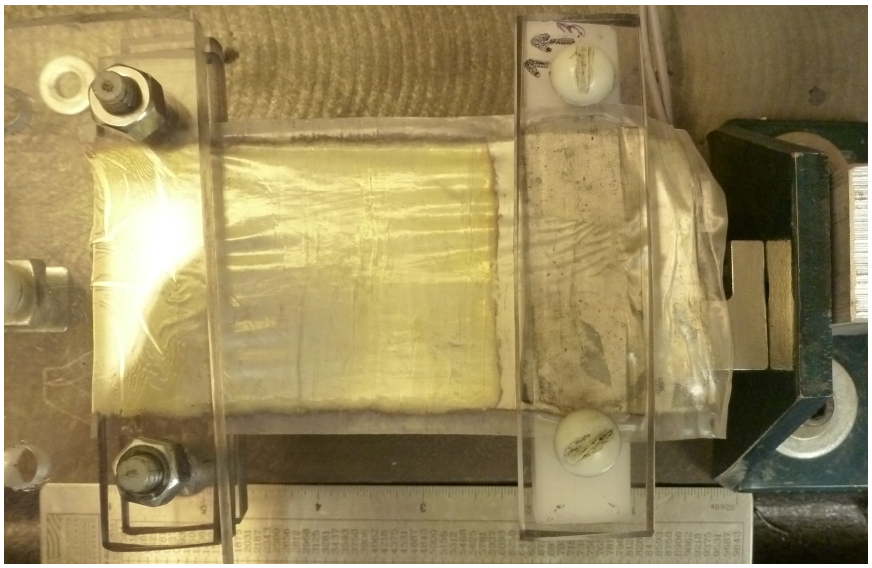

Figure D.1: PolyPower DE uniaxial film on test stand

Graphene and carbon grease configuration / material properties

For the boundary coefficient, Maxwell stress and energy harvesting measurements, not only was PolyPower used, but two other electrode materials were also investigated. The graphene DE film was fabricated manually using dielectric polymer the commercially produced for PolyPower and a graphene powder, N006-01-P from Angstron Materials. The graphene

particles contained in this powder have the following specifications: X-Y Dimensions < 14 um, and Thickness < 10 nm.

The graphene powder was applied dry by hand directly to the DE film using the following process. The film was cut to the required size and then the desired shape on the bottom size of the DE was masked on the film. A thin layer of graphene was spread onto the film by hand, and excess material was removed. The mask was removed, and the film was placed into the test fixture with the wire leads connected to the graphene via pressure generated by the fixture. The strands of the leads were fanned out to create as much surface area for electrical contact with the graphene as possible.

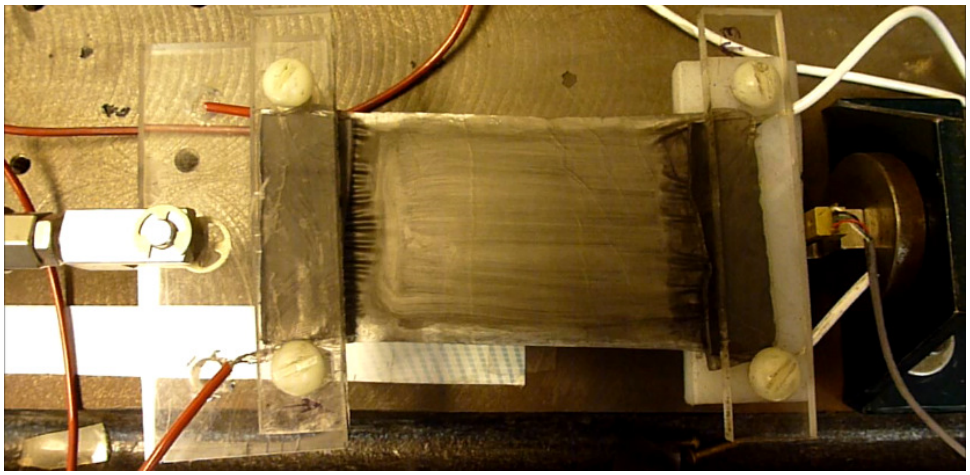

Figure D.2: Graphene DE uniaxial film on test stand

The carbon grease DE film was made in a manner similar to that of the graphene device. A photo of the completed device can be seen in Figure D.3.

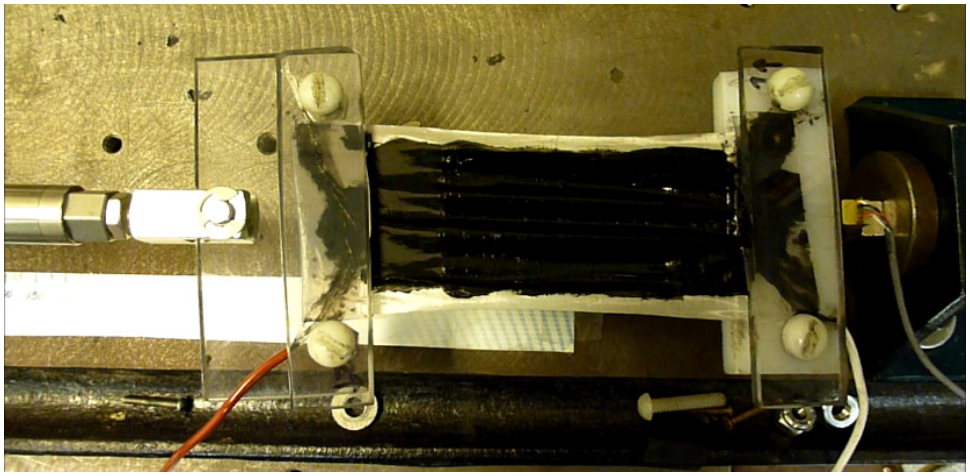

Figure D.3: Carbon grease DE uniaxial film on test stand

The electrode material used was 846 Carbon conductive grease from MG Chemicals. This grease was a viscous paste rather than a powder, and it has a volume resistivity of 117 Ω-cm. It was also applied by hand, using a squeegee to spread the grease as evenly as possible across the bottom surface of the dielectric. The devices was then placed into the test stand and the electrode grease was applied to the top side of the electrode. High voltage leads were once again, electrically connected to the electrode using fanned stranded wire and compressive force.

REFERENCES

[1] D. Jia and L. Jing, "Human power-based energy harvesting strategies for mobile electronic devices," *Frontiers of Energy and Power Engineering in China,* vol. 3, pp. 27-46, 2009.

[2] R. N. Mayo and P. Ranganathan, "Energy consumption in mobile devices: why future systems need requirements-aware scale-down," in *Power-Aware Computer Systems. Third International Workshop, PACS 2003. Revised Papers, 1 Dec. 2003*, Berlin, Germany, 2004, pp. 26-40.

[3] J. Paulo and P. D. Gaspar, "Review and Future Trend of Energy Harvesting Methods for Portable Medical Devices," in *World Congress on Engineering 2010. WCE 2010, 30 June-2 July 2010*, Hong Kong, China, 2010, p. 6 pp.

[4] J. C. Kim, F. Garzotto, F. Nalesso, D. Cruz, J. H. Kim, E. Kang*, et al.*, "A wearable artificial kidney: technical requirements and potential solutions," *Expert Review of Medical Devices,* vol. 8, pp. 567-579, Sep 2011.

[5] H. Hwang and N. M. Kim, "An Enhanced Frame Transmission Method for Medical Devices with Ultra Low Power Operation," *IEEE Transactions on Consumer Electronics,* vol. 58, pp. 154-160, Feb 2012.

[6] H. K. Cha, D. L. Yan, M. K. Raja, and M. Je, "A 1-V 1.2-mW CMOS medradio receiver for biomedical applications," *Microwave and Optical Technology Letters,* vol. 54, pp. 2821-2825, Dec 2012.

[7] S. Marinkovic and E. Popovici, "Ultra Low Power Signal Oriented Approach for Wireless Health Monitoring," *Sensors,* vol. 12, pp. 7917-7937, Jun 2012.

[8] S. R. Sridhara, M. DiRenzo, S. Lingam, S. J. Lee, R. Blazquez, J. Maxey, *et al.*, "Microwatt Embedded Processor Platform for Medical System-on-Chip Applications," *IEEE Journal of Solid-State Circuits,* vol. 46, pp. 721-730, Apr 2011.

[9] D. J. Leo, *Engineering Analysis of Smart Material Systems*. Blacksburg, VA: John Wiley and Sons, Inc, 2007.

[10] R. Riemer and A. Shapiro, "Biomechanical energy harvesting from human motion: theory, state of the art, design guidelines, and future directions," *Journal of NeuroEngineering and Rehabilitation,* 26 April 2011 2011.

[11] E. Daoutova. (4/3/2011). *BionicPower: Energy Harvester Data Sheet*. Available: http://www.bionic-power.com/downloads/Bionic_Energy_Harvester_Datasheet.pdf

[12] J. Andrysek, T. Liang, and B. Steinnagel, "Evaluation of a prosthetic swing-phase controller with electrical power generation," *IEEE Transactions on Neural Systems and Rehabilitation Engineering,* vol. 17, pp. 390-396, 2009.

[13] B. Warneke, B. Atwood, and K. S. J. Pister, "Smart dust mote forerunners," in *14th IEEE International Conference on Micro Electro Mechanical Systems (MEMS 2001), January 21, 2001 - January 25, 2001*, Interlaken, Switzerland, 2001, pp. 357-360.

[14] S. Chalasani and J. M. Conrad, "A survey of energy harvesting sources for embedded systems," in *IEEE SoutheastCon 2008, April 3, 2008 - April 6, 2008*, Huntsville, AL, United states, 2008, pp. 442-447.

[15] C.-T. Hsu, G.-Y. Huang, H.-S. Chu, B. Yu, and D.-J. Yao, "Experiments and simulations on low-temperature waste heat harvesting system by thermoelectric power generators," *Applied Energy,* vol. 88, pp. 1291-1297, 2011.

[16] C. Min, G. Junling, K. Zhengdong, and Z. Jianzhong, "Design Methodology of Large-scale Thermoelectric Generation: A Hierarchical Modeling Approach," *Journal of Thermal Science and Engineering Applications,* vol. 4, p. 041003 (9 pp.), 12/ 2012.

[17] C. Baker, P. Vuppuluri, S. Li, and M. Hall, "Model of heat exchangers for waste heat recovery from diesel engine exhaust for thermoelectric power generation," *Journal of Electronic Materials,* vol. 41, pp. 1290-1297, 06/ 2012.

[18] R. Yang, Y. Qin, C. Li, G. Zhu, and Z. L. Wang, "Converting biomechanical energy into electricity by a muscle-movement- driven nanogenerator," *Nano Letters,* vol. 9, pp. 1201-1205, 2009.

[19] C. Chang, V. H. Tran, J. Wang, Y.-K. Fuh, and L. Lin, "Direct-write piezoelectric polymeric nanogenerator with high energy conversion efficiency," *Nano Letters,* vol. 10, pp. 726-731, 2010.

[20] B. J. Hansen, Y. Liu, R. Yang, and Z. L. Wang, "Hybrid Nanogenerator for Concurrently Harvesting Biomechanical and Biochemical Energy," *ACS Nano,* vol. 4, pp. 3647-3652, 2010/07/27 2010.

[21] Y. Yang, W. Xiao-Juan, and L. Jing, "Suitability of a thermoelectric power generator for implantable medical electronic devices," *Journal of Physics D: Applied Physics,* vol. 40, pp. 5790-800, 2007.

[22] R. Kornbluh, H. Prahlad, R. Pelrine, S. Stanford, M. Rosenthal, and P. Von Guggenberg, "Rubber to rigid, clamped to undamped: Toward composite materials with wide-range controllable stiffness and damping," in *Smart Structures and Materials 2004 - Industrial and Commercial Applications of Smart Structures Technologies, March 16, 2004 - March 18, 2004*, San Diego, CA, United states, 2004, pp. 372-386.

[23] Q. G. Li, V. Naing, and J. M. Donelan, "Development of a biomechanical energy harvester," *Journal of Neuroengineering and Rehabilitation,* vol. 6, Jun 2009.

[24] J. Kymissis, C. Kendall, J. Paradiso, and N. Gershenfeld, "Parasitic power harvesting in shoes," in *Digest of Papers. Second International Symposium on Wearable Computers, 19-20 Oct. 1998*, Los Alamitos, CA, USA, 1998, pp. 132-9.

[25] R. Kornbluh, "Power from Plastic: How Electroactive Polymer "Artificial Muscles" will Improve Portable Power Generation in the 21st Century Military," ed, 2003.

[26] K. R. Acharya, G. F. Harris, S. A. Riedel, and L. Kazarian, "Force magnitude and spectral frequency content of heel strike during gait," in *Images of the Twenty-First Century. Proceedings of the Annual International Conference of the IEEE Engineering in Medicine and Biology Society (Cat. No.89CH2770-6), 9-12 Nov. 1989*, New York, NY, USA, 1989, pp. 826-7.

[27] L. C. Rome, L. Flynn, E. M. Goldman, and T. D. Yoo, "Biophysics: Generating electricity while walking with loads," *Science,* vol. 309, pp. 1725-1728, 2005.

[28] P. Niu, P. Chapman, L. DiBerardino, and E. Hsiao-Wecksler, "Design and optimization of a biomechanical energy harvesting device," in *Power Electronics Specialists Conference, 2008. PESC 2008. IEEE*, 2008, pp. 4062-4069.

[29] J. K. Hitt, T. G. Sugar, M. Holgate, and R. Bellman, "An Active Foot-Ankle Prosthesis With Biomechanical Energy Regeneration," *Journal of Medical Devices,* vol. 4, p. 011003 (9 pp.), 2010.

[30] Z. Rubinshtein, R. Riemer, and S. Ben-Yaakov, "Modeling and analysis of brushless generator based biomechanical energy harvesting system," in *2012 IEEE Energy*

Conversion Congress and Exposition (ECCE), 15-20 Sept. 2012, Piscataway, NJ, USA, 2012, pp. 2784-9.

[31] M. Pozzi, M. S. H. Aung, M. Zhu, R. K. Jones, and J. Y. Goulermas, "The pizzicato knee-joint energy harvester: Characterization with biomechanical data and the effect of backpack load," *Smart Materials and Structures,* vol. 21, 2012.

[32] C. Jean-Mistral, S. Basrour, and J. J. Chaillout, "Dielectric polymer: scavenging energy from human motion," in *Electroactive Polymer Actuators and Devices (EAPAD) 2008, 10 March 2008*, USA, 2008, pp. 692716-1.

[33] C. Jean-Mistral and S. Basrour, "Scavenging energy from human motion with tubular dielectric polymer," in *Electroactive Polymer Actuators and Devices (EAPAD) 2010, 8 March 2010*, USA, 2010, p. 764209 (12 pp.).

[34] J. R. Slade, J. Bowman, and R. Kornbluh, "Bio-kinetic energy harvesting using electroactive polymers," in *Head- and Helmet-Mounted Displays XVII; and Display Technologies and Applications for Defense, Security, and Avionics VI, April 25, 2012 - April 26, 2012*, Baltimore, MD, United states, 2012, pp. The Society of Photo-Optical Instrumentation Engineers (SPIE).

[35] K. M. Farinholt, N. Miller, W. Sifuentes, J. MacDonald, P. Gyuhae, and C. R. Farrar, "Energy Harvesting and Wireless Energy Transmission for Embedded SHM Sensor Nodes," *Structural Health Monitoring,* vol. 9, pp. 269-80, 2010.

[36] D. Dondi, A. Di Pompeo, C. Tenti, and T. i. Rosing, "Shimmer: A wireless harvesting embedded system for active ultrasonic structural health monitoring," in *9th IEEE Sensors Conference 2010, SENSORS 2010, November 1, 2010 - November 4, 2010*, Waikoloa, HI, United states, 2010, pp. 2325-2328.

[37] S. W. Arms, J. H. Galbreath, C. P. Townsend, D. L. Churchill, B. Corneau, R. P. Ketcham, *et al.*, "Energy harvesting wireless sensors and networked timing synchronization for aircraft structural health monitoring," in *2009 1st International Conference on Wireless Communication, Vehicular Technology, Information Theory and Aerospace & Electronic Systems Technology (Wireless VITAE), 17-20 May 2009*, Piscataway, NJ, USA, 2009, pp. 16-20.

[38] C. A. Featherston, K. M. Holford, and B. Greaves, "Harvesting vibration energy for structural health monitoring in aircraft," *Key Engineering Materials,* vol. 413-414, pp. 439-46, 2009.

[39] Y. Xuan, Z. Zhao, Z. Fang, D. Geng, and Y. Shi, "3ACare: A wireless body sensor network for health alert and monitoring," in *2011 1st International Conference on High Performance Structures and Materials Engineering, ICHPSM 2011, May 5, 2011 - May 6, 2011*, Beijing, China, 2011, pp. 1075-1080.

[40] U. Anliker, J. A. Ward, P. Lukowicz, G. Troster, F. Dolveck, M. Baer, *et al.*, "AMON: A wearable multiparameter medical monitoring and alert system," *IEEE Transactions on Information Technology in Biomedicine,* vol. 8, pp. 415-427, 2004.

[41] M. Di Rienzo, F. Rizzo, G. Parati, G. Brambilla, M. Ferratini, and P. Castiglioni, "MagIC system: a new textile-based wearable device for biological signal monitoring. Applicability in daily life and clinical setting," in *2005 27th Annual International Conference of the IEEE Engineering in Medicine and Biology Society, 31 Aug.-3 Sept. 2005*, Piscataway, NJ, USA, 2006, p. 3 pp.

[42] G. Lopez, V. Custodio, and J. I. Moreno, "LOBIN: E-Textile and Wireless-Sensor-Network-Based Platform for Healthcare Monitoring in Future Hospital Environments,"

IEEE Transactions on Information Technology in Biomedicine, vol. 14, pp. 1446-58, 2010.

[43] G. Kwakkel, R. C. Wagenaar, J. W. Twisk, G. J. Lankhorst, and J. C. Koetsier, "Intensity of leg and arm training after primary middle-cerebral-artery stroke: a randomised trial," *Lancet,* vol. 354, pp. 191-6, Jul 17 1999.

[44] S. Chalupka, "Internet-based outpatient telerehabilitation following total knee arthroplasty," *AAOHN J,* vol. 59, p. 144, Mar 2011.

[45] V. H. Hermann, M. Herzog, R. Jordan, M. Hofherr, P. Levine, and S. J. Page, "Telerehabilitation and electrical stimulation: an occupation-based, client-centered stroke intervention," *Am J Occup Ther,* vol. 64, pp. 73-81, Jan-Feb 2010.

[46] T. G. Russell, P. Buttrum, R. Wootton, and G. A. Jull, "Internet-based outpatient telerehabilitation for patients following total knee arthroplasty: a randomized controlled trial," *J Bone Joint Surg Am,* vol. 93, pp. 113-20, Jan 19 2011.

[47] W. Durfee, J. Carey, D. Nuckley, and J. Deng, "Design and implementation of a home stroke telerehabilitation system," *Conf Proc IEEE Eng Med Biol Soc,* vol. 2009, pp. 2422-5, 2009.

[48] D. Fitzgerald, J. Foody, D. Kelly, T. Ward, C. Markham, J. McDonald*, et al.*, "Development of a wearable motion capture suit and virtual reality biofeedback system for the instruction and analysis of sports rehabilitation exercises," *Conf Proc IEEE Eng Med Biol Soc,* vol. 2007, pp. 4870-4, 2007.

[49] J. Ko, C. Lu, M. B. Srivastava, J. A. Stankovic, A. Terzis, and M. Welsh, "Wireless Sensor Networks For Healthcare," *Proceedings of the IEEE,* vol. 98, pp. 1947-60, 2010.

[50] P. D. Mitcheson, E. M. Yeatman, G. K. Rao, A. S. Holmes, and T. C. Green, "Energy harvesting from human and machine motion for wireless electronic devices," *Proceedings of the IEEE,* vol. 96, pp. 1457-86, 2008.

[51] J. S. Plante and S. Dubowsky, "On the performance mechanisms of Dielectric Elastomer Actuators," *Sensors and Actuators A (Physical),* vol. 137, pp. 96-109, 2007.

[52] S. K. Sabut and M. Manjunatha, "Neuroprosthesis-functional electrical stimulation: Opportunities in clinical application for correction of drop-foot," in *1st International Conference on Emerging Trends in Engineering and Technology, ICETET 2008, July 16, 2008 - July 18, 2008*, Nagpur, Maharashtra, India, 2008, pp. 950-953.

[53] B. Khattar, A. Banerjee, R. Reddi, and A. Dutta, "Feasibility of Functional Electrical Stimulation-Assisted Neurorehabilitation following Stroke in India: A Case Series," *Case Report Neurol Med,* vol. 2012, p. 830873, 2012.

[54] S. K. Sabut, C. Sikdar, R. Kumar, and M. Mahadevappa, "Improvement of gait & muscle strength with functional electrical stimulation in sub-acute & chronic stroke patients," *Conf Proc IEEE Eng Med Biol Soc,* vol. 2011, pp. 2085-8, 2011.

[55] L. A. Prosser, L. A. Curatalo, K. E. Alter, and D. L. Damiano, "Acceptability and potential effectiveness of a foot drop stimulator in children and adolescents with cerebral palsy," *Dev Med Child Neurol,* vol. 54, pp. 1044-9, Nov 2012.

[56] M. H. Cameron and J. M. Wagner, "Gait abnormalities in multiple sclerosis: pathogenesis, evaluation, and advances in treatment," *Curr Neurol Neurosci Rep,* vol. 11, pp. 507-15, Oct 2011.

[57] Y. J. Chang, M. J. Hsu, S. M. Chen, C. H. Lin, and A. M. Wong, "Decreased central fatigue in multiple sclerosis patients after 8 weeks of surface functional electrical stimulation," *J Rehabil Res Dev,* vol. 48, pp. 555-64, 2011.

[58] A. M. Courtney, W. Castro-Borrero, S. L. Davis, T. C. Frohman, and E. M. Frohman, "Functional treatments in multiple sclerosis," *Curr Opin Neurol,* vol. 24, pp. 250-4, Jun 2011.

[59] S. K. Sabut, R. Kumar, P. K. Lenka, and M. Mahadevappa, "Surface EMG analysis of tibialis anterior muscle in walking with FES in stroke subjects," in *2010 32nd Annual International Conference of the IEEE Engineering in Medicine and Biology Society (EMBC 2010), 31 Aug.-4 Sept. 2010*, Piscataway, NJ, USA, 2010, pp. 5839-42.

[60] R. B. Stein, D. G. Everaert, A. K. Thompson, S. L. Chong, M. Whittaker, J. Robertson*, et al.*, "Long-term therapeutic and orthotic effects of a foot drop stimulator on walking performance in progressive and nonprogressive neurological disorders," *Neurorehabil Neural Repair,* vol. 24, pp. 152-67, Feb 2010.

[61] G. Zhu, A. C. Wang, Y. Liu, Y. Zhou, and Z. L. Wang, "Functional Electrical Stimulation by Nanogenerator with 58 V Output Voltage," *Nano letters,* vol. 12, pp. 3086-3090, 2012.

[62] H. M. Herr and R. D. Kornbluh, "New horizons for orthotic and prosthetic technology: artificial muscle for ambulation," in *Smart Structures and Materials 2004. Electroactive Polymer Actuators and Devices (EAPAD), 15-18 March 2004*, USA, 2004, pp. 1-9.

[63] A. Anders. (2006, 4/3/2011). *Energy for Free - Wireless Technology without Batteries*. Available: http://www.enocean.com/fileadmin/redaktion/pdf/white_paper/wp_energyforfree_en.pdf

[64] MicroStrain. (2011). *EH-Link: 2.4 GHz Energy Harvesting Wireless Sensor Node Data Sheet*. Available: http://www.microstrain.com/product_datasheets/EH-Link-Data-Sheet.pdf

[65] S. W. Arms, C. P. Townsend, J. H. Galbreath, D. L. Churchill, and N. Phan, "Synchronized system for wireless sensing, RFID, data aggregation, remote reporting," in *65th Annual Forum Proceedings - AHS International, May 27, 2009 - May 29, 2009*, Grapevine, TX, United states, 2009, pp. 939-945.

[66] G. Park, T. Rosing, M. Todd, C. Farrar, and W. Hodgkiss, "Energy Harvesting for Structural Health Monitoring Sensor Networks," *Journal of Infrastructure Systems,* vol. 14, pp. 64-79, 2008/03/01 2008.

[67] S. W. Arms, C. P. Townsend, D. L. Churchill, S. M. Moon, and N. Phan, "Energy harvesting wireless sensors for helicopter damage tracking," in *AHS Internaitonal 62nd Annual Forum, May 9, 2006 - May 11, 2006*, Phoenix, AZ, United states, 2006, pp. 1336-1341.

[68] P. J. Sloetjes and A. De Boer, "Vibration reduction and power generation with piezoceramic sheets mounted to a flexible shaft," *Journal of Intelligent Material Systems and Structures,* vol. 19, pp. 25-34, 2008.

[69] J. Wilhelm and R. Rajamani, "Methods for multimodal vibration suppression and energy harvesting using piezoelectric actuators," *Journal of Vibration and Acoustics,* vol. 131, p. 011001 (11 pp.), 2009.

[70] E. Daoutova. (4/3/2011). *BionicPower: Military Applications*. Available: http://www.bionic-power.com/app_military.html

[71] S. W. Arms, Townsend C.P., Churchill, D.L., Hamel, M.J., Augustin, and Y. M., D., Phan, N, in *International Workshop on Structural Health Monitoring*, Stanford, CA, 2007, pp. 1741-1748.

[72] S. W. Arms, C. P. Townsend, D. L. Churchill, J. H. Galbreath, B. Corneau, R. P. Ketcham, *et al.*, "ENERGY HARVESTING, WIRELESS, STRUCTURAL HEALTH MONITORING and REPORTING SYSTEM " in *2nd Asia-Pacific Workshop on SHM, Melbourne, 2-4 December 2008* Melbourne, Austrailia, 2008.

[73] K. Sangani, "The sun in your pocket [Solar power for electronic consumer devices]," *Engineering & Technology,* vol. 2, pp. 36-8, 08/ 2007.

[74] F. Fei and W. J. Li, "A fluttering-to-electrical energy transduction system for consumer electronics applications," in *2009 IEEE International Conference on Robotics and Biomimetics, ROBIO 2009, December 19, 2009 - December 23, 2009*, Guilin, China, 2009, pp. 580-585.

[75] J. Marek, "MEMS for Automotive and Consumer Electronics," in *2010 IEEE International Solid-State Circuits Conference - (ISSCC), 7-11 Feb. 2010*, Piscataway, NJ, USA, 2010, pp. 9-17.

[76] R. Pelrine, R. Kornbluh, J. Joseph, R. Heydt, Q. Pei, and S. Chiba, "High-field deformation of elastomeric dielectrics for actuators," *Materials Science & Engineering C, Biomimetic and Supramolecular Systems,* vol. C11, pp. 89-100, 2000.

[77] K. Meijer, M. Rosenthal, and R. J. Full, "Muscle-like actuators? A comparison between three electroactive polymers," in *Smart Structures and Materials 2001: Electroactive Polymer Actuators and Devices, 5-8 March 2001*, USA, 2001, pp. 7-15.

[78] J. Kwangmok, J. H. Lee, M. S. Cho, J. C. Koo, J.-d. Nam, Y. K. Lee, *et al.*, "Development of enhanced synthetic rubber for energy efficient polymer actuators," in *Smart Structures and Materials 2006: Electroactive Polymer Actuators and Devices (EAPAD), 27 Feb. 2006*, USA, 2006, pp. 61680-1.

[79] R. Shankar, T. K. Ghosh, and R. J. Spontak, "Dielectric elastomers as next-generation polymeric actuators," *Soft Matter,* vol. 3, pp. 1116-1129, 2007.

[80] M. Matysek, P. Lotz, K. Flittner, and H. F. Schlaak, "High-precision characterization of dielectric elastomer stack actuators and their material parameters," in *Electroactive Polymer Actuators and Devices (EAPAD) 2008, March 10, 2008 - March 13, 2008*, San Diego, CA, United states, 2008, pp. 692722-1 (10 pages).

[81] A. Rajamani, M. D. Grissom, C. D. Rahn, and Q. Zhang, "Wound roll dielectric elastomer actuators: Fabrication, analysis, and experiments," *IEEE/ASME Transactions on Mechatronics,* vol. 13, pp. 117-124, 2008.

[82] T. A. Gisby, S. Xie, E. P. Calius, and I. A. Anderson, "Integrated sensing and actuation of muscle-like actuators," in *Electroactive Polymer Actuators and Devices (EAPAD) 2009, March 9, 2009 - March 12, 2009*, San Diego, CA, United states, 2009, pp. 728707-1(12 pages).

[83] G. Kovacs and L. During, "Contractive tension force stack actuator based on soft dielectric EAP," in *Electroactive Polymer Actuators and Devices (EAPAD) 2009, March 9, 2009 - March 12, 2009*, San Diego, CA, United states, 2009, pp. 72870A1-15.

[84] E. Biddiss and T. Chau, "Dielectric elastomers as actuators for upper limb prosthetics: Challenges and opportunities," *Medical Engineering and Physics,* vol. 30, pp. 403-418, 2008.

[85] B. M. O'Brien, E. P. Calius, T. Inamura, S. Q. Xie, and I. A. Anderson, "Dielectric elastomer switches for smart artificial muscles," *Applied Physics A: Materials Science and Processing,* vol. 100, pp. 385-389, 2010.

[86] S. Chiba, M. Waki, R. Kornbluh, and R. Pelrine, "Innovative power generators for energy harvesting using electroactive polymer artificial muscles," in *Electroactive Polymer Actuators and Devices (EAPAD) 2008, March 10, 2008 - March 13, 2008*, San Diego, CA, United states, 2008, pp. 692715-1 (9 pages).

[87] S. Chiba, M. Waki, K. Masuda, and T. Ikoma, "Current status and future prospects of electric generators using electroactive polymer artificial muscle," in *OCEANS'10 IEEE Sydney, OCEANSSYD 2010, May 24, 2010 - May 27, 2010*, Sydney, NSW, Australia, 2010.

[88] I. A. Anderson, I. A. Ieropoulos, T. McKay, B. O'Brien, and C. Melhuish, "Power for robotic artificial muscles," *IEEE/ASME Transactions on Mechatronics,* vol. 16, pp. 107-111, 2011.

[89] R. Pelrine, R. Kornbluh, Q. Pei, S. Stanford, S. Oh, J. Eckerle*, et al.*, "Dielectric elastomer artificial muscle actuators: Toward biomimetic motion," in *Smart Structures and Materials 2002: Electroactive Polymer Actuators and Devices (EAPAD), March 18, 2002 - March 21, 2002*, San Diego, CA, United states, 2002, pp. 126-137.

[90] Y. H. Iskandarani, R. W. Jones, and E. Villumsen, "Modeling and experimental verification of a dielectric polymer energy scavenging cycle," in *Electroactive Polymer Actuators and Devices (EAPAD) 2009, 9 March 2009*, USA, 2009, p. 72871Y (12 pp.).

[91] P. Brochu, H. Li, X. Niu, and Q. Pei, "Factors influencing the performance of dielectric elastomer energy harvesters," in *Electroactive Polymer Actuators and Devices (EAPAD)*

2010, March 8, 2010 - March 11, 2010, San Diego, CA, United states, 2010, pp. 76422J-1 (12 pages).

[92] G. Gallone, F. Carpi, F. Galantini, D. De Rossi, and G. Levita, "Enhancing the electro-mechanical response of Maxwell stress actuators," in *3rd International Conference on Smart Materials, Structures and Systems - Artificial Muscle Actuators using Electroactive Polymers, CIMTEC 2008, June 8, 2008 - June 13, 2008*, Acireale, Sicily, Italy, 2008, pp. 46-52.

[93] G. Gallone, F. Galantini, and F. Carpi, "Perspectives for new dielectric elastomers with improved electromechanical actuation performance: Composites versus blends," *Polymer International,* vol. 59, pp. 400-406, 2010.

[94] A. K. Geim, "Graphene: status and prospects," *Science,* vol. 324, pp. 1530-4, 2009.

[95] K. Min, J. Y. Jung, T. H. Han, Y. Park, C. Jung, S. M. Hong*, et al.*, "Graphene Electrodes for Artificial Muscles," *Molecular Crystals and Liquid Crystals,* vol. 539, pp. 260-5, 2011.

[96] M. F. L. De Volder, S. H. Tawfick, R. H. Baughman, and A. J. Hart, "Carbon nanotubes: present and future commercial applications," *Science,* vol. 339, pp. 535-9, 02/01 2013.

[97] W. Yuan, L. Hu, S. Ha, T. Lam, G. Gruner, and Q. Pei, "Self-clearable carbon nanotube electrodes for improved performance of dielectric elastomer actuators," in *Electroactive Polymer Actuators and Devices (EAPAD) 2008, March 10, 2008 - March 13, 2008*, San Diego, CA, United states, 2008, p. The International Society for Optical Engineering (SPIE); American Society of Mechanical Engineers.

[98] W. Yuan, H. Li, P. Brochu, X. Niu, and Q. Pei, "Fault-tolerant silicone dielectric elastomers," *International Journal of Smart and Nano Materials,* vol. 1, pp. 40-52, 2010.

[99] H.-Y. Kwon, A. Kuang Jun, K. Junmo, P. Vuong Hong, T. Nguyen Canh, K. Baek Chul, *et al.*, "Transparent Active Skin," in *Electroactive Polymer Actuators and Devices (EAPAD) 2011, 7-10 March 2011*, USA, 2011, p. 79760T (8 pp.).

[100] T. McKay, B. O'Brien, E. Calius, and I. Anderson, "Self-priming dielectric elastomer generators," *Smart Materials and Structures,* vol. 19, p. 055025 (7 pp.), 2010.

[101] S. Bae, K. Hyeongkeun, L. Youngbin, X. Xiangfan, P. Jae-Sung, Z. Yi, *et al.*, "Roll-to-roll production of 30-inch graphene films for transparent electrodes," *Nature Nanotechnology,* vol. 5, pp. 47-51, 2010.

[102] H. Shen, H. Ji, J. Qiu, and K. Zhu, "A semi-passive vibration damping system powered by harvested energy," *International Journal of Applied Electromagnetics and Mechanics,* vol. 31, pp. 219-233, 2009.

[103] J. H. Qiu, H. L. Ji, and H. Shen, "Energy harvesting and vibration control using piezoelectric elements and a nonlinear approach," in *2009 18th IEEE International Symposium on the Applications of Ferroelectrics, ISAF 2009, August 23, 2009 - August 27, 2009*, Xian, China, 2009.

[104] S. Zhu, W.-a. Shen, and Y.-l. Xu, "Linear electromagnetic devices for vibration damping and energy harvesting: Modeling and testing," *Engineering Structures,* vol. 34, pp. 198-212, 2012.

[105] F. Massaad, T. M. Lejeune, and C. Detrembleur, "The up and down bobbing of human walking: a compromise between muscle work and efficiency (vol 582, pg 789, 2007)," *Journal of Physiology-London,* vol. 583, pp. 413-413, Aug 2007.

[106] D. A. Winter, A. E. Patla, J. S. Frank, and S. E. Walt, "BIOMECHANICAL WALKING PATTERN CHANGES IN THE FIT AND HEALTHY ELDERLY," *Physical Therapy,* vol. 70, pp. 340-347, Jun 1990.

[107] B. G. A. Lambrecht and H. Kazerooni, "Design of a semi-active knee prosthesis," in *2009 IEEE International Conference on Robotics and Automation, ICRA '09, May 12, 2009 - May 17, 2009*, Kobe, Japan, 2009, pp. 639-645.

[108] Q. Li, V. Naing, J. A. Hoffer, D. J. Weber, A. D. Kuo, and J. M. Donelan, "Biomechanical energy harvesting: Apparatus and method," in *2008 IEEE International Conference on Robotics and Automation, ICRA 2008, May 19, 2008 - May 23, 2008*, Pasadena, CA, United states, 2008, pp. 3672-3677.

[109] T. McKay, B. O'Brien, E. Calius, and I. Anderson, "An integrated dielectric elastomer generator model," in *Electroactive Polymer Actuators and Devices (EAPAD) 2010, March 8, 2010 - March 11, 2010*, San Diego, CA, United states, 2010, pp. The Society of Photo-Optical Instrumentation Engineers (SPIE); American Society of Mechanical Engineers.

[110] G.-K. Lau, S. C.-K. Goh, and L.-L. Shiau, "Dielectric elastomer unimorph using flexible electrodes of electrolessly deposited (ELD) silver," *Sensors and Actuators, A: Physical,* vol. 169, pp. 234-241, 2011.

[111] C. Jean-Mistral, S. Basrour, and J. J. Chaillout, "Modelling of dielectric polymers for energy scavenging applications," *Smart Materials and Structures,* vol. 19, p. 105006 (11 pp.), 2010.

[112] M. Benslimane, M. J. Tryson, J. Oubak, and H.-E. Kiil, "Scalable design of DEAP for energy harvesting utilizing PolyPower," 2011, p. 79760I.

[113] P. Lochmatter, G. Kovacs, and S. Michel, "Characterization of dielectric elastomer actuators based on a hyperelastic film model," *Sensors and Actuators, A: Physical,* vol. 135, pp. 748-757, 2007.

[114] L. Liu, S. Shouhua, Y. Kai, L. Bo, L. Yanju, and L. Jinsong, "The area of allowable states in Mooney-Rivlin type dielectric elastomer generators," in *Electroactive Polymer Actuators and Devices (EAPAD) 2010, 8 March 2010*, USA, 2010, p. 764238 (8 pp.).

[115] C. Graf, M. Aust, J. Maas, and D. Schapeler, "Simulation Model for Electro Active Polymer Generators," in *2010 10th IEEE International Conference on Solid Dielectrics (ICSD 2010), 4-9 July 2010*, Piscataway, NJ, USA, 2010, p. 4 pp.

[116] P. A. L. S. Martins, R. M. Natal Jorge, and A. J. M. Ferreira, "A comparative study of several material models for prediction of hyperelastic properties: application to silicone-rubber and soft tissues," *Strain,* vol. 42, pp. 135-47, 2006.

[117] M. Wissler and E. Mazza, "Modeling of a pre-strained circular actuator made of dielectric elastomers," *Sensors and Actuators, A: Physical,* vol. 120, pp. 184-192, 2005.

[118] M. Wissler and E. Mazza, "Modeling and simulation of dielectric elastomer actuators," *Smart Materials and Structures,* vol. 14, pp. 1396-1402, 2005.

[119] C. Hackl, H.-Y. Tang, R. D. Lorenz, L.-S. Turng, and D. Schroder, "A multi-physics model of planar electro-active polymer actuators," in *Conference Record of the 2004 IEEE Industry Applications Conference; 39th IAS Annual Meeting, October 3, 2004 - October 7, 2004*, Seattle, WA, United states, 2004, pp. 2125-2130.

[120] C. Graf, J. Maas, and D. Schapeler, "Energy harvesting cycles based on electro active polymers," in *Electroactive Polymer Actuators and Devices (EAPAD) 2010, March 8, 2010 - March 11, 2010*, San Diego, CA, United states, 2010, pp. 764217-1 (12 pages).

[121] Danfoss. (2012). Available: http: // www. polypower.com/ Technology/Overview/ PolyPower+DEAP+Technology/ PolyPower+DEAP+material.htm

[122] Z. Suo, "Theory of dielectric elastomers," *Acta Mechanica Solida Sinica,* vol. 23, pp. 549-578, 2010.

[123] R. Kaltseis, C. Keplinger, R. Baumgartner, M. Kaltenbrunner, L. Tiefeng, P. Machler*, et al.*, "Method for measuring energy generation and efficiency of dielectric elastomer generators," *Applied Physics Letters,* vol. 99, p. 162904 (3 pp.), 2011.

[124] S. J. A. Koh, C. Keplinger, T. Li, S. Bauer, and Z. Suo, "Dielectric Elastomer Generators: How Much Energy Can Be Converted?," *IEEE/ASME Transactions on Mechatronics,* vol. 16, pp. 33-41, 2011.

[125] G. Kofod, P. Sommer-Larsen, R. Kornbluh, and R. Pelrine, "Actuation response of polyacrylate dielectric elastomers," *Journal of Intelligent Material Systems and Structures,* vol. 14, pp. 787-793, 2003.

[126] G. Gallone, F. Carpi, D. De Rossi, G. Levita, and A. Marchetti, "Dielectric constant enhancement in a silicone elastomer filled with lead magnesium niobate-lead titanate," *Materials Science and Engineering C,* vol. 27, pp. 110-116, 2007.

[127] M. R. Begley and H. Bart-Smith, "The electro-mechanical response of highly compliant substrates and thin stiff films with periodic cracks," *International Journal of Solids and Structures,* vol. 42, pp. 5259-73, 2005.

[128] C. Graf and J. Maas, "Evaluation and optimization of energy harvesting cycles using dielectric elastomers," 2011, p. 79760H.

[129] T. Lu, J. Huang, C. Jordi, G. Kovacs, R. Huang, D. R. Clarke*, et al.*, "Dielectric elastomer actuators under equal-biaxial forces, uniaxial forces, and uniaxial constraint of stiff fibers," *Soft Matter,* 2012.

[130] G. A. Lesieutre, G. K. Ottman, and H. F. Hofmann, "Damping as a result of piezoelectric energy harvesting," *Journal of Sound and Vibration,* vol. 269, pp. 991-1001, 2004.

[131] J. Liang and W.-H. Liao, "Energy harvesting and dissipation with piezoelectric materials," Zhangjiajie, Hunan, China, 2008, pp. 446-451.

[132] J. R. Liang and W. H. Liao, "Piezoelectric energy harvesting and dissipation on structural damping," *Journal of Intelligent Material Systems and Structures,* vol. 20, pp. 515-27, 2009.

[133] N. W. Hagood and A. Von Flotow, "Damping of structural vibrations with piezoelectric materials and passive electrical networks," *Journal of Sound and Vibration,* vol. 146, pp. 243-268, 1991.

[134] C. Graf and J. Maas, "Electroactive polymer devices for active vibration damping," 2011, p. 79762I.

[135] R. Lakes, *Viscoelastic Materials*. Cambridge: Cambridge University Press, 2009.

[136] K. P. Menard, *Dynamic mechanical analysis : a practical introduction*. Boca Raton, Fla.: CRC Press, 1999.

[137] A. M. Hollister, S. Jatana, A. K. Singh, W. W. Sullivan, and A. G. Lupichuk, "The axes of rotation of the knee," *Clin Orthop Relat Res,* pp. 259-68, May 1993.

[138] H. Iwaki, V. Pinskerova, and M. A. Freeman, "Tibiofemoral movement 1: the shapes and relative movements of the femur and tibia in the unloaded cadaver knee," *J Bone Joint Surg Br,* vol. 82, pp. 1189-95, Nov 2000.

[139] S. Nakagawa, Y. Kadoya, S. Todo, A. Kobayashi, H. Sakamoto, M. A. Freeman*, et al.*, "Tibiofemoral movement 3: full flexion in the living knee studied by MRI," *J Bone Joint Surg Br,* vol. 82, pp. 1199-200, Nov 2000.

[140] C. A. Oatis, "The use of a mechanical model to describe the stiffness and damping characteristics of the knee joint in healthy adults," *Phys Ther,* vol. 73, pp. 740-9, Nov 1993.

[141] C. A. Oatis, "Correction," *Physical Therapy,* vol. 85, pp. 1390-1391, 2005.

[142] D. A. Winter, *Biomechanics and motor control of human movement*: Wiley, 2009.

[143] T. F. Novacheck, "The biomechanics of running," *Gait & posture,* vol. 7, pp. 77-95, 1998.

[144] J. J. Eng and D. A. Winter, "Kinetic analysis of the lower limbs during walking: what information can be gained from a three-dimensional model?," *Journal of Biomechanics,* vol. 28, pp. 753-8, 1995.

[145] F. Galantini, G. Gallone, F. Carpi, G. Levita, and D. De Rossi, "Soft elastomeric electrets for electro-active polymers," in *2011 IEEE 14th International Symposium on Electrets, 28-31 Aug. 2011*, Piscataway, NJ, USA, 2011, pp. 31-2.

[146] F. Galantini, G. Gallone, and F. Carpi, "Effects of Corona treatment on electrical and mechanical properties of a porous dielectric elastomer," *IEEE Transactions on Dielectrics and Electrical Insulation,* vol. 19, pp. 1203-7, 08/ 2012.

[147] C. Jean-Mistral, T. Vu Cong, and A. Sylvestre, "Advances for dielectric elastomer generators: Replacement of high voltage supply by electret," *Applied Physics Letters,* vol. 101, pp. 162901-162901-5, 2012.

[148] A. N. Gent, "New constitutive relation for rubber," *Rubber Chemistry and Technology,* vol. 69, pp. 59-59, 1996.

[149] M. Y. Benslimane, "Dielectric electro-active polymer push actuators: performance and challenges," *Polymer international,* vol. 59, pp. 415-421, 03 2010.

ABSTRACT

INDUCED DAMPING AND ITS RELATIONSHIP TO BENEFICIAL ENERGY HARVESTING IN DIELECTRIC ELASTOMERS WITH APPLICATION TO WALKING

by

HEATHER LOUISE LAI

May 2013

Advisor: Dr. Chin An Tan

Major: Mechanical Engineering

Degree: Doctor of Philosophy

This dissertation presents a novel, interdisciplinary research which addresses the potential of applying soft polymeric materials to strategically harvest biomechanical energy in a beneficial manner for use as a viable, low power source for on-board electronics. Of particular interest are electroactive polymers (EAP), which unlike other types of electromechanical smart materials such as piezoelectric ceramics, which are often brittle, have low elastic modulus and can exhibit large strains without substantial stress generations. One type of EAP, the dielectric elastomer (DE), which utilizes electrostatic forces built up across the dielectric polymer to convert between electrical and mechanical energy, is employed in this research. As with most EAPs, DE materials are highly nonlinear and require novel models to understand the electromechanical coupling and the effects of energy harvesting on the host structure which it is attached to.

Since energy harvesting fundamentally involves harnessing the dissipative energy in a system, this research specifically investigates the relationship between biomechanical damping and energy harvesting induced by DE thin films affixed to the knee and operated during walking. This research has three objectives: (1) energy harvesting characterization of composite

electrode/DE polymers under uniaxial stretching and electrical loading by improved hyperelastic modeling and experiments; (2) development of relationships between energy harvesting and damping for the DE materials in uniaxial stretching and on a biofidelic knee model; and (3) investigation of the kinetic effects of beneficial DE energy harvesting during walking. Our empirical modeling leads to a more comprehensive constitutive relation for DE materials and allows a means to directly assess the effects of energy harvesting on the wearer. By selectively inducing damping through coordinated mechanical and electrical loading of the DE device, it is demonstrated through simulations that beneficial energy harvesting strategies that account for the various mechanisms of metabolisms and energy expenditure involved in walking can be archived.

This research is significant as it lays the foundation for future work in the integration of wearable technology using dielectric elastomers with sensing, actuation, and energy harvesting, and establishes a pathway for the integration of DE energy harvesting into a broad spectrum of applications where comfortable, inconspicuous, wearable devices can be designed to harvest energy in an unobtrusive manner.

AUTOBIOGRAPHICAL STATEMENT

Heather Lai is currently the undergraduate design instructor in the Biomedical Engineering Department at Wayne State University. She is interested in developing innovative educational constructs which facilitate the holistic development of engineering skills through student engagement with fundamental engineering principles using practical experimental and design initiatives. Her specific areas of interest include dynamics, vibration, computer interface and computational programming.

Education

Wayne State University Detroit, MI 2013
Doctor of Philosophy in Mechanical Engineering
Graduate Certificate in College and University Teaching

University of Illinois Urbana-Champaign, IL 1998
Masters degree in Mechanical Engineering

Case Western Reserve University Cleveland, Ohio 1996
Bachelor of Science in Mechanical Engineering

Publications / Conferences

"Dielectric elastomer energy harvesting and its application to human walking"
Lai, H. Tan, C.A., Xu, Y. ASME IMECE conference, Denver, CO, November 2011.

"Characterization of the effect of energy harvesting on the dynamic response of dielectric elastomers." Lai, H. Tan, C.A., Xu, Y.
SPIE Smart Structures/NDE Conference, San Diego, CA, February. 2011.

"Transfer Function Modeling of Distributed Piezoelectric Vibration Energy Harvesters,"
Tan, C. A., Heather L. Lai
ASME Internl. Design Engineering Technical Conference, San Diego, CA, Aug. 2009.

"Controller With Helical Spring Contacts," Patent number: WO/2002/017439, Feb. 28, 2002.
Alexander, Andrew, D.; Havlicsek, Heather, L.; Loewe, Kevin, C.; Zito, Donald, J.

"Nonlinear Control of an Electrohydraulic Injection Molding Machine via Iterative Adaptive Learning," Havlicsek, H. and A. Alleyne,
IEEE/ASME Transactions on Mechatronics, Vol. 4, No. 3, pp. 312-323, Sept. 1999.

"Nonlinear Modeling of an Electrohydraulic Injection Molding Machine"
Havlicsek, H., and Alleyne, A.
1999 American Controls conference, San Diego, CA, 171-175, Jun. 1999.

"Nonlinear control of an electrohydraulic injection molding machine via iterative learning"
Havlicsek, H.; Alleyne, A.
1999 American Controls conference, San Diego, CA, 176-181, Jun. 1999.